

Advanced dual-sided microstructured semiconductor neutron detectors
and instrumentation

by

Taylor R. Ochs

B.S., Kansas State University, 2015

AN ABSTRACT OF A DISSERTATION

submitted in partial fulfillment of the requirements for the degree

DOCTOR OF PHILOSOPHY

Department of Mechanical and Nuclear Engineering
Carl R. Ice College of Engineering

KANSAS STATE UNIVERSITY
Manhattan, Kansas

2020

Abstract

Dual-Sided Microstructured Semiconductor Neutron Detectors (DS-MSNDs) have been developed as a viable alternative to expensive ^3He for thermal-neutron detection. DS-MSNDs were designed as an advancement on single-sided MSNDs which comprise high-aspect ratio trenches backfilled with ^6LiF neutron conversion material etched deep into silicon *pvn*-junction diodes. Neutrons react in the conversion material, which produces energetic charged-particle reaction products that are measured in the adjacent silicon microfeatures. Single-sided MSNDs have been produced with an intrinsic thermal-neutron detection efficiency of 30-35% for normally incident neutrons, and the key limiting factor in detection efficiency is neutron free streaming paths through the neutron insensitive silicon fins. The DS-MSND incorporates a second set of ^6LiF -backfilled trenches etched on the back-side of a thicker silicon diode that are offset from the front-side trenches to eliminate the neutron free streaming paths. Monte Carlo simulations show DS-MSNDs only 1.5-mm thick are theoretically capable of 80% intrinsic thermal-neutron detection efficiency, which could directly match commonly available ^3He detectors. This work describes the design of DS-MSNDs including electric field modeling and microfeature geometry optimization with MCNP simulations, and fabrication process improvements implemented that elevate the state-of-the-art. The previous world record for intrinsic thermal-neutron detection efficiency for semiconductor neutron detectors was $53.5 \pm 0.6\%$. Advancements in deep-trench etching and ^6LiF backfilling methods presented herein have increased the current record intrinsic-thermal neutron detection efficiency to $69.3 \pm 1.5\%$.

Several prototype detector systems were fabricated implementing DS-MSND and MSND technology to aid in search and localization of special nuclear material. Drop-in replacements for small-diameter, high-pressure ^3He detectors, and the DS-MSND-based HeRep Mk IV measured 80% to 115% of the count rate of a similarly sized 10-atm ^3He detector based on the detector and source moderation configuration. Additionally, modular neutron detectors were developed for use in a high-sensitivity, low profile, wearable neutron detector for covert or overt source detection missions by warfighters, first responders, or law enforcement personnel. Additionally, MCNP simulations show the wearable detectors have potential to as operate as high-accuracy, real-time, neutron dose meters. The DS-MSND-based detector systems with on-board electronics offer a low-cost, low-power, compact, high sensitivity, alternative to ^3He neutron detection.

Advanced dual-sided microstructured semiconductor neutron detectors
and instrumentation

by

Taylor R. Ochs

B.S., Kansas State University, 2015

A DISSERTATION

submitted in partial fulfillment of the requirements for the degree

DOCTOR OF PHILOSOPHY

Department of Mechanical and Nuclear Engineering
Carl R. Ice College of Engineering

KANSAS STATE UNIVERSITY
Manhattan, Kansas

2020

Approved by:

Major Professor
Douglas S. McGregor

Copyright

© Taylor R. Ochs 2020.

Abstract

Dual-Sided Microstructured Semiconductor Neutron Detectors (DS-MSNDs) have been developed as a viable alternative to expensive ^3He for thermal-neutron detection. DS-MSNDs were designed as an advancement on single-sided MSNDs which comprise high-aspect ratio trenches backfilled with ^6LiF neutron conversion material etched deep into silicon *pvn*-junction diodes. Neutrons react in the conversion material, which produces energetic charged-particle reaction products that are measured in the adjacent silicon microfeatures. Single-sided MSNDs have been produced with an intrinsic thermal-neutron detection efficiency of 30-35% for normally incident neutrons, and the key limiting factor in detection efficiency is neutron free streaming paths through the neutron insensitive silicon fins. The DS-MSND incorporates a second set of ^6LiF -backfilled trenches etched on the back-side of a thicker silicon diode that are offset from the front-side trenches to eliminate the neutron free streaming paths. Monte Carlo simulations show DS-MSNDs only 1.5-mm thick are theoretically capable of 80% intrinsic thermal-neutron detection efficiency, which could directly match commonly available ^3He detectors. This work describes the design of DS-MSNDs including electric field modeling and microfeature geometry optimization with MCNP simulations, and fabrication process improvements implemented that elevate the state-of-the-art. The previous world record for intrinsic thermal-neutron detection efficiency for semiconductor neutron detectors was $53.5 \pm 0.6\%$. Advancements in deep-trench etching and ^6LiF backfilling methods presented herein have increased the current record intrinsic-thermal neutron detection efficiency to $69.3 \pm 1.5\%$.

Several prototype detector systems were fabricated implementing DS-MSND and MSND technology to aid in search and localization of special nuclear material. Drop-in replacements for small-diameter, high-pressure ^3He detectors, and the DS-MSND-based HeRep Mk IV measured 80% to 115% of the count rate of a similarly sized 10-atm ^3He detector based on the detector and source moderation configuration. Additionally, modular neutron detectors were developed for use in a high-sensitivity, low profile, wearable neutron detector for covert or overt source detection missions by warfighters, first responders, or law enforcement personnel. Additionally, MCNP simulations show the wearable detectors have potential to as operate as high-accuracy, real-time, neutron dose meters. The DS-MSND-based detector systems with on-board electronics offer a low-cost, low-power, compact, high sensitivity, alternative to ^3He neutron detection.

Table of Contents

List of Figures	xi
List of Tables	xxv
Abbreviations	xxviii
Acknowledgements	xxx
Chapter 1 - Introduction	1
1.1. Motivation for Detector Development	1
1.2. Contributions to DS-MSND Technology, Science, and Instrumentation	2
1.3. Organization of Thesis	3
Chapter 2 - Introduction to Neutron Detection	5
2.1. Discovery of the Neutron	5
2.2. Methods of Interaction	6
2.3. Review of Common Thermal Neutron Detectors	9
2.3.1. Gas-Filled Thermal-Neutron Detectors	9
2.3.2. Scintillation Neutron Detectors	11
2.3.3. Semiconductor Neutron Detectors	12
2.3.4. Design Considerations	12
Chapter 3 - Semiconductor Radiation Detectors Basics	14
3.1. Semiconductor Physical Properties	14
3.2. Semiconductor Depletion Region Formation	18
3.3. Charge Carrier Production and Signal Generation in Semiconductors	22
Chapter 4 - Dual-Sided Microstructured Semiconductor Neutron Detectors: Design	25
4.1. Design and Operation	25
4.1.1. Thin-Film Coated Semiconductor Detectors	25
4.1.2. Single-Sided Microstructured Semiconductor Neutron Detectors	26
4.1.3. Dual-Sided Microstructured Semiconductor Neutron Detectors	28
4.1.4. Design Considerations	29
Semiconductor	29
Neutron Conversion Material	30
Microfeature Geometry	31

4.2. Silvaco TCAD Simulations for Electrical Properties	32
4.2.1. MSND TCAD Simulations	34
Conformal <i>pvn</i> -MSNDs	35
Partial-Conformal <i>pvn</i> -MSNDs	37
4.2.2. DS-MSND TCAD Simulations.....	40
Conformal <i>pvp</i> -DS-MSND	40
Partial Conformal <i>pvp</i> -DS-MSND.....	43
Partial-Conformal <i>pvn</i> -DS-MSND	45
Partial-Conformal <i>pvp</i> -DS-MSND with <i>n</i> -ring	48
4.2.3. TCAD Simulations Summary	50
4.3. DS-MSND Detection Efficiency Optimization Simulations	51
4.3.1. Monte Carlo Simulation Overview	52
4.3.2. DS-MSND Simulation with MCNP6.....	54
Simulations for 50% Backfill Packing Fraction	55
¹⁰ B backfilled DS-MSNDs.....	56
¹⁰ B-Backfilled Offset Patterns	57
¹⁰ B-Backfilled Opaque Patterns	58
⁶ LiF-backfilled DS-MSNDs.....	60
⁶ LiF-Backfilled Offset Patterns.....	61
⁶ LiF-Backfilled Opaque Patterns	62
Angular Response	64
Gamma-Ray Sensitivity	66
Simulations for Variable Backfill Packing Fractions	68
Fabrication Considerations	71
Chapter 5 - Dual-Sided Microstructured Semiconductor Neutron Detectors: Fabrication and Characterization	74
5.1. Detector Fabrication	74
5.1.1. Silicon Processing.....	74
Oxide Growth.....	76
Photolithography and Oxide Etching.....	77
KOH Wet Etching.....	79

Junction Doping and Contact Metallization	83
Dopant Deposition	84
Dopant Diffusion	87
Contact Metallization.....	89
5.1.2. ⁶ LiF Backfilling.....	90
⁶ LiF Backfill Packing Fraction Measurement Methodology	91
⁶ LiF Powder Production.....	94
Powder Packing Considerations	95
⁶ LiF Powder Backfilling Methods	96
Centrifugal and Hand-packed Backfilling	97
Isostatic Press.....	100
Vibration Table (Dry)	101
Ink Roller Press.....	102
Suspended ⁶ LiF in Ultrasonic Vibration Bath followed Ink Roller Press	104
5.1.3. Diode Packaging	106
5.2. Detector Characterization	106
5.2.1. Electrical Properties	107
1-mm thick, <i>pvn</i> -DS-MSNDs	108
1-mm thick <i>pvp</i> -DS-MSNDs	108
1.5-mm thick <i>pvp</i> -DS-MSNDs	109
1.5-mm thick <i>pvp</i> - <i>n</i> -ring DS-MSNDs.....	110
5.2.2. Radiation Sensitivity.....	110
Alpha-Particle Measurements.....	110
Neutron Measurements	113
Diffracted Neutron Beam Port Measurements.....	113
Moderated ²⁵² Cf Measurements	116
Gamma-Ray Measurements.....	118
5.3. Other MSND and DS-MSND Variants	120
5.3.1. Fast Charge Collection MSNDs.....	120
Co-Doped MSNDs.....	120
Alternating Trench MSNDs.....	123

L-Shaped Doping Profile MSND.....	127
5.3.2. Other DS-MSND Variants	129
Interdigitated DS-MSND	129
LL-Shaped Doping Profile DS-MSND.....	131
Spin-on-Dopant DS-MSND.....	132
Chapter 6 - Microstructured Semiconductor Neutron Detectors Instruments: Design and Characterization.....	133
6.1. Direct ³ He-Replacement (HeRep) Detectors	134
6.1.1. HeRep Mk III	134
6.1.2. HeRep Mk IV	137
6.1.3. HeRep Mk V	140
6.2. Modular Neutron Detectors (MND)	141
6.2.1. MND Mk III.....	141
6.2.2. MRD Mk I.....	144
6.3. Wearable Radiation Detectors	147
6.3.1. WDD V.1	148
6.3.2. Wired WDD V.2	153
6.3.3. Wireless WDD V.2	156
6.3.4. Reconfigurable Wearable Detector (RWD).....	160
RWD MCNP Simulations.....	161
Simulation of RWD with MRDs Utilizing DS-MSND	162
Point Source Localization	169
6.3.5. Neutron Dosimetry Capabilities of the RWD.....	170
Neutron Dosimetry Overview.....	171
Single Channel RWD Neutron Dosimeter	174
Multi-Channel RWD Neutron Dosimeter	176
Chapter 7 - Conclusions.....	179
References.....	182
List of Publications (as of March 2020)	194
Appendix A - TCAD Simulations	196
Example TCAD Command File Partial Conformal <i>pvp</i> -DS-MSND with <i>n</i> -ring.....	196

Example TCAD input file to calculate internal potential and electric field	199
Example TCAD input file to calculate current from single event upset in DS-MSND..	201
Appendix B - DS-MSND Simulations	203
MCNP Input Card Examples	203
MCNP Simulation Results	207
Appendix C - Sample MCNP Code for Instrumentation	214
Appendix D - Moving Source Measurements for WDD V.1	225

List of Figures

Fig. 2-1. Total neutron interaction cross sections and neutron absorption cross sections for ^3He , ^{10}B , and ^6Li , the most common conversion materials for thermal neutron detectors [47].	7
Fig. 2-2. Thermal neutron (0.025eV) capture cross section and reaction product energies for common thermal neutron conversion materials, ^3He , ^{10}B , and ^6Li [44].	8
Fig. 2-3. Simplified diagrams of gas-filled neutron detectors. (Left) Cross section of a cylindrical detector where the fill gas is the conversion material. (Right) Rectangular detector with suspended ^6Li -foils and ^6Li coated walls.	10
Fig. 3-1. Diagrams of energy band electron populations for insulators, semiconductors, and conductors. Image was based on images from [108, 109].	15
Fig. 3-2. Simplified diagram depicting formation of valence band and conduction band in silicon. As additional silicon atoms are bonded to the system the original discrete allowed electron energy states split to form quasi-continuous energy bands with a forbidden (band) gap forming between the valence band and conduction band.	16
Fig. 3-3. Diagrams of electrons, holes, and Fermi level in an intrinsic semiconductor and n-type semiconductor.	17
Fig. 3-4. (Left) Band diagram of p-type and n-type semiconductors. (Middle) Diagram showing a pn-junction. (Right) Diagram of electron and hole diffusion and drift caused by charge carrier imbalances and the electric field formed in the space charge region.	19
Fig. 3-5. (a) Simplified 1-D, abrupt junction, pn-junction diagram with the p-side having higher dopant concentration than the n-side. (b) Net dopant concentration on each side of the junction. (c) Electric field in the depletion region. (d) Voltage potential in the depletion region.	20
Fig. 3-6. Theoretical (Left) IV and (Right) CV curves for a pn-junction diode.	22
Fig. 3-7.(left) Diagram of radiation interaction in a pvn-diode and subsequent charge drift from the electric field present in diode shown on the right. (right) Electric field strength in the pvn-diode.	23
Fig. 3-8. Example of simultaneous drift and diffusion of charge carrier clouds within a semiconductor. The electron-hole pairs are initially created at $x=0$	24

Fig. 4-1. Example of neutron detection process for thin-film coated neutron detector. Neutrons are absorbed in the conversion material layer which then causes the release of charge- particle reaction products that can enter semiconductor diode. The reaction products deposit energy in the semiconductor diode, thereby creating electron-hole pairs that are then drifted and measured. 26

Fig. 4-2. Example of neutron detection process for a MSND. Neutrons are absorbed in the conversion material in a MSND microcavity which produces charged-particle reaction products that can enter the semiconductor diode. The reaction products deposit energy in the semiconductor diode creating electron-hole pairs that are then drifted and measured. 27

Fig. 4-3. Example of neutron detection process for a DS-MSND. Neutrons are absorbed in the conversion material in a DS-MSND microcavity which produces charged-particle reaction products that can enter semiconductor diode. The reaction products deposit energy in the semiconductor diode creating electron-hole pairs that are then drifted and measured. 28

Fig. 4-4. Total linear attenuation coefficient for photons for Si, C, SiC, and GaAs. Cross section data were retrieved from [132]. 30

Fig. 4-5. Drawings of MSND doping profiles used in initial TCAD simulations to estimate the validity of simulations when compared to actual device performance. 34

Fig. 4-6. Doping profiles for boron (p-type) and phosphorus (n-type) dopants in the TCAD simulations used to estimate the internal electric field of DS-MSNDs for various doping schemes. The doping profiles were estimated from total dose and drive in procedures for solid-source diffusion commonly used to process MSNDs and DS-MSNDs..... 34

Fig. 4-7. (Top) Voltage potential (Bottom Left) internal electric field and (Bottom Right) vertical component of electric field for a conformal pvn-MSND with -2.7-V bias on the p-type contact on the top of the fins. 35

Fig. 4-8. Simulated signal current for SEUs at 150, 300, and 400 μm in the fin of the conformal pvn-MSND doping profile. The amount of signal induced increases as the interaction depth increases, because more electrons can diffuse beneath the fins where the weighting potential is the largest. 36

Fig. 4-9. Time-reel for a horizontal SEU at a depth of 300 μm for a conformal pvn-MSND. The simulations indicate that the majority of the charge carrier motion is driven by diffusion for this doping profile. Snapshots are at $t=0, 1, 2, 5, 10,$ and $20 \mu\text{s}$ 37

Fig. 4-10. (Top Left) Dopant concentration (Top Right) Voltage potential (Bottom Left) internal electric field and (Bottom Right) vertical component of electric field for a partial-conformal pvn-MSND with -2.7-V bias on the p-type contact on the top of the fins.	38
Fig. 4-11. Simulated signal current for SEUs at depths of 150, 300, and 400 μm in the fin of the partial-conformal pvn-MSND doping profile.	39
Fig. 4-12. Time-reel for a horizontal SEU at a depth of 300 μm for a partial-conformal pvn-MSND. The simulations indicate that the charge carriers are drifted by the internal electric field in addition to diffusion. The signal induction is more uniform as function of interaction depth than the conformal pvn-design. Snapshots are at $t=0, 1, 2, 5, 10,$ and $20 \mu\text{s}$	39
Fig. 4-13. Drawings of the DS-MSND doping profiles for Silvaco TCAD simulations. The simulations were used to model the internal electric field of the DS-MSND and estimate charge induction in the detection circuitry from charged-particle interactions in the silicon. The vertical dimension on the DS-MSND is not drawn to scale.	40
Fig. 4-14. (Left) Voltage potential and (Right) electric field within a 0-V bias, conformal, pvp-DS-MSND. The device operates solely on the built-in electrochemical potential created by the highly doped p-type region at the pn-junction on the surface of the fins and trenches.	41
Fig. 4-15. Simulated signal current for SEUs at depths of 150, 300, 450, 600, 900, 1050, 1200, and 1350 μm in the fins of the conformal pvp-DS-MSND doping profile.	42
Fig. 4-16. Time-reel for a horizontal SEU at a depth of 300 μm for a conformal pvp-DS-MSND. Significant diffusion occurs to the electron charge cloud following the interaction. The charge cloud then slowly is extracted upwards and outwards at the anode on the top-side fin. Snapshots are at $t=0, 1, 2, 5, 10,$ and $20 \mu\text{s}$	42
Fig. 4-17. (Left) Voltage and (Right) intrinsic electric field for the partial conformal pvp-DS-MSND operated at 0-V bias.	43
Fig. 4-18. Simulated signal current for SEUs at depths of 150, 300, 450, 600, 900, 1050, 1200, and 1350 μm in the fins of the partial conformal pvp-DS-MSND doping profile.	44
Fig. 4-19. Time-reel for a horizontal SEU at a depth of 300 μm for a partial conformal pvp-DS-MSND. Charge diffusion is still dominate due to the weak electric field. Snapshots are at $t=0, 1, 2, 5, 10,$ and $20 \mu\text{s}$	44
Fig. 4-20. (Left) Potential and (Right) electric field for 50-V reverse bias, partial conformal, pvn-DS-MSND. Only the top fin is fully depleted. However, a mostly horizontal electric field	

exists in the back-side fins from the n-n+ homojunction formed from the highly doped n-type contact adjacent to v material.....	46
Fig. 4-21. Simulated signal current for SEUs at depths of 150, 300, 450, 600, 900, 1050, 1200, and 1350 μm in the fins of the partial conformal pvn-DS-MSND doping profile.	47
Fig. 4-22. Time-reel for a horizontal SEU at a depth of 300 μm for a partial conformal pvn-DS-MSND. Charge diffusion is still dominate due to the weak electric field. Snapshots are at t=0, 1, 2, 5, 10, and 20 μs	47
Fig. 4-23. Time-reel for a horizontal SEU at a depth of 1200 μm for a partial conformal pvn-DS-MSND. Charge diffusion is still dominate due to the weak electric field. Snapshots are at t=0, 1, 2, 5, 10, and 20 μs	48
Fig. 4-24. (Top) Potential and (Bottom) electric field for the partial conformal pvp-DS-MSND with n-ring. The left images display the anode and cathode. The images on the right show the details within the two closest fins. The diode was reverse biased with 10 V.	49
Fig. 4-25. Simulated signal current for SEUs at depths of 150, 300, 450, 600, 900, 1050, 1200, and 1350 μm in the fins of the partial conformal pvn-DS-MSND doping profile.	49
Fig. 4-26. Time-reel of electron concentration for a horizontal SEU at a depth of 300 μm for a partial conformal pvp-DS-MSND with n-ring and -10-V bias. Snapshots are at t=0, 1, 2, 5, 10, and 20 μs	50
Fig. 4-27. Comparison of signal current for SEUs at 150 μm (left) and 300 μm (right) for partial conformal pvn-MSNDs, partial conformal pvp-DS-MSNDs, partial conformal pvn-DS-MSNDs, and partial conformal pvp-DS-MSNDs with n-ring.	51
Fig. 4-28. Example of offset straight-trench DS-MSND. The feature height, unit cell width, and trench width were adjusted in MCNP simulations for detector optimization.....	52
Fig. 4-29. Drawing of DS-MSND geometries considered for microfeature size optimization study with MCNP simulation. The geometries nomenclature was the following: (a) offset straight-trench DS-MSND, (b) offset circular-hole DS-MSND, (c) offset circular-pillar DS-MSND, (d) opaque straight-trench DS-MSND, (e) opaque circular-hole DS-MSND, (f) opaque circular-pillar DS-MSND. Geometries (e) and (f) are identical; however, in the simulations (e) was irradiated on the circular-hole side and (f) was irradiated on the circular-pillar side.	56

Fig. 4-30. Simulation estimations for the intrinsic thermal-neutron detection efficiencies for ^{10}B -backfilled, offset DS-MSND with 4- μm wide (left) and 6- μm wide (right) unit cells and microfeature depths of 80 μm . The optimum microfeature width to unit cell ratio for a 300 keV LLD was plotted for each microfeature shape. Legend: Straight Trench (ST), Circular Hole (CH), Circular Pillar (CP), Unit Cell width (UC), Trench width (T), Hole or Pillar Diameter (D). 58

Fig. 4-31. Simulated reaction product spectra for ^{10}B -backfilled, offset DS-MSND with 4- μm wide (left) and 6- μm wide (right) unit cells and microfeature depths of 80 μm . The optimum microfeature width to unit cell ratio for a 300 keV LLD was plotted for each microfeature shape. Legend: Straight Trench (ST), Circular Hole (CH), Circular Pillar (CP), Unit Cell width (UC), Trench width (T), Hole or Pillar Diameter (D)..... 58

Fig. 4-32. Simulation estimations for the intrinsic thermal-neutron detection efficiencies for ^{10}B -backfilled, opaque DS-MSND with 4- μm wide (left) and 6- μm wide (right) unit cells and microfeature depths of 80 μm . The optimum microfeature width to unit cell ratio for a 300 keV LLD was plotted for each microfeature shape. Legend: Straight Trench (ST), Circular Hole (CH), Circular Pillar (CP), Unit Cell width (UC), Trench width (T), Hole or Pillar Diameter (D). 60

Fig. 4-33. Simulated reaction product spectra for ^{10}B -backfilled, opaque DS-MSND with 4- μm wide (left) and 6- μm wide (right) unit cells and microfeature depths of 80 μm . The optimum microfeature width to unit cell ratio for a 300 keV LLD was plotted for each microfeature shape. Legend: Straight Trench (ST), Circular Hole (CH), Circular Pillar (CP), Unit Cell width (UC), Trench width (T), Hole or Pillar Diameter (D)..... 60

Fig. 4-34. Simulation estimations for the intrinsic thermal-neutron detection efficiencies for ^6LiF -backfilled, offset DS-MSND with 20- μm wide (left) and 40- μm wide (right) unit cells and microfeature depths of 650 μm . The optimum microfeature width to unit cell ratio for a 300 keV LLD was plotted for each microfeature shape. Legend: Straight Trench (ST), Circular Hole (CH), Circular Pillar (CP), Unit Cell width (UC), Trench width (T), Hole or Pillar Diameter (D). 62

Fig. 4-35. Simulated reaction product spectra for ^6LiF -backfilled, offset DS-MSND with 20- μm wide (left) and 40- μm wide (right) unit cells and microfeature depths of 650 μm . The optimum microfeature width to unit cell ratio for a 300 keV LLD was plotted for each microfeature

shape. Legend: Straight Trench (ST), Circular Hole (CH), Circular Pillar (CP), Unit Cell width (UC), Trench width (T), Hole or Pillar Diameter (D)..... 62

Fig. 4-36. Simulation estimations for the intrinsic thermal-neutron detection efficiencies for ${}^6\text{LiF}$ -backfilled, opaque DS-MSND with 20- μm wide (left) and 40- μm wide (right) unit cells and microfeature depths of 650 μm . The optimum microfeature width to unit cell ratio for a 300 keV LLD was plotted for each microfeature shape. Legend: Straight Trench (ST), Circular Hole (CH), Circular Pillar (CP), Unit Cell width (UC), Trench width (T), Hole or Pillar Diameter (D). 63

Fig. 4-37. Simulated reaction product spectra for ${}^6\text{LiF}$ -backfilled, opaque DS-MSND with 20- μm wide (left) and 40- μm wide (right) unit cells and microfeature depths of 650 μm . The optimum microfeature width to unit cell ratio for a 300 keV LLD was plotted for each microfeature shape. Legend: Straight Trench (ST), Circular Hole (CH), Circular Pillar (CP), Unit Cell width (UC), Trench width (T), Hole or Pillar Diameter (D)..... 64

Fig. 4-38. (Left) DS-MSND and MSND angular response to a collimated thermal-neutron beam. The DS-MSND CP and DS-MSND ST response are nearly identical. (Right) Example of DS-MSND straight trench geometry used for angular response simulations. The neutron beam was rotated around the y-axis with 0° corresponding to the negative x-direction and 90° was the beam pointed in the negative z direction towards the DS-MSND. Similar orientations were used for the other DS-MSND and MSND patterns. 66

Fig. 4-39. (Left) Theoretical intrinsic gamma-ray detection efficiency of a DS-MSND and MSND with parameters described in Table 4-4. The DS-MSND is significantly more sensitive to gamma rays primarily because of the increased thickness of the diode. (Right) DS-MSND pulse height spectra for normally incident gamma rays in and thermal neutrons showcasing the lower level discriminator can be increased significantly with minimal effect on the neutron detection efficiency while drastically reducing the gamma-ray sensitivity..... 68

Fig. 4-40. Results from the ${}^6\text{LiF}$ backfill optimization study for straight-trench, offset DS-MSNDs with 0.65 trench width to unit cell width ratio. The intrinsic thermal-neutron detection efficiency is plotted as a function of ${}^6\text{LiF}$ packing fraction for trench depths of 300, 400, 500, and 600 μm . (Left) 25- μm wide unit cell. (Right) 30- μm wide unit cell. 70

Fig. 4-41. ${}^6\text{LiF}$ packing fraction optimization simulation results for unit cell widths of 20-40 μm . The trench depth was set to 500 μm , and the trench width to unit cell width ratio was 0.6 for the reported results. Only offset, straight-trench DS-MSNDs were simulated..... 71

Fig. 4-42. ${}^6\text{LiF}$ packing fraction optimization simulation results for unit cell widths of 20-40 μm . The trench depth was set to 500 μm , and the trench width to unit cell width ratio was 0.6 for the reported results. Only offset, straight-trench DS-MSNDs were simulated..... 71

Fig. 4-43. Schematic visualizing the relative size of the “dead” region and “active” regions in silicon microfeatures. The perforation-width to unit-cell-width ratio was 0.75 for both the 20- μm and 40- μm wide unit cells shown here. This effect is especially bad for ${}^{10}\text{B}$ -backfilled devices, because the short reaction-product ranges require smaller unit cell widths. 73

Fig. 5-1. Simplified process flow for pvn-DS-MSND fabrication. The process for pvp-DS-MSNDs is identical except only one diffusion (junction doping) process is required where both sets of trenches are doped simultaneously. The diffusion window patterning is omitted in the diagram for clarity but is required to insulate the diode from the diced edge. The process diagram for pvp-n-dot DS-MSNDs requires an additional photolithography process. Finally, after the electrical contacts are deposited the diodes are diced from the wafer and mounted into ceramic detector boards. 75

Fig. 5-2. Basic diagram showing oxide patterning process with photolithography. The pattern on the mask is transferred to the oxide layer with positive-tone photoresist in this example. .. 78

Fig. 5-3. SEM image of the patterned oxide layer on a corner of a DS-MSND diode before KOH wet etching. The image shows the diffusion window surrounding the trenches that have pre-etch width of approximately 13 μm and a pitch of 30 μm 79

Fig. 5-4. Diagram of silicon wafer before and after anisotropic KOH wet-etch used to form deep, high-aspect ratio straight trenches in the DS-MSND diode. The diagram depicts both the trench and diffusion window mask that are patterned in the SiO_2 layer via photolithography. 81

Fig. 5-5. (Left) Wafer orientation and (Right) trench alignment used to form the high-aspect ratio straight trenches for DS-MSND. The anisotropy of the KOH etch allows for deep trenches to be etched vertically in the [110]-direction with minimal lateral etch in the [111]-direction..... 81

Fig. 5-6. SEM of cross section of an etched, offset, straight-trench DS-MSND on a 1.5-mm thick silicon wafer. The trenches are approximately $625\pm 25\text{-}\mu\text{m}$ deep and $21\text{-}\mu\text{m}$ wide. The unit cell width is $30\text{ }\mu\text{m}$ 83

Fig. 5-7. Example of solid-source diffusion. The DS-MSND wafers are loaded next to source wafers with or without blocking dummy wafers depending on the desired dopant profile. Dopants diffuse from the source wafers and deposit on the adjacent silicon wafers. High temperatures then drive in and activate dopant atoms in the wafer. 85

Fig. 5-8. Example of ion implantation geometry required to implant dopants into the sidewall of and MSND or DS-MSND. The wafer offset angle, θ , for high aspect ratio trenches is ranges from $1\text{-}3^\circ$ 86

Fig. 5-9. Normalized dopant distributions for constant surface concentration (Eq. 5-8) and constant total dopant (Eq. 5-9) for boron in Si with a one-hour drive-in time at 1000°C 88

Fig. 5-10. Example of diffusion process timelines for p-type and n-type solid-source diffusion. The p-type diffusion utilizes H_2 injection to promote B_2O_3 growth and HBO_2 transfer from the source wafer to silicon wafer. The diagrams are adapted from [152]. 89

Fig. 5-11. Example of DS-MSND mounted in a ceramic detector board (CDB) with metalized contacts. 90

Fig. 5-12. Cross-sectional SEM image of a ^6LiF -backfilled DS-MSND showing only small void regions within the trenches. Later analysis of ^6LiF PF indicate the apparent density of ^6LiF within the trenches was significantly less than previously assumed. 92

Fig. 5-13. Results of MCNP simulation for thermal-neutron attenuation by a ^6LiF -backfilled DS-MSND with trench geometry described in Table 5-3 and ^6LiF PF ranging from 0% to 100%. 93

Fig. 5-14. MCNP simulation results for intrinsic thermal-neutron detection efficiency for a ^6LiF -backfilled DS-MSND with trench geometry described in Table 5-3 and ^6LiF PF ranging from 0% to 100%. 94

Fig. 5-15. SEM image of titrated ^6LiF powder. Particle sizes up to $20\text{-}\mu\text{m}$ have been obtained through the $\text{LiOH} + \text{HF}$ reaction process [21]. 95

Fig. 5-16. (Left) Ball mill used to reduce the particle size of ^6LiF powder harvested titration of LiOH . (Right) SEM image of ball-milled LiF nano-powder. The average particle size is significantly reduced, and the shape is less cuboid than the original powder. 96

Fig. 5-17. SEM images of nano-only methanol-wetted hand packed backfill (left) and nano-only, H₂O₂:methanol centrifuge backfill (right) experiments. Large void regions within the trenches persisted in both methods..... 98

Fig. 5-18. SEM images of ⁶LiF backfill experiment results for samples 4 (top right), 6 (top left), 11 (bottom right), and 15 (bottom left). 100

Fig. 5-19. (Left) Diagram showing the basic theory behind the isostatic press backfill methodology. (Middle) SEM image of Sample 18 (Right) SEM image of Sample 19. 101

Fig. 5-20. SEM images of sample 21 (left) and sample (22) right backfilled by shaking dry LiF powder into the trenches on a vibration table. 102

Fig. 5-21. Samples 28 (top left), 30 (top right), and C1 (bottom) backfilled with the ink roller method..... 104

Fig. 5-22. (Left) Picture of ultrasonic vibration tank and beaker jig for ⁶LiF-backfilling. (Right) SEM image of DS-MSND backfilled with ultrasonic vibration followed by ink roller method. The packing fraction was greater than 45%..... 105

Fig. 5-23. (Left) DS-MSND mounted in ceramic detector board with metal shield. (Right) SEM image of wire bonds connecting the top-side of a DS-MSND to a CDB. 106

Fig. 5-24. (Left) IV-curve and (Right) CV-curve for 1-mm thick, partial-conformal, pvn-DS-MSNDs. 108

Fig. 5-25. (Left) IV-curve and (Right) CV-curve for 1-mm thick, partial-conformal, pvp-DS-MSNDs. 109

Fig. 5-26. (Left) IV-curve and (Right) CV-curve for 1.5-mm thick, partial-conformal, pvp-DS-MSNDs. 109

Fig. 5-27. (Left) IV-curve and (Right) CV-curve for 1.5-mm thick, partial-conformal, pvp-n-ring-DS-MSNDs. 110

Fig. 5-28. Experiment configuration for alpha-particle charge collection efficiency measurement. 111

Fig. 5-29. Pulse height spectra from ²⁴¹Am alpha-particle measurements for 1-mm thick pvn-DS-MSNDs and 1-mm thick pvp-DS-MSNDs. 112

Fig. 5-30. Pulse height spectra for ²⁴¹Am alpha-particle measurements comparing normal and angled alpha-particle incidence. The y-axis limit is reduced on the right-side plot to show how the high-energy peak for normal incidence is eliminated when the alpha particles intersect the

DS-MSND at an angle so that the alpha particle cannot reach the bottoms of the trenches.	113
Fig. 5-31. Pulse height spectra for first DS-MSNDs with intrinsic thermal-neutron detection efficiencies greater than 60%. Measurements were performed at the diffracted beamport with a 2.5-mm cadmium wide shutter open (S\O) and shutter closed (S\C).....	116
Fig. 5-32. Diagram of test setup for moderated ^{252}Cf measurements. Adapted from [29].	117
Fig. 5-33. Pulse height spectrum for DS-MSND B0812 which had an intrinsic thermal neutron detection efficiency of $69.3\% \pm 1.5\%$	118
Fig. 5-34. Pulse height spectra from DS-MSND B0812 for background, moderated ^{252}Cf , and ^{137}Cs	119
Fig. 5-35. Co-doped Fast-MSND designs. All were fabricated with solid-source diffusion on v-type silicon.	121
Fig. 5-36. IV curves for Co-Doped MSNDs. The MSNDs with shallow junctions on the tops of the fins showed good rectifying behavior.	122
Fig. 5-37. Pulse height spectra for ^{241}Am charge collection efficiency measurements for (Top Left) traditional pvn-MSND, (Top Right) npn-co-doped MSND, and (Bottom Left) npp co-doped MSND. (Bottom Right) Ratio of the false full energy peak (FEP) to true FEP for the three designs shown.	123
Fig. 5-38. Alternating Trench MSND diffusion profiles. Alternating n- and p-type trenches will create an intrinsic electric field within the fins causing charge carries to be swept out laterally. There are no floating contacts in this design.	124
Fig. 5-39. Fabrication process for ion-implanted, alternating trench MSNDs.	124
Fig. 5-40. DFPR on an MSND showing minimal extrusion into the trenches and providing an adequate ion implantation mask on the surface.	125
Fig. 5-41. (left) Severe photoresist delamination during ion implantation. Heat and damage incurred during the process degrades photoresist adhesion to the underlying substrate. (right) Example of a dry-film photoresist mask with good adhesion to the substrate.	126
Fig. 5-42. (Left) IV and (Right) CV curves for alternating trench MSND prototype diodes.	126
Fig. 5-43. <i>Alpha-particle charge-collection-efficiency experiment for alternating trench MSND prototype wafer. Distinct full-energy peaks were observed for shaping times greater than 1 μs.</i>	127

Fig. 5-44. “L-shaped” diffusion profile. This profile was fabricated with a combination of ion implantation (p-type) and solid-source diffusion (n-type). An implantation mask was not required to achieve the desired junction geometry. 128

Fig. 5-45. (Left) IV and (Right) CV curves for L-shaped MSND prototypes. 128

Fig. 5-46. (Left) Alpha-particle charge-collection experiments performed with an 241Am source. The shift in the “false full-energy peak” indicates not all charge was collected for the 1 μs shaping time. The MSND was operated with -2.5 V bias. (Right) Reaction-product spectrum for “L-shaped” MSND measurements with moderated 252Cf. The shaping time for the 252Cf measurement was 12 μs. 129

Fig. 5-47. Interdigitated DS-MSND design. One side of the DS-MSND is conformally doped with p-type dopant, and the opposite side is doped with n-type dopant. Lateral charge carrier movement should be induced with this design and thus sub-microsecond shaping times may be achieved. 130

Fig. 5-48. (Left) IV measurements for interdigitated DS-MSNDs. (Right) Reaction product spectra for an interdigitated DS-MSND. Low count rates were likely due to a poor LiF backfill, and the low signal to noise ratio may be attributed to high capacitance. 131

Fig. 5-49. (Left) Drawing of npn-type, LL-shaped, DS-MSND. (Right) Pulse height spectra for a moderated 252Cf source and background. Elevated noise floor and poor packing fraction limits detection efficiency to ~31%. The shaping time was 12 μs for both measurements. 132

Fig. 5-50. (Left) Schematic of diffusion profile formed from SOD processing. (Right) Pulse height spectrum of pvp-type DS-MSND fabricated with boron-loaded SOD. 132

Fig. 6-1. FR4-based HeRep Mk III with 12 DS-MSNDs. 135

Fig. 6-2. HeRep Mk IV response to moderated 252Cf at 25 cm. The responses for the unmoderated FR4 and unmoderated flexible Kapton based HeReps are nearly identical. The background count rate ranged from 1.5 cps to 3.3 cps for all measurements. 135

Fig. 6-3. (Left) Bare HeRep Mk III and (Right) Moderated HeRep Mk IV response for the interior moderator and no-interior moderator configurations to moderated 252Cf at 0.25 m. 136

Fig. 6-4. (Top) 0.75-in by 0.75-in by 3.1-in HeRep Mk IV (Bottom) 0.75-in by 0.75-in by 6.1-in HeRep Mk IV. Each were populated with 15 DS-MSNDs and 16 pieces of HDPE moderator placed in void spaces between adjacent detectors and electronics in the longer HeRep Mk IV. 137

Fig. 6-5. (Left and Middle) HeRep Mk V detector system with 20 DS-MSNDs that have intrinsic thermal-neutron detection efficiencies of at least 50%. (Right) Angular response of the HeRep Mk V compared to both HeRep Mk IV detectors and the HeRep Mk III detector.....	140
Fig. 6-6. Image of a wireless MND Mk III populated with 24, 1-cm ² MSNDs with intrinsic thermal neutron detection efficiencies of 30%.....	142
Fig. 6-7. Schematic of MND electronics.	142
Fig. 6-8. MCNP model of the MND Mk III. The “front” side is nearest the MSNDs, and the “back” side is nearest to the battery.	143
Fig. 6-9. Concept drawing of MRD Mk I with an array of DS-MSNDs and a spectroscopic gamma-ray detector.....	147
Fig. 6-10. (Left) MND and CAN communications dongle in HDPE moderator case. (Right) Example of MNDs connected to quad-connector boards. One output on the quad-connector board is terminated with a 50-ohm terminator.....	149
Fig. 6-11. (Left) Schematic of connections in the WDD Mk I [33, 119]. (Right) Image of the WDD Mk I connected to the Android readout device.....	149
Fig. 6-12. (Left) Real-time neutron count rate of all MNDs in the WDD. (Right) Real-time count rate of individual MNDs in the WDD.....	150
Fig. 6-13. Results of neutron response measurements for WDD V.1. Note the error bars are smaller than the data points.	151
Fig. 6-14. WDD V.1 normalized angular response to moderated ²⁵² Cf at 1.5 m. The error bars on the measurement are smaller than the data points.	151
Fig. 6-15. WDD V.1 response to a moving neutron source. The distance of closest approach was 1.5 m and occurred at approximately the 70-second mark. Elevated background at the starting and end location mask the transient signal for some measurements.....	153
Fig. 6-16. (Left) Diagram of the wired connections in the WDD V.2. (Right) Photo of wired MND installation into a concealed pocket in a prototype garment.	154
Fig. 6-17. (Left) Count rate as a function of distance for the wired WDD V.2 for bare ²⁵² Cf, moderated ²⁵² Cf, and bare AmBe. (Right) Counts per second per unit flux from the three neutron sources as a function of distance for V.1 and V.2 WDDs. The error bars are within the size of the data point.	155
Fig. 6-18. Angular response of WDDs to moderated ²⁵² Cf normalized at 0°.....	155

Fig. 6-19. Screenshots of count rate vs time plot from Android application for moving source measurements with the wired WDD V.2. The distance of closest approach was 1 m for all measurements. Statistically significant detection was achieved for all but the bare ^{252}Cf moving at 1.5 m/s scenario. 156

Fig. 6-20. Modular Gamma-ray Detector (MGD) with seven LND model 713 Geiger-Müller detectors. The wireless MGD has an onboard rechargeable battery, BLE communications board, and all required signal processing electronics. 157

Fig. 6-21. Wireless WDD in prototype garment mounted on an ANSI 42.53 phantom..... 158

Fig. 6-22. Wireless WDD V.2 response to bare ^{252}Cf , moderated ^{252}Cf , and bare AmBe for neutron fluxes of 0.1, 1, 5, and 10 $\text{n cm}^{-2} \text{s}^{-1}$ from measurements performed at PNNL and KSU. The error bars are smaller than the data point..... 159

Fig. 6-23. Wireless WDD V.2 angular response to bare ^{252}Cf . The neutron measurements were performed at PNNL, and the gamma-ray measurements were performed at KSU..... 160

Fig. 6-24. Diagram of moving source and phantom geometry for neutron alarm requirements. The depicted configuration was considered the 0° test case. 162

Fig. 6-25. Critical decision level and detection level with 95% confidence for RWDs with up to 24 MRDs containing 16 or 12, 65% ϵ_{int} , DS-MSNDs. An average net count rate over the duration of the decision window above the critical decision level triggers a neutron alarm. The background calibration measurement was 2 minutes and decisions windows of 1, 2, 3, and 4 seconds are shown..... 166

Fig. 6-26. RWD moving source simulation results for bare ^{252}Cf and moderated ^{252}Cf passing by the torso (y-direction), and side of the phantom (x-direction). MRDs with 12 and 16 DS-MSNDs with ϵ_{int} of 65% were modeled. RWDs containing 8 to 24 MRDs were considered, see Table 6-7 for MRD orientation. 167

Fig. 6-27. Expected average count rate of RWD during 1, 2, 3, and 4 second measurements for moving bare and moderated ^{252}Cf sources compared to 95% confidence L_c and L_D thresholds. 169

Fig. 6-28. Expected average count rate of RWD during 1, 2, 3, and 4 second measurements for moving bare and moderated ^{252}Cf sources compared to 90% confidence L_c and L_D thresholds. 169

Fig. 6-29. Detector configuration and location identification for 14 MRD RWD system. 170

Fig. 6-30. x, y, and z components of directional vector as a moderated ^{252}Cf is rotated around the phantom..... 170

Fig. 6-31. ICRP 74 neutron fluence to ambient dose conversion coefficients. The detector response function of rem meters is tailored to try match the shape of $H^*(10)/\Phi$ curve [167]. 172

Fig. 6-32. Relative response per unit dose equivalent for the PRESCILA, WENDI-II, Anderson-Braun (AB), and Hankins-NRD dose meters as a function of neutron energy. Calculated from data presented in [48]...... 173

Fig. 6-33. (Left) 3D model of MRD centrally located on ANSI 42.53 phantom. (Middle and Right) Visualizations of neutron irradiation on front side and back side of phantom by a mono-energetic, mono-directional neutron beam with beam diameter of 1 meter. 175

Fig. 6-34. (Left) MRD energy dependent response per unit fluence. (Right) Relative response per unit flux for a single MRD on a phantom normalized to 1 eV. 175

Fig. 6-35. Thermal, epithermal, and fast sensitive MRDs. Cadmium absorbers were positioned to either absorb initially thermal neutrons or absorb neutrons thermalized in the phantom. The fast-neutron sensitive MRD replaces ^6LiF convertor material with hydrogenous wax that relies on proton recoil to produce a charged-particle reaction product that interacts in the adjacent silicon microfeatures..... 177

Fig. 6-36. (Left) Detector response per unit fluence for all six MRDs in the three-channel RWD dosimeter system. (Right) Response per unit ambient dose equivalent for the three-channel system using calibration coefficients of the form shown in Eq. 6-11..... 178

Fig. 6-37. Comparison of the three-channel RWD dosimeter to other common commercial dose monitors. 178

Fig. D-1. (Left) Diagram and (Right) image of experiment configuration for the WDD moving source measurements. Note that the background level with the source behind the neutron shield was 3x-6x the normal background level without a neutron source in the room..... 225

Fig. D-2. WDD V.1 response to a moving neutron source. The distance of closest approach was 1 m and occurred at approximately the 70-second mark except for the 1.2 m/s bare ^{252}Cf measurements. For Bare ^{252}Cf moving at 1.2 m/s the source movements occurred at approximately 70 s, 125 s, and 90 s for Trial0, Trial1, and Trial2, respectively. 225

List of Tables

Table 4-1. Properties for common semiconductor materials investigated for thin-film coated semiconductor neutron detectors, MSNDs, and DS-MSNDs. X represents that property is generally accepted as true.	30
Table 4-2. Cross Sections and reaction products for common neutron conversion materials.	31
Table 4-3. MCNP problem geometry parameters for the DS-MSND and MSND angular response simulations.	65
Table 4-4. Parameters used for DS-MSND gamma-ray sensitivity simulations.	66
Table 4-5. Simulation parameters used for ^6LiF -backfill optimization study for offset, straight-trench DS-MSNDs.	69
Table 5-1. Chemical cleaning baths for DS-MSND wafers after KOH etch and before diffusion processes.	84
Table 5-2. Diffusion coefficients, D, for B and P in Si and SiO_2 at 1000°C [143].	88
Table 5-3. Results of first quantitative measurement of ^6LiF PF in a DS-MSND found by comparing the mass of the wafer before and after backfilling to the known volume of the trenches.	92
Table 5-4. Results of DS-MSND neutron attenuation measurements performed with reference neutron detector (HeRep).	93
Table 5-5. Backfilling experiment results for nano- ^6LiF backfilling.	97
Table 5-6. Results from LiF backfill experiments focusing on the centrifuge and hand packing backfill methodologies.	99
Table 5-7. Results from LiF backfill experiments utilizing the isostatic press.	101
Table 5-8. Vibration table with dry LiF powder backfill experiment results.	102
Table 5-9. Results from ink roller backfill method experiments. For the first time, packing fractions above 40% were routinely achieved for powder backfill.	103
Table 5-10. ^6LiF backfill packing fractions achieved with ultrasonic vibration backfill with ^6LiF suspended in methanol followed by shortened ink roller backfill.	105
Table 5-11. Results from diffracted beamport measurements to determine intrinsic thermal-neutron detection efficiency for 1-mm thick, pvp-DS-MSNDs.	115

Table 5-12. Intrinsic thermal-neutron detection efficiencies of 1.5-mm thick DS-MSND measured with the moderated ^{252}Cf source method.	118
Table 6-1. Direct comparison to ^3He for a moderated 30-ng ^{252}Cf source at 25 cm.	136
Table 6-2. HeRep Mk IV direct comparison to a 0.75-in diameter by 3.1-in long, 10-atm ^3He detector. A 26.5-ng ^{252}Cf source and an AmBe source emitting 200,000 neutrons per second were used for the measurements. The source-to-detector distance was 25 cm for all measurements.....	139
Table 6-3. Simulation and measurement results for an MND in stand-alone configuration for ^{252}Cf . The source to detector distance was 25 cm.....	143
Table 6-4. Measurement results for one MND Mk III centrally located on a phantom to a 12.3-ng ^{252}Cf source located 25 cm from the detector.	144
Table 6-5. Results of MCNP6 simulations for the MRD implementing 60% and 70% intrinsic thermal-neutron detection efficiency DS-MSNDs. All simulations were run until the relative error of the tally was less than or equal to 0.01.	146
Table 6-6. DS-MSND specification for MRD optimization simulations.	162
Table 6-7. MRD locations on phantom for ANSI 42.53 neutron alarming requirement optimization simulations.	163
Table 6-8. Simulation results for a single MRD mounted on a phantom in a background neutron flux environment.	164

Appendices

Table B-1. Theoretical intrinsic thermal-neutron detection efficiency MCNP simulation results for offset, straight-trench DS-MSNDs with conversion material density set at half of the enriched crystalline density of the material to simulate a 50% packing fraction for the powder backfill.	208
Table B-2. Theoretical intrinsic thermal-neutron detection efficiency MCNP simulation results for offset, circular hole DS-MSNDs with conversion material density set at half of the enriched crystalline density of the material to simulate a 50% packing fraction for the powder backfill.	209
Table B-3. Theoretical intrinsic thermal-neutron detection efficiency MCNP simulation results for offset, circular pillar DS-MSNDs with conversion material density set at half of the enriched	

crystalline density of the material to simulate a 50% packing fraction for the powder backfill.	210
Table B-4. Theoretical intrinsic thermal-neutron detection efficiency MCNP simulation results for opaque, straight trench DS-MSNDs with conversion material density set at half of the enriched crystalline density of the material to simulate a 50% packing fraction for the powder backfill.	211
Table B-5. Theoretical intrinsic thermal-neutron detection efficiency MCNP simulation results for opaque, circular hole DS-MSNDs with conversion material density set at half of the enriched crystalline density of the material to simulate a 50% packing fraction for the powder backfill.	212
Table B-6. Theoretical intrinsic thermal-neutron detection efficiency MCNP simulation results for opaque, circular pillar DS-MSNDs with conversion material density set at half of the enriched crystalline density of the material to simulate a 50% packing fraction for the powder backfill.	213

Abbreviations

2D – Two Dimensional

3D – Three Dimensional

B – Boron

CAN – Controller Area Network

CLLB – $\text{Cs}_2\text{LiLaBr}_6:\text{Ce}$

CLLBC – $\text{Cs}_2\text{LiLa}(\text{Br},\text{Cl})_6:\text{Ce}$

CLYC – $\text{Cs}_2\text{LiYCl}_6:\text{Ce}$

CV – Current vs Voltage

DFPR – Dry-Film Photoresist

DS-MSND – Dual-Sided Microstructured Semiconductor Neutron Detector

GaAs – Gallium Arsenide

GADRAS – Gamma Detector Response and Analysis Software

GARRn – Gamma Absolute Rejection Ratio for neutrons

Gd – Gadolinium

HeRep – ^3He -Replacement

ICP-RIE – Inductively Coupled Plasma Reactive Ion Etching

ICRP – International Commission on Radiation Protection

ICRU – International Commission on Radiation Units and Measurements

IV – Current vs Voltage

Li – Lithium

LiF – Lithium Fluoride

LLD – Lower Level Discriminator

MND – Modular Neutron Detector

MRD – Modular Radiation Detector

MSND – Microstructured Semiconductor Neutron Detectors

P – Phosphorus

PMT – Photomultiplier Tube

PNNL – Pacific Northwest National Laboratory

RIE – Reactive Ion Etching

RTA – Rapid Thermal Annealing

SEU – Single Event Upset

Si – Silicon

SiC – Silicon Carbide

SiPM – Silicon Photomultiplier

SNM – Special Nuclear Material

SOD – Spin-on Dopant

SWAP – Size, Weight, and Power

TCAD – Technology Computer-Aided Design

VLSI – Very-Large Scale Integration

WDD – Wearable Detector Device

WND – Wearable Neutron Detector

Acknowledgements

The work presented herein was performed at the Kansas State University Semiconductor Materials and Radiological Technologies (S.M.A.R.T. Laboratory) with electronics support provided by the KSU Electronics Design Laboratory and detector characterization made possible at the KSU TRIGA Mk II Nuclear Reactor. This research was supported in part by the Defense Threat Reduction Agency (DTRA) through grants HDTRA1-14-C0032, HDTRA1-14-C0128, and HDTRA-18-R-0049.

I would like to acknowledge the guidance, support, and efforts put forth by my family, friends, professors, mentors, and colleagues. I would like to extend a special thank you to the following people for your help throughout this journey: Brienna Ochs, Kevin and Margo Ochs, Dr. Douglas McGregor, Dr. William Dunn, Dr. Larry Weaver, Dr. Amir Bahadori, Dr. Zayd Leseman, Dr. J. Kenneth Shultis, Dr. Walter McNeil, Dr. Jeremy Roberts, Dr. Hitesh Bindra, Dr. Ryan Fronk, Dr. Michael Reichenberger, Dr. Steven Bellinger, Dr. Nathaniel Edwards, Dr. Benjamin Montag, Daniel Nichols, Priyarshini Ghosh, Jacob Terrell, Luke Henson, Hai Vo, Neal Stratham, Logan Whitmore, Grace Friedel, Robyn Hutchins, Scott DeMint, Graham Schlaikjer, Colten Smith, Adam Van Bergeijk, Cody Rietcheck, Tim Sobering, Russell Taylor, Dave Huddleston, and many others.

Chapter 1 - Introduction

1.1. Motivation for Detector Development

National security concerns focusing on nuclear non-proliferation in a post 9/11 era has spurred renewed interest in the development of new, high efficiency, thermal-neutron detectors. The next-generation detectors would serve as a replacement for expensive neutron detectors based on rare ^3He -gas, which has been in limited supplied in the post nuclear warhead production era [1].

Detecting special nuclear material (SNM), which can be used to make weapons of mass destruction, is a significant research area for neutron detectors, because a common method for locating and interdicting illicit trafficking of SNMs is to detect the radiation emitted from the material, namely, gamma rays and neutrons. Focusing on neutron detection is attractive, because the spontaneous fission neutrons may be more challenging to shield than the gamma rays emitted from SNM. The neutrons must first be slowed by a low Z -material and then absorbed by certain isotopes with high neutron capture cross sections like ^3He , ^6Li , ^{10}B , or ^{113}Cd . Comparatively, gamma rays can be shielded by surrounding the source with high- Z material like lead. Neutron signatures are also relatively unique in nature, limited to only a few sources that often warrant additional investigation if detected. Additionally, the natural neutron radiation background level tends to be much lower and more constant than background gamma-ray levels [2-4]. Therefore, neutron detectors provide a measurable advantage in the search and localization of SNM mission space.

Neutron detectors also play an important role in radiation health physics. Neutron detectors can be used to estimate the neutron dose or dose rate an individual receives while working in radiation areas. The estimations can then be correlated with stochastic and deterministic health effects. Neutron dosimeters are commonly employed in radiation facilities such as nuclear reactors and particle accelerators. Additionally, neutron detectors have applications in space exploration, science, and industry. One common application is deploying a neutron detector to monitor neutron scattering characteristics of terrestrial or extra-terrestrial soil to estimate its hydrogen content while searching for oil or water. Thus, a market need has persisted for inexpensive, high-efficiency neutron detectors with many of the applications benefiting from reduction in Size, Weight, and Power (SWAP) parameters. Dual-Sided Microstructured Semiconductor Neutron Detectors (DS-

MSNDs) have emerged as a feasible next-generation neutron detector technology with reduced SWAP parameters and high thermal neutron-detection efficiency.

Reducing the SWAP parameters is critical for many radiation detection applications including battery-operated handheld or wearable instrumentation and detectors deployed on satellites, rovers, or probes for space exploration where increased size, weight, and power significantly increase mission cost. Retaining high detection efficiency is also critical, because the relative precision of a radiation measurement is inversely proportional to the square root of the total number of counts recorded. Thus, a neutron measurement can be performed in a much shorter period of time if the neutron detector has high detection efficiency, which becomes extremely important for detecting weak sources and in applications where the detector may only be in the vicinity of the source for a short period of time. Built upon previous successes with thin-film coated detectors [5-14] and single-sided Microstructured Semiconductor Neutron Detectors [15-28], the newest generation of DS-MSNDs have achieved intrinsic thermal-neutron detection efficiencies on par with common ^3He neutron detectors at a fraction of the cost [29-33].

1.2. Contributions to DS-MSND Technology, Science, and Instrumentation

The following list is a brief summary of the significant contributions that advanced the state of the art for MSND and DS-MSND technology detailed within this dissertation.

- In-depth characterization and measurement of ^6LiF backfill powder packing fraction critical for solving neutron detection efficiency discrepancies between simulation and measurement
- Development of simulations for ^6LiF and ^{10}B DS-MSNDs with realistically achievable powder packing fractions
- Development of simulations showing the benefits of packing fraction optimization based on microfeature geometry
- Application of computer-aided modeling for alternative *pn*-junction configurations on DS-MSNDs ultimately providing evidence to support fabrication of new *pvp-n*-ring profile DS-MSNDs
- Fabricated prototype *pvn*- and *pvp*-DS-MSNDs to validate results from computer models

- Developed VLSI processes to achieve deeper, higher-aspect ratio, microfeatures on 1.5-mm thick Si substrates to ultimately improve neutron detection efficiency
- Characterized factors effecting ${}^6\text{LiF}$ backfill packing fraction and developed process to improve the powder packing fraction from 30% to approximately 50%
- Fabricated DS-MSNDs with new record intrinsic thermal-neutron detection efficiency at $69.3 \pm 1.5\%$
- Performed studies and prototyped alternative doping profiles for fast charge collection DS-MSNDs
- Investigated spin-on-dopant and ion implantation as a means to form various diffusion profiles for MSNDs and DS-MSNDs
- Designed and characterized HeRep Mk V detector implementing DS-MSNDs
- Fabricated and characterized wearable detector systems implementing modular neutron detectors outfitted with single-sided MSNDs
- Designed and simulated neutron response for state-of-the-art modular radiation detectors implementing high-efficiency DS-MSNDs
- Performed simulation ground work showcasing the DS-MSND-based modular radiation detector's potential to operate as a highly accurate neutron dosimeter

1.3. Organization of Thesis

DS-MSNDs have evolved from the earliest inception of the single-sided MSND by McGregor [15] showing a small but statistically significant improvement in neutron detection efficiency over thin-film coated neutron detectors to presently having the highest reported intrinsic thermal-neutron detection efficiency for a semiconductor-based neutron detector [29]. Previous work by McNeil [20], Bellinger [21], and Fronk [33] describe the efforts to produce MSNDs with large improvements (5X) in intrinsic thermal-neutron detection efficiency over thin-film coated detectors, the development of a batch processing method for single-sided MSNDs along with further improved intrinsic thermal-neutron detection efficiency ($\sim 30\%$), and the realization of the first DS-MSNDs which achieved an intrinsic thermal-neutron detection efficiency of 53.5% with the implementation of a novel *pvp*-type doping scheme, respectively. All three dissertations detail

the challenges of tailoring the Very-Large Scale Integration (VLSI) processing techniques required to fabricate successful detectors.

A brief overview of the aspects of neutron detection and semiconductor detectors is provided in Chapters 2 and 3, respectively. Discussed in Chapter 4 is the design of DS-MSNDs including internal electrical property models for optimized doping profiles as well as MCNP simulations used to optimize the microfeature geometry of DS-MSNDs based on new ${}^6\text{LiF}$ packing fraction studies carried out after the conclusion of Fronk's work [33]. Detailed in Chapter 5 are major processing hurdles that have been overcome to achieve further improved neutron detection efficiency with an emphasis on deeper trench etching, ${}^6\text{LiF}$ backfilling, and alternative junction formation. Characterization of individual DS-MSND diodes is also discussed in Chapter 5.

The small form factor, readily array-able, DS-MSNDs serve as a top candidate for alternatives to ${}^3\text{He}$ for thermal neutron detection especially where low-profile, lightweight, and low-power consumption are desired such as handheld and wearable radiation detectors that can be used for detection and localization of SNM. Detailed in Chapter 6 is the design and characterization of radiation detector prototype systems implementing MSND and DS-MSND technology. Finally, outlined in Chapter 7 are conclusions from the content presented herein and suggestions for future work.

Chapter 2 - Introduction to Neutron Detection

Ionizing radiation was first discovered in 1895 by Röntgen when x rays emanating from a Crookes tube across the room caused barium-platinocyanide-coated plates to scintillate [34]. Over the next few years, alpha particles, beta particles, and gamma rays were discovered by several esteemed researchers [35-37]. Today, nearly 125 years later, radiation is measured and utilized all around us in fields including space exploration, particle physics, energy production, medical imaging, radiotherapy, industrial manufacturing, and, of great importance to this work, nuclear non-proliferation. The remainder of this chapter will focus primarily on neutron interactions and detection to provide a brief overview of considerations required for neutron detector design.

2.1. Discovery of the Neutron

James Chadwick identified the neutron in 1932 by measuring the properties of the emissions from beryllium and boron targets irradiated with polonium alpha particles [38, 39]. Although speculated to have existed as early as 1920 by Rutherford [40], neutrons were discovered after the discovery of many the other types of radiation including x rays, gamma rays, alpha particles, beta particles, and protons, partly because neutrons are more challenging to detect due to their charge neutrality.

Neutrons are composed of two down quarks and one up quark and are part of the nucleus of an atom¹. Free neutrons can be produced in a variety of ways, e.g. cosmic-ray interactions, fission (spontaneous or nuclear), fusion, and bombardment of specific target material with radiation, e.g. (α, n) , (γ, n) , (p, n) reactions. Cosmic-ray interactions are the primary source of natural neutron background radiation. Highly energetic charged particles interact in Earth's atmosphere and produce a variety of secondary radiation which includes neutrons. The neutron background energy spectrum peaks around 1 MeV on Earth's surface, and neutron flux levels vary from approximately 0.01 to 0.03 n cm⁻² s⁻¹ [2, 41]. Man-made neutron emitting sources such as AmBe, where the alpha-particle emission from ²⁴¹Am produces highly energetic ($E_{\text{avg}} = 5$ MeV) neutrons from the (α, n) reaction in the beryllium target, are commonly found in soil density gauges used for applications ranging from soil moisture monitoring to construction to oil well logging. Spallation neutron sources use highly energetic protons to eject neutrons from targets and are often

¹ Hydrogen is the one exception.

used to study molecular material properties. Neutrons are also produced through fission, and the neutron flux in a nuclear reactor can be monitored to determine the reactor power level. Also, radiation workers who interact with or around any of these neutron sources or facilities must keep track of not only their dose from gamma rays and charged particles, but also from neutrons, which are more challenging to detect and to accurately measure radiation dose. As the primary motivation for the development of the technology in this work, the detection of spontaneous fission sources classified as SNM is of interest in nuclear non-proliferation efforts.

2.2. Methods of Interaction

Neutrons are neutral, and therefore, neutrons do not interact coulombically with the surrounding medium like electrons, protons, alpha particles, and heavy charged particles. Instead, neutrons interact through scattering or absorption with a target nucleus. At low energies, neutron scattering and absorption events are both prominent. When a neutron scatters off a target nucleus, the neutron imparts some energy into the nucleus, which is scattered and interacts through coulombic interactions until it transfers all its kinetic energy to the surrounding material. The neutron is scattered into a different direction dictated by conservation of energy and momentum. At thermal energies, typically less than 0.5-1 eV, the magnitude of kinetic energy transferred to the target material, which could be a radiation detector, is relatively small and would contribute little to a person's dose or a radiation detector signal. Alternatively, neutrons can be absorbed by a target nucleus, which then produces directly ionizing reaction products. For some targets, thermal-neutron absorption leads to gamma-ray emission, but for the most common thermal-neutron detector conversion materials (^3He , ^{10}B , and ^6Li), charged-particle reaction products are emitted upon absorption of a neutron. The cross section for neutron absorption in these conversion materials is proportional to $1/v$ in the thermal energy region with v being the velocity of the neutron. At high neutron energies, neutron scattering interactions dominate. Shown in Fig. 2-1 are the total interaction and absorption cross sections for ^3He , ^{10}B , and ^6Li . Neutron attenuation when passing through a medium is described by Eq. 2-1 where I is number of remaining unattenuated neutrons at thickness t into the target material, I_0 is the initial intensity of neutrons, and Σ is the total macroscopic interaction cross section, defined as the probability per unit path length that a neutron interaction occurs [42-46].

$$I(t) = I_0 e^{-\Sigma t}$$

Eq. 2-1

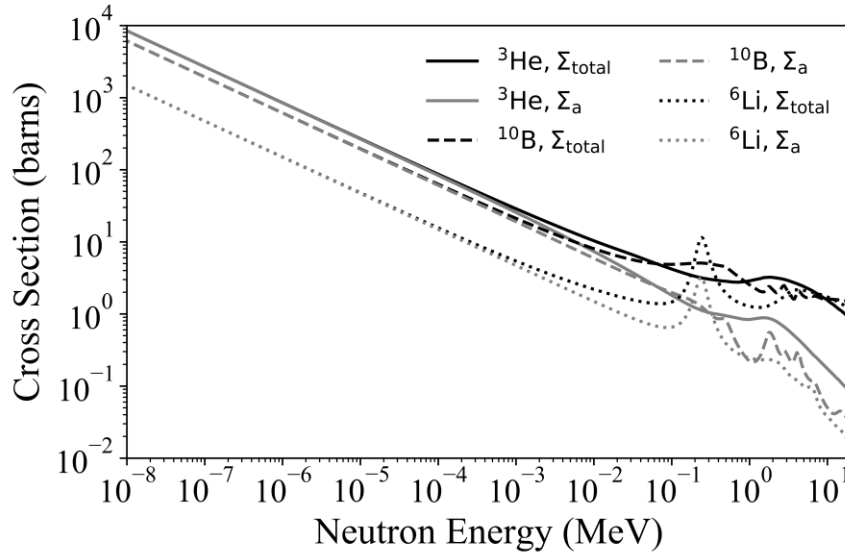


Fig. 2-1. Total neutron interaction cross sections and neutron absorption cross sections for ^3He , ^{10}B , and ^6Li , the most common conversion materials for thermal neutron detectors [47].

One method of neutron interaction is scattering wherein an energetic neutron hits and scatters off the nucleus of an atom transferring some or all its energy to the recoil atom. Neutron scattering events can be elastic or inelastic and is described by Eq. 2-2 where E and E' are the initial and scattered energies of the incident neutron, respectively, A is the atomic mass of the target nucleus, θ_s is the neutron scattering angle, and Q is the Q-value of the interaction [43].

$$E' = \frac{1}{(1-A)^2} \left[\sqrt{E} \cos \theta_s \pm \sqrt{E(A^2 - 1 + \cos^2 \theta_s) + A(A+1)Q} \right]^2 \quad \text{Eq. 2-2}$$

$$\frac{E'_{min}}{E} = \alpha = \left[\frac{1-A}{1+A} \right]^2 \quad \text{Eq. 2-3}$$

$$\frac{T}{E} = 1 - \alpha \quad \text{Eq. 2-4}$$

In an elastic scatter, the kinetic energy of the neutron and target nucleus before the scatter equals the kinetic energy of the neutron and nucleus after the scattering interaction. In an inelastic scatter, kinetic energy is not conserved, and the target nucleus is left in an excited state, which often decays to the ground state by emitting a gamma ray. For elastic scattering, the minimum fraction of initial energy of the incident neutron after a scatter interaction is a function of the atomic number of the target material, shown in Eq. 2-3. The maximum fraction of energy imparted on the recoil nucleus is shown in Eq. 2-4 [43]. Highly hydrogenous materials are considered the best

neutron moderators, because all the energy of an incident neutron can be transferred to the recoil proton for scattering events with ^1H nuclei. For isotropic scattering, the average fraction of energy transferred to the recoil proton for elastic scatters is $0.5(1 - \alpha)$ [43].

Many common neutron detectors rely on neutron moderation to thermalize neutrons so they can be efficiently absorbed by a conversion material, which subsequently results in the emission of highly energetic reaction products. The goal is then to detect these reaction products. Some fast neutron detectors are designed to measure the charged-particle interactions of the recoil nuclei from high-energy neutron scatter events, such as the PRESCILA dose meter [48]. The detectors described in this dissertation focus mainly on thermal neutron detection, and the generalized thermal neutron detection process is as follows.

1. Fast neutrons, if present, must be slowed down to thermal energies through neutron scattering events. Typically, the detectors are surrounded by a HDPE moderating cask to achieve this goal.
2. Thermal neutrons are absorbed in neutron conversion material.
3. Charged-particle reaction products are subsequently emitted following the thermal neutron absorption. Some common neutron conversion materials and their reaction products are shown in Fig. 2-2.
4. The reaction products then deposit energy in the detection medium.
5. The deposited energy is measured. The method of measurement varies depending on the type of radiation detector, e.g. collecting electrons and ions (gas detectors), measuring scintillation light (scintillation detectors), or drifting electrons and holes (semiconductor detectors).

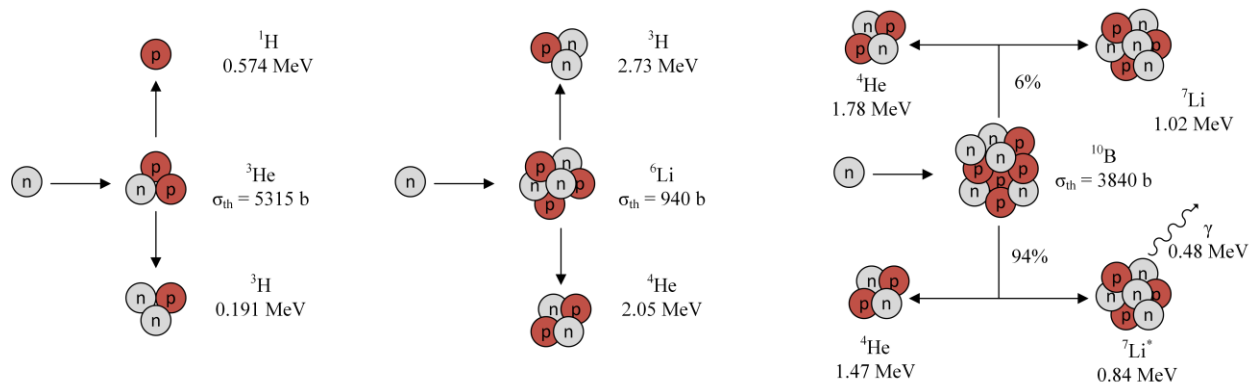


Fig. 2-2. Thermal neutron (0.025eV) capture cross section and reaction product energies for common thermal neutron conversion materials, ${}^3\text{He}$, ${}^{10}\text{B}$, and ${}^6\text{Li}$ [44].

2.3. Review of Common Thermal Neutron Detectors

A radiation detector must be designed so that a measurable phenomenon occurs when radiation interacts within the detector. Some of the earliest radiation detectors were fluorescing plates that gave off visible light that could be qualitatively observed when radiation interacted in the fluorescent coating. Other devices were photographic plates that became exposed through x-ray interaction in the emulsion [34]. Other measurement devices were soon used to measure radiation interactions, such as the gold leaf electroscope used by Rutherford and the spinthariscopes invented by Crookes [49, 50]. Eventually, as other technologies progressed, more sophisticated radiation detectors were developed that convert the energy deposition within the detector to a quantifiable voltage pulse. The three most common types of modern neutron detectors are presently gas-filled detectors, scintillation detectors, and semiconductor detectors. This section aims to provide a brief overview of the design and operation of these modern neutron detectors.

2.3.1. Gas-Filled Thermal-Neutron Detectors

Gas-filled thermal-neutron detectors operate by detecting the interactions of the charged-particle reaction products in the fill gas emitted following the absorption of a neutron in the conversion material. For ^3He and $^{10}\text{BF}_3$ neutron detectors, the conversion material is the detection medium, because ^3He and $^{10}\text{BF}_3$ are gaseous under standard operating conditions. As previously mentioned, ^3He detectors are considered the “gold-standard” for neutron detectors and are capable of achieving high intrinsic thermal-neutron detection efficiencies. This good performance is achieved because ^3He has a high thermal-neutron absorption cross section and emits promptly two energetic charged-particles with appreciable kinetic energy. However, the rising price and limited supply of ^3He has caused concern about the availability of ^3He in the future and has motivated the research into alternative neutron detectors [1]. $^{10}\text{BF}_3$ gas-filled detectors are a long known alternative which utilizes the $^{10}\text{B}(n,\alpha)^7\text{Li}$ reaction. For detectors of similar size, $^{10}\text{BF}_3$ detectors will have lower detection efficiency than ^3He detectors, because $^{10}\text{BF}_3$ has a smaller thermal-neutron absorption cross section than ^3He . Furthermore, the fill pressure of $^{10}\text{BF}_3$ is limited to about 1 atm, because electron and ion transport in $^{10}\text{BF}_3$ is poor at higher pressures [45]. Finally, $^{10}\text{BF}_3$ is toxic thus limiting its marketability. The other category of gas-filled detectors include detectors typically filled with Ar or P-10 gas and have a solid neutron sensitive layer coated onto the inner walls of the detector [44, 45] or suspended inside the detectors [51-60]. The thickness of

the neutron conversion layer is limited by the range of the higher energy reaction product, therefore limiting the neutron detection efficiency. The detection efficiency can be improved by inserting additional suspended neutron conversion layers [60] or incorporating internal coated fins which increases the volume of neutron conversion material within the detector without adversely affecting the reaction product escape probability [61, 62]. Shown in Fig. 2-3 are two examples of gas-filled detectors.

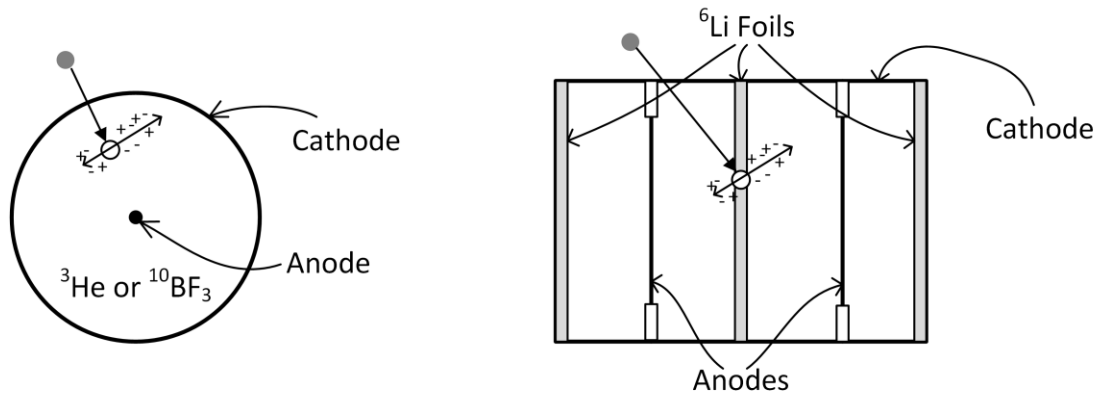


Fig. 2-3. Simplified diagrams of gas-filled neutron detectors. (Left) Cross section of a cylindrical detector where the fill gas is the conversion material. (Right) Rectangular detector with suspended ⁶Li-foils and ⁶Li coated walls.

Many gas-filled neutron detectors operate as proportional counters. The charged particles emitted following a neutron absorption ionize the surrounding gas. Electrons are drifted towards the anode by the influence of the electric field created by the voltage between the cathode and anode. The electric field is high enough to cause Townsend avalanching near the anode which in turn reduces the pulse height dependence on interaction location in the detector. However, if interactions occur near the wall of the detector chamber, the “wall effect” is observed wherein some or all the energy from one of the charged-particle reaction products is absorbed in the detector wall and does not contribute to the signal. For coated detectors, every interaction demonstrates the wall effect. This reduced pulse height from not measuring all the energy of both reaction products can cause some of the neutron-induced signal to overlap and be lost in electronic noise and gamma-ray background at the lower energy portion of the pulse height spectrum [44, 45]. Fortunately, gas-filled neutron detectors are relatively insensitive to gamma rays, because the gamma rays are unlikely to interact in the low-density gas within the detector. Most gamma-ray interactions occur in the metal detector walls and require a freed electron to enter the chamber to be measured.

Finally, since the detectors have strung anodes biased at high voltage (1000-3000 V), the gas filled detectors have microphonic sensitivity to shocks and vibrations, which can induce undesirable spurious counts [45].

2.3.2. Scintillation Neutron Detectors

Scintillation detectors are materials that promptly emit measurable light when irradiated. When ionizing radiation interacts in a scintillation material, electrons are excited to higher energy bands. The electrons then de-excite through an activator site in an inorganic scintillator or between singlet states for organic scintillators and emit visible light. The visible light is then converted to electrons and amplified in either a traditional photomultiplier tube (PMT) composed of a photocathode and cascading array of dynodes in a vacuum tube or a silicon photomultiplier (SiPM) composed of arrays of silicon photodiodes operated near its breakdown voltage. Utilizing either light collection method, the result is an amplified electronic pulse proportional to the amount of light incident on the PMT or SiPM. The electronic pulse can then be further amplified, quantified, and binned into discrete energy bins based on the magnitude of the pulse.

Scintillation neutron detectors are typically based on ^{10}B or ^6Li neutron conversion material. Bulk neutron sensitive scintillating materials include ^6LiI , which has similar chemistry to common NaI scintillation detectors, ^{10}B or ^6Li loaded plastic scintillators, and elpasolite materials like $\text{Cs}_2\text{LiYCl}_6:\text{Ce}$ (CLYC), $\text{Cs}_2\text{LiLaBr}_6:\text{Ce}$ (CLLB), and $\text{Cs}_2\text{LiLa}(\text{Br,Cl})_6:\text{Ce}$ (CLLBC). An alternative to incorporating neutron conversion material into the crystal is to simply coat the material on the surface of the scintillator. Common examples of coated scintillators are ^6Li -coated scintillating fibers and ^6LiF -coated $\text{ZnS}(\text{Ag})$ screens. Scintillation detectors have higher density and often higher Z -number than gas-filled detectors making them more sensitive to gamma rays, which can lead to more gamma-ray induced false alarms. In some cases, the gamma-ray sensitivity is advantageous allowing for simultaneous dual-mode gamma-ray and neutron detection. However, additional pulse processing electronics are required to differentiate the gamma-ray signal from the neutron signal. An alternative to dual-mode detection in a single crystal is to have a dedicated neutron detector with low gamma-ray sensitivity and a dedicated gamma-ray detector within the same package. The separated approach would allow for operation in higher radiation flux environments by reducing the number of interactions processed per detector.

2.3.3. Semiconductor Neutron Detectors

As the name suggests, a semiconductor neutron detector is composed of a semiconductor substrate where neutron sensitive material has either been integrated as part of the crystal lattice, coated onto the surface, or backfilled into perforations in the semiconductor. Neutrons interact with the conversion material and emit reaction products, typically charged particles or gamma rays. The reaction products then interact in the semiconductor substrate creating electron-hole pairs through coulombic interactions. Next, the charge carriers are drifted by the influence of an electric field, and the net movement of the charge carriers induces a measurable current at the detector electrodes.

Bulk semiconductor neutron detectors like LiZnP, LiZnAs, CdZnTe, HgI₂, BN, and LiInSe have been investigated for solid-state thermal-neutron detection, but limitations in crystal growth size, detection efficiency, and poor charge transport properties have limited their deployment in real world detector systems [63-68]. Conversely, thin-film coated detectors with neutron conversion material coated onto *pn*- or Schottky junction diodes have been developed as thermal neutron detectors for decades [5-12, 14]. The planar diodes are rugged, compact, mass producible, and thanks to a booming silicon electronics industry, are relatively inexpensive. Unfortunately, single layer detectors are limited to 4-5% intrinsic thermal-neutron detection efficiency, and stacking multiple thin-film detectors has a diminishing return on improving detection efficiency [6]. The better solution, to improve neutron detection efficiency while retaining all the advantages of semiconductor detectors, was realized through the invention of MSNDs followed by DS-MSNDs, which comprise high-aspect ratio microfeatures etched into the semiconductor diode subsequently backfilled with neutron conversion material. MSNDs were theorized as early as 1987 [69, 70], developed at Kansas State University in recent years [15-27, 71], commercialized by Radiation Detection Technologies, Inc. [28], and has also received research interest from other groups [72-76]. Chapter 4 includes detailed discussions on previous work performed on MSNDs and the current progress of state-of-the-art DS-MSNDs.

2.3.4. Design Considerations

The key criteria for evaluating a neutron detector are intrinsic thermal-neutron detection efficiency, gamma-ray detection efficiency or gamma-ray rejection ratio, size, weight, power consumption, and cost. In nearly all applications high intrinsic thermal-neutron detection

efficiency is desired, except for example, reactor in-core instrumentation where the neutron flux is exceedingly large and needed to sustain the nuclear reactions ultimately responsible for generating electrical power. Intrinsic thermal-neutron detection efficiency is the probability a thermal neutron incident on the detector is measured (Eq. 4-8). For a given measurement time, higher intrinsic detection efficiency improves the precision of a measurement. Therefore, an operator looking for SNM with a neutron detector can search an area quicker, or more measurements can be performed in a laboratory environment in a day generating more data than if a neutron detector with lower detection efficiency was used.

Ideally, the gamma-ray detection efficiency or gamma-ray rejection ratio of a neutron detector should be low. Many radiation environments include a mixed field of neutron and gamma rays. Falsely recording gamma-ray interactions as neutron interactions reduces the certainty of the measurements. The two common methods to improve the gamma-ray rejection ratio of neutron detectors are to only use materials in the detector that are largely insensitive to gamma rays (i.e. low-Z materials) and to implement pulse shape or height discrimination to separate gamma-ray interactions from neutron interactions.

In most scenarios, it is safe to assume that reducing the cost of the detector is desired; hence, the recent research interest in funding alternatives to expensive and rare ^3He for thermal-neutron detection [1]. SWAP parameter constraints of neutron detectors are dictated by the application or mission space. For example, stationary neutron detectors in radiation portal monitors, require large detector active area to improve the solid angle between the detector and the vehicles passing through the inspection area. Detector weight and power consumption are of less concern, because the detector is mounted on the ground and can be connected to a nearby power supply. Gas-filled or plastic-scintillating neutron detectors tend to fit well into this market, because they can be scaled to large sizes cost effectively. On the other side of the scale, reduction in SWAP parameters is desired for handheld, wearable, or space-based neutron detection applications. Semiconductor neutron detectors like the DS-MSND are a viable choice in this arena, because high detection efficiency can be achieved in a comparatively small volume and can be designed to operate with minimal power consumption.

Chapter 3 - Semiconductor Radiation Detectors Basics

Semiconductor detectors were used to measure radiation as early as 1941 [77] and received significant interest throughout the 1960s and 1970s [77-93] and again in recent years [94-107]. Originally, semiconductor detectors became interesting especially in spectroscopy, because they are capable of extremely high energy resolution, only requiring a few eV of energy to create electron-hole pairs, which are the measurable charge carriers [44]. Additionally, semiconductors have much higher density than common gas detectors, and therefore, small semiconductor detectors could replace large gas-filled detectors without reducing radiation stopping power [45]. For thermal neutron detection, energy resolution is not as important than for charged-particle, gamma-ray, and x-ray spectroscopy, but semiconductor-based detectors offer several advantages over other types of neutron detectors including size, weight, micro-machinability, low-voltage requirements, power consumption, gamma-ray insensitivity, and mass-producibility through modern VLSI processing techniques. This chapter provides a very brief overview of the general properties of silicon and its use as a radiation detector pertaining to MSND and DS-MSND operation.

3.1. Semiconductor Physical Properties

Semiconductors are classified as solid materials occupying the partially electrically conductive region between insulators and conductors. Electrical conductivity is largely dependent on the band gap, or lack thereof, between the valence band and conduction band in a material. Generally, in an insulator the valence band has no free electrons, in a semiconductor the valence band contains a few thermally excited electrons at room temperature, and in a conductor the conduction band is partially filled with electrons providing many free electrons capable of charge transport through empty states (Fig. 3-1) [108, 109].

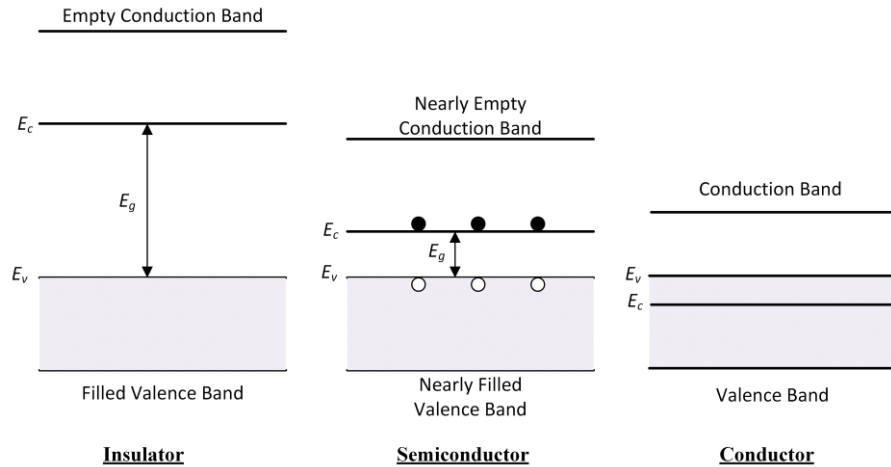


Fig. 3-1. Diagrams of energy band electron populations for insulators, semiconductors, and conductors. Image was based on images from [108, 109].

Early studies of the discretized light emission from excited hydrogen atoms supported Bohr’s model that electrons can only occupy specific energy levels around an atom. An isolated silicon atom has 14 protons and 14 neutrons in its nucleus surrounded by 14 electrons with 10 electrons in tightly bound bands and 4 electrons in the outer 3s and 3p energy bands (Fig. 3-2) [108, 110, 111]. Each electron has discretized energy, and from the Pauli Exclusion Principle, no two electrons can occupy the same state. When two isolated silicon atoms are brought near each other, the allowed energy levels overlap causing the allowed energy states to split, and the two atoms can now share outermost electrons. As more silicon atoms are added to the crystal lattice, the energy bands continue to split forming a quasi-continuum of allowed energy bands. The lower energy band becomes the valence band, which has an upper energy limited denoted as E_v , and the higher energy band becomes the conduction band, which has a lower energy limit designated as E_c . Notice that there is a forbidden energy region between the upper limit of the valence band and lower limit of the conduction band aptly named the band gap, E_g . In silicon, the band gap energy is 1.12 eV [108, 110, 111].

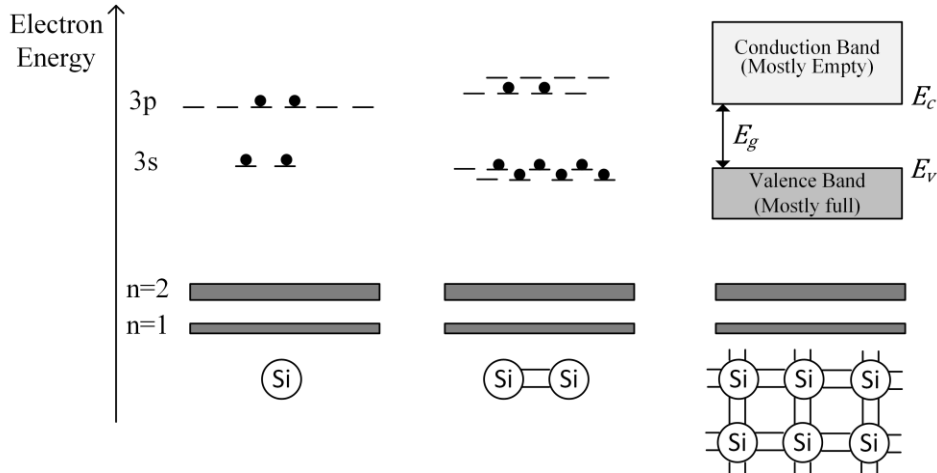


Fig. 3-2. Simplified diagram depicting formation of valence band and conduction band in silicon. As additional silicon atoms are bonded to the system the original discrete allowed electron energy states split to form quasi-continuous energy bands with a forbidden (band) gap forming between the valence band and conduction band.

The movement of charge carriers, electrons in the conduction band and holes in the valence band, induces current in a detector circuit. In semiconductors, thermal energy is enough to cause valence electrons to jump to the conduction band leaving behind a hole. However, at room temperature, the number of free electrons generated by thermal interactions in silicon is small enough to be distinguished from radiation events. In an intrinsic (pure) semiconductor, the electron or hole density at steady state is described as the integral over the energy band of the density of states of that band multiplied by the Fermi-Dirac distribution function (Eq. 3-1) [108]. The density of states is the density of allowed electron energy states in an energy range per unit volume, and the Fermi-Dirac distribution function describes the probability an electron occupies an energy state [108].

$$n = \int_{E_{bottom}}^{E_{top}} N(E)F(E)dE \quad \text{Eq. 3-1}$$

$$F(E) = \frac{1}{1 + e^{(E-E_F)/kT}} \quad \text{Eq. 3-2}$$

k – Boltzmann constant

T – Absolute temperature

E_F – Fermi Level

Substituting the density of state equations found in [108, 112] and solving Eq. 3-1, the electron density in the conduction band and hole density in the valence band for an intrinsic semiconductor

is described by Eq. 3-3 and Eq. 3-4, respectively, where N_c is the effective density of states in the conduction band, and N_v is the effective density of states in the valence band. N_c and N_v for Si is shown in Eq. 3-5 and Eq. 3-6, respectively [108]. m_n and m_p are the effective masses for electrons and holes, respectively, and h is Planck's constant. A diagram depicting the density of states is shown in Fig. 3-3 [108].

$$n = N_c e^{-(E_c - E_F)/kT} \quad \text{Eq. 3-3}$$

$$p = N_v e^{-(E_F - E_V)/kT} \quad \text{Eq. 3-4}$$

$$N_c = 12(2\pi m_n kT/h^2)^{3/2} \quad \text{Eq. 3-5}$$

$$N_v = 2(2\pi m_p kT/h^2)^{3/2} \quad \text{Eq. 3-6}$$

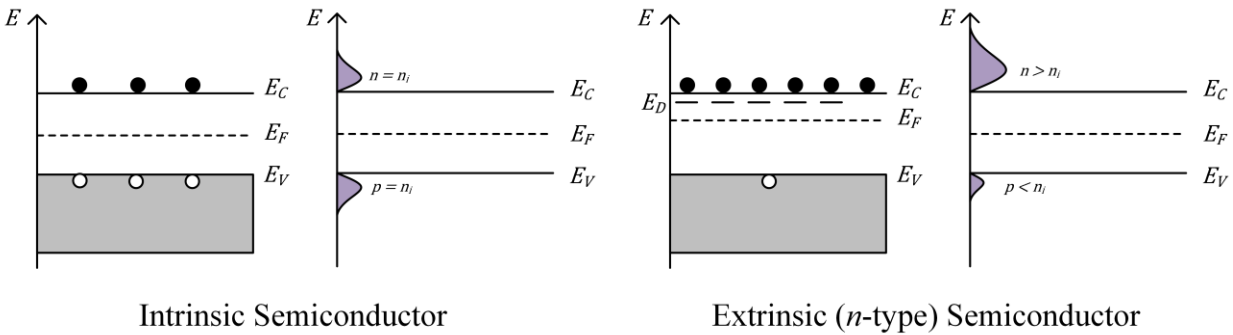


Fig. 3-3. Diagrams of electrons, holes, and Fermi level in an intrinsic semiconductor and *n*-type semiconductor.

In an intrinsic semiconductor, the electron and hole populations are equal, because every thermally generated electron leaves behind a hole, and a perfect crystal does not have any ionized impurities. However, in practice, a small amount of impurities or dopants is intentionally added to the silicon crystal lattice in the ingot growth process to precisely control the charge carrier population. Phosphorus and boron are the most common *n*-type and *p*-type dopants for silicon, respectively. Phosphorus has five valence electrons and therefore can “donate” one electron to the conduction band. Conversely, boron has three valence electron and therefore accepts an electron from the valence band, leaving behind a hole. The donor and acceptor levels are very close to the conduction band and valence band, respectively, and can be considered completely ionized at room temperature. Since the carrier concentration changes as a function of the doping level, the Fermi level shifts up or down based on the dopant type. The dopant concentrations, N_D or N_A , are routinely orders of magnitude greater than the intrinsic carrier concentration, which is nominally 10^{10} cm^{-3} , and therefore the electron and hole density can be estimated by Eq. 3-7 and Eq. 3-8 for

n -type and p -type semiconductors [108]. Eq. 3-9 shows the relationship between the electron concentration, hole concentration and intrinsic carrier concentration. For reference, DS-MSNDs are fabricated on 5 k Ω -cm resistivity, n -type, phosphorus-doped, silicon which corresponds to a donor concentration, N_D , of about 9×10^{11} atoms cm^{-3} .

$$\text{For } n\text{-type silicon, } n \cong N_D \quad \text{Eq. 3-7}$$

$$\text{For } p\text{-type silicon, } p \cong N_D \quad \text{Eq. 3-8}$$

$$np = n_i^2 \quad \text{Eq. 3-9}$$

3.2. Semiconductor Depletion Region Formation

Resistive semiconductor devices have two or more ohmic contacts on a semiconductor substrate, and a bias is applied to create an internal electric field to influence charge carrier motion within the detector. This simpler device requires the resistivity of the device to be sufficiently high, on the order of 10^{10} Ω cm or higher, to limit leakage current across the detector. High leakage current results in a high noise floor which can compete with or completely drown out the radiation induced signal. The resistivity of silicon wafers used to fabricate DS-MSNDs is near 5×10^3 Ω cm, and therefore, DS-MSNDs cannot be operated as resistive devices. Instead, a rectifying contact or junction must be fabricated. DS-MSNDs utilize pn -junctions to limit the leakage current and establish the internal electric field critical for measuring the charge carriers created by radiation interactions within the detector.

A pn -junction is formed when two regions of opposite type silicon are brought together, see Fig. 3-4. In n -type material, the Fermi level is near the conduction band, and in p -type material the Fermi level is near the valence band. When the p -type and n -type regions are brought together, the Fermi level must remain constant [108], and therefore, the bands appear to bend to connect the conduction bands and valence bands between the n -type and p -type material. On the n -type side of the junction, an excess of electrons exist that will diffuse into the p -type region leaving behind positively charged stationary donor sites. Similarly, the concentration of holes on the p -type side of the junction is high compared to the n -type side. The concentration gradient causes holes to diffuse from the p -type side to the n -type side leaving behind stationary, negatively charged, acceptor states. The stationary charged dopant sites in the space charge region create an electric field that opposes the diffusion of electrons and holes across the junction and promote drift of minority carriers across the junction opposite the direction of diffusion. At thermal equilibrium, with no external bias or irradiation, the net current from either charge carrier must equal zero.

Thus, the current contributions from drift and diffusion are equal in magnitude and opposite in direction.

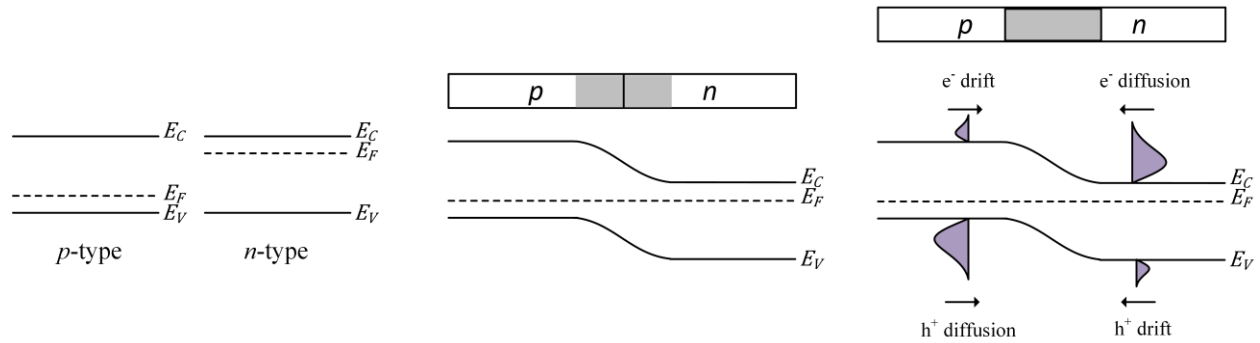


Fig. 3-4. (Left) Band diagram of p-type and n-type semiconductors. (Middle) Diagram showing a pn-junction. (Right) Diagram of electron and hole diffusion and drift caused by charge carrier imbalances and the electric field formed in the space charge region.

The electrostatic potential, $V(x)$, and electric field, $E(x)$, in the space charge (or depletion) region is described by Poisson's equation and shown in Eq. 3-10, where ρ is the net charge density, and ϵ_s is the dielectric permittivity [108]. The built-in potential that arises from the difference in charge density across the junction is defined in Eq. 3-11 [108]. An example of the potential and electric field is shown in Fig. 3-5 for a hypothetical 1-D, abrupt, pn -junction defined by Eq. 3-12 through Eq. 3-15 using the depletion approximation [113]. Notice that the maximum electric field occurs at the interface between the p-type and n-type material. Additionally, in calculating the voltage potential, it was assumed that $V(x_p)$ was equal to zero, and therefore, $V(x_n)$ was equal to the built-in potential.

$$\frac{\partial^2 V(x)}{\partial^2 x} = -\frac{\partial E(x)}{\partial x} = \frac{-\rho}{\epsilon_s} \quad \text{Eq. 3-10}$$

$$V_{bi} = \frac{kT}{q} \ln \left(\frac{N_A N_D}{n_i^2} \right) \quad \text{Eq. 3-11}$$

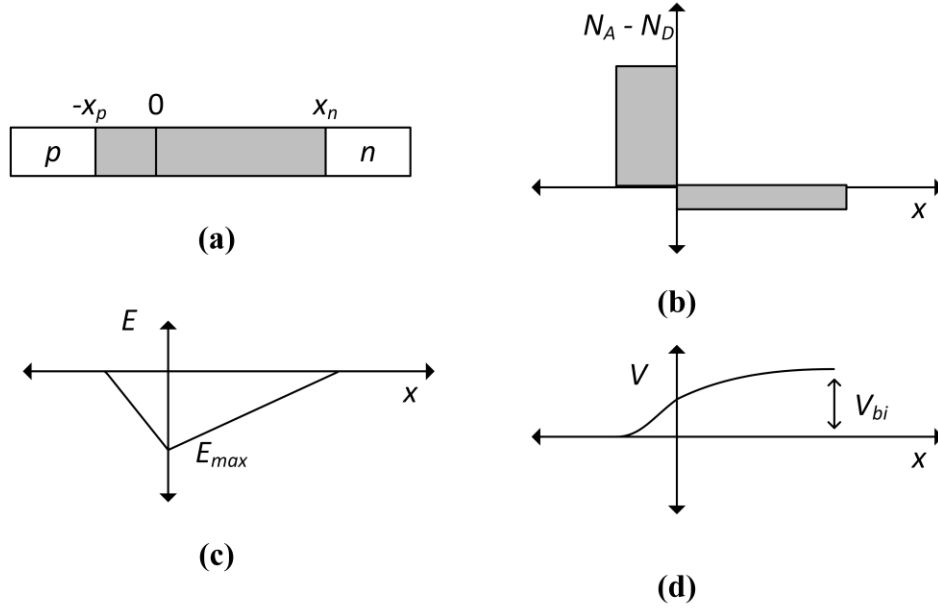


Fig. 3-5. (a) Simplified 1-D, abrupt junction, pn-junction diagram with the p-side having higher dopant concentration than the n-side. (b) Net dopant concentration on each side of the junction. (c) Electric field in the depletion region. (d) Voltage potential in the depletion region.

$$E(x) = \frac{-qN_A}{\epsilon_s}(x_p + x), \text{ for } -x_p \leq x \leq 0 \quad \text{Eq. 3-12}$$

$$E(x) = \frac{-qN_D}{\epsilon_s}(x_n - x), \text{ for } 0 \leq x \leq x_n \quad \text{Eq. 3-13}$$

$$V(x) = \frac{qN_A}{2\epsilon_s}(x_p + x)^2, \text{ for } -x_p \leq x \leq 0 \quad \text{Eq. 3-14}$$

$$V(x) = \frac{-qN_D}{2\epsilon_s}(x_n - x)^2 + V_{bi}, \text{ for } 0 \leq x \leq x_n \quad \text{Eq. 3-15}$$

An important relationship is realized by equating Eq. 3-12 and Eq. 3-13 at x equals 0 and is shown Eq. 3-16 [113]. Thus, if one side of the junction has a much higher dopant concentration the depletion region will extend deep into the lighter doped side. The average dopant concentration for the ν -type material used DS-MSNDs is approximately 10^{12} phosphorus atoms per cm^3 , which is much smaller than the p -type dopants diffused into onto the surface of the microstructures that can range in concentrations from 10^{16} to 10^{19} boron atoms per cm^3 . This phenomenon allows pvp -DS-MSNDs to operate solely on the built-in potential and electric field. The width of the depletion region is given by Eq. 3-17 and can be simplified to a one-sided approximation shown in Eq. 3-18 when the dopant concentration on the p -type side is much higher than the n -type side [108, 113]. Finally, the depletion region width can be manipulated by biasing the diode as shown in Eq. 3-19

with the one-sided junction approximation. MSNDs and *pn*-variants of DS-MSNDs operate with a reverse bias, meaning negative voltage applied on the *p*-type side or positive voltage applied on the *n*-type side, which increases the width of the depletion region and strength of the electric field. Radiation interactions are only measured if they occur in the depletion region, and the electric field is critical for drifting and measuring the charge carriers.

$$N_A x_p = N_D x_n \quad \text{Eq. 3-16}$$

$$W = \sqrt{\frac{2\epsilon_s V_{bi}}{q} \left(\frac{N_A + N_D}{N_A N_D} \right)} \quad \text{Eq. 3-17}$$

$$W \cong \sqrt{\frac{2\epsilon_s V_{bi}}{q N_D}} \quad \text{Eq. 3-18}$$

$$W \cong \sqrt{\frac{2\epsilon_s (V_{bi} - V)}{q N_D}} \quad \text{Eq. 3-19}$$

One way to characterize a *pn*-junction is to measure the current vs. voltage (IV) and capacitance vs. voltage (CV) characteristics. The *pn*-junction should be rectifying, meaning current flow is suppressed in one direction as shown in Fig. 3-6. If a *pn*-junction is forward biased, the voltage potential between the *p*-type and *n*-type side is reduced which increases the diffusion current across the junction. When the junction is reverse biased, the diffusion current is reduced because of the increased voltage potential, and the next current flow is from drifting minority carriers across the junction. When the reverse bias is increased past a critical voltage, the magnitude of the current starts to increase exponentially. The breakdown of the junction is caused by charge carrier avalanching, where the electrons and holes gain enough kinetic energy drifting through the high electric field to excite additional charge carriers when colliding with lattice atoms. The newly excited charge carriers can then be accelerated and create additional electron-hole pairs to further amplify the current. MSNDs and DS-MSNDs are operated with reverse bias below the breakdown voltage where the current is suppressed, which reduces noise, and charge carriers excited within the depletion region of the *pn*-junction can be drifted and measured. Note that real devices deviate from “ideal” *pn*-junctions diode under reverse current due to thermal generation within the depletion region which expands as the voltage increases. A theoretical CV curve is also shown in Fig. 3-6, and the equation describing the capacitance for an abrupt one-sided *pn*-junction as a function of applied bias, *V*, is shown in Eq. 3-20, where *A* is the area of the contact [113]. The capacitance decreases as the depletion width increase until the diode is fully depleted. Additional

discussion on *pn*-junction properties and derivations of the IV and CV curves can be found in the literature [108, 112, 113].

$$C = \frac{\epsilon_s A}{W} = \sqrt{\frac{q \epsilon_s N_D}{2(V_{bi} - V)}} A \quad \text{Eq. 3-20}$$

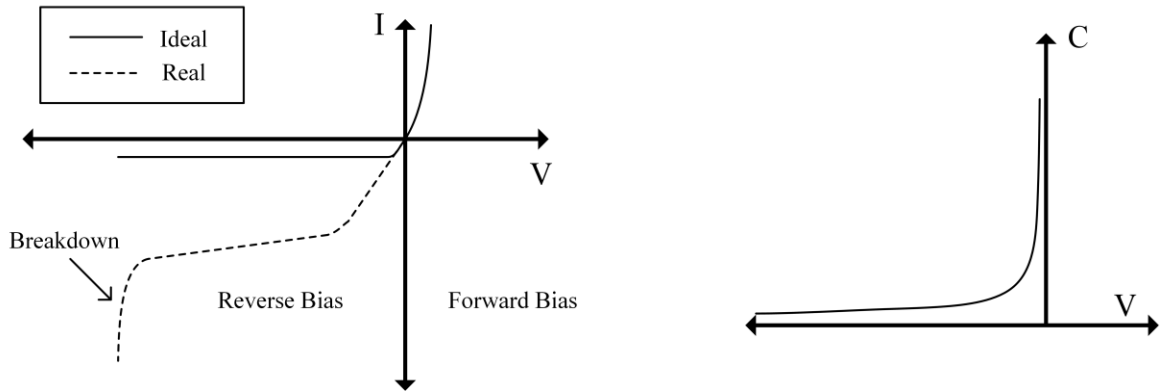


Fig. 3-6. Theoretical (Left) IV and (Right) CV curves for a *pn*-junction diode.

3.3. Charge Carrier Production and Signal Generation in Semiconductors

Radiation detection in semiconductor detectors is much like radiation detection with a gas filled detector. Ionizing radiation incident on semiconductor imparts energy in the medium and creates electron-hole pairs with about 3.6 eV required to create each pair of charge carriers in Si [44, 45, 109, 114]. For MSNDs and DS-MSNDs, the ionizing radiation of interest is the charged-particle reaction products emitted from the neutron conversion material and gamma rays that are commonly present as background radiation. After the charge carriers are created, the internal electric field, either intrinsic or from the applied bias, influences the motion of electrons and holes causing them to drift towards their respective contacts. Current is induced in the electrodes as the charge carriers move through the weighting field of device. The magnitude of charge collected is proportional to the separation distance of the electrons and holes for the planar, two-electrode device shown in Fig. 3-7, because the weighting field is uniform throughout the detector [109]. For low electric fields, the average drift velocity of the electrons and holes are show in Eq. 3-21 and Eq. 3-22, respectively, where \mathbf{E} is the electric field, μ_e is the electron mobility, and μ_h is the hole mobility.

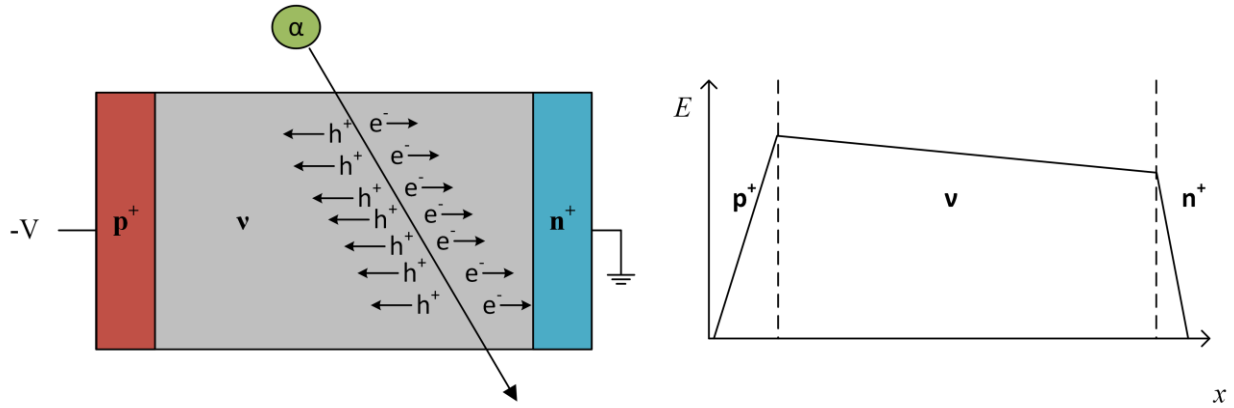


Fig. 3-7.(left) Diagram of radiation interaction in a pvn-diode and subsequent charge drift from the electric field present in diode shown on the right. (right) Electric field strength in the pvn-diode.

$$v_e = \mu_e E \quad \text{Eq. 3-21}$$

$$v_h = \mu_h E \quad \text{Eq. 3-22}$$

While the electrons and holes drift, the localized concentration gradient causes the charge carriers to diffuse outwards equally in both directions. This charge-carrier diffusion induces equal amounts of current on each electrode, resulting in zero net current contribution. If no electric field is present, the electrons and hole will diffuse equally until they recombine, and the radiation interaction would not be detected. However, as long as an electric field is present to drift the expanding charge clouds, the net separation of their centroids will induce current in the detector electrodes. An example of the simultaneous drift and diffusion of electrons and holes is shown in Fig. 3-8. The magnitude of the voltage inputted to the preamplifier from a radiation event is defined in Eq. 3-23 where Q is the amount of charge collected and C is the detector capacitance. An ideal detector would have low capacitance to maximize the voltage output and low leakage current to minimize background noise. Unfortunately, as the bias voltage is increased to increase the width of the depletion region which lowers the capacitance, the leakage current tends to increase. Thus, a tradeoff exists between high bias operation that provides a high internal electric field with low capacitance, and low bias operation which reduces the electronic noise and reduces power consumption.

$$\Delta V = \frac{\Delta Q}{C} \quad \text{Eq. 3-23}$$

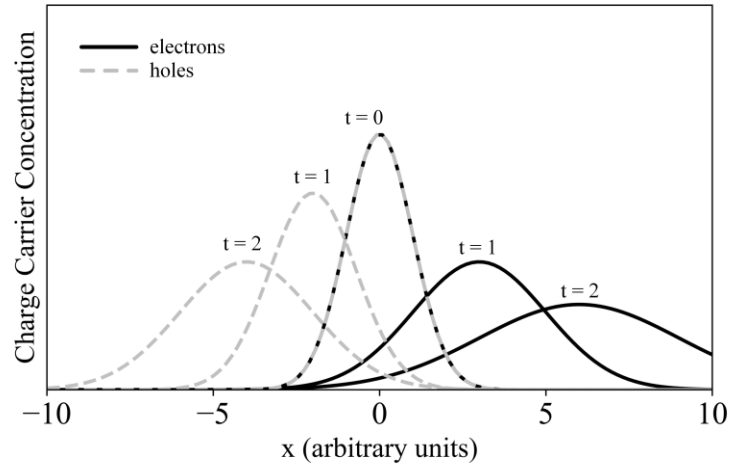


Fig. 3-8. Example of simultaneous drift and diffusion of charge carrier clouds within a semiconductor. The electron-hole pairs are initially created at $x=0$.

Chapter 4 - Dual-Sided Microstructured Semiconductor Neutron

Detectors: Design

4.1. Design and Operation

Dual-Sided Microstructured Semiconductor Neutron Detectors are built upon years of research aimed at developing a cost-efficient, high-efficiency, alternative to rare and expensive ^3He for thermal-neutron detection. This section covers a brief history of detector development leading up to the present state-of-the-art DS-MSNDs.

4.1.1. *Thin-Film Coated Semiconductor Detectors*

One early, solid-state alternative to ^3He for thermal-neutron detection was realized through thin-film coated diodes in which a thin-film of neutron conversion material was deposited on the surface a semiconductor diode, see Fig. 4-1 [5-15, 70, 115, 116]. Incident neutrons are absorbed in the conversion material which produces secondary reaction products, typically energetic charged particles. ^6LiF and ^{10}B are two of the more common conversion materials, because they emit heavy charged particles with relatively high Q-values of 4.78 MeV and 2.79 (6%) / 2.31 (94%) MeV, respectively. For both conversion materials, the reaction products are emitted in opposite directions. If one of the reaction products enters the semiconductor substrate, the reaction product deposits energy through coulombic interactions with electrons in the semiconductor, which produces electron-hole pairs. The electrons and holes can then be drifted through the semiconductor diode by the internal electric field in the depletion region. The motion of the charge carriers (electrons and holes) through the weighting potential in the semiconductor induces current in the detector's electrodes that is used to form a measurable voltage pulse.

Simple thin-film coated diodes are easily mass-produced through simple VLSI processing procedures, and are compact, rugged, and generally operate on low voltage. However, the maximum intrinsic thermal-neutron detection efficiency is limited to 4-5% for the devices as those shown in Fig. 4-1 [6]. The two factors limiting the intrinsic-thermal neutron detection efficiency are neutron absorption efficiency and reaction product escape probability, which is the probability for a reaction product to exit the conversion material and enter the semiconductor. The neutron absorption efficiency is described by Eq. 4-1 where Σ_a is the macroscopic neutron absorption cross section, and t is the neutron pathlength in the absorption material. Σ_a is determined by the

composition and density of conversion material. The thickness can be increased to absorb more neutrons; however, as the thickness of the conversion material increases, the reaction product escape probability decreases due to the finite range of the charged-particle reaction products. The optimum conversion material layer thickness is realized when the product of the neutron absorption efficiency and reaction product escape probability is maximized.

$$\epsilon_{absorption} = 1 - e^{-\Sigma a t} \quad \text{Eq. 4-1}$$

More complicated designs involving multi-layer coatings of different conversion materials can improve the intrinsic thermal-neutron detection efficiency to approximately 13% [6]. Also, stacking multiple thin-film coated detectors can improve the detection efficiency, but there is a limited, non-linear return on the number of detectors required to increase the detection efficiency, and detector stacks require additional signal processing electronics which ultimately increases costs [6].

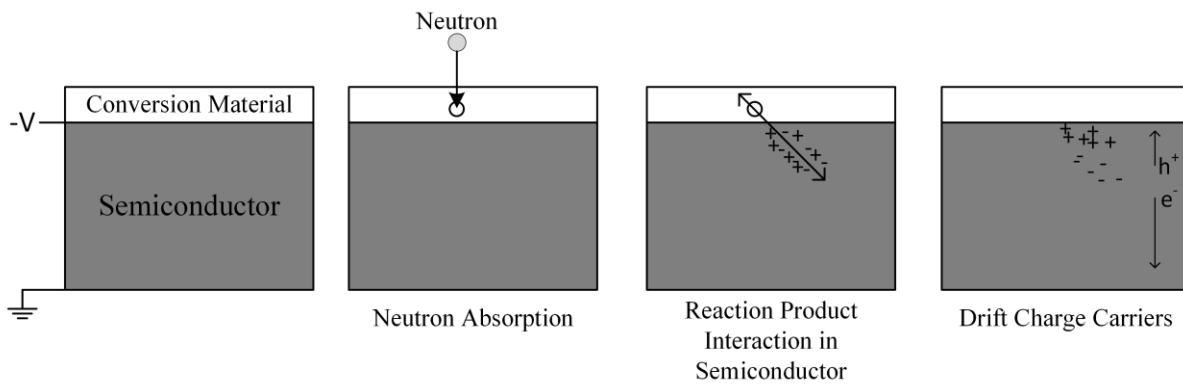


Fig. 4-1. Example of neutron detection process for thin-film coated neutron detector. Neutrons are absorbed in the conversion material layer which then causes the release of charge-particle reaction products that can enter semiconductor diode. The reaction products deposit energy in the semiconductor diode, thereby creating electron-hole pairs that are then drifted and measured.

4.1.2. Single-Sided Microstructured Semiconductor Neutron Detectors

The Microstructured Semiconductor Neutron Detector (MSND) was theorized as early as 1987 [69] and later developed as an improvement on the thin-film coated detector for alternative thermal-neutron detection technology [15-27, 69, 70, 72-76, 117, 118]. MSNDs have perforations etched into the semiconductor substrate that are subsequently backfilled with neutron conversion material, commonly ${}^6\text{LiF}$ or ${}^{10}\text{B}$. MSNDs operate in the same method as the thin-film coated detectors as shown in Fig. 4-1. Neutrons are absorbed in the neutron conversion material. Immediately afterwards, reaction products are emitted from the neutron absorption, and if one of

the charged-particle reaction products enters the semiconductor substrate, then electron-hole pairs are created. The electrons and holes are drifted and induce current at the electrodes which is measured indicating a neutron had been absorbed by the detector.

The MSND improved on both factors limiting the detection efficiency of thin-film-coated detectors. First, more neutron conversion material can be placed in the detector without adversely affecting the reaction product escape probability. Second, the geometry of the micro-perforations can be tailored to improve the reaction product escape probability by limiting the critical dimension of the micro-cavity to less than the range of the highest energy reaction product. Furthermore, in MSNDs it is possible to have both reaction products enter the semiconductor substrate and deposit energy unlike in the thin-film coated design, because the reaction products are emitted in opposite directions. These two major improvements increase the theoretical limit for thermal-neutron detection efficiency to greater than 45% for a 500- μm thick detector [18], and single-sided, straight-trench MSNDs have been fabricated with detection efficiencies greater than 35% [26].

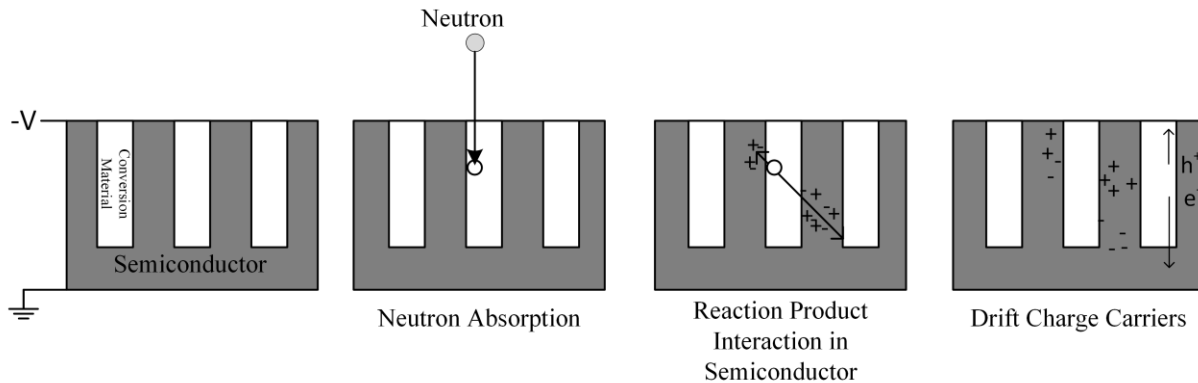


Fig. 4-2. Example of neutron detection process for a MSND. Neutrons are absorbed in the conversion material in a MSND microcavity which produces charged-particle reaction products that can enter the semiconductor diode. The reaction products deposit energy in the semiconductor diode creating electron-hole pairs that are then drifted and measured.

MSNDs retain many of the benefits realized with the thin-film coated diode neutron detectors. MSNDs can still be batch processed with common VLSI processing techniques which lowers overall manufacturing costs as production volume increases. They operate on low bias which simplifies the electronics and reduces power consumption. The detectors are also compact and rugged, and therefore, can be deployed in a wide range of detection systems [119-130]. At the time of this work, MSNDs are commercially available with intrinsic thermal-neutron detection efficiencies of 30% [28].

4.1.3. Dual-Sided Microstructured Semiconductor Neutron Detectors

The Dual-Sided Microstructured Semiconductor Neutron Detector (DS-MSND) was devised and developed as an improvement over the single-sided MSND [29-33]. DS-MSNDs have microfeatures on the back-side of the semiconductor substrate that are can either be offset or inverse images of the front-side microfeatures to eliminate neutron free streaming paths through the semiconductor, i.e., if a neutron passes through a fin on the front-side of the device, it will intersect a conversion-material backfilled trench on the back-side of the device. Shown in Fig. 4-3 is an example of the detection process for a DS-MSND, which similar to that of MSNDs. However, different doping schemes are possible on DS-MSNDs, which have different influences on the charge carrier drift properties. Several doping profiles for DS-MSNDs are described in Section 4.2.2.

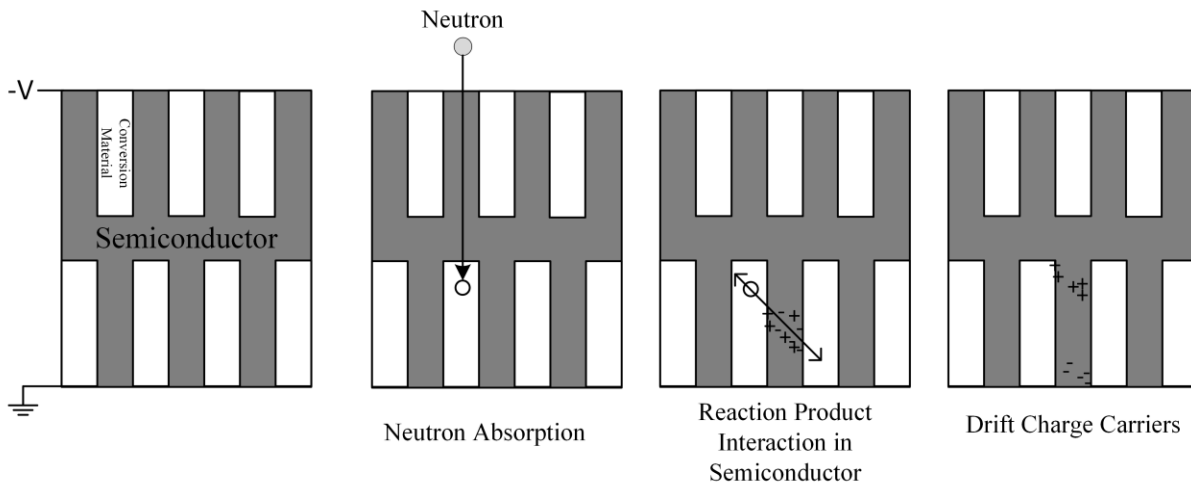


Fig. 4-3. Example of neutron detection process for a DS-MSND. Neutrons are absorbed in the conversion material in a DS-MSND microcavity which produces charged-particle reaction products that can enter semiconductor diode. The reaction products deposit energy in the semiconductor diode creating electron-hole pairs that are then drifted and measured.

Back-side features on DS-MSNDs complement front side-features to increase the neutron absorption efficiency of the detector without adversely affecting the reaction product escape probability. The increased sensitivity boosts the theoretical maximum intrinsic thermal-neutron detection efficiency to over 75% which is on par with small-diameter, high-pressure ^3He detectors [33, 131]. Again, the DS-MSND retains many of the properties desired in a ^3He replacement technology being affordable, mass-producible, compact, rugged, power-efficient, and now having a detection efficiency truly comparable to common gold standard ^3He detectors. Previous work

reports progress made to develop and improve the intrinsic thermal-neutron detection efficiency of DS-MSNDs to $53.5 \pm 0.6\%$ [33], and described in the next two chapters is the progress made to develop the current state-of-the-art DS-MSNDs.

4.1.4. Design Considerations

Semiconductor

Several practical decisions must be made when designing solid-state thermal neutron detectors, The first of which is the choice of the semiconductor substrate. The common options included Si, GaAs, SiC, and diamond detectors, all of which have unique advantages and disadvantages, listed in Table 4-1. Much of the recent work on MSNDs and DS-MSNDs and the present work utilize Si as the semiconductor substrate, because Si has many beneficial features. The cost of Si has been reduced drastically by its widespread use in the semiconductor industry, making high purity Si readily available and affordable. Additionally, Si with a relatively low Z-number and density has limited sensitivity to gamma rays, an ideal property for a neutron detector (see Fig. 4-4). Furthermore, Si is relatively simple to process into diodes. Common VLSI processing techniques and anisotropic wet etching can be used to batch process racks of wafers simultaneously with a high degree of accuracy. Microfeature etching in GaAs, SiC, and diamond detectors have to utilize reactive ion etching (RIE) systems which are costlier and have limited throughput. If certain features are mission critical, such as high temperature operation or radiation hardness, then GaAs, SiC, and diamond become more attractive options, but for many applications, Si is the best choice and can be orders of magnitude more cost effective.

Table 4-1. Properties for common semiconductor materials investigated for thin-film coated semiconductor neutron detectors, MSNDs, and DS-MSNDs. X represents that property is generally accepted as true.

	Si	GaAs	SiC	Diamond
Bandgap (eV)	1.12	1.42	2.3-3.2	5.45
Density (g/cm ³)	2.32	5.32	3.21	3.51
Low Bias Voltage	X	X		
Radiation Hard		X	X	X
Low Gamma-Ray Sensitivity	X		X	X
Low-Cost	X			
Large Wafer Size	X			
High-Temperature Operation			X	X
Ease of Machinability	X			

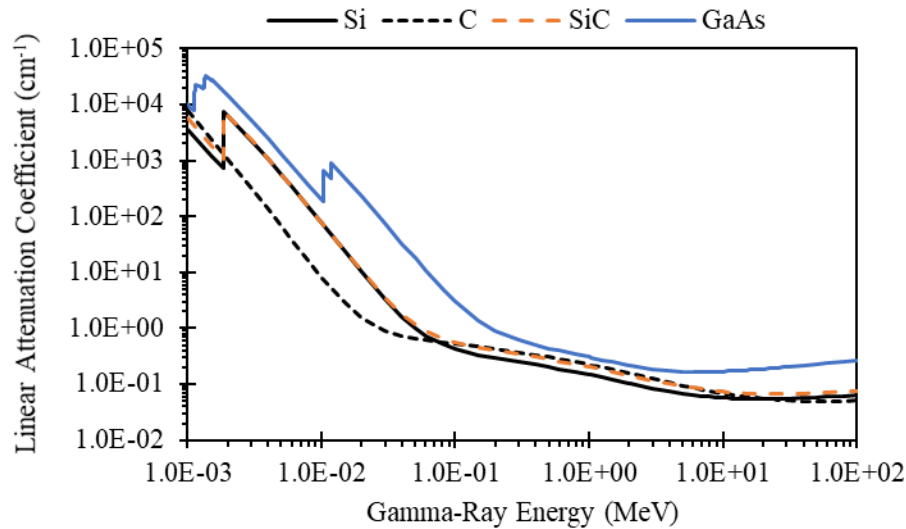


Fig. 4-4. Total linear attenuation coefficient for photons for Si, C, SiC, and GaAs. Cross section data were retrieved from [132].

Neutron Conversion Material

¹⁰B, ⁶Li, and ¹⁵⁷Gd have been the three main conversion materials studied as alternatives to ³He for thermal neutron detection (see Table 4-2). ¹⁰B has a relatively high thermal-neutron capture cross section and a Q-value of 2.8 MeV. ¹⁰B or ¹⁰B₄C have also been used in neutron detectors where the converter is either coated on the interior of a gas-filled detector, coated onto a thin-film detector, or backfilled into a MSND. ⁶Li has a lower, but not insignificant, thermal-

neutron capture cross section and has the largest Q-value at 4.78 MeV. The range of the ${}^6\text{Li}(n,t)\alpha$ reaction products are longer than ${}^{10}\text{B}(n,\alpha){}^7\text{Li}$ reaction products, and therefore, larger conversion material layers can be used while still retaining high reaction product escape probability. Pure ${}^6\text{Li}$ metal has been implemented in detectors, however, the metal must be handled and sealed in a water-free environment to prevent degradation. ${}^6\text{LiF}$ is non-reactive and commonly used in thin-film and microstructured detectors. A tradeoff between ${}^{10}\text{B}$ and ${}^6\text{Li}$ is neutron absorption efficiency vs. reaction product range. ${}^{10}\text{B}$ -based detectors can be slightly smaller than ${}^6\text{LiF}$ -based detectors but must have smaller features to capture energy from the reaction products. ${}^6\text{LiF}$ -based detectors must be slightly thicker to achieve the same detection-efficiency. However, the signal to noise ratio is better for ${}^6\text{LiF}$ -based detectors, because the ${}^6\text{Li} + {}^1_0\text{n}$ reaction has a higher Q-value. ${}^{157}\text{Gd}$ is an interesting option for ${}^3\text{He}$ alternatives because of the extremely large thermal-neutron capture cross-section, which would allow for extremely thin conversion material layers. However, the reaction products for a thermal-neutron absorption include a cascade of gamma rays and conversion electrons, which can be challenging to capture and measure because they produce signals near the noise floor of the pulse height spectrum and are difficult to differentiate from electronic noise and background gamma-ray radiation.

Table 4-2. Cross Sections and reaction products for common neutron conversion materials.

Isotope	Thermal Neutron (0.0253 eV) Absorption Cross Section [47]	Reaction Products
${}^3\text{He}$	5315 b	p (0.574 MeV) + t (0.191 MeV)
${}^{10}\text{B}$	3844 b	94%: α (0.84 MeV) + ${}^7\text{Li}$ (0.84 MeV) + γ (0.48 MeV) 6%: α (1.78 MeV) + ${}^7\text{Li}$ (1.02 MeV)
${}^6\text{Li}$	938 b	t (2.73 MeV) + α (2.05 MeV)
${}^{157}\text{Gd}$	252928 b	Gamma rays and electrons

Microfeature Geometry

The final consideration is the microfeature or microcavity shape. The most common shapes are circular hole, circular pillars, and straight trenches, however, other interesting shapes like a sinusoidal trench pattern have been investigated [16]. Key factors to consider when choosing the microcavity geometry are neutron absorption efficiency, reaction product escape probability, and manufacturability. Holes have the highest reaction product escape probability, but like pillars,

often require slow and more costly manufacturing processes like RIE. In the straight trench geometry, a small reduction in reaction product escape probability is made for a large gain in manufacturability, because the trenches can be etched in a scalable anisotropic wet etching bath. Section 4.3 contains an in-depth MCNP simulation study of the three main microfeature geometries and their theoretical intrinsic thermal-neutron detection efficiencies.

4.2. Silvaco TCAD Simulations for Electrical Properties

Silvaco's Technology Computer-Aided Design (TCAD) software [133] was used to model the electric field for different doping profiles and detector biases for MSNDs and DS-MSNDs. Additionally, the current induced in the detector's electrodes from a Single Event Upset (SEU) in the fins, which simulates a charged-particle track, was calculated to compare the charge collection efficiency of presently used and proposed doping profiles. The ATLAS program within the Silvaco TCAD package is a physics-based device simulator for two-dimensional (2D) and three-dimensional (3D) devices. All the simulations presented herein were 2D simulations. The 2D simulations should give a good approximation of the center of the diode (away from the diced edges) but would likely not accurately model edge effects at the perimeter of the detector. The program solves coupled Poisson's Equation, carrier continuity equations, and drift-diffusion equations at prespecified nodes to predict the electrostatic potential, electric field, and charge carrier motion leading to current induction within the device. Eq. 4-2 through Eq. 4-7 show the coupled equations used in the ATLAS simulations [133]. Example input files for the TCAD simulations are in Appendix A.

The electric field within the DS-MSND is critical for drifting the electrons and holes within the silicon to induce current in the detector electrodes which ultimately forms a measurable voltage pulse. Silvaco's TCAD software was used to simulate the internal electric field and the signal current induced in the detection circuitry from a charged-particle interaction for several MSND and DS-MSND contact configurations shown in Fig. 4-5 and Fig. 4-13 [133]. Conformal, planar, and partial-conformal diffusion profiles were considered. In a conformal diffusion profile, the dopant is deposited evenly on all surfaces of the microfeature (bottom of trench, trench sidewalls and tops of fins). A planar diffusion profile only has dopant only on the tops of the fins, and in a partial-conformal diffusion profile, the dopant covers the tops of the fins and extends partway down the trench sidewalls but tapers off before reaching the bottom of the trench. Phosphorus was

used for the n -type dopant, and boron was used for the p -type dopant. The resistivity of the silicon was set at 5 k Ω -cm with phosphorus has the n -type dopant resulting in bulk, v -type silicon. The minority carrier lifetime was set to 1000 μ s based on specifications delivered from silicon suppliers for 5 k Ω -cm resistivity silicon.

$$\text{Poisson's} \quad \nabla \cdot \epsilon \nabla \psi = -\rho \quad \text{Eq. 4-2}$$

$$\vec{E} = -\nabla \psi \quad \text{Eq. 4-3}$$

$$\text{Carrier Continuity} \quad \frac{\partial n}{\partial t} = \frac{1}{q} \nabla \cdot \vec{J}_n + \vec{G}_n - \vec{R}_n \quad \text{Eq. 4-4}$$

$$\frac{\partial p}{\partial t} = \frac{1}{q} \nabla \cdot \vec{J}_p + \vec{G}_p - \vec{R}_p \quad \text{Eq. 4-5}$$

$$\text{Drift-Diffusion Transport Model} \quad \vec{J}_n = qn\mu_n\vec{E}_n + qD_n\nabla n \quad \text{Eq. 4-6}$$

$$\vec{J}_p = qn\mu_p\vec{E}_p + qD_p\nabla p \quad \text{Eq. 4-7}$$

ϵ – local permittivity

ψ – electrostatic potential

ρ – local space charge density

\vec{E} – electric field

n – electron concentration

p – hole concentration

$\vec{J}_{n,p}$ – electron or hole current density

$\vec{G}_{n,p}$ – electron or hole generation rate

$\vec{R}_{n,p}$ – electron or hole recombination rate

q – electron charge

$\mu_{n,p}$ – electron or hole mobility

$\vec{E}_{n,p}$ – electron or hole effective electric field

$D_{n,p}$ – electron or hole diffusion coefficient

The dopant distributions for the p -type and n -type dopants are shown in Fig. 4-6. For the p -type contacts, the peak boron concentration was 6.2×10^{19} atoms cm^{-3} at the surface of the silicon. The peak concentration for the n -type, phosphorus-doped contacts was 4.75×10^{19} . Each doping profile was estimated to be Gaussian, serving as a good approximation for drive-in diffusion processes where an initial amount of impurity is introduced to the wafer, with the temperature subsequently ramped to drive the dopant into the silicon. This solution can be used as long as the characteristic diffusion length during predeposition is significantly less than the characteristic diffusion length for drive-in [134].

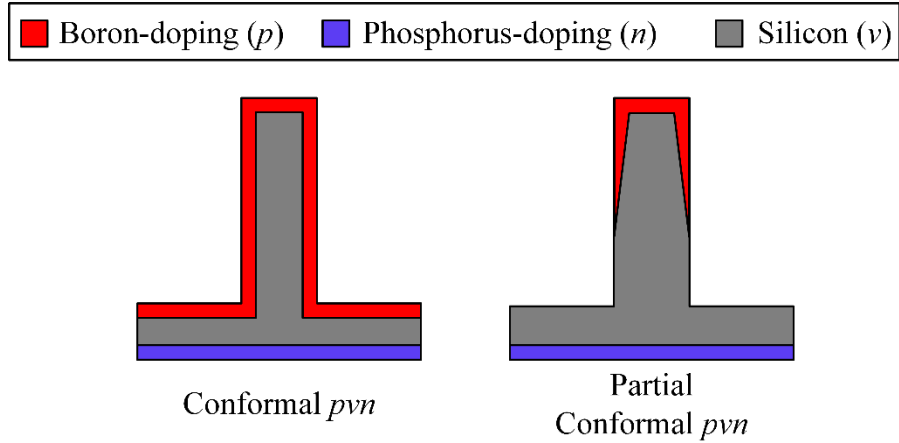


Fig. 4-5. Drawings of MSND doping profiles used in initial TCAD simulations to estimate the validity of simulations when compared to actual device performance.

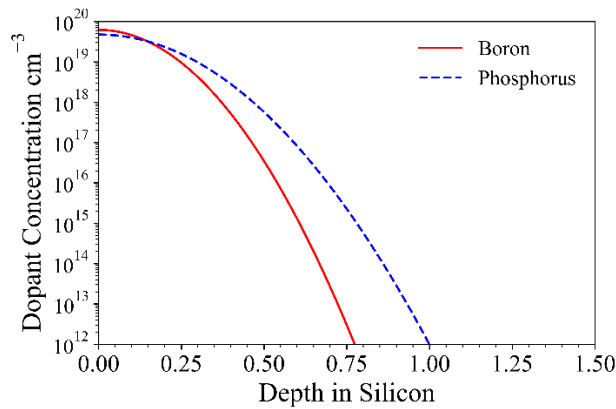


Fig. 4-6. Doping profiles for boron (p -type) and phosphorus (n -type) dopants in the TCAD simulations used to estimate the internal electric field of DS-MSNDs for various doping schemes. The doping profiles were estimated from total dose and drive in procedures for solid-source diffusion commonly used to process MSNDs and DS-MSNDs.

4.2.1. MSND TCAD Simulations

Single-sided pvn -MSNDs were simulated first so that the simulation results could be compared to previously completed TCAD simulations [20, 21] and well-characterized MSNDs [16, 17, 19-24, 26-28]. The internal potential, electric field, and charge induction from a single event upset were determined for the conformal and partial-conformal doping profiles. The trench depth and fin width for the TCAD models was $400\ \mu\text{m}$ and $10\ \mu\text{m}$, respectively. The total thickness of the diode was $500\ \mu\text{m}$, and the unit cell width was $30\ \mu\text{m}$.

Conformal *pvn*-MSNDs

The internal electric field and voltage potential for the conformal *pvn*-MSNDs from Fig. 4-5 was determined with a -2.7-V bias applied to the top of the fin on the *p*-type contact, and the results are shown in Fig. 4-7. Charge induction in the detection circuitry occurs when charged carriers move through the weighting potential of device. In the conformal MSND most of the charge induction occurs when electrons are swept through the bulk silicon under the fins where the largest potential gradient occurs. Some signal will be induced when electrons and holes move horizontally across the voltage gradient within the fins. An electric field is present nearly everywhere within the conformal *pvn*-MSND. However, there is no vertical component to the electric field within the fins of the MSND meaning electrons ionized from the charged-particle interactions will not be drifted vertically and must rely on diffusion to travel to the bottom portion of the fins where charge can be induced.

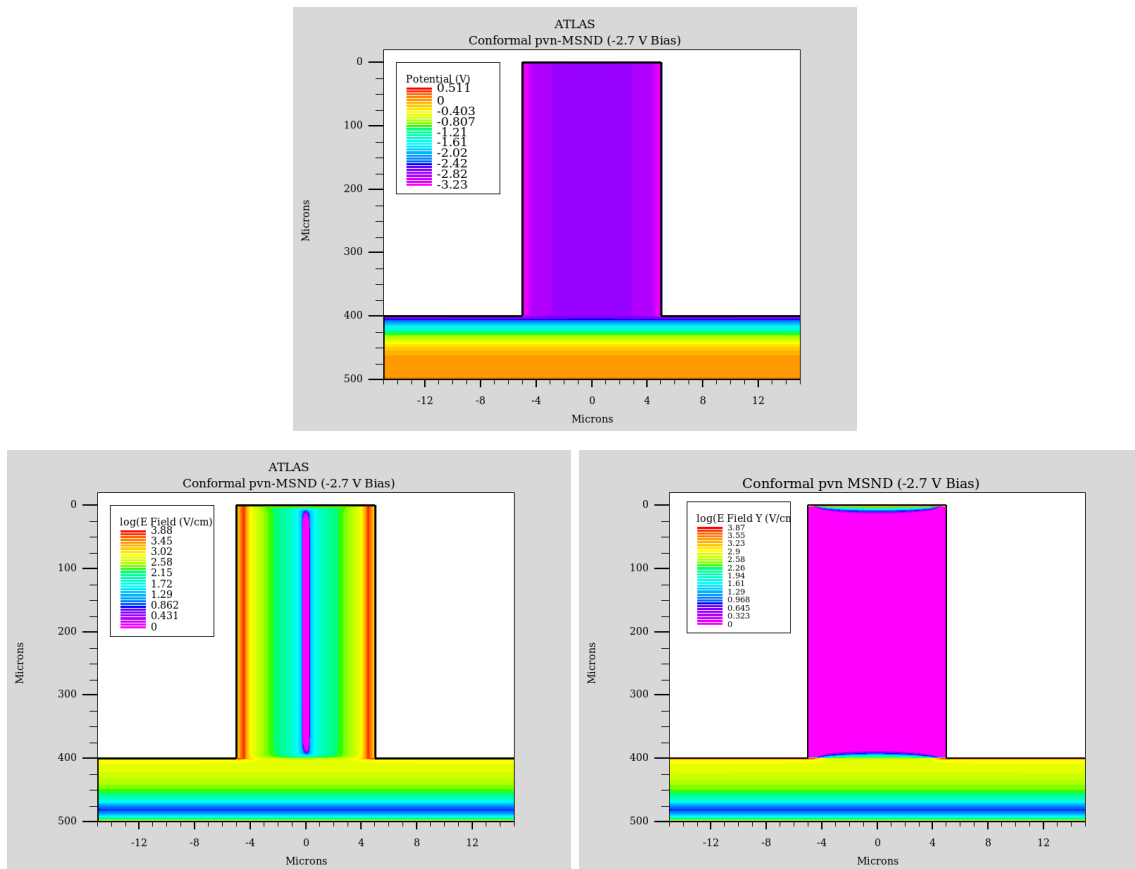


Fig. 4-7. (Top) Voltage potential (Bottom Left) internal electric field and (Bottom Right) vertical component of electric field for a conformal *pvn*-MSND with -2.7-V bias on the *p*-type contact on the top of the fins.

Time-dependent charge induction from SEUs were modeled at different heights within the MSND fin to simulate charge induction following energy deposition from a charged-particle reaction product such as the triton or alpha particle from the ${}^6\text{Li}(n,t)\alpha$ reaction. A 5- μm radius, horizontal charge-particle track was modeled at 150, 300, and 400 μm with a charge density of 2×10^{14} electron-hole pairs cm^{-3} . The current induced from the charge motion within the MSND is shown in Fig. 4-8. The amount of charge induced from the motion of the electrons and holes increases as the distance from the top of the fin increases with comparatively little charge induced for interactions occurring at depths of 150 μm and above.

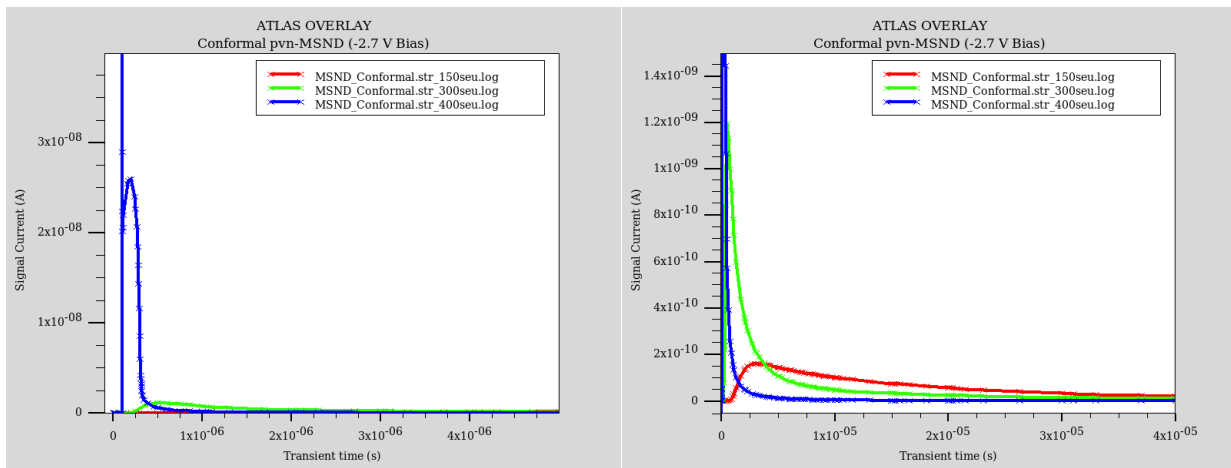


Fig. 4-8. Simulated signal current for SEUs at 150, 300, and 400 μm in the fin of the conformal pvn-MSND doping profile. The amount of signal induced increases as the interaction depth increases, because more electrons can diffuse beneath the fins where the weighting potential is the largest.

Recall there is little to no vertical component to the electric field with the conformal pvn-doping profile, and most charge will be induced when charge carriers travel through the bulk silicon beneath the fins. Therefore, most of the charge induction must come from diffusion of the charge carriers within the device, because the charge-carriers cannot be drifted vertically by the internal electric field. This claim is supported by the time-reel of SEU simulations shown in Fig. 4-9 and simulations presented in previous work [20]. The time-reel shows the electron concentration at 0 s, 1 μs , 2 μs , 5 μs , 10 μs and 20 μs after the SEU. Electrons that diffuse to the bulk silicon between the fin and back-side contact are quickly collected when they enter the high electric field regions. Electrons that diffuse upwards towards the top of the fin are slow moving and likely to eventually recombine. An ideal detector would have a strong electric field throughout the entire active region to promote good charge collection and prevent electron-hole

recombination, which reduces the average pulse height for neutron interactions. Similar results shown in [20] indicated that charge motion within the fins of the MSND were largely diffusion dependent.

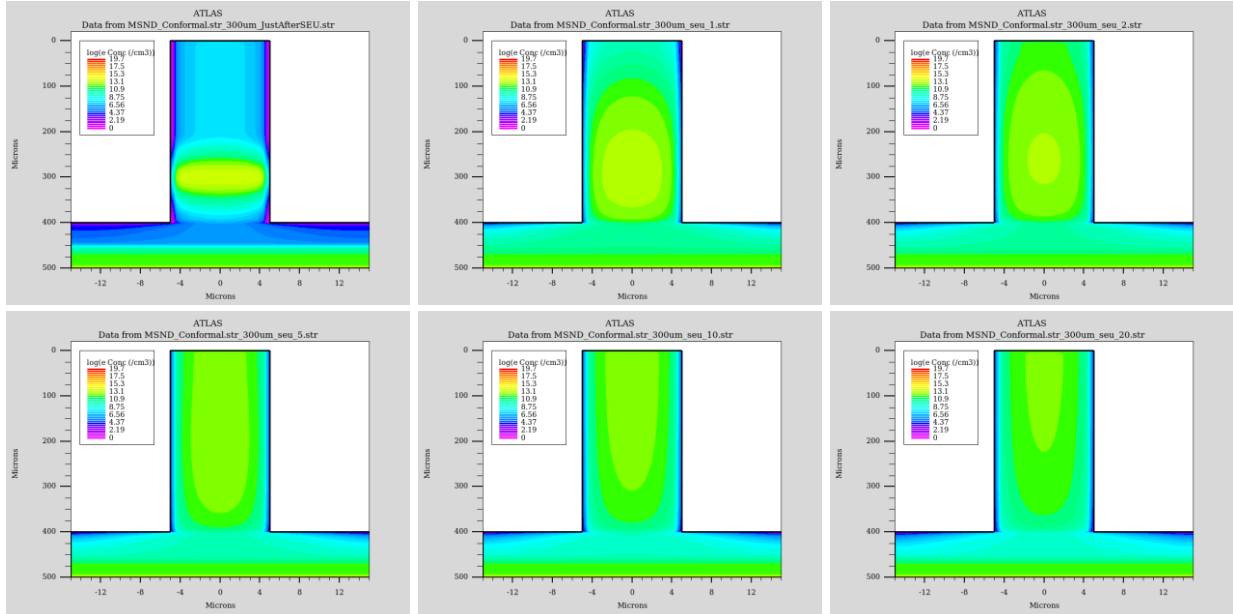


Fig. 4-9. Time-reel for a horizontal SEU at a depth of 300 μm for a conformal *pvn*-MSND. The simulations indicate that the majority of the charge carrier motion is driven by diffusion for this doping profile. Snapshots are at $t=0, 1, 2, 5, 10,$ and $20 \mu\text{s}$.

The results for the conformal *pvn*-MSND doping profile simulations indicated that up to half of the MSND fins would have poor charge collection efficiency which would significantly reduce the neutron detection efficiency of the device by shifting a portion of the pulse height spectrum towards the noise/background signal. The downshifted spectrum would reduce or eliminate the theoretically valley between background and neutron signal; however, previous work shows a valley persists between the neutron signal and background signal [22, 24]. Thus, the actual doping profile of fabricated MSNDs may not be fully conformal.

Partial-Conformal *pvn*-MSNDs

The simulated electrical characteristics of a partial-conformal *pvn*-MSND are shown in Fig. 4-10. The *p*-type contact extends part way down the fins but tapers off before reaching the bottom of the fin. Negative 2.7-V bias was applied to the top of the fin as in the conformal *pvn*-MSND simulations. With the partial-conformal design, more signal is induced with charge carrier

motion within the fin, and electric field is present within nearly all the fin. Also, a vertical electric field is present at the edges of the fins and directly following the bottom edge of the p -type dopant on the fin sidewalls.

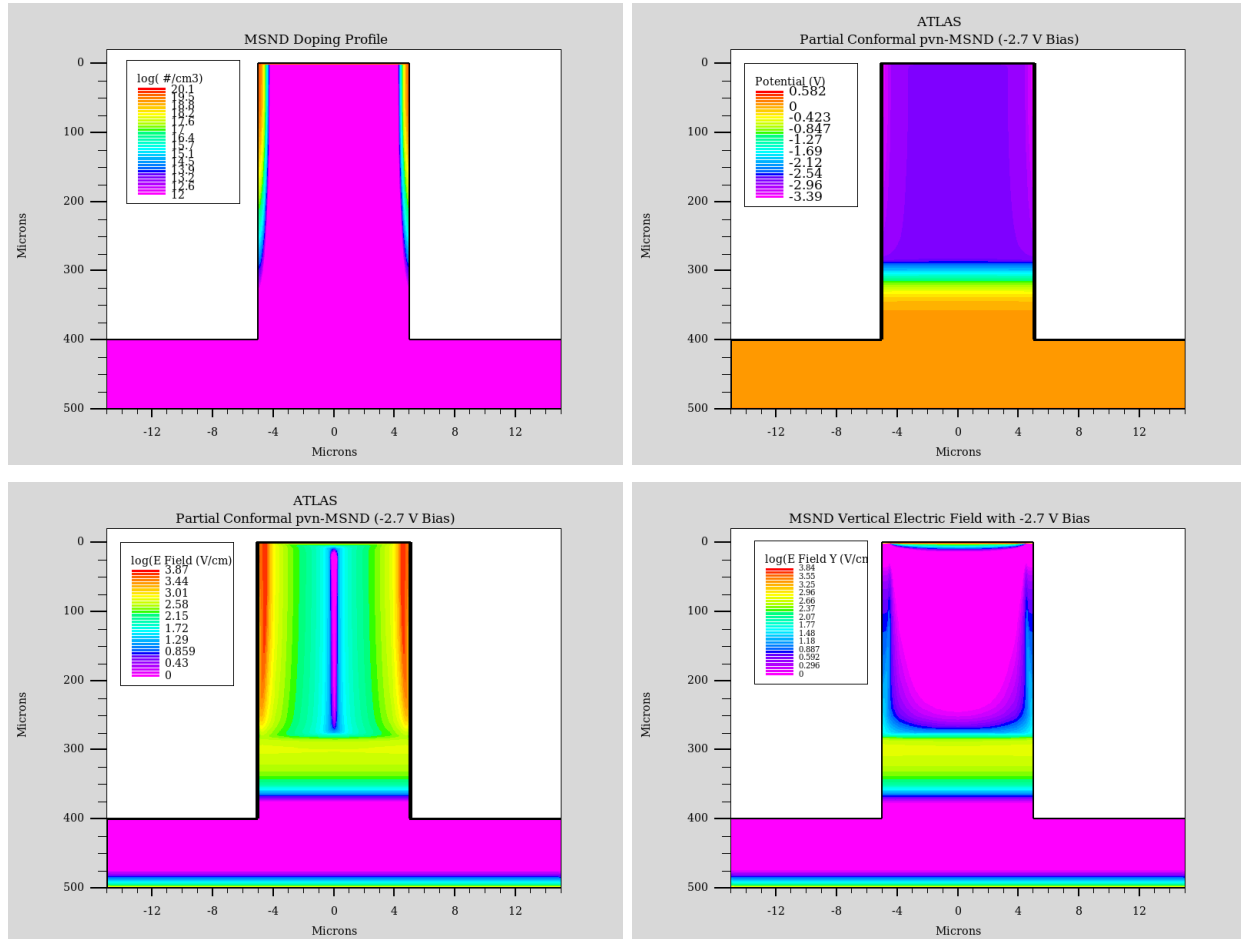


Fig. 4-10. (Top Left) Dopant concentration (Top Right) Voltage potential (Bottom Left) internal electric field and (Bottom Right) vertical component of electric field for a partial-conformal pvn-MSND with -2.7-V bias on the p -type contact on the top of the fins.

SEUs were modeled at depths of 150, 300, and 400 μm with the same parameters described in the previous section, and the time-dependent induced current is shown in Fig. 4-11. Each SEU induced measurable charge in detection circuitry, and the induced charge is less dependent on the location of the charged-particle interaction location than the conformal design. However, the signal is still suppressed near the top of the fins where the p -type dopant concentration on the fin sidewalls is higher which reduces the vertical electric field.

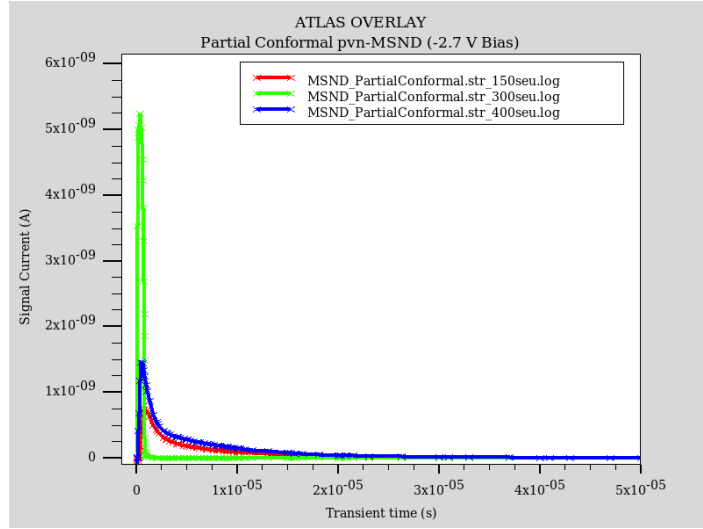


Fig. 4-11. Simulated signal current for SEUs at depths of 150, 300, and 400 μm in the fin of the partial-conformal pvn-MSND doping profile.

The time-reel for the SEU at 150 μm is shown in Fig. 4-12. The majority of the electrons are swept out almost immediately, the location of the interaction coincides with the high electric field region of the device. With the high electric field region closer to the center of the fin, the location of the charged-particle interaction has less effect on the signal. The effect of the doping-profile shape on induced signal should be similar for DS-MSND designs and are discussed in the next section.

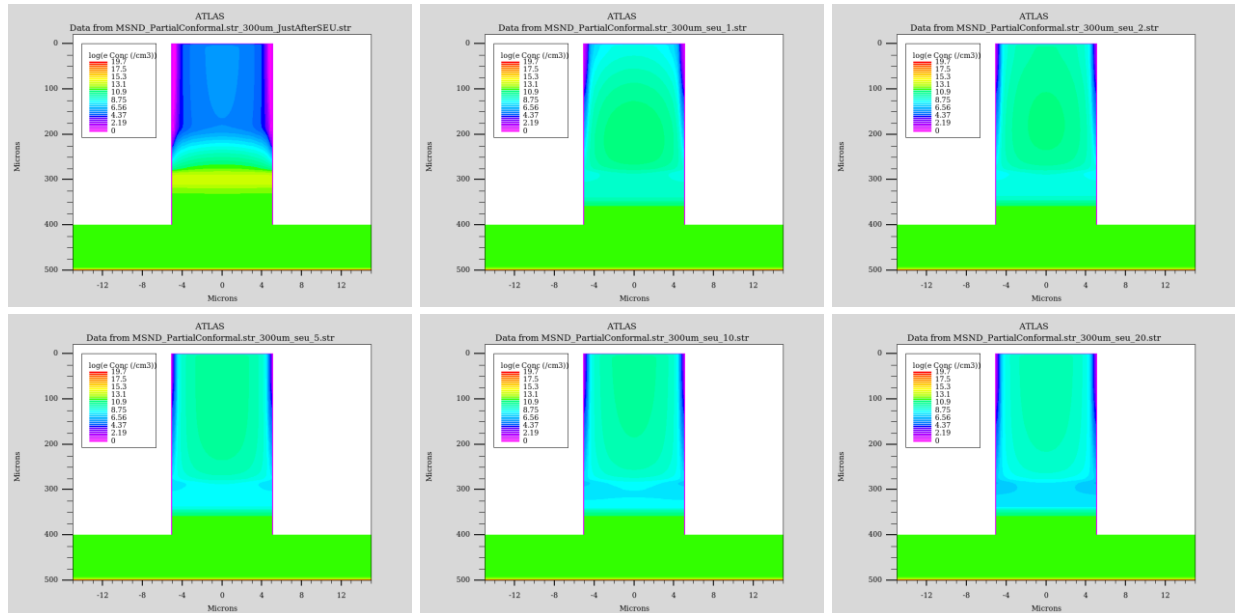


Fig. 4-12. Time-reel for a horizontal SEU at a depth of 300 μm for a partial-conformal pvn-MSND. The simulations indicate that the charge carriers are drifted by the internal electric field in addition to diffusion. The signal induction is more uniform as function of interaction depth than the conformal pvn-design. Snapshots are at $t=0, 1, 2, 5, 10,$ and $20 \mu\text{s}$.

4.2.2. DS-MSND TCAD Simulations

The doping profiles DS-MSNDs shown in Fig. 4-13 were modeled in TCAD to estimate the electrical properties and to predict the charge collection characteristics of the thicker (1.5 mm) dual-sided detectors. Just like the single-sided MSND, the resistivity was set to 5 k Ω -cm n -type, the unit cell width was 30 μ m, and the fin width was 10 μ m. The dopant distribution for the boron and phosphorus, p - and n -type, contacts remained the same and are depicted in Fig. 4-6. The trench depth was increased to 600 μ m, and the thickness of the diode was increased to 1500 μ m to more accurately model DS-MSNDs capable of greater than 60% intrinsic thermal-neutron detection efficiency [29].

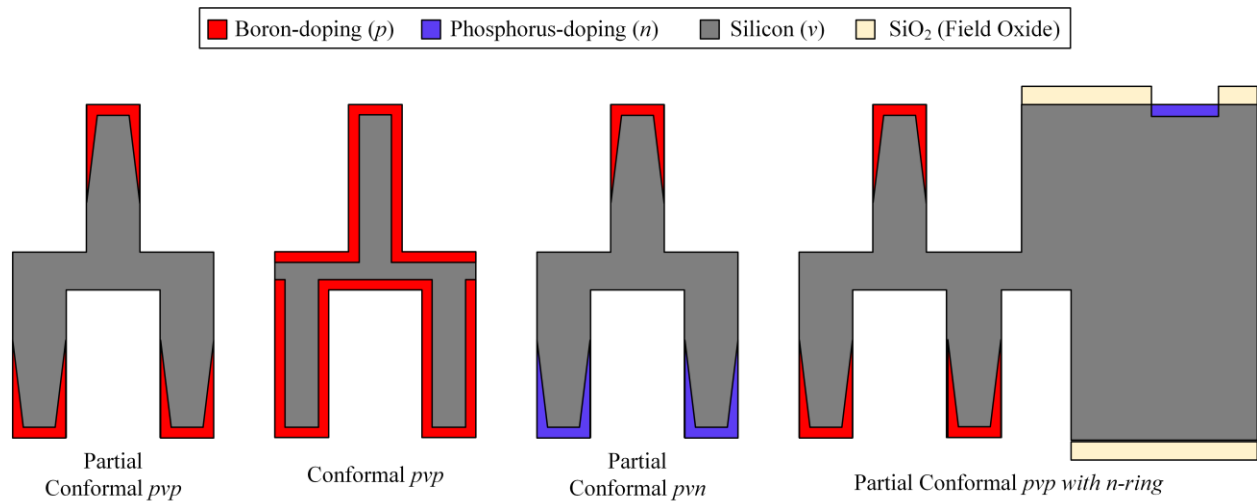


Fig. 4-13. Drawings of the DS-MSND doping profiles for Silvaco TCAD simulations. The simulations were used to model the internal electric field of the DS-MSND and estimate charge induction in the detection circuitry from charged-particle interactions in the silicon. The vertical dimension on the DS-MSND is not drawn to scale.

Conformal pvp -DS-MSND

The conformal pvp -DS-MSND have p -type contacts (boron) uniformly covering the fins and trenches on both sides of the DS-MSND. The pvp -DS-MSND design was developed to eliminate charge collection problems with early DS-MSNDs fabricated with a vertical pvn -type structure [33]. The anode and cathode are the top-side fins and back-side fins, respectively. The pvp -DS-MSNDs operate on 0-V bias and rely solely on the built-in potential at the pn -junction for

an internal electric field. Since both sides of the diode are doped p -type the direction of the electric field in the top-side fins is opposite the direction of the electric-field in the back-side fins. Therefore, the polarity of the voltage pulse formed created depends on which set of fins in which the reaction occurs. Although, this device eliminates the need for bias electronics, an additional set of signal processing electronics or bipolar amplifier is required to measure interactions in both sides of the device. The potential and electric-field within the 0-V bias, conformal pvp -DS-MSND is shown in Fig. 4-14. The built in electric-field depletes the entire fin, because the fins are only 10- μm wide. Again, the electric field is largely horizontal which will promote lateral charge motion.

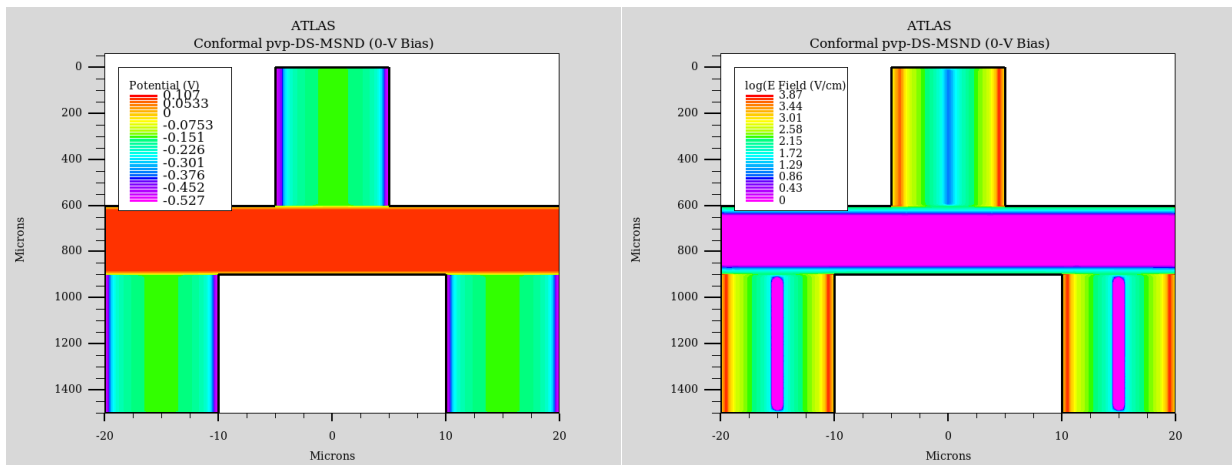


Fig. 4-14. (Left) Voltage potential and (Right) electric field within a 0-V bias, conformal, pvp -DS-MSND. The device operates solely on the built-in electrochemical potential created by the highly doped p -type region at the pn -junction on the surface of the fins and trenches.

SEUs were modeled in the top-side fin at depths of 150, 300, 450, and 600 μm , and in the back-side left fin at depths of 900, 1050, 1200, and 1350 μm . The parameters of the charged cloud remaining the same as described in the MSND TCAD simulation section. The predicted current induced in the DS-MSND electrodes following the SEUs is shown in Fig. 4-15. The simulations show that the polarity of the resulting pulse is indeed dependent on which side of the DS-MSND the interaction occurred. Additionally, like the conformal MSNDs, the amount of charged induced in the detection circuit is largely dependent on the depth of the charged-particle interaction. Interactions near the tops of the fins induced less charge than interactions closer to the bulk silicon between the sets of fins. Also, note that the total amount of charge induced is significantly less than the biased, pvn -MSND designs, and the charge induction is slower requiring longer

integration times to measure all the current. The time-reel for an SEU at 300- μm depth in the top-side fin is shown in Fig. 4-16. Charge motion is largely diffusion dominated due to the relatively weak internal electric field.

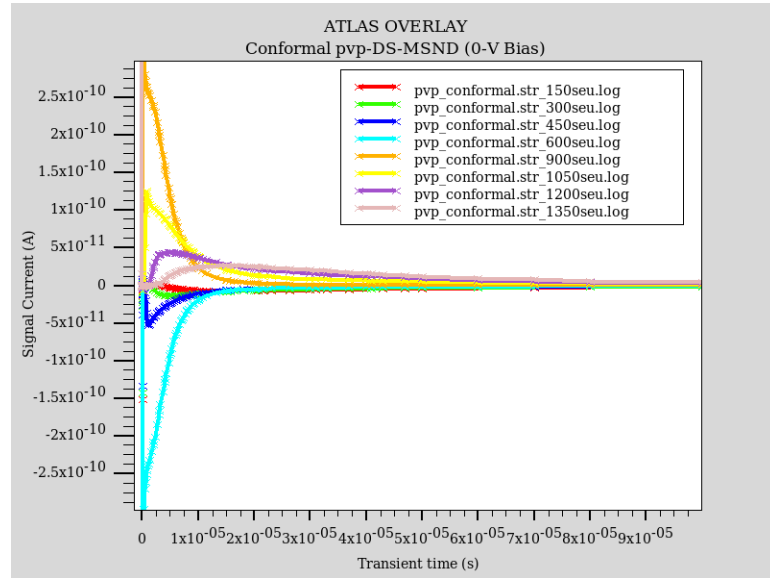


Fig. 4-15. Simulated signal current for SEUs at depths of 150, 300, 450, 600, 900, 1050, 1200, and 1350 μm in the fins of the conformal pvp-DS-MSND doping profile.

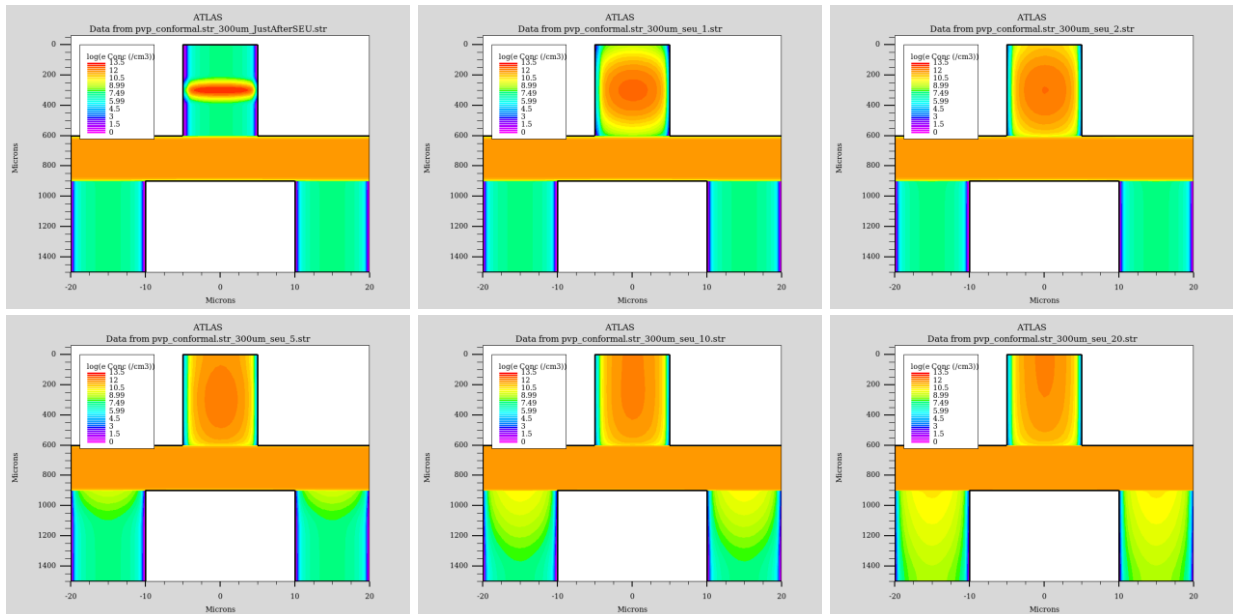


Fig. 4-16. Time-reel for a horizontal SEU at a depth of 300 μm for a conformal pvp-DS-MSND. Significant diffusion occurs to the electron charge cloud following the interaction. The charge cloud then slowly is extracted upwards and outwards at the anode on the top-side fin. Snapshots are at $t=0, 1, 2, 5, 10,$ and $20 \mu\text{s}$.

Partial Conformal *pvp*-DS-MSND

The partial conformal *pvp*-DS-MSND has *p*-type dopant on both sides of the diode extending partway down the fin and tapering off before reaching the bottom of the trench. The design also must be operated at 0-V bias to prevent forward biasing on the of the contacts, therefore relying on the built-in potential of the *pn*-junction on both sides to drift charge. The potential and electric field of the 0-V bias, partial conformal, *pvp*-DS-MSND is shown in Fig. 4-17. The intrinsic electric field the forms the built-in potential is present in most of the fin volume with this design. Again, the only vertical electric field lines are beneath the end of the *p*-type dopant. The electric field is mostly horizontal in the rest of the fin. The signal current for horizontal SEUs at different vertical locations within the DS-MSND is shown in Fig. 4-18. The amount of charge induced as a function of interaction location is more uniform than the fully conformal *pvp*-DS-MSND design, but the average amount of charge induced is less. The time-reel for a SEU at 300 μm is shown in Fig. 4-19.

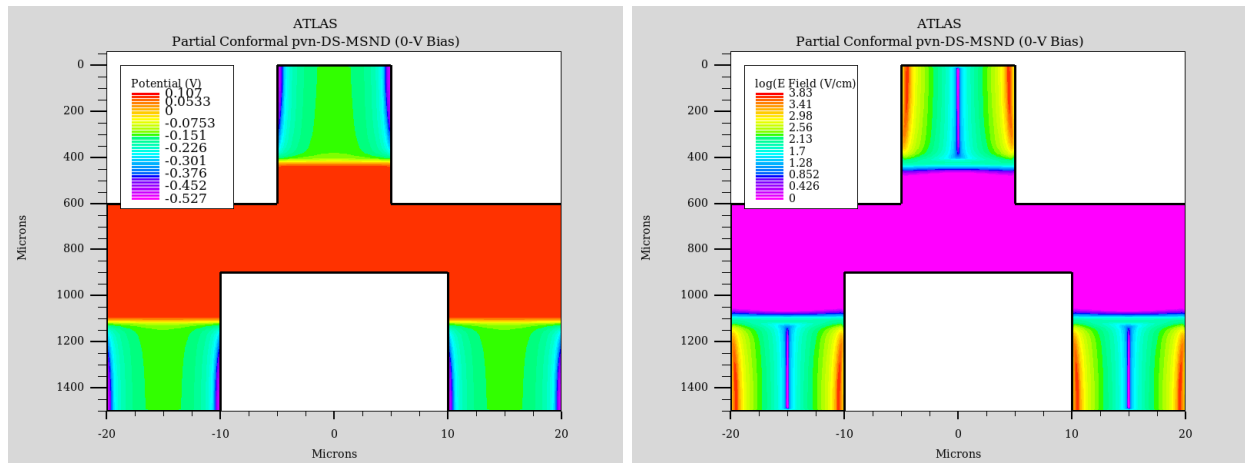


Fig. 4-17. (Left) Voltage and (Right) intrinsic electric field for the partial conformal *pvp*-DS-MSND operated at 0-V bias.

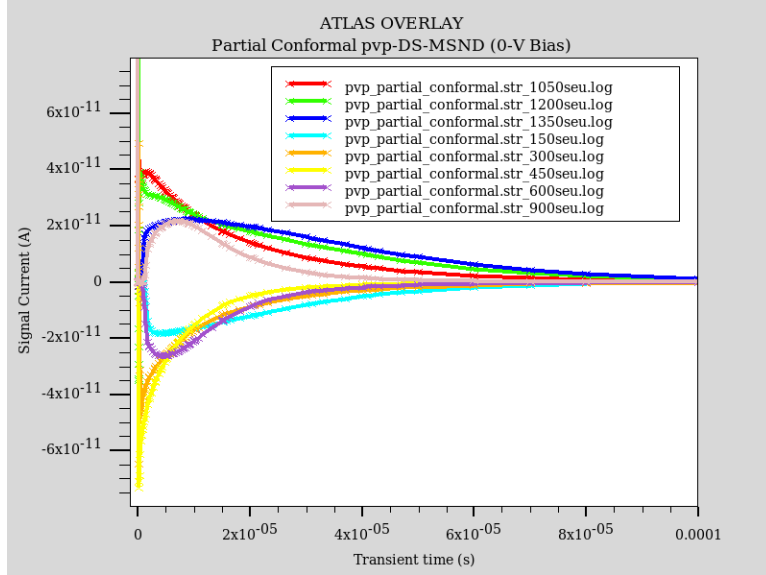


Fig. 4-18. Simulated signal current for SEUs at depths of 150, 300, 450, 600, 900, 1050, 1200, and 1350 μm in the fins of the partial conformal pvp-DS-MSND doping profile.

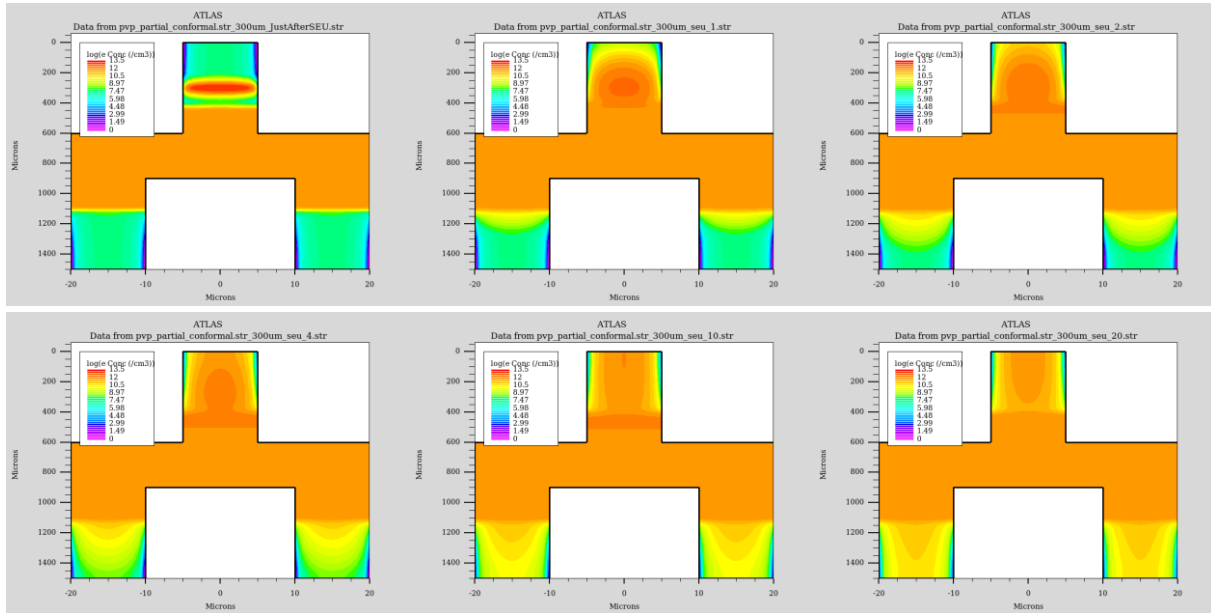


Fig. 4-19. Time-reel for a horizontal SEU at a depth of 300 μm for a partial conformal pvp-DS-MSND. Charge diffusion is still dominate due to the weak electric field. Snapshots are at $t=0, 1, 2, 5, 10,$ and $20 \mu\text{s}$.

One explanation for the reduced charge induction in the pvp-DS-MSNDs compared to the pvn-MSNDs is evident on the time-reels of the electron concentration for the pvp-DS-MSNDs. The motion of the electrons appears to be diffusion dominated; and therefore, a significant portion of the current is canceled out because current with opposite signs is induced in both electrodes simultaneously. The weak electric field within the device only can cause a small net charge motion

and only this small drift distance is what is recorded. The reduced charge induction downshifts the neutron spectrum towards the noise floor which negatively impacts the gamma-ray rejection properties of the detector [29].

Partial-Conformal *pvn*-DS-MSND

The partial-conformal *pvn*-DS-MSND was briefly studied by Fronk et. al. in [30, 31], but was abandoned because it was assumed that poor charge collection efficiency in the *n*-type side of the DS-MSND was the cause of lower than expected thermal-neutron detection efficiency. Later in [29, 33] more accurate measurements of the ${}^6\text{LiF}$ powder packing fraction indicated that the ${}^6\text{LiF}$ density assumed in the MCNP simulations was significantly higher than the apparent ${}^6\text{LiF}$ powder density in the DS-MSNDs. Interestingly, when correcting for the reduced ${}^6\text{LiF}$ density, the measured detection efficiency reported by Fronk [33] matches well with simulation results, and the measured pulse height spectrum shows good separation between background and neutron signal. Thus, the partial conformal *pvn*-DS-MSND was revisited with TCAD simulations.

The partial conformal *pvn*-DS-MSND has a *p*-type dopant extending partway down the top-side fins and *n*-type dopant extending partway down the back-side fins. The vertically operated *pvn*-diode can be biased to increase the depletion depth and magnitude of the electric field within the diode. For the simulations presented, a maximum bias of -50 V was applied, because the DS-MSNDs were ultimately designed for compact, low power operation. Higher voltage circuitry typically requires larger components, standoffs, and board space to operate properly. Additionally, as the voltage increases, the dark current also increases, thereby increasing power consumption. The voltage potential and electric field for the partial conformal *pvn*-DS-MSND with 50-V reverse bias is shown in Fig. 4-20. The results indicate the top fins are depleted, but the depletion region does not extend very far into the bulk silicon between the sets of fins. The electric field on the back-side diodes is then likely created by the *n-n+* homojunction caused by the mismatch in dopant concentration near the surface of the detector [135]. The direction of the electric field is uniform with respect to the electrical contacts indicating all pulses will have the same polarity.

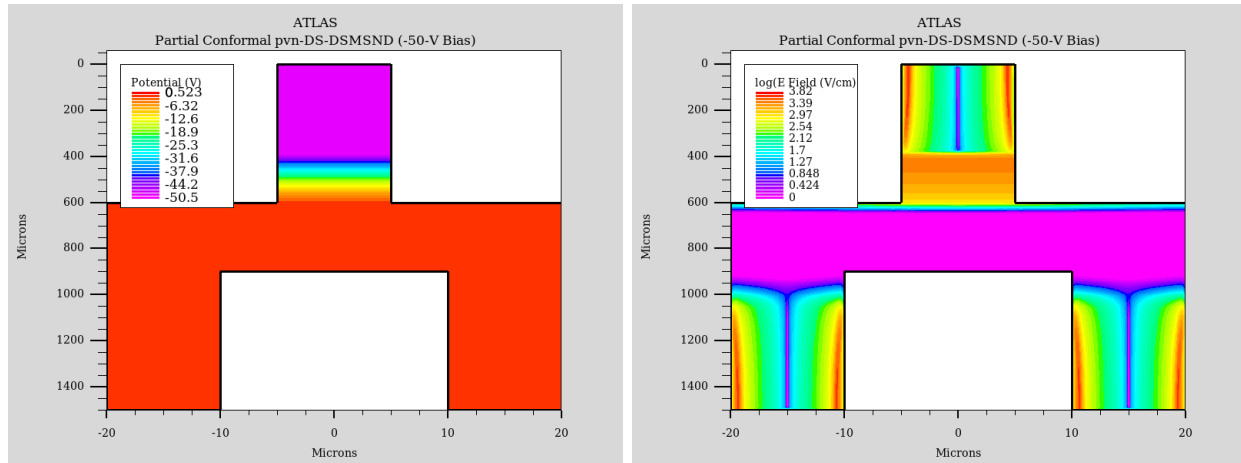


Fig. 4-20. (Left) Potential and (Right) electric field for 50-V reverse bias, partial conformal, pvn-DS-MSND. Only the top fin is fully depleted. However, a mostly horizontal electric field exists in the back-side fins from the n - n^+ homojunction formed from the highly doped n -type contact adjacent to v material.

The same SEUs were modeled in the partial conformal pvn-DS-MSND, and the transient signal current is shown in Fig. 4-21. The charge induced for interactions in the p -type doped fins is much greater than either of the pvp -DS-MSNDs designs. Interactions in the backside, n -type doped fins induce current in the detector electrodes much slower, and the resulting voltage pulse will likely be truncated by the comparatively short charge integration times (10-20 μ s) of the preamplifier/amplifier circuit.

Time reels for interactions in the top-side and back-side fins are shown in , respectively Fig. 4-22 and Fig. 4-23. In the top-side fin, charge is swept out and measured quickly due to the high electric field region that exists below the p -type contact. The charge motion for events in the back-side fins is slower. Electrons are swept out horizontally in the weak electric field on the back-side of the diode, and holes must slowly diffuse across the diode to the high electric field in the top-side fin to be measured.

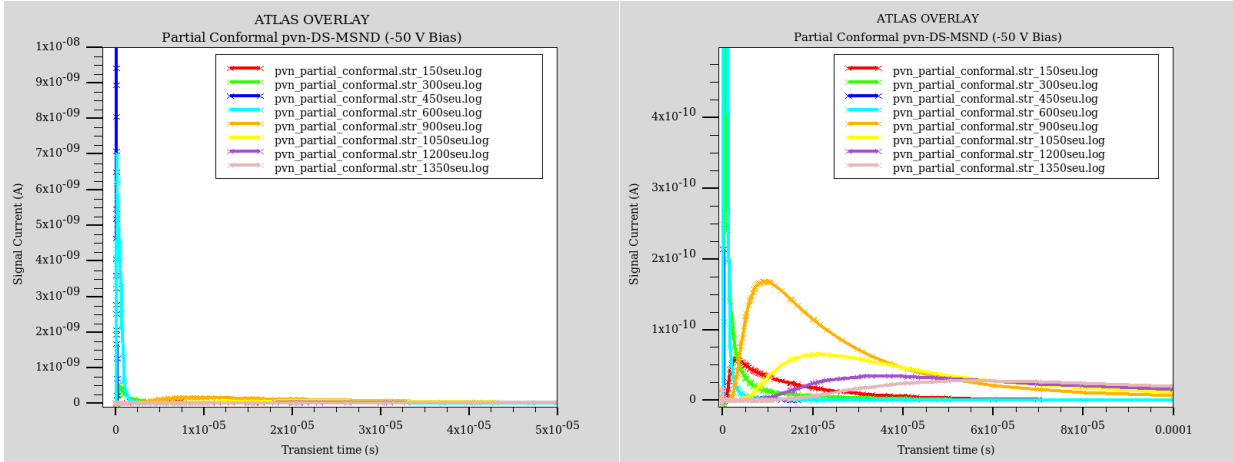


Fig. 4-21. Simulated signal current for SEUs at depths of 150, 300, 450, 600, 900, 1050, 1200, and 1350 μm in the fins of the partial conformal pvn-DS-MSND doping profile.

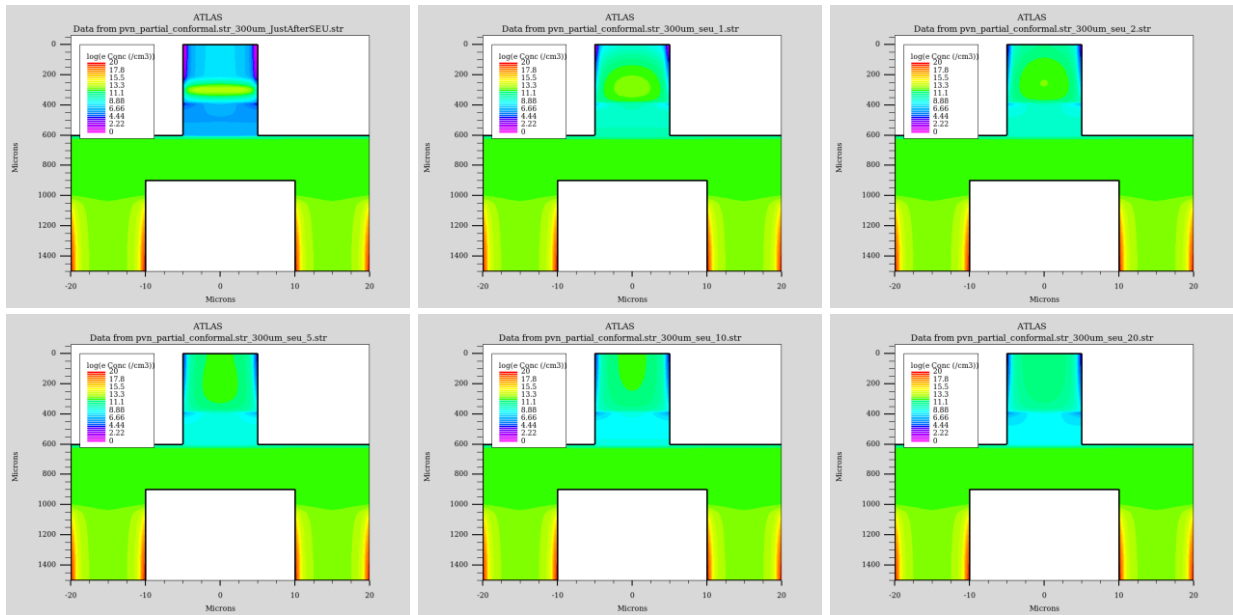


Fig. 4-22. Time-reel for a horizontal SEU at a depth of 300 μm for a partial conformal pvn-DS-MSND. Charge diffusion is still dominate due to the weak electric field. Snapshots are at $t=0, 1, 2, 5, 10,$ and $20 \mu\text{s}$.

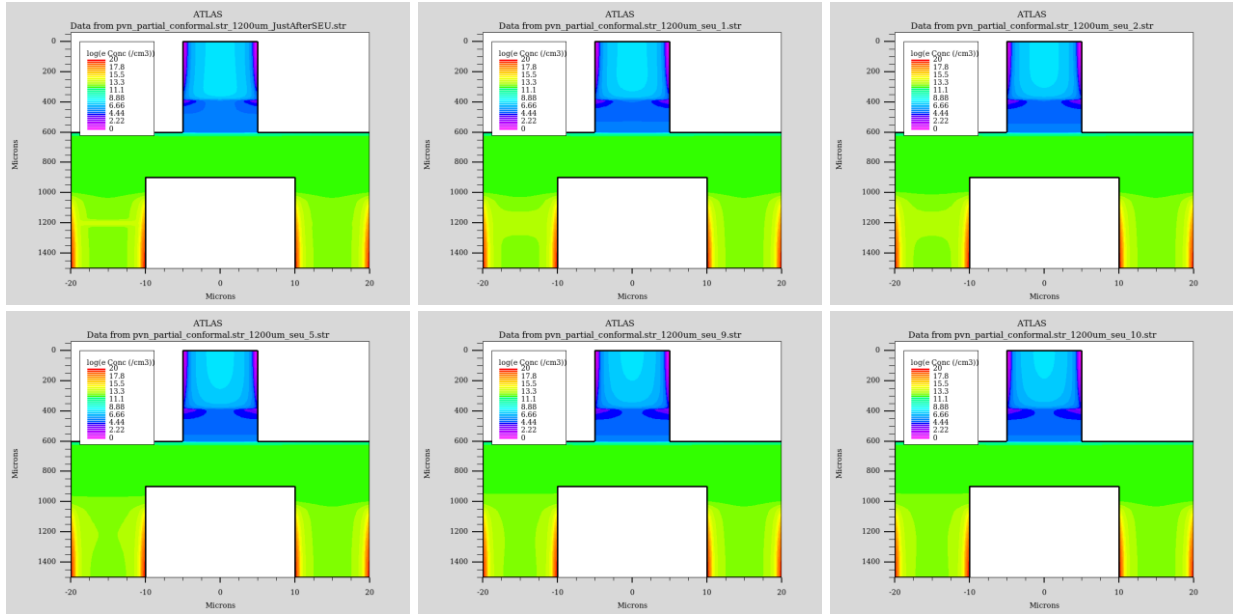


Fig. 4-23. Time-reel for a horizontal SEU at a depth of 1200 μm for a partial conformal *pvp*-DS-MSND. Charge diffusion is still dominate due to the weak electric field. Snapshots are at $t=0, 1, 2, 5, 10,$ and $20 \mu\text{s}$.

Partial-Conformal *pvp*-DS-MSND with *n*-ring

The partial-conformal *pvp*-DS-MSND with an *n*-type ring was designed as a way to operate the *pvp*-type DS-MSND doping scheme with an applied bias. The front and back-side fins are doped with *p*-type dopant, and an *n*-type ring is deposited on the top surface surrounding the *p*-type doped features and is separated by an oxide layer to prevent the contacts from shorting on the surface. The two *p*-type sides of the diode can be connected to form the anode, and the *n*-type ring becomes the cathode. The outside set of trenches next to the bulk silicon at the edge of the diode were not doped to prevent unnecessary depletion into the bulk silicon adjacent to the microfeatures. The voltage potential and internal electric field under 10 V reverse bias is shown in Fig. 4-24. The results are similar to the original *pvp*-DS-MSND design except now a larger potential gradient and electric field forms below the *p*-type contacts. Additionally, the electric field points in the same direction with respect to the anode for both sets of fins meaning all radiation induced voltage pulses will have the same polarity as seen in Fig. 4-25. The amount of charge induced on the electrodes is greatest when the interaction occurs near the high electric field region below the edge of the *p*-type contact at about 450 and 1050 μm . Also, the signal produced for interactions elsewhere in the fin is still significant and greater than signals for interactions at the same location in the original, unbiased, *pvp*-DS-MSND.

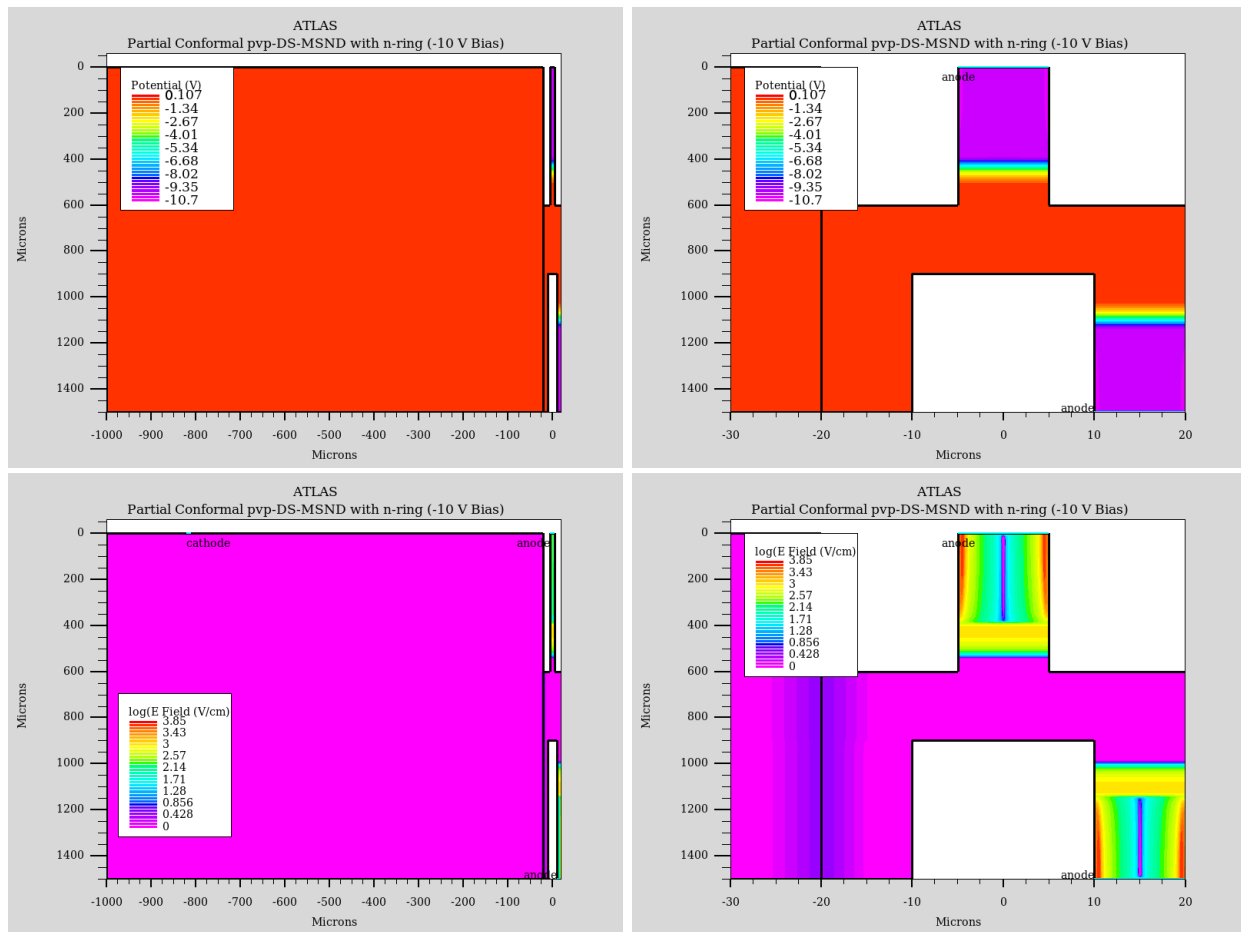


Fig. 4-24. (Top) Potential and (Bottom) electric field for the partial conformal pvp-DS-MSND with n-ring. The left images display the anode and cathode. The images on the right show the details within the two closest fins. The diode was reverse biased with 10 V.

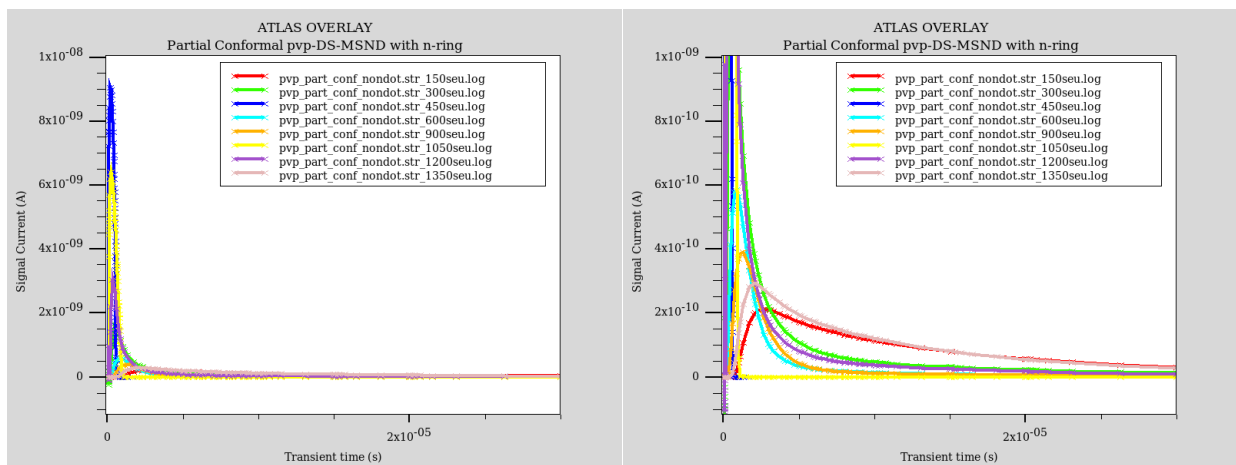


Fig. 4-25. Simulated signal current for SEUs at depths of 150, 300, 450, 600, 900, 1050, 1200, and 1350 μm in the fins of the partial conformal pvp-DS-MSND doping profile.

The time-reel of the electron cloud after an SEU at a depth of 300 μm is shown in Fig. 4-26. Electrons that diffuse down towards the bulk silicon are quickly swept out while some electrons still slowly diffuse upwards towards the top of the fin. However, unlike the 0-V bias, *pvp*-DS-MSND, the electrons do not enter the backside fin which would decrease the current measured at the electrodes. Instead, the strong electric field in the backside fins blocks the electrons from the backside anode. Also, a further increased bias can enhance the strength of the electric field in the fins if necessary.

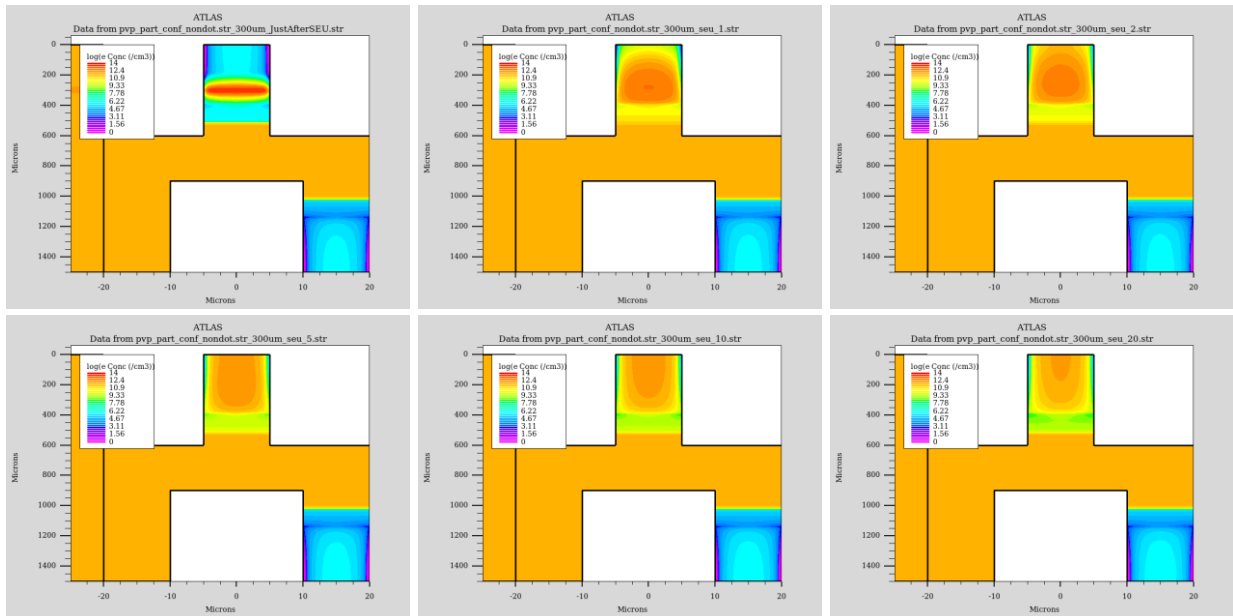


Fig. 4-26. Time-reel of electron concentration for a horizontal SEU at a depth of 300 μm for a partial conformal *pvp*-DS-MSND with *n*-ring and -10-V bias. Snapshots are at $t=0, 1, 2, 5, 10,$ and $20 \mu\text{s}$.

4.2.3. TCAD Simulations Summary

Four different DS-MSND *pn*-junction doping schemes were analyzed and compared with single-sided MSNDs doping schemes with known, good charge collection efficiency. The *pvp*-DS-MSND was developed under Fronk [32, 33] and later improved to achieve 69.2% intrinsic thermal-neutron detection efficiency [29]; however the gamma-ray discrimination was relatively poor compared to the single-sided DS-MSNDs. The results from the TCAD simulations indicate the magnitude of the signal for charged-particle interactions in the silicon fins (SEUs) indicate the conformal and partial-conformal *pvp*-DS-MSNDs operated at 0-V bias have orders of magnitude lower signal current induction than their *pvn*-MSND counterpart for the same energy deposited in

the silicon fin. The partial conformal *pvn*-DS-MSND with 50-V reverse bias showed better signal current in the top-side, *p*-type doped, fins, but the charge induced in the electrodes from interaction in the backside fins was significantly slower, on the order of 100 μ s, likely caused by the relying on diffusion for vertical charge transport due to the weak vertical electric field. Finally, the biased (-10 V), *pvp*-DS-MSND with top-side *n*-ring showed the best charge collection efficiency of all the proposed DS-MSND doping profiles. By attaching the cathode to the *n*-ring and shorting the two sets of *p*-type doped fins together, the applied bias increases the electric field within the fins and improved charge carrier transport. The *n*-ring *pvp*-DS-MSND requires extra fabrication steps than the *pvp*- or *pvn*-DS-MSND, but the tradeoff for improved performance may compensate the extra costs. The higher charge collection efficiency should shift the neutron induced signal to higher energy channels leading to better gamma-ray discrimination and a higher range of temperature operation capabilities, because the LLD can be set higher without adversely affecting the neutron detection efficiency. Comparisons for two SEUs for the different DS-MSND doping schemes compared to partial-conformal *pvn*-MSNDs are shown in Fig. 4-27.

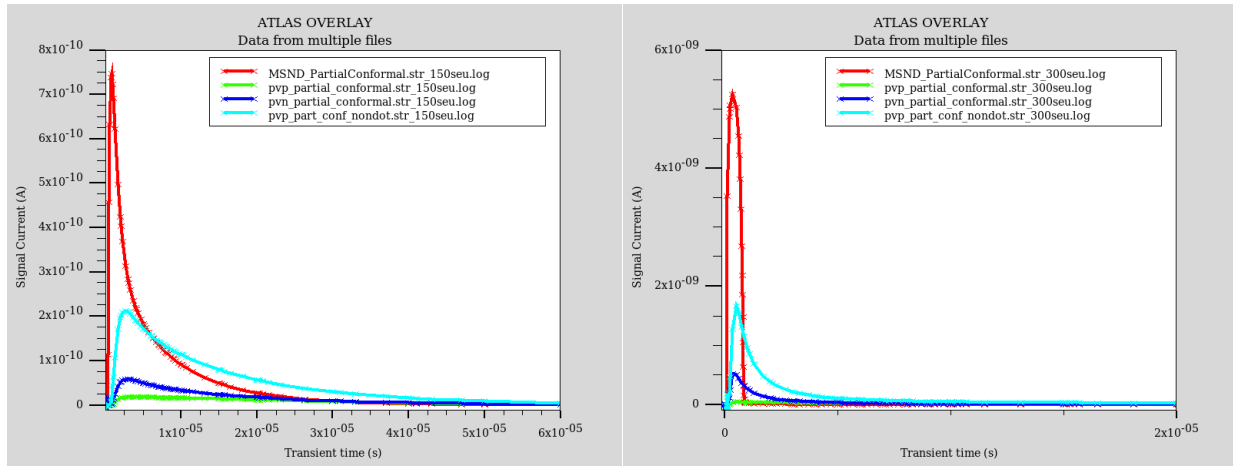


Fig. 4-27. Comparison of signal current for SEUs at 150 μ m (left) and 300 μ m (right) for partial conformal *pvn*-MSNDs, partial conformal *pvp*-DS-MSNDs, partial conformal *pvn*-DS-MSNDs, and partial conformal *pvp*-DS-MSNDs with *n*-ring.

4.3. DS-MSND Detection Efficiency Optimization Simulations

One of the most important performance metrics for a thermal-neutron detector is the intrinsic thermal-neutron detection efficiency. Intrinsic thermal-neutron detection efficiency, ϵ_{th} , is described in Eq. 4-8 where n is the net number of counts recorded by the detector, A is the activity of the source, BR_{th} is the branching ratio for thermal-neutrons, and Ω_f is the fractional solid

angle between the neutron source and detector [44, 45]. Simply stated, the intrinsic thermal-neutron detection efficiency is the number of neutrons counted by the detector divided by the number of neutrons incident on the detector. For DS-MSNDs, the goal was to maximize the intrinsic-thermal neutron detection efficiency. High detection efficiency can decrease the required time and increase the certainty of measurements of neutron sources both in laboratory settings, where the size and location of a source is known, and in search and locate missions where the source size and location are not known to the operator,

$$\varepsilon_{th} = \frac{n}{A(BR_{th})\Omega_f}. \quad \text{Eq. 4-8}$$

4.3.1. Monte Carlo Simulation Overview

Monte Carlo simulation is a common method to model neutron transport and can be used to determine optimal detector geometries to maximize detection efficiency prior to device fabrication thereby saving time and money. The detection efficiency of DS-MSNDs was estimated using a Monte Carlo simulation platform developed by Los Alamos National Laboratory, MCNP6.1 [136]. The first step of the simulation was to set up the problem geometry. For all the efficiency simulations presented here, the active area of the DS-MSND was 1 cm², and a 0.5-cm diameter circular beam of thermal neutrons, 0.0253 eV, was set to normally intersect the surface of the DS-MSND. The following parameters pertaining to the DS-MSND geometry were then defined, see Fig. 4-28: substrate material, wafer thickness, microfeature shape, microfeature depth, microfeature width, pitch or unit cell width, backfill material, and backfill material density.

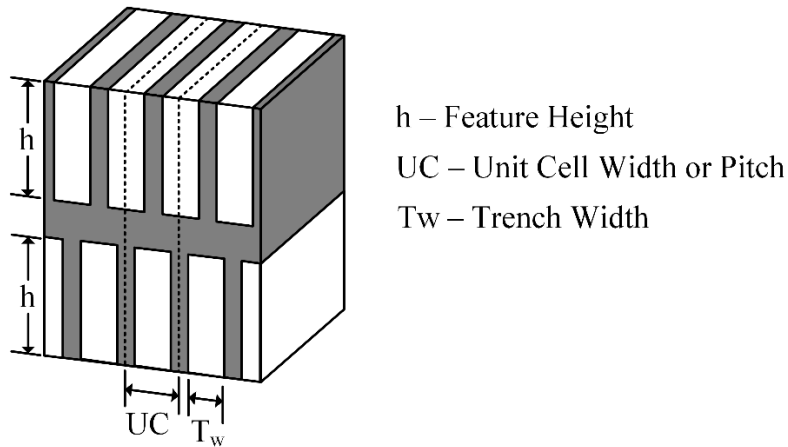


Fig. 4-28. Example of offset straight-trench DS-MSND. The feature height, unit cell width, and trench width were adjusted in MCNP simulations for detector optimization.

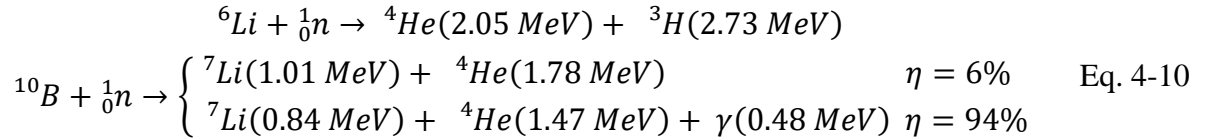
After the device and problem geometry are defined, the simulation begins by randomly sampling the initial location of the incident thermal neutron within the diameter of the neutron beam. To uniformly sample the neutron starting location in the beam, two random numbers are required. The first number is between 0 and the radius of the beam and the second number is between 0 and 2π to give the radial and azimuthal coordinates of the starting location, respectively. Then, a new random number is sampled to determine if an interaction occurs in the DS-MSND based on the underlying probability density function (PDF) of the interaction probability in the material on which the neutron is incident (see Eq. 4-9) [42]. If no interaction occurs, then the neutron is transported to the boundary of next material, and the process is repeated. If no interaction occurs before the neutron exits the problem geometry, no tally is recorded, and the next neutron history is started in the initial neutron beam. If a neutron scatter event occurs, a new neutron direction would be randomly sampled, and the corresponding neutron energy is calculated by the scatter angle. The neutron would then continue to be transported through the problem geometry until it exits the problem space or another interaction occurs. If an absorption event occurs, likely in the neutron-conversion material filling the microfeatures, the charged-particle reaction products are created at the location of the absorption. For ${}^6\text{Li}$ and ${}^{10}\text{B}$, two charged-particle reaction product energies are created based on Eq. 4-10, and the initial direction of one of the reaction products is randomly sampled uniformly in 4π steradians. The second reaction product travels in the opposite direction of the first reaction product to satisfy conservation of momentum. The paths of the reaction products are tracked as they traverse the detector, and the energy deposited in the semiconductor substrate through coulombic interactions is tallied. If the sum of the reaction product energy deposition in the semiconductor material is above the lower level discriminator (LLD), which was 300 keV for these simulations, a “count” is tallied. The entire process is repeated for as many neutron histories required to have low uncertainty in the result (often more than 1 million), and then, the intrinsic thermal-neutron detection efficiency can be determined by dividing the number of tallies by the number of neutrons incident on the detector. Eq. 4-8 reduces to Eq. 4-11, because the fractional solid angle and branching ratio are unity for the problem geometry. The net count rate, n , is the number of “counts” tallied, and the activity, A , is the total number of neutron histories. Additionally, the energy deposition in the semiconductor can be tallied with a F8 tally and used to create theoretical pulse height spectra for the detector [136].

$$d = -\frac{1}{\lambda} \ln \rho \quad \text{Eq. 4-9}$$

d = depth of interation

λ = mean free path of neutron

ρ = random number betwee



$$\varepsilon_{th} = \frac{n}{A} = \frac{\text{Tallies above LLD}}{\text{Num. of Neutrons}} \quad \text{Eq. 4-11}$$

4.3.2. DS-MSND Simulation with MCNP6

MCNP6.1 simulation software was used to optimize the DS-MSND microfeature geometries. Straight trenches, circular holes, and circular pillars were the three microfeature types simulated for the detection efficiency optimization simulations, because they have been the most prominent microfeatures investigated for single-sided MSNDs [15-19, 21-27, 29-33, 69, 70, 72-76, 118, 137-141]. Both ${}^6\text{LiF}$ and ${}^{10}\text{B}$ were considered as neutron conversion material. ${}^6\text{Li}$ has a lower thermal-neutron absorption cross section at 938 b than ${}^{10}\text{B}$, which has a thermal-neutron absorption cross section of 3844 b [47]. However, the Q-value of the ${}^6\text{Li}(n,t)\alpha$ reaction is 4.78 MeV is higher than the Q-value of the ${}^{10}\text{B}(n,\alpha){}^6\text{Li}$ reaction which is 2.79 MeV for 6% of neutron absorptions and 2.31 MeV for 94% of neutron absorptions [45], which is one factor that dictates the average energy imparted in the surrounding semiconductor material and plays a large role for noise and gamma-ray radiation discrimination.

The three microfeature shapes were considered in an “offset” DS-MSND design and an “opaque” DS-MSND design. For the offset DS-MSNDs, the microfeature from the front-side of the diode was repeated on the back-side of the diode and offset by half of a unit cell. For the straight-trenches, the back-side trench was shifted laterally by half a unit cell. For the circular holes and pillars, the back-side microfeature was shifted diagonally to the corner of the unit cell, i.e. if the hole was centered in the unit cell on the front-side of the diode, a hole was centered on each of the corners of the unit cell on the back-side of the diode. For the opaque DS-MSNDs, the back-

side microfeature was the inverse of the front-side microfeature, i.e. if the front-side of the DS-MSND contained an array of repeated circular holes, the back-side of the DS-MSND had an array of circular pillars aligned vertically with the circular holes. By definition, the opaque DS-MSND design does not have any neutron free streaming paths for normally incident neutrons, because the back-side microfeatures are the inverse of the front side features.

The offset DS-MSND design is easier to fabricate than the opaque design, because the size and shape of the microfeature is the same on the front and back of the diode and therefore, can be processed with the same photomask. Additionally, the etch, diffusion, and backfill characteristics for the front and back microfeatures should be identical. One drawback of the offset DS-MSND is that neutron free streaming paths, where a neutron can pass through the diode without intersecting neutron conversion material, exist for normally incident neutrons if the trench width to unit cell width ratio is less than 0.5 for the straight trench design. Additionally, for the hole and pillar designs, if the hole width to unit cell width ratio is less than 1.0 for the circular hole design, and if the pillar diameter to unit cell width is greater than $\sqrt{2}/2$ for the circular pillar design.

Simulations for 50% Backfill Packing Fraction

The six simulated DS-MSND geometries are shown in Fig. 4-29. The simulation environment was similar to previous work done for MSND and DS-MSND optimization [18, 33] and listed in more detail in [131]. The intrinsic thermal-neutron (0.0253 eV) detection efficiency for normally incident thermal neutrons was determined for DS-MSNDs with various microfeature widths and depths, unit cell widths, and neutron conversion material. Each microfeature pattern in Fig. 4-29 was simulated with the microfeatures backfilled with ^6LiF and repeated with the microfeatures backfilled with ^{10}B . For the ^6LiF -backfilled DS-MSNDs, the device thickness was limited to 1500 μm to compensate for the lower neutron absorption efficiency, but the dimensions of the features were larger to capitalize on the longer reaction-product ranges. The device thickness for the ^{10}B -backfilled DS-MSNDs was limited to 500 μm and the microfeature dimensions were smaller to accommodate the higher thermal-neutron absorption efficiency and shorter reaction-product ranges, respectively. The density of ^6LiF was defined as 1.27 g cm^{-3} , and the density of ^{10}B was defined as 1.075 g cm^{-3} to represent 95% enriched backfill powder with a 50% powder particle packing fraction, which was near the maximum achievable packing fraction at the time

[29]. All DS-MSNDs in the simulation were made of silicon, because of silicon's availability, cost, machineability, and gamma-ray insensitivity.

A F8 tally was used to record reaction-product energy deposition in the Si substrate [136]. The simulations reported here assume all energy deposited in the silicon from the reaction products can be collected and measured, in other words, perfect charge collection efficiency. Therefore, the simulations serve as a best-case scenario benchmark for a given geometry and conversion material specification.

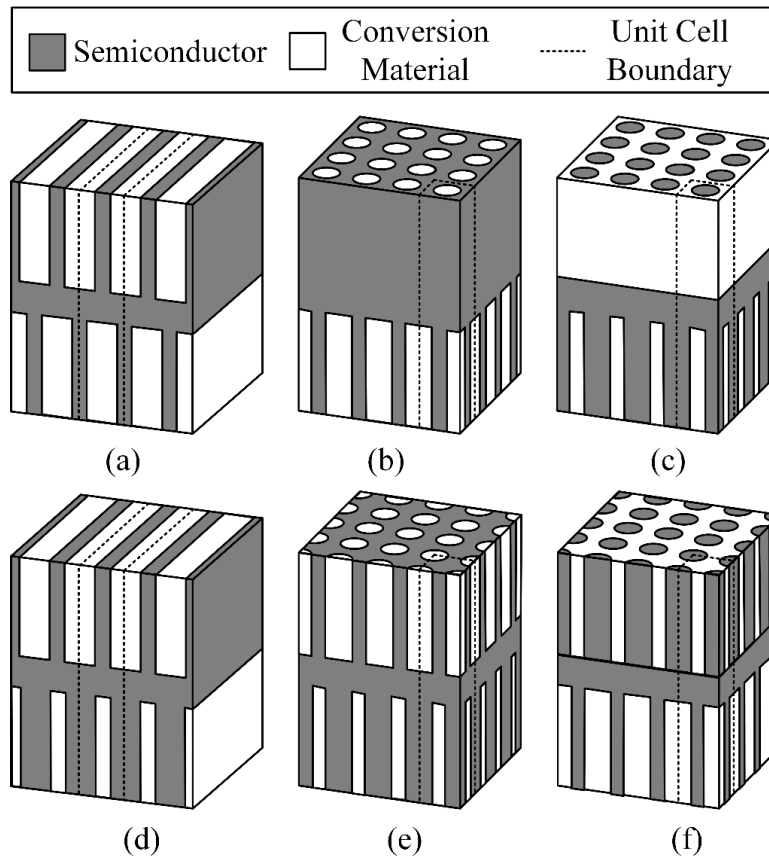


Fig. 4-29. Drawing of DS-MSND geometries considered for microfeature size optimization study with MCNP simulation. The geometries nomenclature was the following: (a) offset straight-trench DS-MSND, (b) offset circular-hole DS-MSND, (c) offset circular-pillar DS-MSND, (d) opaque straight-trench DS-MSND, (e) opaque circular-hole DS-MSND, (f) opaque circular-pillar DS-MSND. Geometries (e) and (f) are identical; however, in the simulations (e) was irradiated on the circular-hole side and (f) was irradiated on the circular-pillar side.

¹⁰B backfilled DS-MSNDs

MCNP6 simulations were performed for opaque and offset DS-MSNDs with straight trenches, circular holes, or circular pillars utilizing ¹⁰B as the neutron conversion material with an effective density of 1.075 g cm⁻³. For each design, the microcavities were assumed to be

completely and uniformly backfilled with the conversion material. Microcavity depths of 20, 40, 60, and 80 μm were considered representing 0.5, 1, 1.5, and 2 mean free path lengths for thermal neutrons, respectively. The following sections display the results for a subset of the ^{10}B -backfilled DS-MSND optimization simulations. The entirety of the simulation results are shown in Appendix B, and an example MCNP input card for ^{10}B -backfilled DS-MSND is also in Appendix B.

^{10}B -Backfilled Offset Patterns

The results of the MCNP optimization simulations for theoretical intrinsic thermal-neutron detection efficiencies for the ^{10}B -backfilled, offset DS-MSNDs shown in Fig. 4-29 (a-c) are shown in Table B-1 through Table B-3 in the Appendix B. Greater than 70% intrinsic thermal-neutron detection efficiency is achievable for all the offset geometries. The maximum intrinsic thermal-neutron detection efficiency with an LLD of 300 keV was 81.4% and was achieved with the offset, circular hole DS-MSND with 80- μm deep holes, a unit cell width of 4 μm , and a 3.6- μm diameter hole. The optimum microfeature width to unit cell ratio was 0.5, 0.8-0.9, and 0.7-0.8 for the straight trench, circular hole, and circular pillar microfeature patterns, respectively.

The intrinsic thermal-neutron detection efficiency as a function of LLD for the three offset DS-MSND geometries with a 4- μm and 6- μm wide unit cell is shown in Fig. 4-30. For 4- μm wide unit cells, the circular hole pattern has the highest intrinsic thermal-neutron detection efficiency, but the detection efficiency rapidly decreases for LLD settings greater than 300 keV. Thus, the circular hole pattern can work well if the LLD can remain low by limiting the background gamma-ray flux and temperature. If the detector is deployed in high ($>45^\circ\text{C}$) temperature environments or in a high gamma-ray field, the LLD will need to be increased to maintain sufficient noise suppression and gamma-ray discrimination which will then significantly reduce the neutron detection efficiency. Comparatively, the straight trench design is affected the least by the LLD setting, indicating that on average the reaction products deposit more energy in the surrounding Si per neutron interaction than in the other designs. The detection efficiency for the pillar design falls between the detection efficiencies for the circular hole and straight trench design but suffers similar LLD dependencies as the circular hole pattern. For the 6- μm wide unit cell, the different microfeature patterns perform more similarly, because the LLD dependency for the circular hole and circular pillar patterns is reduced. The reaction product spectra shown in Fig. 4-31 also indicate that the average energy deposited in the Si substrate by the reaction products is greatest for the

straight trench design. Although the straight trench design may not offer the highest detection efficiency, it should have the best signal-to-noise ratio and gamma-ray discrimination.

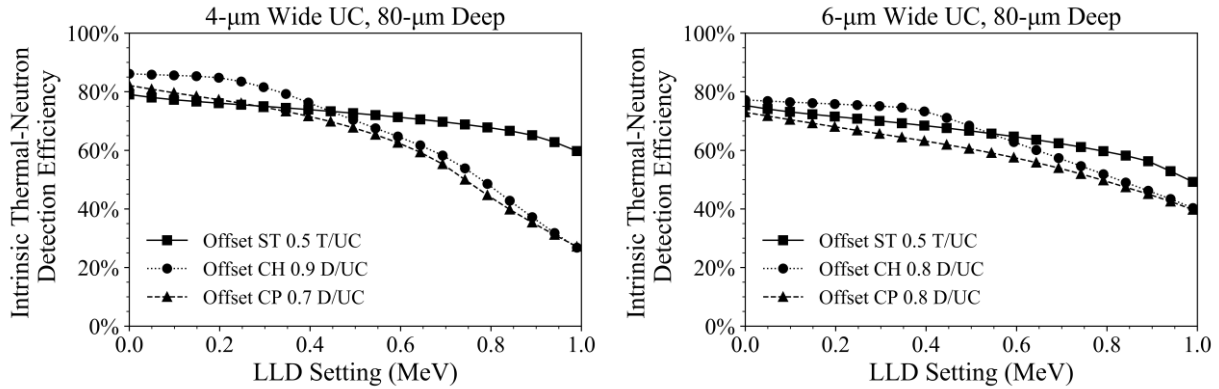


Fig. 4-30. Simulation estimations for the intrinsic thermal-neutron detection efficiencies for ^{10}B -backfilled, offset DS-MSND with 4- μm wide (left) and 6- μm wide (right) unit cells and microfeature depths of 80 μm . The optimum microfeature width to unit cell ratio for a 300 keV LLD was plotted for each microfeature shape. Legend: Straight Trench (ST), Circular Hole (CH), Circular Pillar (CP), Unit Cell width (UC), Trench width (T), Hole or Pillar Diameter (D).

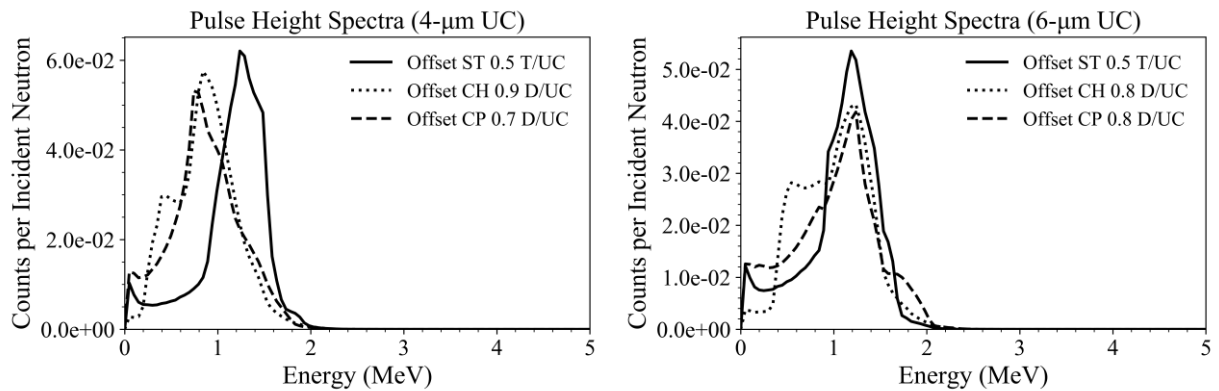


Fig. 4-31. Simulated reaction product spectra for ^{10}B -backfilled, offset DS-MSND with 4- μm wide (left) and 6- μm wide (right) unit cells and microfeature depths of 80 μm . The optimum microfeature width to unit cell ratio for a 300 keV LLD was plotted for each microfeature shape. Legend: Straight Trench (ST), Circular Hole (CH), Circular Pillar (CP), Unit Cell width (UC), Trench width (T), Hole or Pillar Diameter (D).

^{10}B -Backfilled Opaque Patterns

The results of the MCNP optimization simulations for theoretical intrinsic thermal-neutron detection efficiencies for the ^{10}B -backfilled, opaque DS-MSNDs shown in Fig. 4-29 (d-f) are listed in Table B-4 through Table B-6 in Appendix B. Note that the opaque circular hole and opaque circular pillar device are physically the same, but the opaque circular hole DS-MSND was

irradiated on the hole side of the detector, and the opaque circular pillar DS-MSND was irradiated on the circular pillar side. Again, greater than 70% intrinsic thermal-neutron detection efficiency is achievable with all the designs. The opaque circular pillar pattern has the highest intrinsic thermal-neutron detection efficiency with a 300 keV LLD at 81.0% for 80- μm deep features on a 4- μm wide unit cell with 0.9 diameter to unit cell ratio. Intuitively, the next highest efficiency design was the opaque circular-hole pattern at 80.6% with the same cell and depth and a 0.8 diameter to unit cell ratio. Interestingly, the straight-trench design has a flat response over a large range of trench width to unit cell ratios. For 4- μm wide unit cells and 80- μm deep trenches, the intrinsic thermal neutron detection efficiency varies between 70.5% to 75.0% for trench width to depth ratios ranging from 0.2 to 0.8 with the maximum detection efficiency occurring with a trench width to depth ratio of 0.5.

The intrinsic thermal-neutron detection efficiency as a function of LLD for the 300 keV, optimized opaque DS-MSND is shown in Fig. 4-32. For 4- μm unit cells, the circular hole and pillar design slightly outperforms the straight trench design at low LLD levels, but as the LLD increases, the straight trench design is dominant. All the designs have similar performance when the unit cell width was increased to 6 μm . The opaque circular hole and pillar pattern is slightly less affected by changes in the LLD than the offset design. However, care must be taken in the fabrication process for the optimized circular hole and pillar pattern opaque DS-MSND to ensure good etching and diffusion process outcomes for microfeatures with different shapes and sizes. The simulated reaction product spectra for the opaque DS-MSNDs are shown in Fig. 4-33. The average energy deposition is highest in the straight-trench design. The reaction product spectra for the circular hole and circular pillar opaque DS-MSND with 6- μm wide unit cells are nearly identical, because the device geometry is the same with the side irradiated being the only difference.

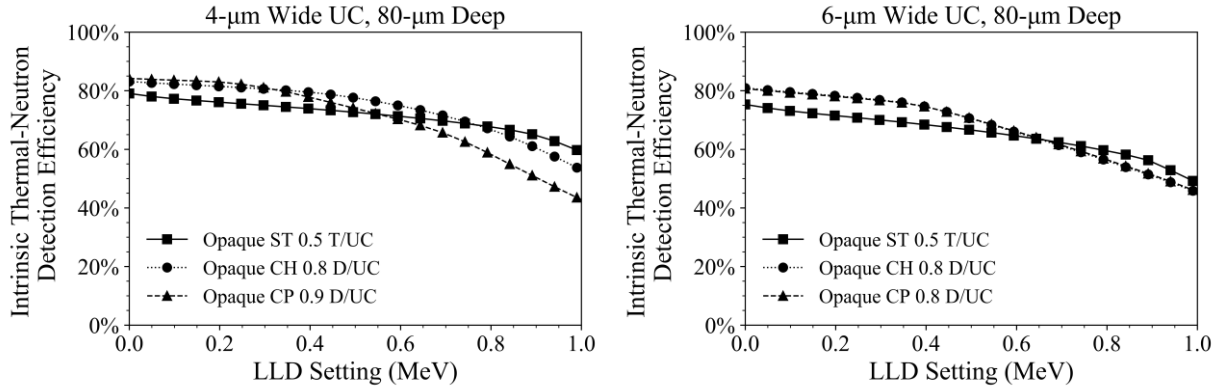


Fig. 4-32. Simulation estimations for the intrinsic thermal-neutron detection efficiencies for ^{10}B -backfilled, opaque DS-MSND with 4- μm wide (left) and 6- μm wide (right) unit cells and microfeature depths of 80 μm . The optimum microfeature width to unit cell ratio for a 300 keV LLD was plotted for each microfeature shape. Legend: Straight Trench (ST), Circular Hole (CH), Circular Pillar (CP), Unit Cell width (UC), Trench width (T), Hole or Pillar Diameter (D).

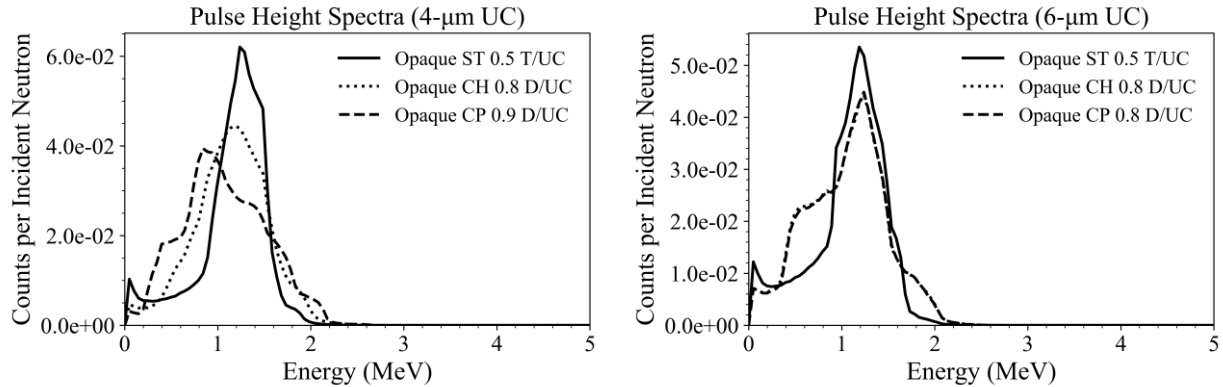


Fig. 4-33. Simulated reaction product spectra for ^{10}B -backfilled, opaque DS-MSND with 4- μm wide (left) and 6- μm wide (right) unit cells and microfeature depths of 80 μm . The optimum microfeature width to unit cell ratio for a 300 keV LLD was plotted for each microfeature shape. Legend: Straight Trench (ST), Circular Hole (CH), Circular Pillar (CP), Unit Cell width (UC), Trench width (T), Hole or Pillar Diameter (D).

^6LiF -backfilled DS-MSNDs

MCNP6 simulations were repeated for the opaque and offset DS-MSND patterns with straight trenches, circular holes, or circular pillars now utilizing ^6LiF as the neutron conversion material with an apparent density of 1.273 g cm^{-3} representing a 50% powder packing fraction. As with the last set of simulations, the microcavities were assumed to be completely and uniformly backfilled with the conversion material. ^6LiF has a smaller thermal-neutron capture cross section than ^{10}B , and therefore, deeper microfeatures are required to achieve the same neutron absorption efficiency. The silicon diode thickness was increased to 1500 μm , depths of 175, 350, 500, and 650 μm were considered representing 0.5, 1, 1.4, and 1.9 mean free path length for thermal

neutrons in the reduced density ${}^6\text{LiF}$. Unit cell widths of 20, 40, 60, 80, and 100 μm were considered for the simulations. The following sections display the results for a subset of the ${}^6\text{LiF}$ -backfilled DS-MSND optimization simulations. The entirety of the simulation results and an example MCNP input card for ${}^6\text{LiF}$ -backfilled DS-MSNDs is in Appendix B.

${}^6\text{LiF}$ -Backfilled Offset Patterns

The results of the MCNP optimization simulations for the ${}^6\text{LiF}$ -backfilled, offset DS-MSNDs shown in Fig. 4-29 (a-c) are listed in Table B-1 through Table B-3 in Appendix B. Over 70% intrinsic thermal-neutron detection efficiency is achievable for all the offset geometries. The maximum intrinsic thermal-neutron detection efficiency with an LLD of 300 keV was 84.2% and was achieved with the offset, circular hole DS-MSND with 650- μm deep holes, a unit cell width of 20 μm , and 18- μm diameter holes. The optimum microfeature width to unit cell ratio was 0.5-0.8, 0.8-0.9, and 0.7-0.8 for the straight trench, circular hole, and circular pillar microfeature patterns, respectively, dependent on the unit cell size.

The intrinsic thermal-neutron detection efficiency as a function of LLD for the three offset DS-MSND geometries with a 20- μm and 40- μm wide unit cell are shown in Fig. 4-34. The circular hole-pattern had the highest intrinsic thermal-neutron detection efficiency for the 20- μm wide unit cells and was affected the least by changes in LLD setting. In order to achieve ultra-high detection efficiency, large feature width to unit cell width ratios are required. The circular hole and circular-pillar designs can achieve higher average energy deposition per reaction product than the straight trench pattern for these designs. However, one has to consider the practicality of achieving such high-aspect ratio microstructures while retaining good charge collection efficiency after the diffusion processes where dead regions are formed in the silicon on the p -type side of the junction. In the 40- μm wide unit cell patterns, the circular-hole shape still retains the highest detection efficiency for low LLD settings. However, the straight-trench design has comparable efficiency and a nearly flat response to changes in LLD settings up to 1 MeV primarily attributed to the larger fin dimensions of the optimized design which has a 0.5 fin width to unit cell width ratio. This effect is also shown in the reaction product spectra shown in Fig. 4-35. Note that counts in the pulse height spectra appear in higher energy channels than the ${}^{10}\text{B}$ -backfilled counterparts due to the higher energy reaction products from neutron absorption with ${}^6\text{Li}$.

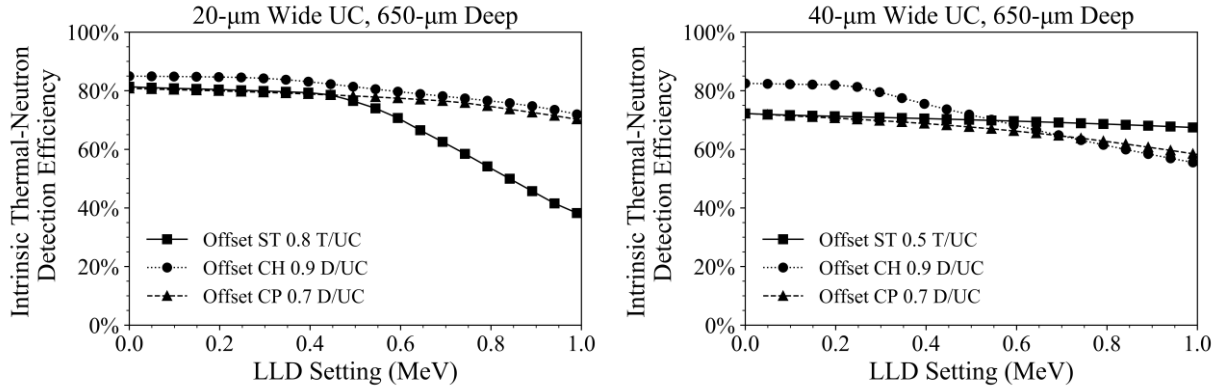


Fig. 4-34. Simulation estimations for the intrinsic thermal-neutron detection efficiencies for ${}^6\text{LiF}$ -backfilled, offset DS-MSND with 20- μm wide (left) and 40- μm wide (right) unit cells and microfeature depths of 650 μm . The optimum microfeature width to unit cell ratio for a 300 keV LLD was plotted for each microfeature shape. Legend: Straight Trench (ST), Circular Hole (CH), Circular Pillar (CP), Unit Cell width (UC), Trench width (T), Hole or Pillar Diameter (D).

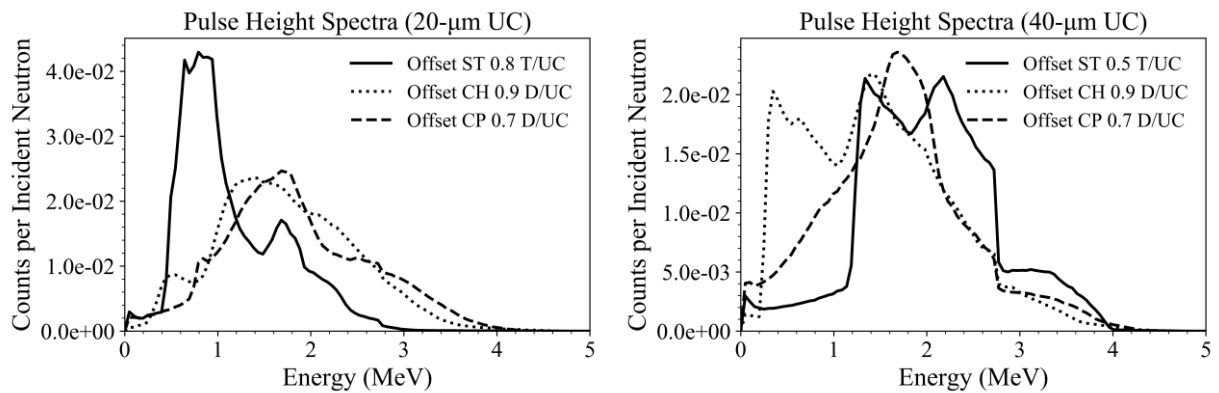


Fig. 4-35. Simulated reaction product spectra for ${}^6\text{LiF}$ -backfilled, offset DS-MSND with 20- μm wide (left) and 40- μm wide (right) unit cells and microfeature depths of 650 μm . The optimum microfeature width to unit cell ratio for a 300 keV LLD was plotted for each microfeature shape. Legend: Straight Trench (ST), Circular Hole (CH), Circular Pillar (CP), Unit Cell width (UC), Trench width (T), Hole or Pillar Diameter (D).

${}^6\text{LiF}$ -Backfilled Opaque Patterns

The intrinsic thermal-neutron detection efficiency simulation results for the opaque DS-MSNDs (Fig. 4-29 e-f) are listed in Table B-4 through Table B-6 in Appendix B. Over 70% detection efficiency is possible with all designs for normally incident thermal-neutrons, and very-high-aspect-ratio, circular hole-pillar DS-MSNDs can theoretically achieve 80% detection efficiency with a 300 keV LLD. The circular hole/pillar design capable of 81.8%-82.0% intrinsic thermal-neutron detection efficiency can be obtained with a hole diameter to unit cell width ratio of 0.9 and 650- μm deep perforations. The optimum trench width to unit cell ratio for the straight trench

opaque DS-MSND was 0.5 resulting in 77.1% intrinsic thermal-neutron detection efficiency. Additionally, the conservative trench width to unit cell ratio can be more easily manufactured than DS-MSNDs with higher feature width to unit cell ratios.

The intrinsic thermal-neutron detection efficiency as a function of LLD setting for the 20- μm wide and 40- μm wide unit cell, opaque DS-MSNDs are shown in Fig. 4-36. The straight-trench pattern was least affected by changes in LLD settings but was slightly less sensitive to neutrons than the circular hole and pillar patterns for both the 20 μm and 40 μm unit cell widths. The pulse height spectra shown in Fig. 4-37 indicated that the reaction products deposit more energy in the silicon substrate on average with the straight trench design. The feasibility of a 650- μm deep hole/pillar with 20- μm wide unit cells and 18- μm diameter features is questionable, but those dimensions can theoretically break past the 80% detection efficiency threshold. For more easily attainable feature width to unit cell width ratios (i.e., 0.5) the straight-trench design exhibits higher detection efficiency than the circular holes and pillars design. Again, note that the counts in the pulse height spectra of ^6LiF -backfilled DS-MSND tend to fall in higher energy channels than ^{10}B -backfilled DS-MSND; however, deeper microcavities are required to attain high detection efficiency.

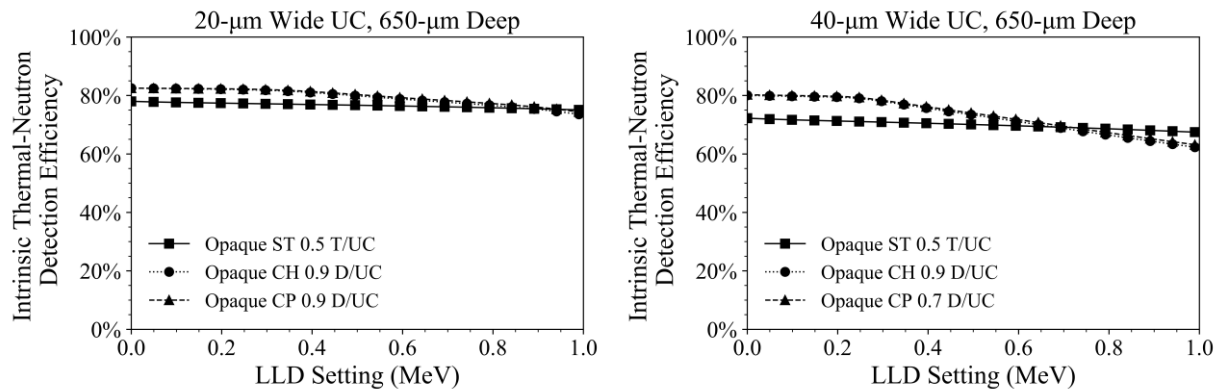


Fig. 4-36. Simulation estimations for the intrinsic thermal-neutron detection efficiencies for ^6LiF -backfilled, opaque DS-MSND with 20- μm wide (left) and 40- μm wide (right) unit cells and microfeature depths of 650 μm . The optimum microfeature width to unit cell ratio for a 300 keV LLD was plotted for each microfeature shape. Legend: Straight Trench (ST), Circular Hole (CH), Circular Pillar (CP), Unit Cell width (UC), Trench width (T), Hole or Pillar Diameter (D).

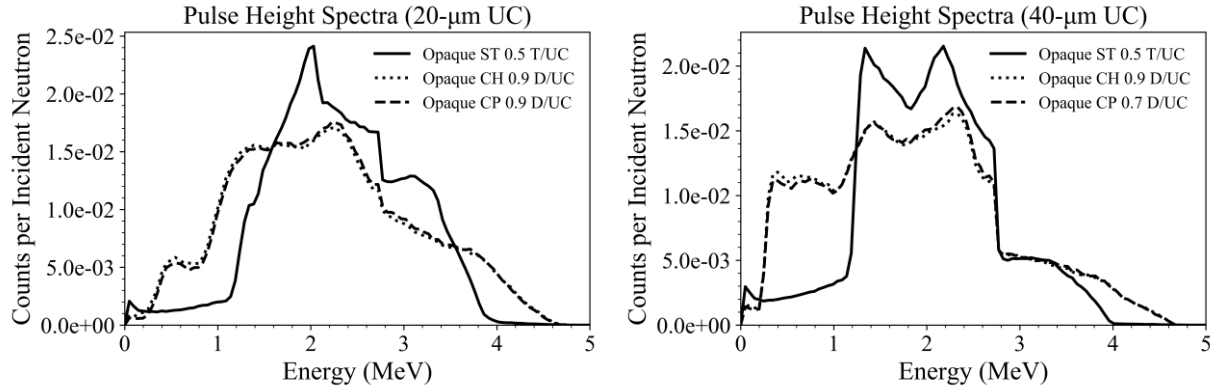


Fig. 4-37. Simulated reaction product spectra for ${}^6\text{LiF}$ -backfilled, opaque DS-MSND with 20- μm wide (left) and 40- μm wide (right) unit cells and microfeature depths of 650 μm . The optimum microfeature width to unit cell ratio for a 300 keV LLD was plotted for each microfeature shape. Legend: Straight Trench (ST), Circular Hole (CH), Circular Pillar (CP), Unit Cell width (UC), Trench width (T), Hole or Pillar Diameter (D).

Angular Response

In the previous simulations, a thermal-neutron beam was normally incident on the front-side of the DS-MSND. This simulation environment is beneficial, because it can be easily reproduced in the diffracted thermal-neutron beam port at the Kansas State University TRIGA Mk II nuclear reactor. However, when deployed in the field, the DS-MSNDs are likely to be intersected by neutrons from a variety of angles. Therefore, MCNP simulations were performed on DS-MSNDs and MSNDs to compare the detector response to angle of incidence for thermal neutrons. It is already known that the angular response for straight-trench DS-MSNDs is flatter than the angular response for straight-trench MSNDs [33]; however the simulations presented herein were performed with more readily achievable backfill packing fractions and straight trench, circular hole, and circular pillar patterned DS-MSNDs and MSNDs. The simulation parameters are listed in Table 4-3. The DS-MSNDs and MSNDs were modeled with similar dimensions to recent work performed in [29] and [28, 124]. The thermal-neutron (0.0253 eV) beam diameter was the same width as the thickness of the DS-MSND or MSND diode and was rotated from 0° to 90° angle of incidence, with 0° being normally incident on the front-side of the detector. Charge collection efficiency within the silicon diode was assumed to be perfect.

Table 4-3. MCNP problem geometry parameters for the DS-MSND and MSND angular response simulations.

Parameter	DS-MSND (Offset)	MSND
Microfeature Shapes	Straight Trench, Circular Hole, & Circular Pillar	Straight Trench, Circular Hole, & Circular Pillar
Wafer Thickness	1500 μm	500 μm
Microfeature Depth	600 μm	400 μm
Unit Cell Width	30 μm	30 μm
Microfeature Width to Cell Width Ratio	0.67	0.67
Backfill Material	^6LiF	^6LiF
Packing Fraction	50%	50%
Lower Level Discriminator	300 keV	300 keV
Neutron Energy	0.0253 eV	0.0253 eV
Neutron Beam Diameter	1.5 mm	0.5 mm
Angle of Incidence	0-90°	0-90°

Shown in Fig. 4-38 are the angular response to thermal neutrons for straight trench, circular hole, and circular pillar patterned DS-MSNDs and MSNDs. The straight trench and circular pillar DS-MSNDs have the flattest response out of all the simulated geometries. The intrinsic thermal-neutron detection efficiency was about 73% for normally incident neutrons (0°) and peaks at 85% for 80° angle of incidence before dropping to approximately 38% for side-on irradiation (90°). The slight increase in detection efficiency for the DS-MSNDs stems from longer neutron path tracks through the ^6LiF neutron conversion material which increases the probability for neutron absorption. The intrinsic-detection efficiency for single-sided MSNDs is strongly affected by the neutron angle of incidence. For example, the detection efficiency for the straight trench MSND ranges from 38% at 0° all the way to 80% at 80°. The change in detection efficiency as a function of neutron angle is initially dominated by closing neutron free streaming paths through the silicon microfeatures where neutrons can pass directly through the detector diode without traversing any conversion material. Once the neutron free streaming paths are eliminated, the detection efficiency continues to rise as the track length in the conversion material increases as a function of incident angle up to about 80°. All the detectors have suppressed detection efficiencies for side-on irradiation caused by neutron streaming paths in the bulk silicon below microfeatures for the MSNDs and between the front-side and back-side microfeatures in the DS-MSND. However, the

solid angle for side-on irradiation is comparatively small and DS-MSNDs-based instruments can be designed to limit the probability of side-on irradiation during operation.

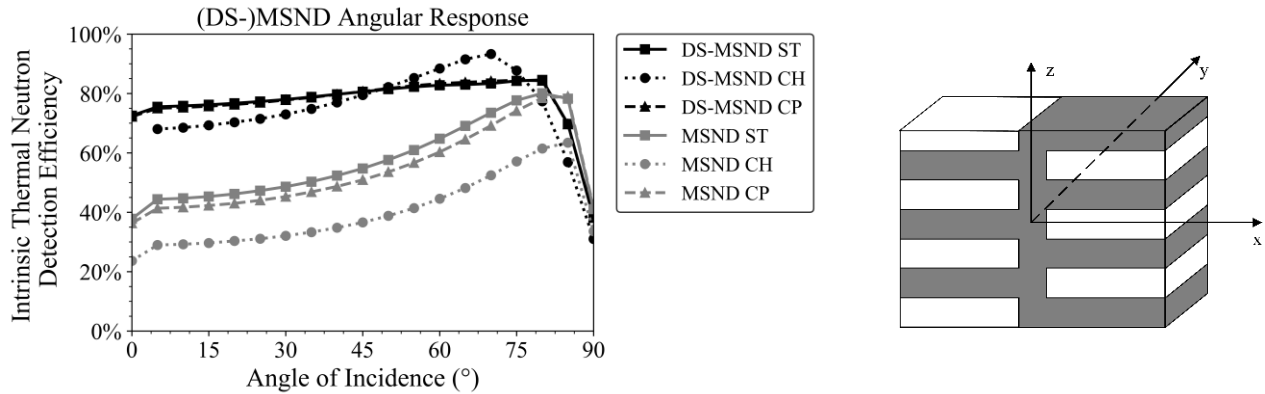


Fig. 4-38. (Left) DS-MSND and MSND angular response to a collimated thermal-neutron beam. The DS-MSND CP and DS-MSND ST response are nearly identical. (Right) Example of DS-MSND straight trench geometry used for angular response simulations. The neutron beam was rotated around the y-axis with 0° corresponding to the negative x-direction and 90° was the beam pointed in the negative z direction towards the DS-MSND. Similar orientations were used for the other DS-MSND and MSND patterns.

Gamma-Ray Sensitivity

MCNP6 simulations were performed to estimate the gamma-ray sensitivity of an offset, straight-trench DS-MSND for photons with energies ranging from 10 keV to 10 MeV. A collimated beam of monoenergetic gamma rays was normally incident on the front face of the DS-MSND for the simulations. It was assumed that all silicon within the DS-MSND was active which may not be a completely accurate correlation to real-world devices but should give a worst-case scenario estimation for gamma-ray sensitivity. The parameters used for the simulations are outlined in

Table 4-4.

Parameter	DS-MSND (Offset)	MSND
Microfeature Shape	Straight Trench	Straight Trench
Wafer Thickness	1500 μm	500 μm
Microfeature Shape	Straight Trench	Straight Trench
Microfeature Depth	600 μm	400 μm
Wafer Thickness	1500 μm	500 μm
Unit Cell Width	30 μm	30 μm
Microfeature Depth	600 μm	400 μm
Microfeature Width to Cell Width Ratio	0.67	0.67
Unit Cell Width	30 μm	30 μm
Backfill Material	^6LiF	^6LiF
Microfeature Width to Cell Width Ratio	0.67	0.67
Packing Fraction	50%	50%
Backfill Material	^6LiF	^6LiF
Lower Level Discriminator	300 keV	300 keV
Packing Fraction	50%	50%
Gamma-ray Energy	10 keV - 1 MeV	10 keV - 1 MeV
Lower Level Discriminator	300 keV	300 keV
Neutron Beam Diameter	50 mm	50 mm
Gamma-ray Energy	10 keV - 1 MeV	10 keV - 1 MeV
Angle of Incidence	50°	0°
Neutron Beam Diameter	50 mm	50 mm

Table 4-4. Parameters used for DS-MSND gamma-ray sensitivity simulations.

The theoretical gamma-ray detection efficiency for DS-MSNDs as a function of gamma-ray energy with and LLD setting of 300 keV is shown in Fig. 4-39. One can notice that the DS-MSND is much more sensitive to gamma rays than its MSND counterpart at approximately 10^{-3} compared to 3×10^{-5} . The increased sensitivity is most likely caused by the increased thickness of the DS-MSND, which is 1.5-mm thick compared to 0.5-mm thick, allowing for significantly more gamma-ray interactions and subsequent electron energy deposition in the silicon. High gamma-ray detection efficiency is undesirable in neutron detectors. Neutron detectors are often deployed in mixed radiation fields consisting of gamma rays and neutrons, and a high sensitivity to gamma ray will trigger “false” neutron counts in the neutron detection system. There are a couple methods to discriminate or reduce the sensitivity to the gamma rays. One method would be to implement pulse shape discriminating electronics that can determine when charge deposition in the silicon was caused by electron interactions or heavy charged-particle interactions such as tritons and alpha particles. This method can greatly improve the gamma-ray discrimination capabilities of the system, but comes at the price of increased electronics cost, increased power consumption, and increased dead time from the increased processing time required to measure the pulse shape. Another method to reduce the gamma-ray sensitivity would be to reduce the thickness of the DS-MSND diode. By reducing the volume of the DS-MSND, the probability for gamma-ray interactions within the detector will decrease; however, smaller microfeatures and more optimized ${}^6\text{LiF}$ backfill packing fraction would be required to retain high detection efficiencies. Finally, the easiest method to decrease the gamma-ray sensitivity of the DS-MSND is to increase the LLD setting. The right-side image in Fig. 4-39 is the reaction product spectra for a neutron-irradiated DS-MSNDs and a number of gamma-ray-irradiated DS-MSNDs. The gamma-ray interactions tend to fall in the lower energy channels due to the small feature sizes of the DS-MSND and relatively low stopping power of electrons in silicon. If the LLD was increased to 600 keV, the gamma-ray detection efficiency drops into the 10^{-5} to 10^{-6} for the gamma-ray energies simulated while the intrinsic thermal-neutron detection efficiency only falls to 72.6%. The neutron detection efficiency is less affected by the increased LLD, because the reaction product escape probability for tritons and alpha particles are high, and the energy deposition per unit path length (dE/dx) in silicon for alpha particles and tritons is much greater than dE/dx for electrons.

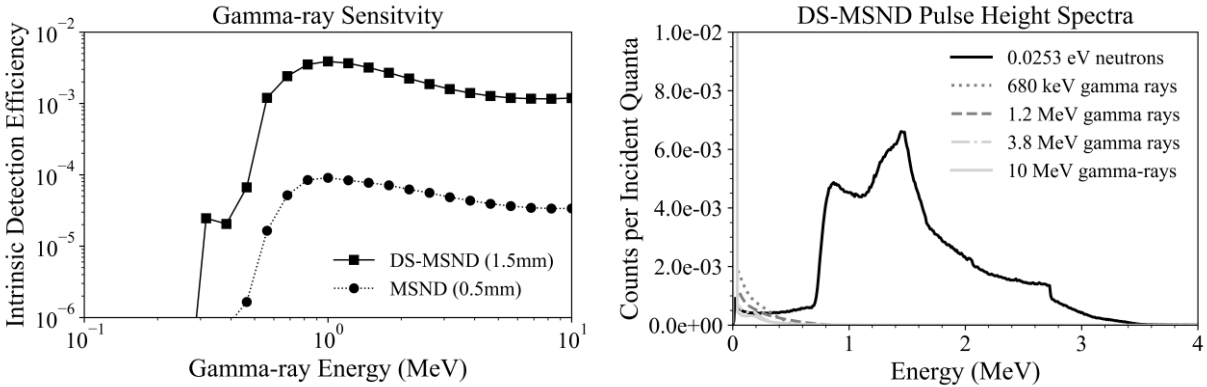


Fig. 4-39. (Left) Theoretical intrinsic gamma-ray detection efficiency of a DS-MSND and MSND with parameters described in

Table 4-4. The DS-MSND is significantly more sensitive to gamma rays primarily because of the increased

Parameter	DS-MSND (Offset)	MSND
Microfeature Shape	Straight Trench	Straight Trench
Wafer Thickness	1500 μm	500 μm
Microfeature Depth	600 μm	400 μm
Unit Cell Width	30 μm	30 μm
Microfeature Width to Cell Width Ratio	0.67	0.67
Backfill Material	⁶ LiF	⁶ LiF
Packing Fraction	50%	50%
Lower Level Discriminator	300 keV	300 keV
Gamma-ray Energy	10 keV – 1 MeV	10 keV – 1 MeV
Neutron Beam Diameter	50 mm	50 mm
Angle of Incidence	0°	0°

thickness of the diode. (Right) DS-MSND pulse height spectra for normally incident gamma rays in and thermal neutrons showcasing the lower level discriminator can be increased significantly with minimal effect on the neutron detection efficiency while drastically reducing the gamma-ray sensitivity.

Simulations for Variable Backfill Packing Fractions

Thus far, for all of the DS-MSND and MSND simulations, it was assumed that the backfill packing fraction was 50%, because it was the highest achieved and reported packing fraction for ⁶LiF powder particles [29]. However, 50% packing fraction may not necessarily be the optimum packing fraction for MSND and DS-MSNDs currently in production. Therefore, MCNP simulations were performed to determine the optimum packing fraction for a subset of ⁶LiF-backfilled, offset, straight-trench DS-MSND geometries commonly produced in the KSU S.M.A.R.T Laboratory. Only ⁶LiF was considered, because it allows for larger features within the DS-MSND easing the manufacturing burden. The following DS-MSND dimensions were

considered for this simulation study: trench depths of 300 μm to 600 μm in 50 μm increments, unit cell widths of 20 μm to 40 μm in 5 μm increments, trench width to unit cell width ratios from 0.5 to 0.8 in 0.05 increments, and ^6LiF backfill packing fractions from 0.05 to 1.0 with increments of 0.05. All neutrons were normally incident on the front-face of the DS-MSND with initial energy of 0.0253 eV, and the LLD was 300 keV. The simulation parameters are summarized in Table 4-5.

Table 4-5. Simulation parameters used for ^6LiF -backfill optimization study for offset, straight-trench DS-MSNDs.

Parameter	DS-MSND (Offset)
Microfeature Shape	Straight Trench
Wafer Thickness	1500 μm
Microfeature Depth	300-600 μm
Unit Cell Width	20-40 μm
Microfeature Width to Cell Width Ratio	0.5-0.8
Backfill Material	^6LiF
Packing Fraction	5-100%
Lower Level Discriminator	300 keV
Neutron Energy	0.0253 eV
Neutron Beam Diameter	50 mm
Angle of Incidence	0°

The relationship between the ^6LiF powder packing fraction and neutron detection efficiency for straight trench, offset DS-MSNDs with different trench depth for a 30- μm wide unit cell and a 25- μm wide unit cell is shown in Fig. 4-40. The trench width to unit cell ratio (T/UC) was constant for both unit cell widths. As the trench depth increased, the optimum packing fraction to maximize intrinsic thermal-neutron detection efficiency decreased. For example, the optimum packing fraction for 300- μm deep trenches was nearly 100% indicating that improving neutron absorption efficiency is the most important factor for DS-MSNDs with shallower trenches. When the trench depth was increased to 600- μm , the optimum packing fraction was reduced to approximately 60%. In the deeper-trenched DS-MSND, the neutrons have longer track lengths in the ^6LiF powder. Therefore, the macroscopic neutron absorption cross section does not need to be as high to achieve the same absorption efficiency of tightly packed shallow trenches, and the reduced powder density in the deep-trenched DS-MSND improves the reaction product escape probability from the trenches into the adjacent silicon fins.

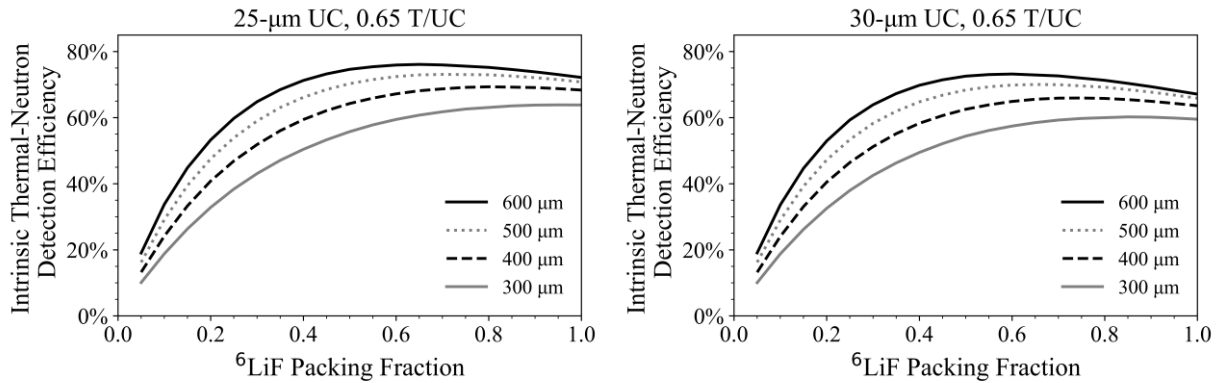


Fig. 4-40. Results from the ${}^6\text{LiF}$ backfill optimization study for straight-trench, offset DS-MSNDs with 0.65 trench width to unit cell width ratio. The intrinsic thermal-neutron detection efficiency is plotted as a function of ${}^6\text{LiF}$ packing fraction for trench depths of 300, 400, 500, and 600 μm . (Left) 25- μm wide unit cell. (Right) 30- μm wide unit cell.

The effect of unit cell width on the optimum ${}^6\text{LiF}$ packing fraction is shown in Fig. 4-41. For packing fractions less than 30%, the DS-MSND detection efficiency is nearly identical for all unit cell widths between 20 μm and 40 μm . As the ${}^6\text{LiF}$ packing fraction increases, the performance between different unit cell widths begins to separate with smaller unit cell widths having higher detection efficiency for a given ${}^6\text{LiF}$ backfill density. The optimum packing fraction for a given unit cell width also changes as the unit cell width changes. For the unit cell widths ranging from 30 μm to 40 μm , the optimum packing fraction ranges from 60-80%. When the unit cell width is only 20 μm , 100% backfill density is optimum. For all unit cell widths, higher ${}^6\text{LiF}$ packing fraction increases the neutron absorption efficiency, but it also decreases the range of the charged-particle reaction products within the trenches. When the unit cell width is small, the decreased range has minimal effect of the reaction product escape probability, because the trenches are already narrow. However, when the unit cell width is increased and the trench width is also increased to retain the same T/UC ratio, the range of the charged-particle reaction products becomes more significant thereby reducing the optimum packing fraction.

Finally, the effect of changing the trench width to unit cell ratio (T/UC) on the optimum packing fraction is shown in Fig. 4-42. When the packing fraction is below 60%, larger T/UC ratio are desired due to the increased reaction product range in the trenches. At higher packing fractions,

smaller T/UC ratios have higher detection efficiency, because the improved neutron absorption efficiency begins to offset the reduced reaction product range.

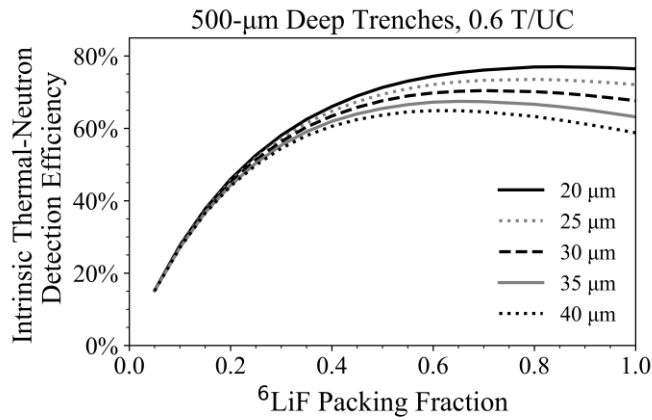


Fig. 4-41. ${}^6\text{LiF}$ packing fraction optimization simulation results for unit cell widths of 20-40 μm . The trench depth was set to 500 μm , and the trench width to unit cell width ratio was 0.6 for the reported results. Only offset, straight-trench DS-MSNDs were simulated.

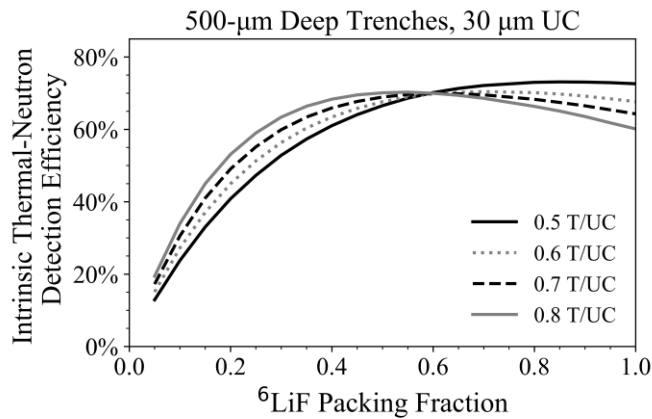


Fig. 4-42. ${}^6\text{LiF}$ packing fraction optimization simulation results for unit cell widths of 20-40 μm . The trench depth was set to 500 μm , and the trench width to unit cell width ratio was 0.6 for the reported results. Only offset, straight-trench DS-MSNDs were simulated.

Fabrication Considerations

The two prominent methods for forming microstructures in silicon are dry etching or wet etching processes. Dry etching techniques, such as inductively coupled plasma reactive ion etching (ICP-RIE), utilize a reaction gas and carrier gas to interact with the silicon and then subsequently passivate the microfeature sidewall, respectively. The ICE-RIE process can have significant lateral etch, bottle necking, ribbing or some combination of all three when etching deep, high-aspect ratio microfeatures. However, the dry etching techniques are not crystalline plane-orientation specific;

theoretically, any microfeature shape can be etched with this process. Additionally, the dry etching process can be used to etch a wider array of materials including Si, SiC, and GaAs.

Alternatively, anisotropic wet etching processes can be used for certain microfeature geometries on specific substrates. Conveniently, potassium hydroxide (KOH) and tetramethylammonium hydroxide (TMAH) selectively etch in the [110]- and [100]-direction in Si much faster than the [111]-direction. Therefore, straight trenches can be aligned parallel to the (111)-plane of [110]-orientated Si wafers to form high-aspect ratio, deep straight trenches, and trenches up to 600- μm deep by 20- μm wide have been fabricated in KOH with this method. Additionally, KOH wet etching results in smooth sides walls that do not need additional processing to eliminate excess leakage from sharp or damaged edges. Furthermore, for mass production, wet etching is more ideal, because the process is typically faster, and the wafer capacity is limited by the heated bath size. In an RIE system, the wafer capacity is defined by the size of the reaction chamber, which is more expensive to scale up for large production.

It was assumed in the MCNP simulations that 100% charge collection efficiency was achieved for the reaction products in the silicon microfeatures. Unfortunately, 100% charge collection efficiency is not normally achieved in real-world devices, and thus, the simulation results indicate a best-case scenario. From the TCAD simulation section, it was evident that the charge collection efficiency changed as function of dopant profile and interaction location. Imperfect charge collection efficiency smears and shifts the reaction-product pulse height spectrum to lower energy bins nearer to the background and gamma-ray noise. If the charge collection efficiency is poor, neutron detection efficiency decreases, and gamma-ray rejection worsens. Therefore, dopant profiles with uniform, strong electric fields are desired to maximize charge collection efficiency.

Also note that all the silicon was considered “active” in the simulations. However, in practical devices, the boron or phosphorus dopant diffuses between 0.5 to 1.5- μm deep into the silicon surface and forms a “dead” region where only a fraction of the deposited energy will be measured again shifting the pulse height spectrum to lower energy bins [45]. In some *p-i-n* silicon detectors only about 50% of energy deposited in the dead region is measured [142]. This effect is especially troublesome for DS-MSND designs with small unit cells and large perforation-width to unit-cell-width ratios, because the volume of “dead” silicon becomes large compared to the volume of “active” silicon in the microfeatures (Fig. 4-43).

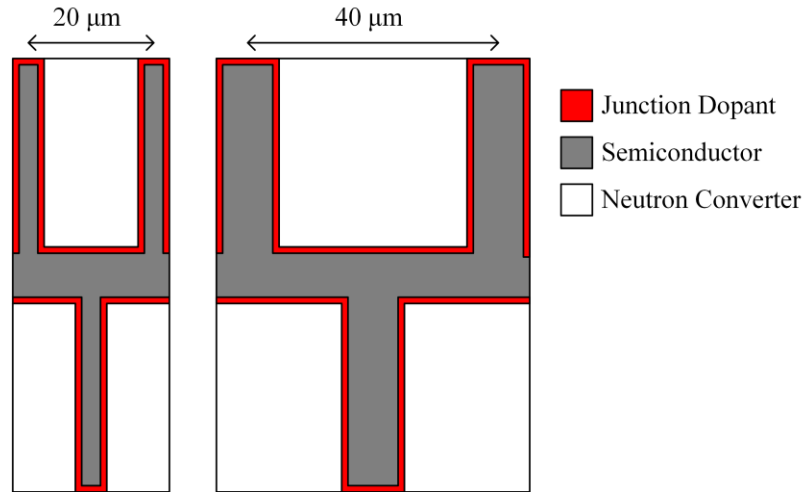


Fig. 4-43. Schematic visualizing the relative size of the “dead” region and “active” regions in silicon microfeatures. The perforation-width to unit-cell-width ratio was 0.75 for both the 20-μm and 40-μm wide unit cells shown here. This effect is especially bad for ¹⁰B-backfilled devices, because the short reaction-product ranges require smaller unit cell widths.

Chapter 5 - Dual-Sided Microstructured Semiconductor Neutron

Detectors: Fabrication and Characterization

Detailed in this chapter are the fabrication processes involved in making Dual-Sided Microstructured Semiconductor Neutron Detectors and the characterization measurements performed after detector fabrication. The *pvp*-, *pvn*, and *pvp-n-dot* DS-MSND designs and several fast charge collection doping schemes are covered herein.

5.1. Detector Fabrication

The detector fabrication process is described in three subsections. The first subsection covers silicon wafer processing including oxide growth, photolithography, wet etching, dopant diffusion, and metallization. The second subsection details the lessons learned and improvements in the ${}^6\text{LiF}$ backfilling process which was a major contributor to the increase in detection efficiency over previous DS-MSNDs [32, 33]. The final subsection provides an overview of the DS-MSND diode packaging.

5.1.1. Silicon Processing

DS-MSNDs are fabricated from 1.0 to 1.5-mm thick, 100-mm diameter, float-zone refined, high-resistivity, phosphorus-doped, *n*-type (or *v*-type), (110)-silicon wafers. The primary flat on the wafer is cut parallel to the (111)-plane so that the trenches can be properly aligned to utilize the anisotropy of the KOH wet etch. Up to 52 DS-MSNDs can be made on a single wafer, and 25 to 50 wafers can be simultaneously batch processed at the KSU S.M.A.R.T. Laboratory facility. Previous MSNDs and DS-MSNDs had been processed on 33-k Ω -cm resistivity silicon, but the present generation utilizes 5-k Ω -cm resistivity silicon. Higher resistivity silicon improves the detector performance by limiting leakage current, increasing carrier lifetime, and reducing bias required to fully deplete the diode, however the price of the wafers also increases as resistivity increases. The 1.5-mm thick, 5-k Ω -cm wafers are commonly priced between \$120 to \$160 per wafer. Large scale batch processing can be used to reduce production costs, and the cost per DS-MSND could be further reduced by increasing the diameter of silicon wafer. However, larger diameter wafers require larger processing equipment, which would necessitate a large one-time capital expenditure to upgrade the VLSI processing equipment. An overview of the DS-MSND fabrication steps described in this section is shown in Fig. 5-1.

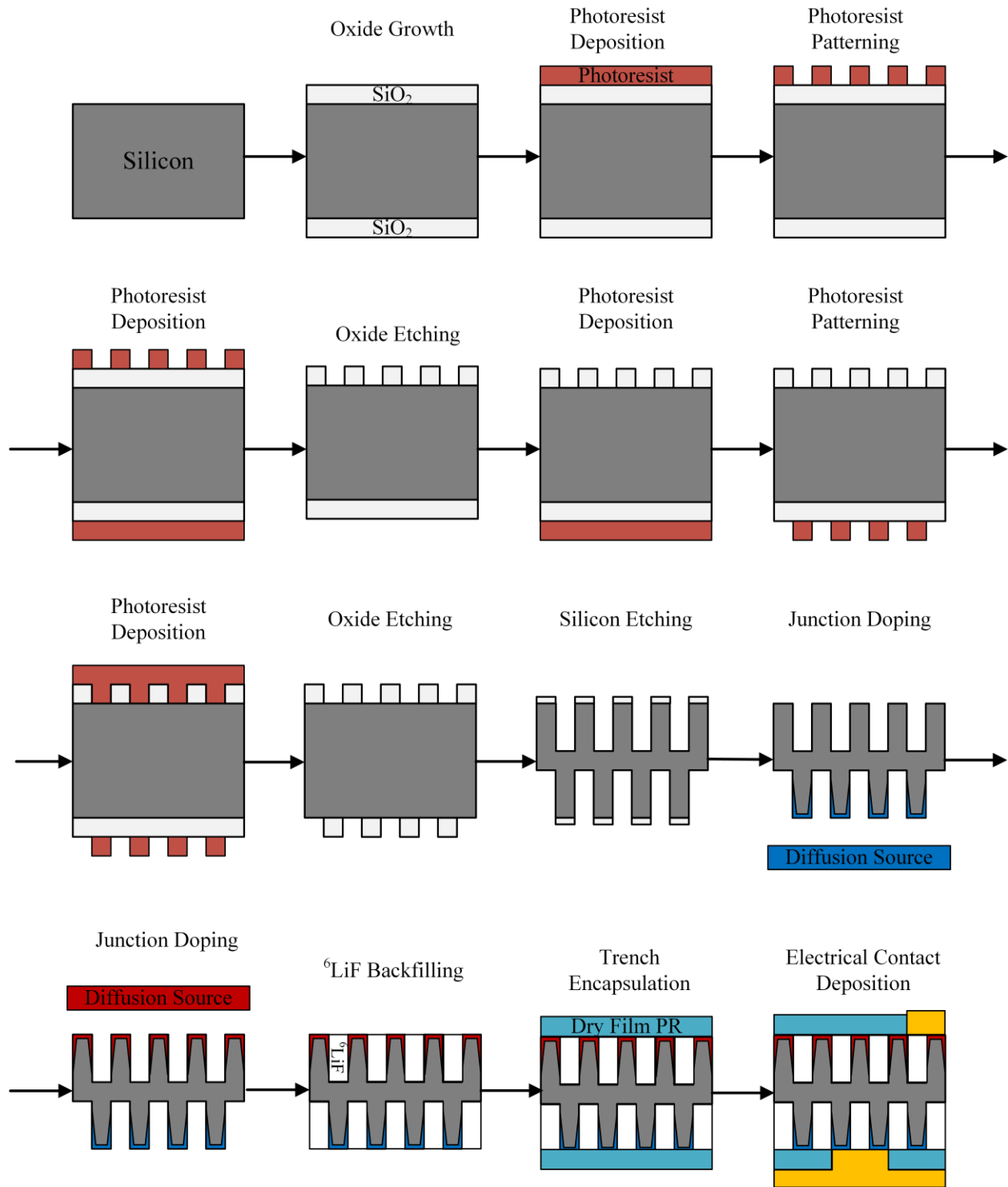
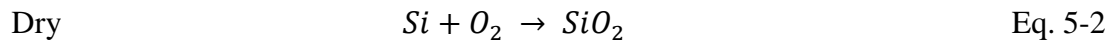
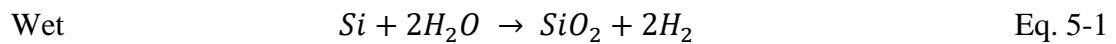


Fig. 5-1. Simplified process flow for pvn-DS-MSND fabrication. The process for pvp-DS-MSNDs is identical except only one diffusion (junction doping) process is required where both sets of trenches are doped simultaneously. The diffusion window patterning is omitted in the diagram for clarity but is required to insulate the diode from the diced edge. The process diagram for pvp-n-dot DS-MSNDs requires an additional photolithography process. Finally, after the electrical contacts are deposited the diodes are diced from the wafer and mounted into ceramic detector boards.

Oxide Growth

After the silicon wafers are sliced from the bulk silicon ingot and cleaned, a silicon dioxide (SiO_2) layer, up to 4- μm thick, is grown simultaneously on both sides of the wafer to serve as an etch and diffusion mask in subsequent processes. To grow the oxide, the wafers are loaded into a high-temperature furnace, and the temperature is ramped to approximately 1000°C while oxygen and hydrogen gas flow through the tube. The hydrogen and oxygen react and form high purity steam that reacts with the Si surface as described in Eq. 5-1 [134, 143]. This process grows a “wet” oxide on the silicon wafer surface.



The interaction occurs at the Si-SiO₂ interface, because the H₂O molecules diffuse faster than the Si atoms through the SiO₂ layer. As a result, impurities in the oxide from external contamination sources are limited as long as the wafers are thoroughly cleaned prior to the oxide growth. Additionally, a portion of the silicon surface is consumed during the process, the interface point of the final SiO₂ layer is about 0.44 t_{ox} below the original silicon surface with t_{ox} being the thickness of the final oxide. If an oxide is grown after the *pn*-junctions have been doped, special considerations are required to ensure the dopant re-distribution from the high temperatures and silicon consumption during the oxide growth process does not adversely affect the performance of the junction.

A “dry” oxide, which is denser and has less defects than the wet oxide, can be made by only flowing O₂ gas during the process, but dry oxide growth is significantly slower and therefore, more expensive than wet oxides of the same thickness. For comparison, using the Deal and Grove model shown in Eq. 5-3 [134, 143], a 3- μm thick wet oxide can be grown in about 34 hours at 1000 °C while the same thickness for a dry oxide requires 812 hours at 1000 °C. Note that a combination of oxide growth types can be used. For example, it is common to start with a dry oxide followed by a wet oxide and then finish with a dry oxide again.

$$t_{ox}^2 + At_{ox} = B(t - \tau) \quad \text{Eq. 5-3}$$

$$A = 2D \left(\frac{1}{k_s} + \frac{1}{h} \right)$$

$$B = \frac{2DHp_g}{N_1}$$

$$\tau = \frac{t_0^2 + At_0}{B}$$

t_{ox} – oxide thickness, *t* – time, *D* – diffusion coefficient, *k_s* – rate constant of chemical surface reaction of silicon oxidation, *h* – gas-phase mass-transfer coefficient in terms of concentration in the solid, *H* – Henry’s law constant, *p_g* – partial pressure in the gas next to oxide surface, *N₁* – number of molecules of oxygen per unit volume of SiO₂ (2.2x10²² for dry oxide, 4.4x10²² for wet oxide), *t₀* – initial thickness of oxide

The oxide on the DS-MSNDs ultimately has two purposes. The first purpose is to serve as a selective etch mask during the KOH etch where the KOH etches silicon in the <110>-direction orders of magnitude faster than the KOH etches the SiO₂ masking layer. The second purpose is to insulate the electrically active DS-MSND trench region from the mechanically diced edge of the die. The initial oxide thickness for DS-MSNDs, typically 3 μm to 4 μm, is governed by the required trench depth.

Photolithography and Oxide Etching

After the oxide layer is grown, the trenches and diffusion windows are patterned into the oxide layer with photolithography followed by an oxide etch. First, a thin layer of positive-tone photoresist is spun onto the surface of the silicon wafer. Then, after a short soft-bake, the wafer is loaded into a photo-aligner, and the straight trenches printed on an UV-opaque photomask are aligned parallel to the (111)-plane by aligning the wafer’s primary flat to the flat alignment marks on the photomask. The wafer is then either pressed against the photomask (contact mode) or raised until it is nearly touching the bottom of the photomask (proximity mode), and the shutter on the photo-aligner is opened to expose the photoresist to UV light that passes through the transparent portions of the photomask (see Fig. 5-2). For positive-tone photoresist, the UV light activates the photosensitizer and caused the photoresist to become soluble in developer. Note that the same process can be performed with negative-tone photoresist if an inverse photomask is used. When

negative photoresist is exposed to UV-light, the photosensitizer cross-links the polymer and reduces the solubility of the exposed regions.

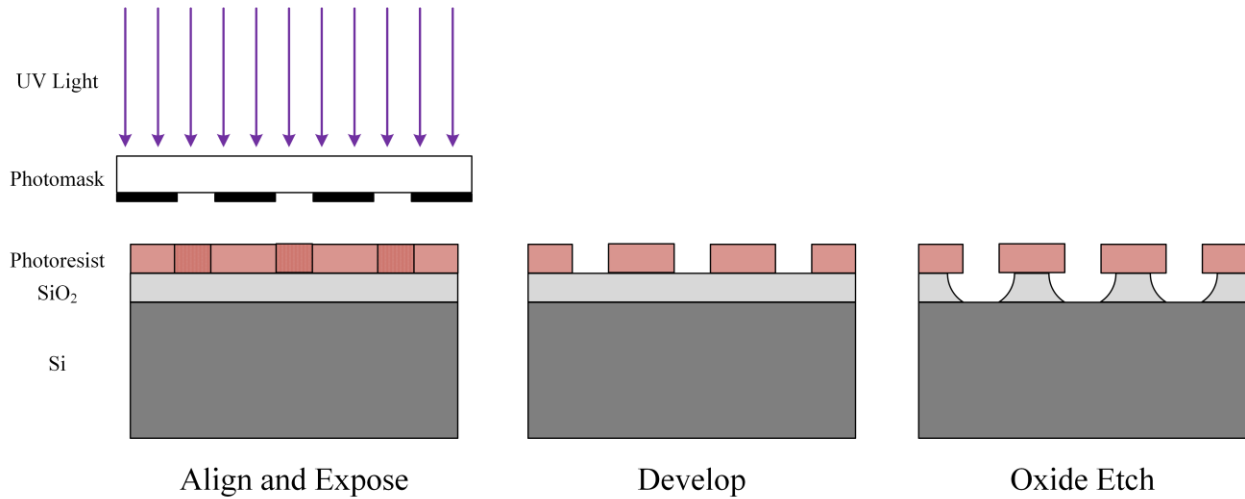
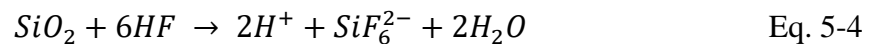


Fig. 5-2. Basic diagram showing oxide patterning process with photolithography. The pattern on the mask is transferred to the oxide layer with positive-tone photoresist in this example.

After the photoresist is exposed, the pattern is developed in photoresist developer to transfer the mask pattern into the photoresist layer on the wafer. Following development, the wafers are baked to remove any residual solvent in the photoresist and moisture on the backside surface of the wafer. A thick layer of positive photoresist is then spun on the back-side of the wafer to protect the back-side oxide from the subsequent chemical etch. The thickness of the photoresist layer can be controlled by adjusting the spin speed of the photoresist spinner and selecting alternative photoresists with different viscosities. Once the backside layer has been deposited, the wafers are hard baked to fully cure the photoresist to the wafer. This final bake promotes adhesion of the photoresist layer to the substrate. Finally, the wafers are placed into a buffered oxide etch to transfer the pattern from the photoresist to the oxide layer. The oxide etch utilizes hydrofluoric acid (HF) to isotropically etch the exposed SiO₂ through the chemical reaction described in Eq. 5-4 [144].



Photoresist has a negligible etch rate in the HF-solution. However, care must be taken in the photomask design process to account for photoresist undercut caused by the isotropic SiO₂ etch. If the features are too close to each other, or the photoresist does not adhere well to the substrate, the oxide etch can completely undercut the photoresist layer effectively reducing the

thickness of the patterned oxide. If the oxide becomes too thin, it will not be an adequate KOH etch mask or dopant diffusion mask.

After the oxide etch, the photoresist is removed with photoresist stripper. Then, the wafers are rinsed and dried, and the wafers are ready for the next process. Four photolithography processes are required to fabricate the *pvn*-type and *pvp*-type DS-MSNDs: front-side trenches, back-side trenches, front-side diffusion window, and back-side diffusion window. One additional photolithography process is required for the *n*-dot or *n*-ring DS-MSND pattern to make the diffusion window for the small *n*-type region at the edge of the diode. An example of an oxide layer patterned with straight trenches and a diffusion window is shown in Fig. 5-3.

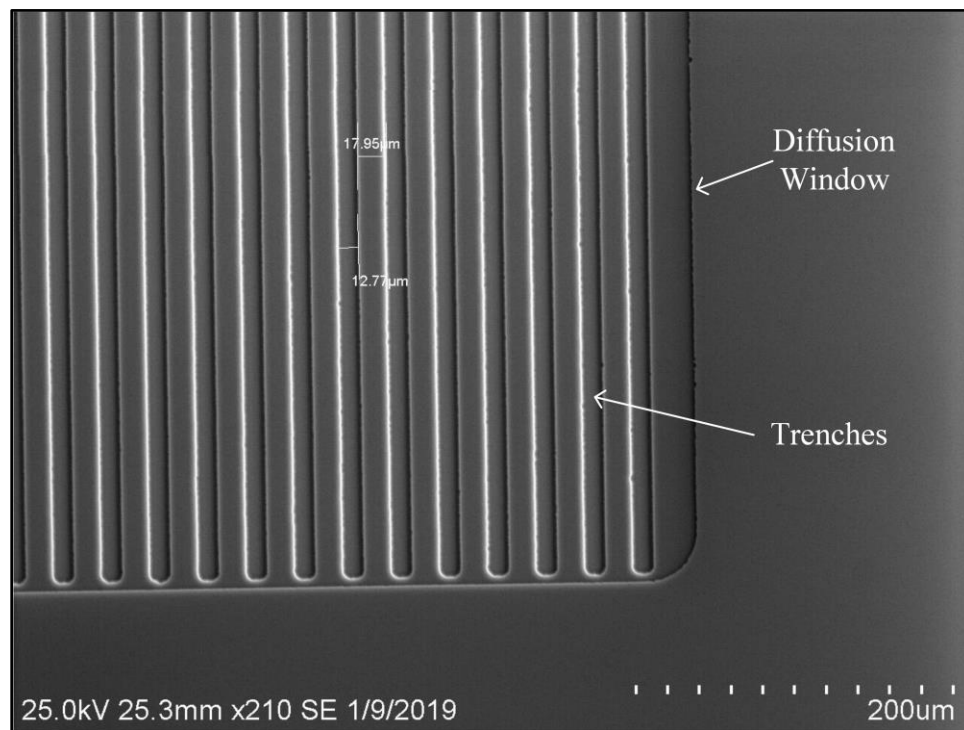
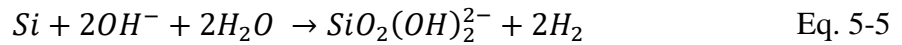


Fig. 5-3. SEM image of the patterned oxide layer on a corner of a DS-MSND diode before KOH wet etching. The image shows the diffusion window surrounding the trenches that have pre-etch width of approximately 13 μm and a pitch of 30 μm .

KOH Wet Etching

After the trench and diffusion window patterns have been etched into the oxide layer on the DS-MSND wafers, the wafers are loaded into a heated KOH bath for the anisotropic wet etching process wherein the deep, high-aspect ratio, straight trenches are etched into the Si substrate, see Fig. 5-4. The Si chemical etching process in KOH is described in Eq. 5-5 [145]. As described by Seidel [145], the KOH molecule disassociates in water to form K^+ and OH^- ions.

Then, two hydroxide ions near the silicon surface bond with dangling Si bonds where two electrons are injected into the conduction band but held near the surface by a potential well. Next, the Si-Si back bonds attaching the silicon to neighboring lattice atoms are broken by thermal excitation of the bonding electrons. The silicon-hydroxide atom can then react with two additional OH⁻ ions to form Si(OH)₄ that will diffuse from the surface of the silicon substrate. The Si(OH)₄ molecule breaks down in the bulk electrolyte, and the process continues at the Si surface [145]. In this process the rate limiting step is the reduction of H₂O at the silicon surface. The reaction rate can be described by Eq. 5-6 where k_0 is an empirical constant, H₂O and KOH are the water and KOH concentration, respectively, E_a is activation energy, k is Boltzmann's constant, and T is temperature [145]. The anisotropic nature of the etch is believed to stem from the number of available bonds and differences in activation energies for the different crystal planes, {110}:{100}:{111} [145]. Anisotropy etch rate ratios ranging from 100:1 to 600:1 for <110>:<111> directions have been reported [134, 145]. The straight-trench DS-MSND design takes advantage of this high anisotropy by aligning the trench side walls to the (111)-plane and etching in the <110>-direction (see Fig. 5-5.) It should be noted that the above explanation of the KOH etching process is debatable. Elwenspoek offers an explanation on the mechanism of silicon anisotropic etching based on the availability of nucleation sites and the step-free energy of the silicon surface [146]. Elwenspoek's model is based on crystal growth principles rather than chemistry principles. In his model, anisotropy is based on differences in the step-free energy of the various silicon crystal planes.



$$R = k_0 [H_2O]^4 [KOH]^{\frac{1}{4}} e^{-E_a/kT} \quad \text{Eq. 5-6}$$

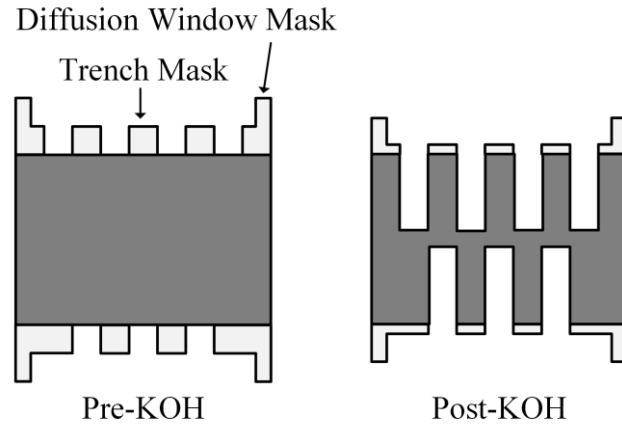


Fig. 5-4. Diagram of silicon wafer before and after anisotropic KOH wet-etch used to form deep, high-aspect ratio straight trenches in the DS-MSND diode. The diagram depicts both the trench and diffusion window mask that are patterned in the SiO₂ layer via photolithography.

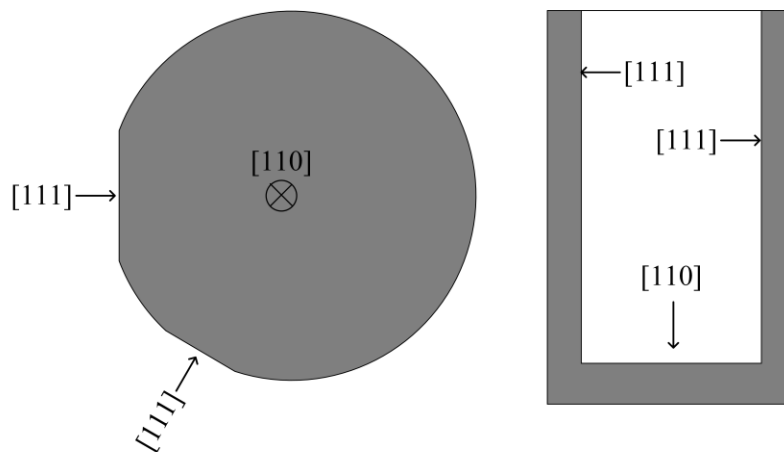


Fig. 5-5. (Left) Wafer orientation and (Right) trench alignment used form the high-aspect ratio straight trenches for DS-MSND. The anisotropy of the KOH etch allows for deep trenches to etched vertically in the [110]-direction with minimal lateral etch in the [111]-direction.

Many aqueous hydroxide solutions can be used to anisotropically etch silicon; however KOH was used rather than the other common anisotropic silicon wet etchants like TMAH and ethylene-diamine in pyrocatechol (EDP) solutions, because KOH has the highest <110>-etch rate, highest <110>:<111> selectivity, and high 110:SiO₂ selectivity [147, 148]. The high <110>:<111> selectivity is critical to form the high-aspect ratio trenches. If the selectivity was significantly reduced, the detection efficiency would suffer, because the deep trenches, which are needed for high thermal-neutron absorption efficiency, would be too wide to have high reaction product

escape probability. Also, the low etch rate of SiO₂ in KOH is important, because it allows for SiO₂ to serve as an etch mask in the KOH bath with minimal required thickness. The etch rate of SiO₂ is orders of magnitude lower than the etch rate of [110]-orientated silicon. Thus, only a 1-2 μm mask thickness of SiO₂ is required to etch trenches 600-μm deep. The high [110]-etch rate shortens the required etch time, which increases throughput and lowers costs in mass production. For example, the etch rates for in the <110>-direction, <111>-direction, and SiO₂ for 20 %wt KOH at 75 °C are 99.7 μm/hr, 1.029 μm/hr, and 179 nm/hr, respectively [149].

The number of microfeature patterns etchable with KOH is limited. To get the vertical sidewall, the sides of the feature must align with the (111)-planes. Straight trenches, rhombohedral holes, and chevron patterns can be fabricated, however; if circular holes, circular pillars, or more complex patterns like sinusoidal trenches are required, other methods like dry etching must be implemented. Early iterations of MSND fabrication used dry etching where circular holes were etched with an ICP-RIE process into GaAs diodes [15]. Sinusoidal trenches in silicon were also fabricated with RIE [16]. Because the RIE process is not crystal-plane-orientation dependent, practically any microfeature pattern can be etched into the semiconductor substrate [134]. Furthermore, dry etching can be used on substrates other than Si such as GaAs and SiC. However, RIE is slow compared to wet etching, has challenges with etching deep features, often creates damaged and rough microfeature sidewalls, and the wafer throughput is limited by the size of the reaction chamber which is costly to upgrade. In comparison, KOH wet etching can etch ultra-deep microfeatures with (110)-orientated Si, results in smooth sidewalls, and is easily and cheaply scaled for mass production with the wafer throughput ultimately limited by the size of the heated tank. Fortunately, the straight trench DS-MSND pattern is a high neutron detection efficiency design and can be achieved with KOH etching which helps reduce manufacturing costs that will in-turn reduce the cost to consumers, a critical factor for viable ³He replacement technologies.

One concern with KOH etching is the K⁺ contaminant left on the substrate after the KOH etch, because K⁺ is a fast diffuser and electrically active in silicon, and will negatively affect the electrical characteristics of the DS-MSND diode. Proper cleaning processes must be performed following the KOH etch step to ensure complete removal of K⁺ ions prior to dopant diffusion. Fig. 5-6 is a SEM image showing an example of deep, high-aspect ratio, offset trenches on a DS-MSND that can be achieved with KOH etching. The trench depth and width are 625 μm and 21 μm, respectively, with a unit cell width of 30 μm.

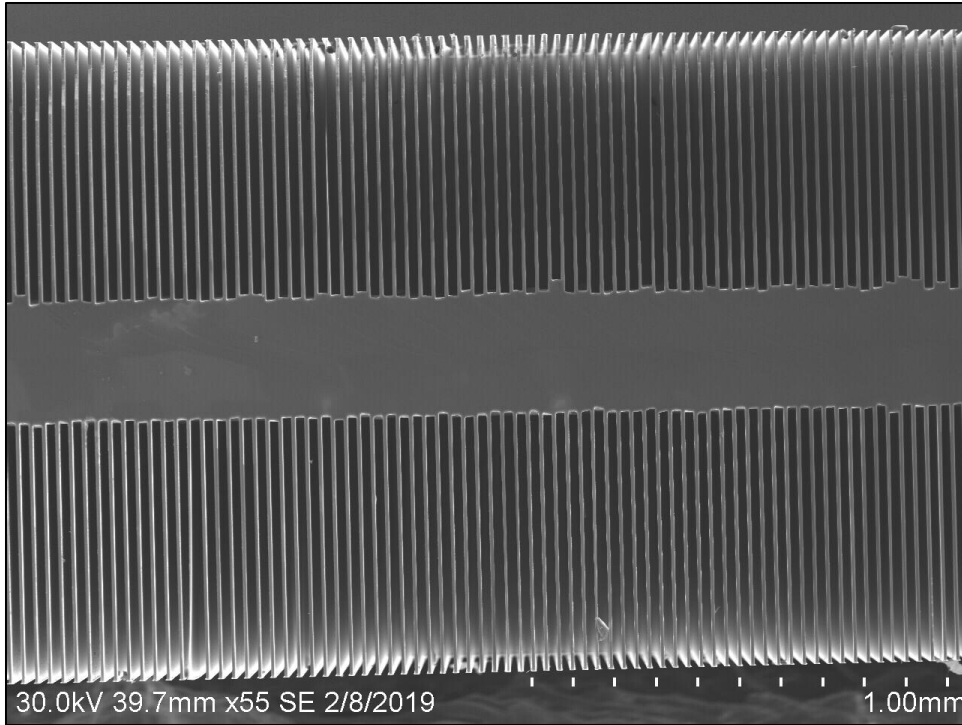


Fig. 5-6. SEM of cross section of an etched, offset, straight-trench DS-MSND on a 1.5-mm thick silicon wafer. The trenches are approximately 625 ± 25 - μm deep and 21 - μm wide. The unit cell width is 30 μm .

Junction Doping and Contact Metallization

After KOH etching, the next step is to clean the silicon wafers in preparation for dopant diffusion to form the *pn*-junctions on the DS-MSNDs. The wafers must be thoroughly cleaned to remove all contaminants prior to the high-temperature diffusion process to prevent any unwanted dopant species from diffusing into the silicon and adversely affecting the junction properties. A list of the cleaning baths is provided in Table 5-1.

Immediately following the KOH etch, the wafers are transferred to a HCl:H₂O₂:H₂O bath commonly called SC-2, typically the second step in the RCA cleaning process [150, 151]. In this bath the alkali ion contaminants, namely K⁺, react with the HCl forming KCl thereby removing the unwanted potassium ions from the surface. Next, the residual oxide layer on the tops of the fins within the diffusion window is removed in a buffered hydrofluoric acid (BHF) bath. The wafers are then loaded into a hot “Piranha” solution (H₂SO₄:H₂O₂:H₂O) to remove organic residuals on the surface of the wafer. A short BHF etch is then used to remove the thin oxide that may have developed in the Piranha bath. Next, the wafers follow the standard RCA cleaning recipe

[151]. The wafers are loaded into a heated SC-1 bath ($\text{NH}_4\text{OH}:\text{H}_2\text{O}_2:\text{H}_2\text{O}$) which will remove any additional organic contamination that may have survived the Piranha clean and remove Group IB and IIB metal contaminants [150]. A short BHF dip then removes the thin oxide grown in the SC-1 bath. Finally, the wafers are placed in a fresh SC-2 bath ($\text{HCl}:\text{H}_2\text{O}_2:\text{H}_2\text{O}$) to remove the alkali contaminants deposited on the silicon during the SC-1 clean [150, 151]. Finally, the wafers are rinsed with deionized (DI) water and loaded into a spin-rinse-dryer for a final rinse and dry before being loaded into the diffusion furnace. High purity chemicals and good laboratory cleanliness practices are necessary to ensure no contaminants are introduced during the cleaning process or after the cleaning process before the wafers are loaded into the diffusion furnace.

Table 5-1. Chemical cleaning baths for DS-MSND wafers after KOH etch and before diffusion processes.

Cleaning Batch	Chemicals
SC-1	$\text{HCl}:\text{H}_2\text{O}_2:\text{H}_2\text{O}$
Piranha	$\text{H}_2\text{SO}_4:\text{H}_2\text{O}_2:\text{H}_2\text{O}$
SC-2	$\text{NH}_4\text{OH}:\text{H}_2\text{O}_2:\text{H}_2\text{O}$
BHF 6:1	$\text{H}_2\text{O}:\text{HF}$

Dopant Deposition

The next step in the DS-MSND fabrication process is to diffuse impurity atoms into the silicon surface to form the desired junction doping profile. The impurity dopants act as either donors (phosphorus) or acceptors (boron). Several methods are available to introduce the dopant atoms to the silicon substrate including solid source diffusion, liquid source diffusion, ion implantation, and spin-on-dopant.

In solid source diffusion, the DS-MSND wafer is loaded adjacent to a source wafer, and a dummy wafer can be inserted on the opposite side of the DS-MSND wafer if dopant is only wanted on one side of the diodes (see Fig. 5-7). For *p*-type deposition, hexagonal boron nitride source wafers are used. The furnace is ramped to high temperatures (850-1000°C) and forming-gas is introduced in the process tube causing B_2O_3 glass to grow on the source wafer which then vaporizes and uniformly coats the surfaces of the DS-MSND wafer [152]. For *n*-type dopant, SiP_2O_7 source wafers are used, and similarly, volatilized P_2O_5 glass from the surface of the source wafer deposits on the DS-MSND wafers under ambient N_2 at high temperatures [152]. The *p*-type dopant deposition process is considered a pre-deposition process, because the dopant is introduced

only while the forming gas is flowing. This type of diffusion is considered constant total dopant diffusion [134, 143]. The *n*-type diffusion would be considered a constant surface concentration diffusion, because the dopant is continually introduced throughout the entire diffusion drive-in process [134, 143]. Solid source diffusion is relatively inexpensive and can be used to form conformal doping profiles or semi-conformal doping profiles.

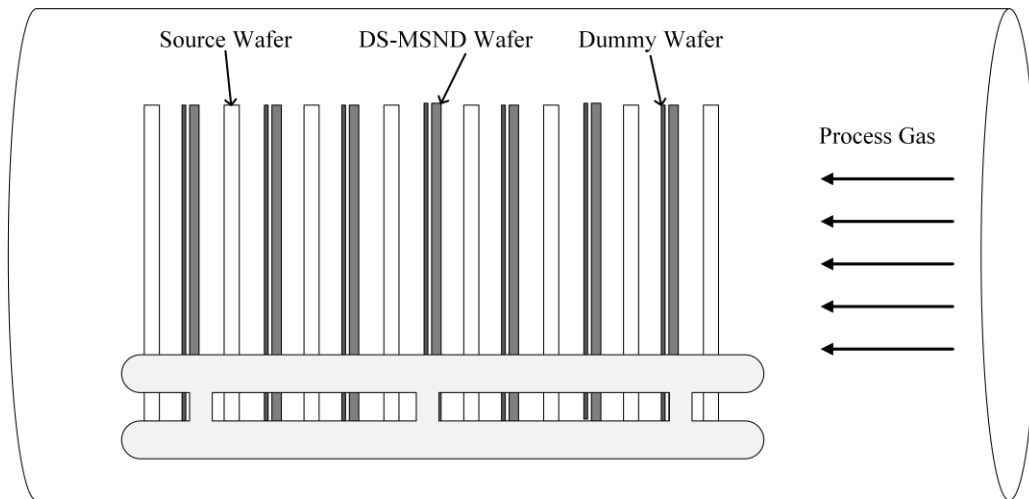


Fig. 5-7. Example of solid-source diffusion. The DS-MSND wafers are loaded next to source wafers with or without blocking dummy wafers depending on the desired dopant profile. Dopants diffuse from the source wafers and deposit on the adjacent silicon wafers. High temperatures then drive in and activate dopant atoms in the wafer.

In liquid-source diffusion, the dopant is carried by the process gas which passes through a bubbler containing the dopant species (i.e. BBr_3 for *p*-type or POCl_4 for *n*-type) and is deposited on exposed surfaces of the target wafer. Again, blocking wafers can be used to shield one side of the wafer if necessary. Also, if the design process allows, an SiO_2 layer can be used to mask regions of the wafer that can then be opened up later for different type doping. Like solid-source diffusion, liquid source diffusion is relatively inexpensive. However, special precautions are required to guard against the release of the toxic dopant sources.

Ion implantation is used when precise control of the dopant concentration and dopant depth is required. In ion implantation, the dopant species is ionized and accelerated into the target DS-MSND wafer. Precise control of the number of dopant ions implanted is possible by adjusting the process time, and the dopant depth is controlled by the adjusting the accelerating voltage. Typically, a small offset is required to reduce implant channeling, but the offset can also be

controlled to dope high-aspect ratio features as shown in Fig. 5-8. One additional benefit of ion implantation is that photoresist only a few microns thick can be used as an implant mask. Also, the dopants can be activated with rapid thermal annealing (RTA) to form shallow, high-concentration *pn*-junctions. Compared to the other deposition methods, ion implantation is significantly more expensive. High implant doses are required to conformally dope high aspect ratio microfeatures because of the small implant angle where many incident ions scatter instead of entering the substrate. Additionally, the majority of the implanted ions do not become electrically active. The high implant doses cause significant damage to the silicon surface and complicates removal of the photoresist masking layer.

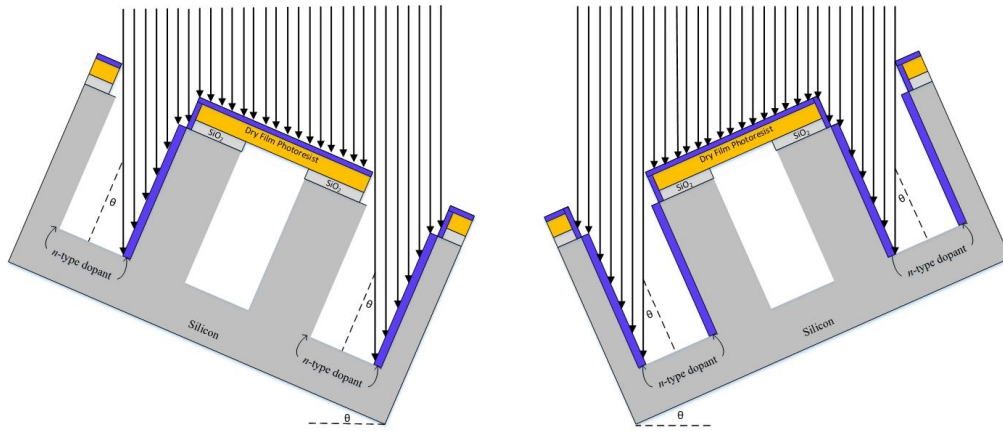


Fig. 5-8. Example of ion implantation geometry required to implant dopants into the sidewall of and MSND or DS-MSND. The wafer offset angle, θ , for high aspect ratio trenches is ranges from 1-3°.

Spin-on-dopant is another technique to deposit the dopant atoms onto the surface of the wafer. In spin-on-dopant, the dopant species is suspended in a solvent, and the solution is spun onto the wafer much in the same way liquid photoresist is spun onto wafers in photolithography. The solvent is then baked out, and the dopant remains on the surface in the form of an oxide. Conformally doping 3D structures with spin-on-dopant has been challenging, and precise humidity and temperature control are required to ensure the integrity of the dopant layer.

Solid-source diffusion has been utilized for most of the DS-MSND fabrication because it is inexpensive, available in-house at the S.M.A.R.T. Laboratory facility, and is relatively safe compared to liquid-source diffusion. Solid-source diffusion can be used to form fully conformal and partially conformal dopant profiles on the MSND trenches. Recall that the Silvaco TCAD simulations show a partial-conformal dopant profile is ideal low bias operation. Some MSND and

DS-MSND doping studies were performed with ion implantation and spin-on-dopant and are discussed in Section 5.3.

Dopant Diffusion

Once the dopant has been deposited on the DS-MSND wafer by one of the aforementioned methods, the wafers undergo a high-temperature “drive-in” process where the dopant is diffused from the surface of the wafer into the silicon and becomes electrically active. The dopant diffusion is driven by the concentration gradient between the dopant at the silicon surface and the bulk silicon, and dopant atoms become electrically active when they replace silicon atoms in the crystal lattice. Boron and phosphorus atoms primarily diffuse through the vacancy method wherein the dopant atoms replace Si vacancy sites left in the silicon crystal lattice after Si lattice atoms gain enough energy from the high temperature to vacate the normal equilibrium lattice site [143]. The dopant diffusion process is described by Fick’s Law shown in Eq. 5-7 where D is the dopant diffusion coefficient and $C(x,t)$ is the dopant concentration at depth x and time t [134, 143].

$$\frac{\partial C(x,t)}{\partial t} = D \frac{\partial^2 C(x,t)}{\partial x^2} \quad \text{Eq. 5-7}$$

Analytical solutions for Eq. 5-7 are found for the special cases of constant surface concentrations and constant total dopant assumptions and are shown in Eq. 5-8 and Eq. 5-9, respectively, where C_s is the constant surface concentration and S is the total dopant per unit area [134, 143]. The diffusion coefficients for boron and phosphorus in Si and SiO₂ are shown in Table 5-2. An example of the dopant distributions for constant surface concentration and constant total dopant is plotted in Fig. 5-9. The diffusion coefficients are much lower in SiO₂ which allows the oxide layer to serve as an effective diffusion barrier to protect the regions where doping is not desired, i.e. at the edges of the diode where the wafer will be diced.

$$C(x,t) = C_s \operatorname{erfc} \left[\frac{x}{2\sqrt{Dt}} \right] \quad \text{Eq. 5-8}$$

$$C(x,t) = \frac{S}{\sqrt{\pi Dt}} \exp \left[-\frac{x^2}{4Dt} \right] \quad \text{Eq. 5-9}$$

Table 5-2. Diffusion coefficients, D , for B and P in Si and SiO₂ at 1000°C [134]

Dopant	D (Si)	D (SiO ₂)
Boron	7.42×10^{-16} cm ² /s	3.18×10^{-18} cm ² /s
Phosphorus	1.26×10^{-14} cm ² /s	2.11×10^{-17} cm ² /s

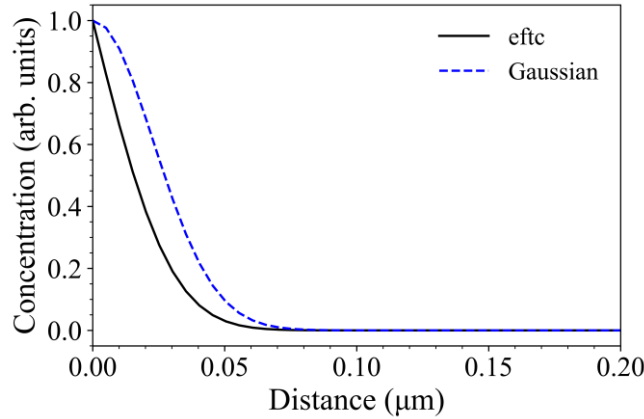


Fig. 5-9. Normalized dopant distributions for constant surface concentration (Eq. 5-8) and constant total dopant (Eq. 5-9) for boron in Si with a one-hour drive-in time at 1000°C.

An outline of p -type and n -type solid-source diffusion processes is shown in Fig. 5-10. For p -type diffusion, clean wafers with their p -type diffusion windows opened (masking oxide removed) are loaded into the diffusion furnace at about 750°C. Then, the temperature is increased and a small amount of H₂ gas is introduced to the process to enhance boron oxide transfer from the source wafer to the silicon wafer. Next, the H₂ gas flow is shut off and the temperature is raised and then held steady to drive-in the boron dopant on the surface of the wafer into the silicon. The drive-in step is performed at approximately 1000°C for 1-2 hours. The time and temperature control the junction depth with longer times and higher temperatures resulting in deeper junctions. After the drive in, the temperature is slowly ramped down, and then the wafers are removed. For pvp -type DS-MSNDs the diffusion process is completed, and the wafers are ready for metallization.

For pvn -DS-MSNDs and pvp - n -dot or pvp - n -ring-DS-MSNDs, an n -type diffusion process is required. After the n -type diffusion windows are opened, the wafers are loaded into the n -type diffusion furnace. The n -type and p -type solid-source diffusion processes are similar except there is no source step for n -type diffusion. Instead, the phosphorus-oxide is continually deposited on the wafer during the drive-in step. Any previously-doped p -type areas that are exposed during the n -type diffusion process will be compensated with n -type dopant. If the n -type dose is low, the p -

type doped regions will remain p -type (although slightly less); however, if the n -type dose is high or comparable to the p -type dose, then the exposed region tends return to neutral or n -type. For pvn -DS-MSNDs, the p -type side is shielded by a dummy wafer during the n -type diffusion to reduce any areas of co-doping. Additionally, protective oxides can be grown on the previously doped regions to eliminate co-doping. On the pvp - n -dot-DS-MSNDs, one p -type side can be shielded, but the side with the n -dot diffusion window is exposed to the n -type source wafers during the n -type diffusion. On this design either the n -type dose must remain low as to not completely compensate the p -type regions on that side, or an additional masking oxide must be deposited on the p -type regions before the n -type diffusion process. Utilizing a doping profile with n -type and p -type regions increases the manufacturing costs, because two diffusion steps are required. However, it allows for an external bias to be applied between the n -type and p -type contacts which increases the internal electric field and ideally improves charge collection efficiency.

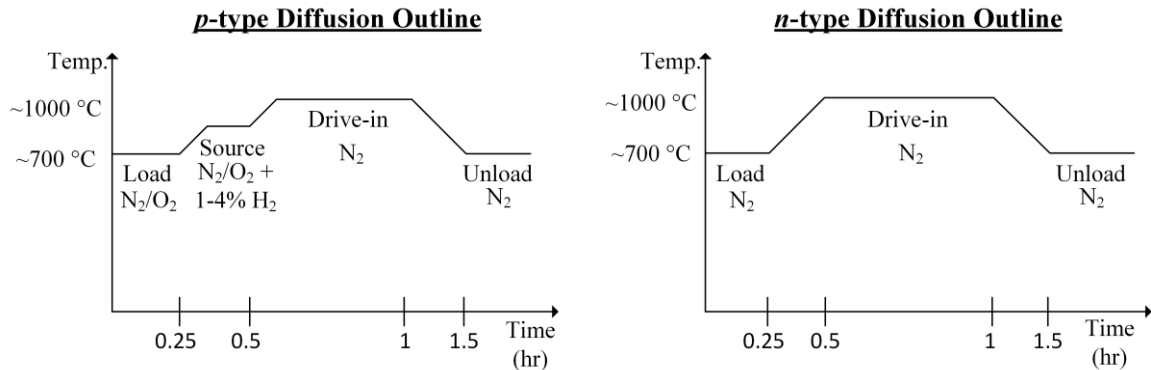


Fig. 5-10. Example of diffusion process timelines for p -type and n -type solid-source diffusion. The p -type diffusion utilizes H_2 injection to promote B_2O_3 growth and HBO_2 transfer from the source wafer to silicon wafer. The diagrams are adapted from [152].

Contact Metallization

After the wafers have been doped, the diffusion oxides are removed with a BHF dip. The wafers are then loaded into an electron-beam (e-beam) evaporator where Ti/Au ohmic contacts are deposited on the surface of the wafer. An energetic electron beam is directed into at a crucible of metal. The metal melts in the crucible and evaporates, thereby coating all surfaces within line-of-sight of the crucible. The titanium layer on the contact is about 250-Å thick and is used to promote adhesion between the silicon and gold and prevent gold from diffusing into the silicon where it is a deep acceptor dopant. The outer gold layer (~1000 Å) helps to make low electrical resistance

contact to the silver epoxy and wire bond in the detector board package and provides a corrosion-resistant electrical contact. If necessary, areas of the wafers can be masked with photoresist that is subsequently lifted off to selectively metalize the different areas of the wafer. The wafers are then flipped to metalize the backside contact if necessary. Shown in Fig. 5-11 are example electrical contacts deposited on a diode. Note that the contact metallization is optional, and some DS-MSNDs have been fabricated without metal contacts.

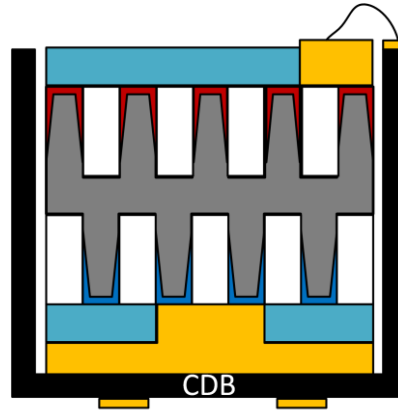


Fig. 5-11. Example of DS-MSND mounted in a ceramic detector board (CDB) with metalized contacts.

5.1.2. ⁶LiF Backfilling

The key characteristic used to identify the quality of the ⁶LiF backfill is the ⁶LiF powder packing fraction (PF) defined in Eq. 5-10. For each DS-MSND geometry, there is an ideal packing fraction that maximizes the product of the neutron absorption efficiency and reaction product escape probability to achieve the highest possible neutron detection efficiency. The ideal ⁶LiF PF for commonly produced DS-MSNDs with 25 to 30- μ m wide unit cells and trench to unit cell width ratios from 0.5-0.67 ranges from about 50% to 80% depending on the trench depth.

$$\text{Packing Fraction (PF)} = \frac{\text{Apparent Density of } ^6\text{LiF in Feature}}{\text{Crystalline Density of } ^6\text{LiF}} \quad \text{Eq. 5-10}$$

Previous work mainly utilized qualitative analysis of SEM images of backfilled MSNDs and DS-MSNDs to judge the quality of the ⁶LiF backfill. If there were no large voids of material in the trench and the trench appeared to be “full” from top to bottom, the backfill was considered to be good [20, 21, 33]. The authors noted that the powder backfill was not 100% and sought some methods to melt ⁶LiF into MSND perforations, but this method proved unsuccessful due to high process temperatures stressing the silicon features and ⁶LiF and other impurities diffusing into the adjacent silicon ruining the *pn*-junction properties [20, 21]. Recently, the ⁶LiF powder PF has been

measured and reported quantitatively [29], and the collected data has provided a more reliable platform to compare ${}^6\text{LiF}$ powder backfilling methods presented herein.

${}^6\text{LiF}$ Backfill Packing Fraction Measurement Methodology

Previously, it was assumed that the backfill density for modern MSNDs and DS-MSNDs was nearly 90% of crystalline density ($\sim 2.55 \text{ g/cm}^3$), because only small voids were immediately apparent in cross-sectional SEM images as shown in Fig. 5-12. The 90% PF fraction assumption was implemented in MCNP simulations that indicated the intrinsic thermal-neutron detection efficiency of DS-MSND should be between 65% and 70%. However, advancements in detection efficiency had seemingly encountered a roadblock, as regardless of the doping chemical or device electrical characteristics, the maximum intrinsic thermal-neutron detection efficiency was limited to 50% to 55% [31-33]. The backfill density of the ${}^6\text{LiF}$ conversion material within the trenches was then more closely investigated as a possible cause for the apparent detection efficiency ceiling. The density of a randomly-selected DS-MSND backfilled with the centrifugal method of backfilling, described and also utilized in [21, 23-27, 30-33, 126], was measured three different ways: weight, neutron attenuation, and measured neutron detection efficiency compared to theoretical MCNP6 models.

In the weight method, the mass of an empty, etched wafer was measured before and after backfilling. A sacrificial diode was then cleaved, and a SEM was used to accurately measure the microfeature geometry, which was used to calculate the total trench volume of the wafer. The ${}^6\text{LiF}$ PF was then calculated by dividing the mass of ${}^6\text{LiF}$ filled into the trenches by the volume of all the trenches in the device, and the resulting density was only 0.77 g/cm^3 , or roughly 30% of ${}^6\text{LiF}$ crystalline density (Table 5-3).

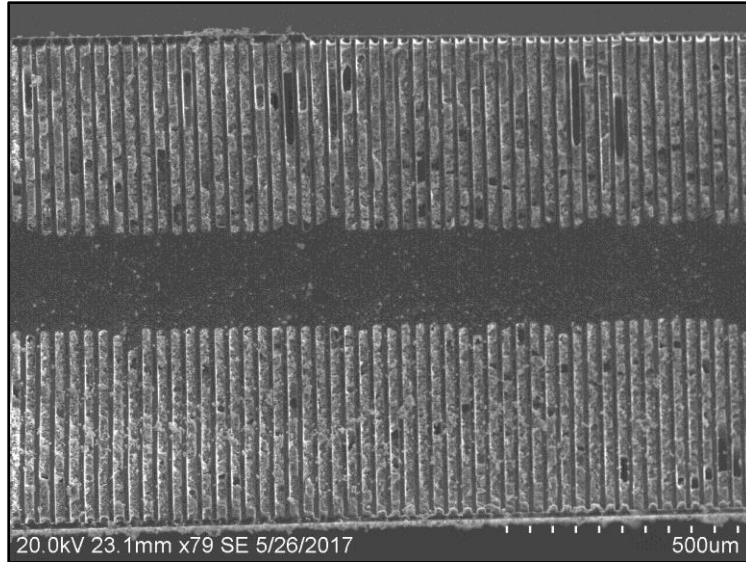


Fig. 5-12. Cross-sectional SEM image of a ${}^6\text{LiF}$ -backfilled DS-MSND showing only small void regions within the trenches. Later analysis of ${}^6\text{LiF}$ PF indicate the apparent density of ${}^6\text{LiF}$ within the trenches was significantly less than previously assumed.

Table 5-3. Results of first quantitative measurement of ${}^6\text{LiF}$ PF in a DS-MSND found by comparing the mass of the wafer before and after backfilling to the known volume of the trenches.

DS-MSND Parameter	Value
Mass of ${}^6\text{LiF}$ filled in trenches (g)	2.015
Number of DS-MSND Diodes per Wafer	52
Number of trenches per diode	666
Trench Width (μm)	20
Trench Length (μm)	10000
Trench Depth (μm)	400
Total Volume (cm^3)	2.632
${}^6\text{LiF}$ Density in Trenches (g/cm^3)	0.766
${}^6\text{LiF}$ Packing Fraction	30%

Next, for the neutron attenuation method, a reference detector was placed in a thermal-neutron beam, and the neutron count rate was recorded. Then, the DS-MSND was placed in the beam-line in front of the reference detector, and the new neutron count rate was recorded. The fraction of the attenuated to unattenuated neutron count rate yielded the total neutron attenuation of the DS-MSND to be roughly 62% (Table 5-4). The neutron attenuation was then compared to MCNP modeled attenuation rates for DS-MSNDs with the same geometry in a thermal neutron beam but with variable packing fractions. As shown in Fig. 5-13, this method of measurement indicated the actual ${}^6\text{LiF}$ PF to be about 35%.

Table 5-4. Results of DS-MSND neutron attenuation measurements performed with reference neutron detector (HeRep).

Detector Configuration	Net Counts	Neutron Attenuation
Bare HeRep	7,888	-
Tape + HeRep	7,875	0.16%
DS-MSND + Tape + HeRep	3,002	61.88%
Expected Neutron Attenuation	-	~91%

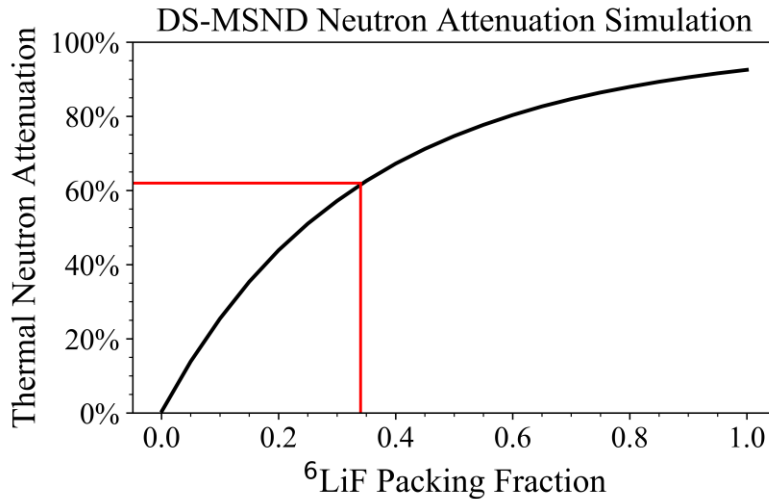


Fig. 5-13. Results of MCNP simulation for thermal-neutron attenuation by a ⁶LiF-backfilled DS-MSND with trench geometry described in Table 5-3 and ⁶LiF PF ranging from 0% to 100%.

In the final method, the measured intrinsic thermal-neutron detection efficiency was compared to MCNP simulation results of intrinsic thermal-neutron detection efficiencies for DS-MSNDs with ⁶LiF PF ranging from 0% to 100% as seen in Fig. 5-14. DS-MSNDs with packing fractions between 30% and 35% had theoretical intrinsic thermal-neutron detection efficiencies between 50 and 55%, which matched the range of intrinsic thermal-neutron detection efficiencies measured with DS-MSNDs at the time. The three methods of measurement conclusively proved that the actual ⁶LiF packing fraction in the DS-MSNDs (and MSNDs) was not the assumed 90% and more likely between 30% and 35%.

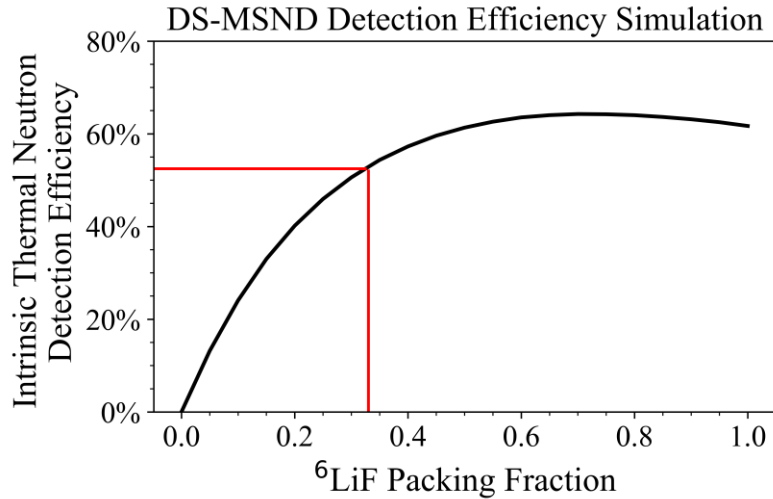
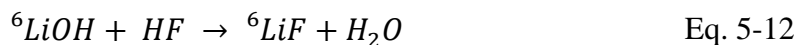
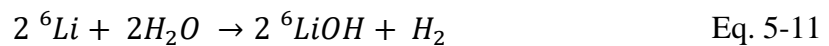


Fig. 5-14. MCNP simulation results for intrinsic thermal-neutron detection efficiency for a ⁶LiF-backfilled DS-MSND with trench geometry described in Table 5-3 and ⁶LiF PF ranging from 0% to 100%.

⁶LiF Powder Production

High purity ⁶LiF powder for DS-MSND trench backfilling is produced by reacting ⁶Li-enriched (95%) metal with distilled water to form aqueous lithium hydroxide (⁶LiOH). After all the ⁶Li-metal has reacted, hydrofluoric acid (HF) is added to the solution and reacts with ⁶LiOH in the manner described in Eq. 5-12 forming ⁶LiF precipitate. HF is continually added until the pH becomes neutral indicating that all ⁶LiOH has reacted. Next, the ⁶LiF powder is compacted to the bottom of the container by placing the solution in a centrifuge, and then, the remaining water in the solution is heated and evaporated leaving behind enriched ⁶LiF powder. An example of the ⁶LiF powder harvested from this production method is shown in Fig. 5-15. A wide range in particle sizes exist with the upper limits in this example measuring nearly 5.5 μm, with larger particle sizes produced from the same method reported in prior work [21].



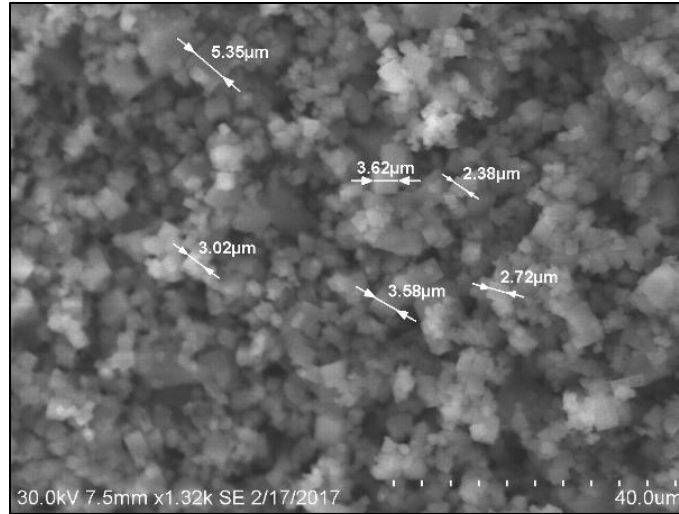


Fig. 5-15. SEM image of titrated ⁶LiF powder. Particle sizes up to 20-μm have been obtained through the LiOH + HF reaction process [21].

Powder Packing Considerations

German [153] identified several major factors affecting particle packing properties including powder size distribution, particle shape and surface texture, agglomeration tendency, surface active agents, internal powder porosity, container wall effects, particle segregation, and bridging and vibration effects. A few of these factors can be easily adjusted in the ⁶LiF powder. For example, a mechanical ball mill was used to grind ⁶LiF harvested from the HF titration process into smaller, less cuboid particles (Fig. 5-16). The “nano” ⁶LiF powder can then theoretically be used to form a bimodal mixture of “coarse” and “nano” LiF for trench backfilling, where theoretically, the nano-LiF fills in void regions between adjacent coarse particles to improve the powder packing fraction [153]. The surface active agent is another easily variable factor in which different wetting solutions can be used to coat or suspend ⁶LiF powder prior to backfilling with the goal of reducing interparticle friction. Several of the other factors are less variable. For example, the container wall effect is dependent on the size of the container, and in the DS-MSND, the trench (“container”) is designed to optimize neutron detection efficiency. Another example is powder porosity, which is determined during the titration process. As with all engineering, each process design decision comes with trade-offs. For example, implementing nano ⁶LiF powder to form a bimodal mixture, which can improve the powder packing fraction, will also increase the propensity of particle agglomeration and premature microcavity bridging due to the increased interparticle friction caused by utilizing smaller particles with larger surface-to-volume ratios. The

next section describes the experiments performed to optimize the backfill packing fraction for high-aspect ratio, ultra-deep DS-MSND trenches while maintaining the integrity of the diode.



Fig. 5-16. (Left) Ball mill used to reduce the particle size of ${}^6\text{LiF}$ powder harvested titration of LiOH . (Right) SEM image of ball-milled LiF nano-powder. The average particle size is significantly reduced, and the shape is less cuboid than the original powder.

${}^6\text{LiF}$ Powder Backfilling Methods

Various methods to backfill MSND and DS-MSND microfeatures have been studied since their invention [15]. Section 4.3.2 of this work covered MCNP simulations indicating ${}^6\text{LiF}$ packing fractions between 50% and 80% were ideal to maximize neutron detection efficiency. Additionally, if DS-MSNDs are destined to be mass produced, one must consider the manufacturing aspects like wafer throughput, yield, and repeatability. McNeil and Bellinger [20, 21] performed in-depth studies on neutron conversion material backfill methods for single-sided MSNDs including electron-beam evaporation, dry powder hand packing, ${}^6\text{LiF}$ melt and casting, and low pressure condensation. Electron beam evaporation and dry powder hand packing showed some success for shallow microfeatures but prematurely capped the cavity for deeper features leaving large void spaces [20, 21]. Melting ${}^6\text{LiF}$ and allowing it to flow into the microfeatures and solidify resulted in high density backfills, but the high temperature required to melt ${}^6\text{LiF}$ (845 °C) caused unwanted dopant diffusion in the adjacent silicon and ruined the *pn*-junction of the diode [20, 21]. Similarly, high temperatures required for low pressure condensation method caused undesirable dopant redistribution and throughput was low [20, 21].

The centrifugal method for backfilling ${}^6\text{LiF}$ into MSND trenches was developed in which ${}^6\text{LiF}$ is suspended in a solution above an etched MSND wafer. The solution and wafer are loaded into a centrifuge, and the high centripetal force from the spinning action forces the ${}^6\text{LiF}$ powder

out of the solution and into the MSND trenches [21, 25]. The centrifugal method was also adapted to backfill early DS-MSND prototypes [33]. As previously stated, the centrifugal method was largely considered to be the best backfill method, because it had relatively high throughput and did not leave large void spaces within the trenches as seen with SEM imaging. However, the more rigorous backfill packing fraction measurements revealed the ^6LiF packing density to be sub-optimal.

The following subsections detail the efforts to develop an alternative high-throughput backfilling method that would yield high ^6LiF packing fractions. For the remaining backfill discussion, the ^6LiF packing fraction was measured by comparing the mass of diode or wafer before and after being backfilled. Then, a SEM was used to measure the trench dimensions, and from that information the volume of the trenches in the diode could be calculated. The backfill density was compared to the crystalline density of enriched ^6LiF (2.55 g cm^{-3}).

Centrifugal and Hand-packed Backfilling

Initial backfill re-design efforts focused on improving previously tried and true methods of hand-packing, where LiF powder sprinkled on top of the detector is physically pressed into the trenches by hand, and the centrifugal techniques. The first idea was to use only nano-sized LiF that contain ^6LiF powder particles with a maximum critical dimension less than $0.5 \mu\text{m}$. Dry and wetted hand packing and centrifugal backfilling was tested with this material, and the results are shown in Table 5-5. The results were worse or no better than the previous centrifugal method using coarse ^6LiF . Specifically, for the nano- ^6LiF centrifuge backfill, we believed the increased surface area of nano-sized LiF particles likely caused an increase in interparticle friction and friction between LiF and the trench side walls. Additionally, smaller particles would feel less centripetal force than the larger, more massive coarse LiF particles, which culminated in lower packing fraction for nano-only LiF backfill trials.

Table 5-5. Backfilling experiment results for nano- ^6LiF backfilling.

Sample #	Nano wt%	Method	Packing Fraction
n1	100%	Dry Hand Pack	17.0%
n2	100%	Methanol-Wetted Hand Pack	30.6%
n3	100%	WD40-Wetted Hand Pack	33.4%
Nano Wafer 3	100%	Centrifuge 5:1 H_2O_2 : Methanol	8.2%

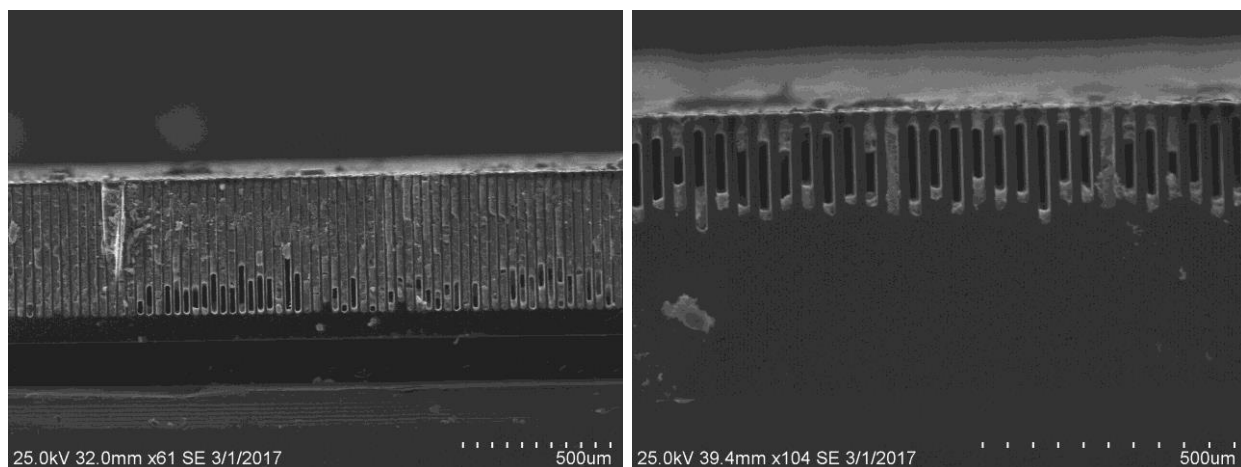


Fig. 5-17. SEM images of nano-only methanol-wetted hand packed backfill (left) and nano-only, H₂O₂:methanol centrifuge backfill (right) experiments. Large void regions within the trenches persisted in both methods.

Next, several variations on the centrifugal and hand packing method were tested to study the effects of different wetting agents and coarse/nano ⁶LiF powder mixtures. A few examples include: changing the LiF wetting-agent to something that may reduce interparticle friction more than the methanol:hydrogen peroxide mixture being used at the time, heating the wetting solution before processing in the centrifuge, and using a mixture of nano and coarse LiF where the nano-sized LiF could fill in the void spaces between the large coarse-LiF particles. There was minimal success in the early attempts at increasing packing fraction with many experiments resulting in about 30% or lower packing fraction (see Table 5-6).

Table 5-6. Results from LiF backfill experiments focusing on the centrifuge and hand packing backfill methodologies.

Sample #	Nano wt%	Method	Packing Fraction
1	0%	Centrifuge w/ Methanol	24.8%
2	100%	Centrifuge w/ Methanol	19.5%
3	33%	Centrifuge w/ Methanol	17.8%
4	33%	Centrifuge w/ Heated Methanol	14.4%
5	0%	Centrifuge w/ Heated Methanol	15.2%
6	0%	Centrifuge 1:5 H2O (DI): Methanol Followed by Methanol Hand Pack	27.1%
7	0%	Centrifuge 1:5 H2O: Methanol Followed by Methanol Hand Pack	30.0%
8	0%	Centrifuge 1.5:5 H2O2: Methanol Followed by Methanol Hand Pack	37.8%
9	40%	Centrifuge 100mL Glycerol	8.6%
10	40%	Glycerol Hand pack + Vibration	23.7%
11	40%	Methanol Hand pack + Vibration	36.2%
14	100%	Centrifuge 1:1 Acetic Acid: Methanol	35.9%
15	40%	Methanol Hand pack + Wetted Centrifuge	40.7%
16	40%	Methanol Hand pack + Wetted Centrifuge	34.8%
Interdig DS- MSND 2	40%	Methanol Hand Pack	27.6%

Several SEM images of some of the early results are shown in Fig. 5-18. Random void regions in the trenches were a common theme for most of the SEM images captured for diodes that were backfilled using the centrifugal method. Several of the latter combined hand pack and centrifuge experiments yielded packing fractions between 35% and 40%, but the results were challenging to consistently reproduce and were still well short of optimal packing fractions. Thus, the next step was to investigate alternative backfilling methods.

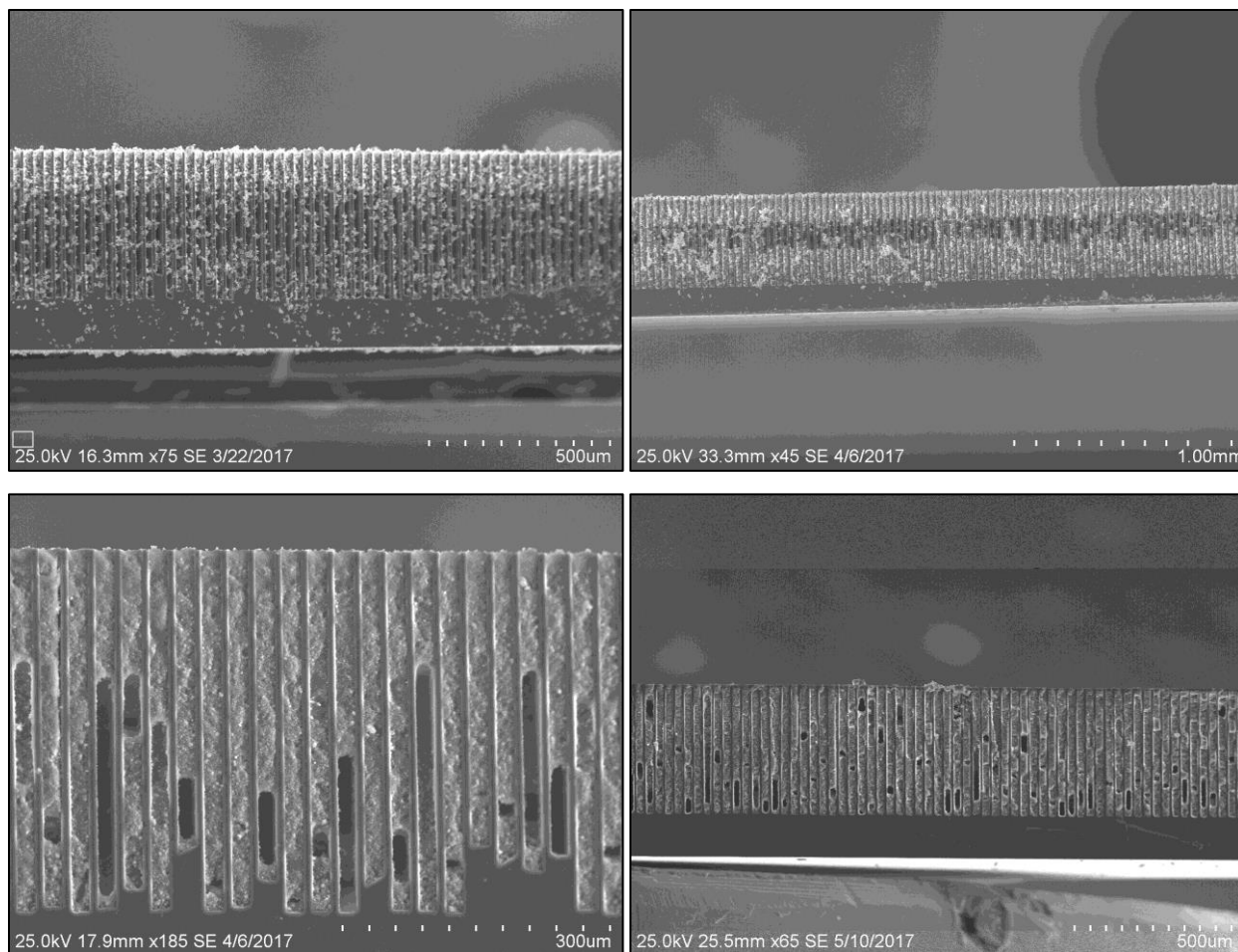


Fig. 5-18. SEM images of ^6LiF backfill experiment results for samples 4 (top right), 6 (top left), 11 (bottom right), and 15 (bottom left).

Isostatic Press

The next backfill test involved loading a MSND or DS-MSND diode with the trenched-surface coated with wetted ^6LiF into a pressure chamber with a gas inlet that allowed compressed gas to flow into the chamber and hold pressure up to 1500 psi, (Fig. 5-19). The gas exerts equal pressure to all exposed surfaces in the chamber, and if the LiF coating forms an air-tight barrier between the gas and the MSND, the LiF would be forced into the trenches. Diodes 17, 18, and 20 all contained some amount of nano-LiF, which resulted in large voids forming in trenches. The increased surface area in the LiF mixtures containing nano-particles likely increases interparticle friction forces and friction between the silicon side wall and LiF, which in turn causes the LiF to “cap-off” and leave a void in parts of the trenches. The isostatic press method worked well with coarse LiF as shown on diode 19, but 35% packing fraction could also be achieved with the centrifuge method. It is possible that the packing fraction may increase with increased operating

pressure, and this method could be used on DS-MSNDs to eliminate the likelihood of the backside LiF being removed while the front side is being backfilled. This method was ultimately abandoned, because of the uncertainty of being able to form an airtight LiF coating across a whole wafer and backfilling individual diodes is slow and costly.

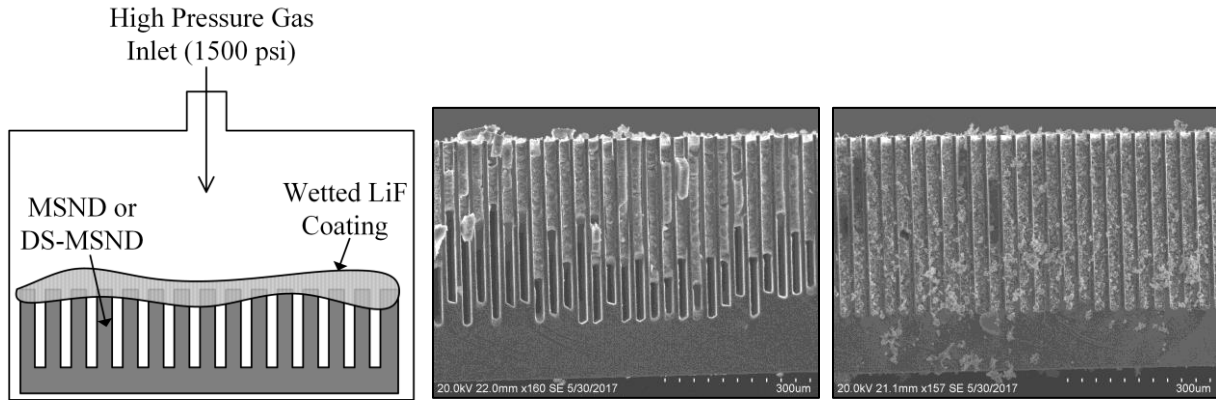


Fig. 5-19. (Left) Diagram showing the basic theory behind the isostatic press backfill methodology. (Middle) SEM image of Sample 18 (Right) SEM image of Sample 19.

Table 5-7. Results from LiF backfill experiments utilizing the isostatic press.

Sample #	Nano wt%	Method	Packing Fraction
17	100%	Isostatic Press 1000 psi	9.8%
18	100%	Isostatic Press 1500 psi	15.1%
19	0%	Isostatic Press 1500 psi	35.6%
20	40%	Isostatic Press 1500 psi	24.4%

Vibration Table (Dry)

Diodes 21-23 were backfilled by attempting to vibrate loose, dry LiF into the trenches of an MSND on top of a vibration table. Some literature suggested the vibration method was the best way to achieve high packing density with reported packing fractions of greater than 60% [154]. They packed cube or cube-like solid particles in a large cylindrical container on top of a vibration table. Unfortunately for MSNDs, the LiF cube-like particle sizes are around the same order of magnitude of the size as the width of their container (trenches), and high interparticle and particle-sidewall friction and possible electrostatic charging of the LiF powder particles resulted in low packing fraction (see Table 5-7 and Fig. 5-20).

Table 5-8. Vibration table with dry LiF powder backfill experiment results.

Sample #	Nano wt%	Method	Packing Fraction
21	0%	Vibration table low amplitude max speed	8.5%
22	0%	Vibration table high amplitude max speed	5.5%
23	0%	Vibration table low amplitude max speed	7.9%

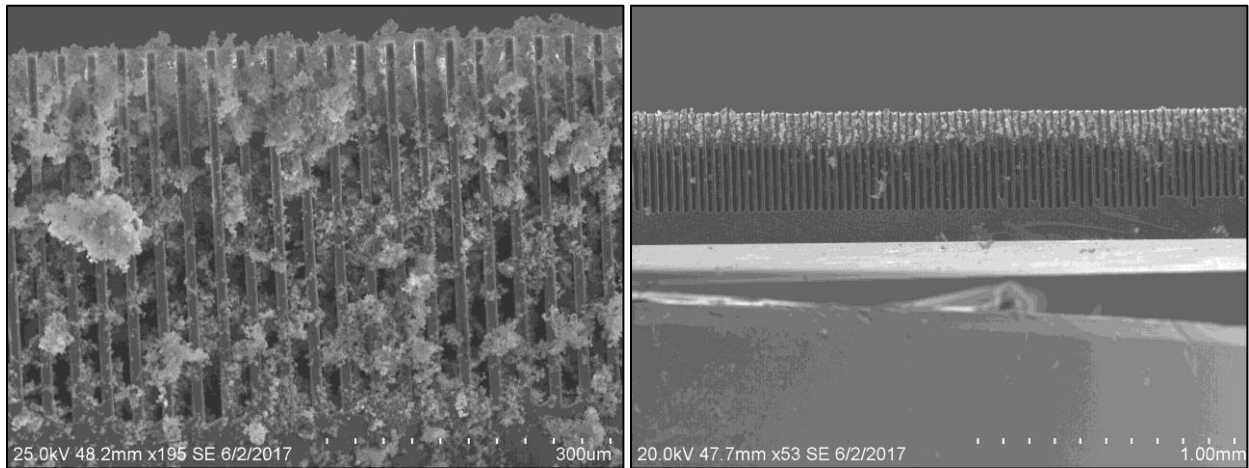


Fig. 5-20. SEM images of sample 21 (left) and sample (22) right backfilled by shaking dry LiF powder into the trenches on a vibration table.

Ink Roller Press

The first breakthrough in the packing fraction studies came when the ink-roller method was implemented. A thick, paste-like solution of LiF wetted with either methanol, methanol: acetic acid: hydrogen peroxide, or ethylene glycol was prepared and applied on top of a blank MSND or DS-MSND. Then, a hand roller was used to force the LiF into the trenches and the wetting agent, which was used to reduce interparticle friction, was subsequently evaporated. Listed in Table 5-9 are the early results of this method of backfilling. LiF packing fractions as high as 55% were achieved, and the packing fractions were consistently above 40%, a marked improvement over the centrifugal method of backfilling. SEM images of three of the samples are shown in Fig. 5-21.

Following the success, the next step was to determine the optimum ratio of nano-sized LiF to coarse LiF in the semi-bimodal powder mixture. Utilizing 15-20% nano-sized LiF by weight was regularly resulting in packing fractions near 50%. The optimum wetting solution was determined to be the methanol: acetic acid: hydrogen peroxide mixture, which regularly yielded packing fractions between 45% and 52% using 15 wt% nano-LiF, and this method was used to fabricate detection efficiency record breaking DS-MSNDs reported in [29]. Unfortunately, this

wetting solution was not ideal because it includes the use of a strong acid with nauseating odor. Additionally, a significant amount of operator skill was involved in the roller backfilling process, and when the method was tested by others, the LiF packing fraction dropped reduced to 30%. Thus, a more easily implemented and reproducible backfill method was sought.

Table 5-9. Results from ink roller backfill method experiments. For the first time, packing fractions above 40% were routinely achieved for powder backfill.

Sample #	Nano wt%	Method	Packing Fraction
28	0%	Ink Roller	43.6%
29	0	Ink Roller	44.7%
30	0	Ink Roller	41.9%
31	20	Ink Roller	37.7%
32	15	Ink Roller	49.2%
33	10	Ink Roller	51.7%
34	5	Ink Roller	55.1%
35	25%	Ink Roller	54.1%
36	0%	Ink Roller	45.5%
37	0%	Ink Roller	41.9%
38	25%	Ink Roller	51.0%
A1	25%	Ink Roller	35.4%
A2	25%	Ink Roller	43.3%
A3	25%	Ink Roller	40.9%
A4	25%	Ink Roller	24.5%
B1	25%	Ink Roller	54.5%
B2	25%	Ink Roller	43.7%
B3	25%	Ink Roller	49.8%
B4	25%	Ink Roller	49.0%
B5	25%	Ink Roller	46.3%
C1	15%	Ink Roller	49.3%

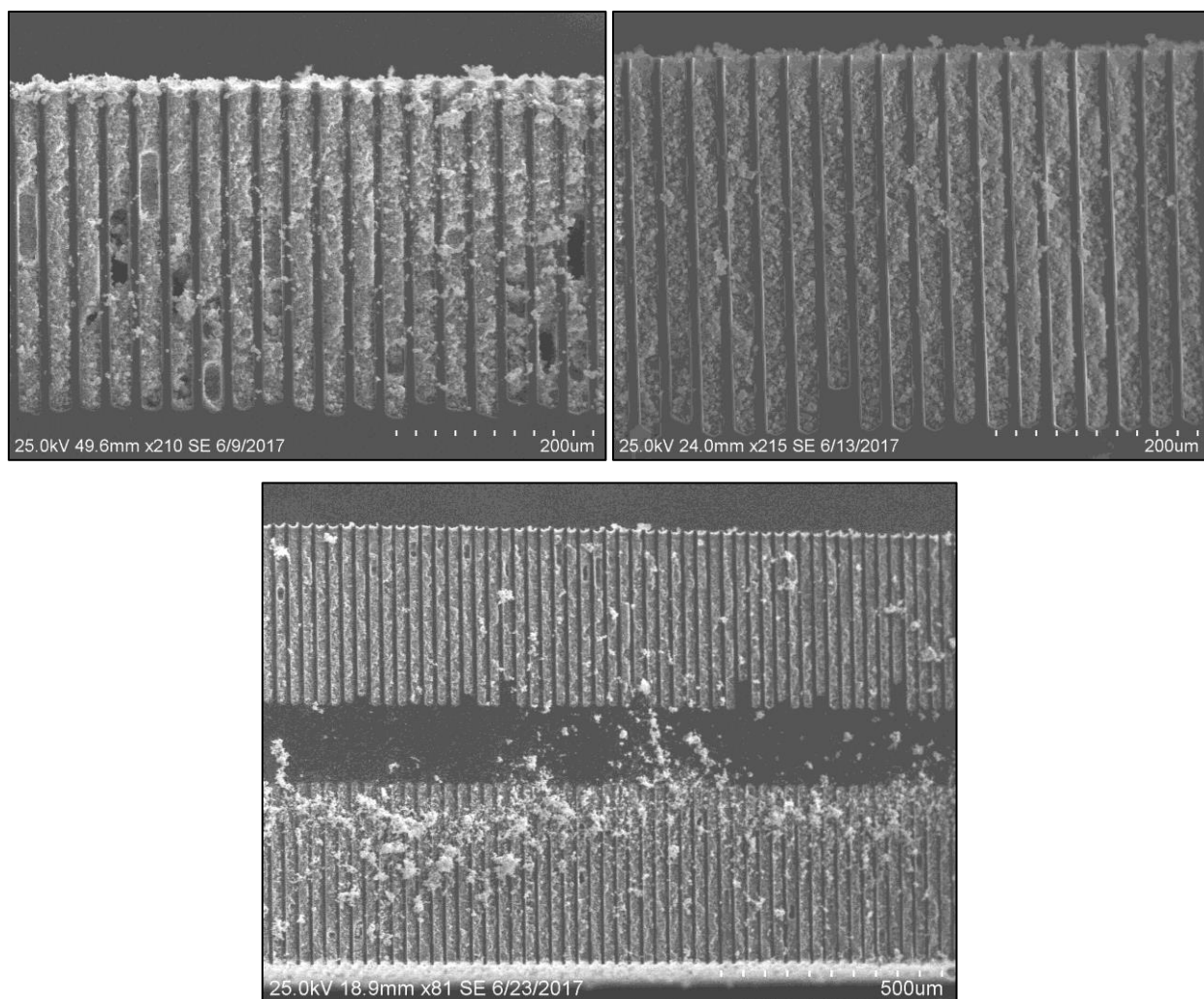


Fig. 5-21. Samples 28 (top left), 30 (top right), and C1 (bottom) backfilled with the ink roller method.

Suspended ${}^6\text{LiF}$ in Ultrasonic Vibration Bath followed Ink Roller Press

The current backfill method is to load a wafer into the bottom of a beaker and pour a solution of titrated ${}^6\text{LiF}$ powder suspended in methanol onto the wafer. The beaker is then loaded into an ultrasonic bath filled with DI water, see Fig. 5-22. The beaker is left in the bath solution for 1 hour during which ${}^6\text{LiF}$ loosely settles into the trenches. Next, the wafer is removed and methanol-wetted ${}^6\text{LiF}$ is pressed into the trenches with an ink roller. The wafer is then dried, and dry film photoresist is applied and cured on the backfilled side of the wafer. The entire process is repeated for the back-side trenches of the DS-MSND. The ${}^6\text{LiF}$ packing fractions achieved with this method ranged between 40% and 50% (see Table 5-10).

Table 5-10. ${}^6\text{LiF}$ backfill packing fractions achieved with ultrasonic vibration backfill with ${}^6\text{LiF}$ suspended in methanol followed by shortened ink roller backfill.

Sample #	Nano wt%	Method	Packing Fraction
V+R 1	0%	Methanol Suspended Vibration + Roller	42.2%
V+R 2	0%	Methanol Suspended Vibration + Roller	45.2%
V+R 3	0%	Methanol Suspended Vibration + Roller	50.0%
V+R 4	0%	Methanol Suspended Vibration + Roller	46.8%
V+R 5	0%	Methanol Suspended Vibration + Roller	43.7%
V+R 6	0%	Methanol Suspended Vibration + Roller	42.2%

The ultrasonic vibration followed roller method tends to increase the repeatability of the backfill procedure over the ink roller only method. During the initial ultrasonic vibration step, ${}^6\text{LiF}$ loosely settles out of the solution and into the trenches. The vibration reduces the probability of the ${}^6\text{LiF}$ bridging within the trenches leaving behind void spaces. The ink roller backfill following the vibration step compacts the powder in the trenches. Additionally, this ink roller step following vibration is shorter needing only about ten passes to complete the backfill compared to hundreds of passes required for a high density backfill in the ink roller only process. The wafer throughput with a six-pocket ultrasonic bath is comparable to the centrifugal method. The throughput could be increased by implementing larger or additional ultrasonic baths, which are relatively inexpensive when compared to other VLSI processing equipment.

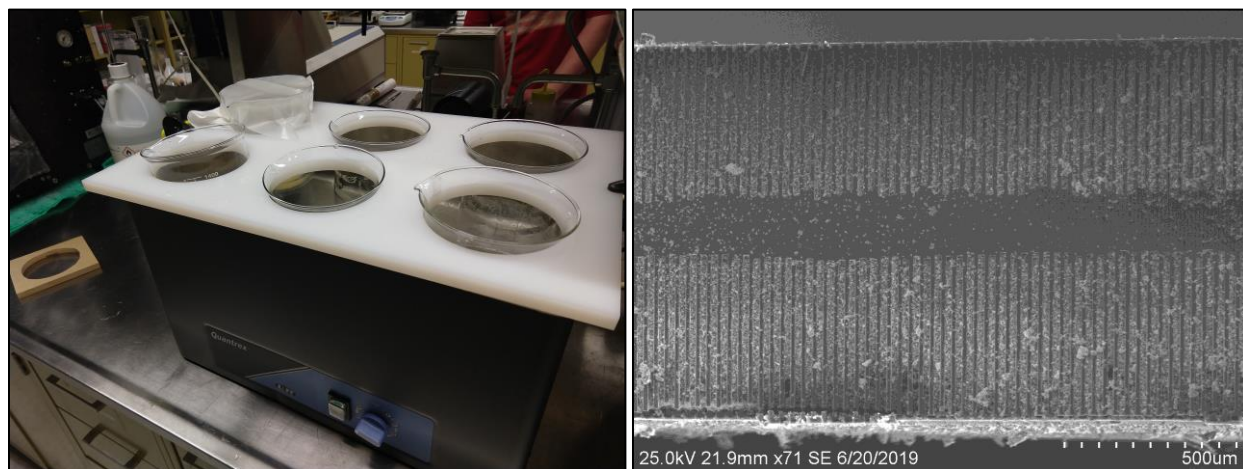


Fig. 5-22. (Left) Picture of ultrasonic vibration tank and beaker jig for ${}^6\text{LiF}$ -backfilling. (Right) SEM image of DS-MSND backfilled with ultrasonic vibration followed by ink roller method. The packing fraction was greater than 45%.

5.1.3. Diode Packaging

After the DS-MSND wafer is backfilled and encapsulated with dry film photoresist, the wafer is mounted on UV-sensitive dicing tape and loaded into the dicing saw. The dicing saw uses a thin diamond-embedded blade to cut the silicon wafers along the bulk silicon paths around each diode with minimal damage to the silicon. The mounted wafers are then flood exposed with UV light to reduce the wafer adhesion to the dicing tape. Next, the diodes are removed from the dicing tape, and the electrical characteristics are measured. DS-MSND diodes with low leakage current and capacitance are mounted into ceramic detector boards (CDBs) (see Fig. 5-23). Silver epoxy secures and electrically connects the bottom-side of the DS-MSND to the CDB, and an Al/Si wire bond connects the top-side DS-MSND bond pad or pads to the CDB. A ceramic lid is then epoxied to the top of the CDB, and a metal shield is secured to the top of the CDB to shield RF signals. Conductive vias in the CDB connect the DS-MSND connection points to gold pads on the bottom of the CDBs, and those surface mount gold pads connect the CDBs onto supporting electronics circuit boards in completed detector systems. The final dimensions of the shielded CDB package are approximately 12 mm x 12 mm x 3.5 mm.

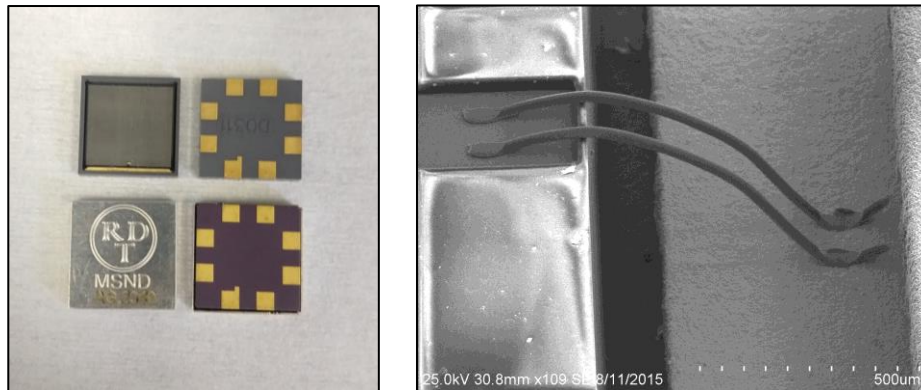


Fig. 5-23. (Left) DS-MSND mounted in ceramic detector board with metal shield. (Right) SEM image of wire bonds connecting the top-side of a DS-MSND to a CDB.

5.2. Detector Characterization

After the DS-MSND are mounted into CDB packages, final electrical and radiological measurements are performed. Discussed in the following subsections are the leakage current vs. voltage (IV) and capacitance vs. voltage (CV) measurements. Radiation sensitivity measurements carried out before DS-MSNDs are implemented with the final detector package are also described.

5.2.1. *Electrical Properties*

The electric properties of the DS-MSND can be measured at different steps during the fabrication process to ensure the processes are successful or to potentially identify fabrication problems such as depleted source wafers or excessive damage from dicing or backfilling. After the diodes are mounted into CDBs, final electrical characterization is performed to ensure all the diodes have adequate performance before they are implemented in larger detector systems like the HeReps or MRDs. The two main electrical properties of interest are the IV and CV curves. The IV curve is determined by monitoring the leakage (or dark) current while adjusting the voltage applied across the DS-MSND electrodes. The capacitance is measured by monitoring the current from the device while an oscillating voltage is superimposed on a constant base voltage that is adjusted through the potential range of operational bias. The capacitance is then derived by calculating the RC time constant from relaxation after the peaks of the oscillating voltage at each step.

Recall, ideal reverse-bias detector diodes have low leakage current and low capacitance. Leakage current is primarily caused by thermal charge generation in the depletion region, and fluctuation of current increases the electronic noise of the system. Therefore, the leakage current can be used to determine the maximum operating voltage based on the tolerance for noise in the system. The capacitance governs the magnitude of the voltage signal from the diode as shown in Eq. 5-13 where ΔQ is the total charge induced on the detector electrodes and C is the capacitance of the detector. The capacitance of the diode is defined in Eq. 5-14 where ϵ is the permittivity of the substrate, A is the surface area of the electrode, and W is the depletion layer width. Therefore, the detector must be designed such that it can be operated at high enough bias, which increases the depletion width to have minimal capacitance while simultaneously maintaining low leakage current which governs the background noise level.

$$\Delta V = \frac{\Delta Q}{C} \quad \text{Eq. 5-13}$$

$$C = \frac{\epsilon A}{W} \quad \text{Eq. 5-14}$$

All the following IV measurements were performed in an electromagnet radiation shielded dark box with a Keithley 237 High Voltage Source Measurement Unit, and the CV measurements were performed with a Hewlett-Packard 4280A 1MHz C Meter/C-V Plotter.

1-mm thick, *pvn*-DS-MSNDs

Several *pvn*-DS-MSNDs with 400- μm deep by 16- μm wide trenches with 30- μm wide unit cells were processed on 1-mm thick, 5-k Ω -cm resistivity wafers to verify results from previous work [30, 33]. IV and CV-curves for several of the 1-cm² active area DS-MSNDs mounted in CDBs are shown in Fig. 5-24. The IV chart indicates the upper limit for operation for these devices is around 5-V reverse bias, which is safely below the breakdown voltage at about -10 V where larger leakage currents would cause too much noise in the system. From the CV-curve, the capacitance at -5 V would be between 50 and 100 pF, well within acceptable limits.

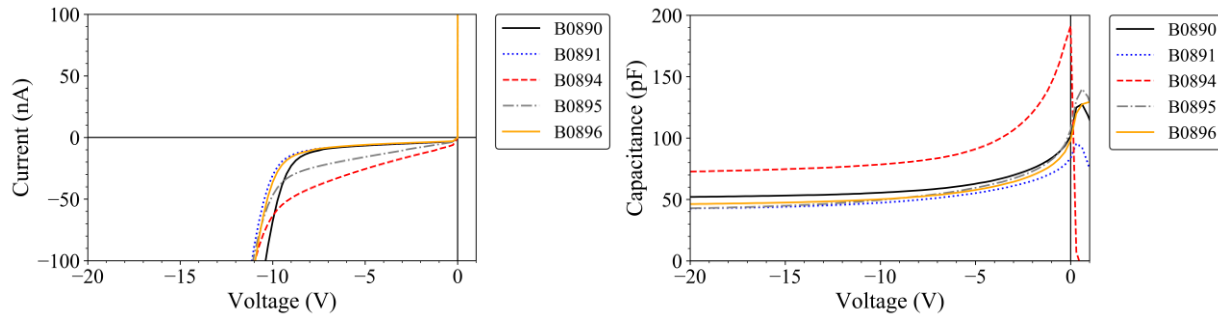


Fig. 5-24. (Left) IV-curve and (Right) CV-curve for 1-mm thick, partial-conformal, *pvn*-DS-MSNDs.

1-mm thick *pvp*-DS-MSNDs

For direct comparison with the 1-mm thick, *pvn*-DS-MSNDs, several 1-mm thick *pvp*-DS-MSNDs with the same microfeature dimensions as their *pvn*-counterparts were prepared and mounted into CDBs. The *pvp*-DS-MSNDs are operated at 0-V bias so neither side of the DS-MSND is forward biased, which would cause an undesirable increase in leakage current. Therefore, the IV curve in Fig. 5-25 is of little use other than indicating small biases nominally, less than 0.5 V in either direction can be tolerated without excessive dark current. The CV-curves show that the *pvp*-DS-MSNDs have about the same capacitance of the biased *pvn*-DS-MSND which is between 50 pF and 100 pF.

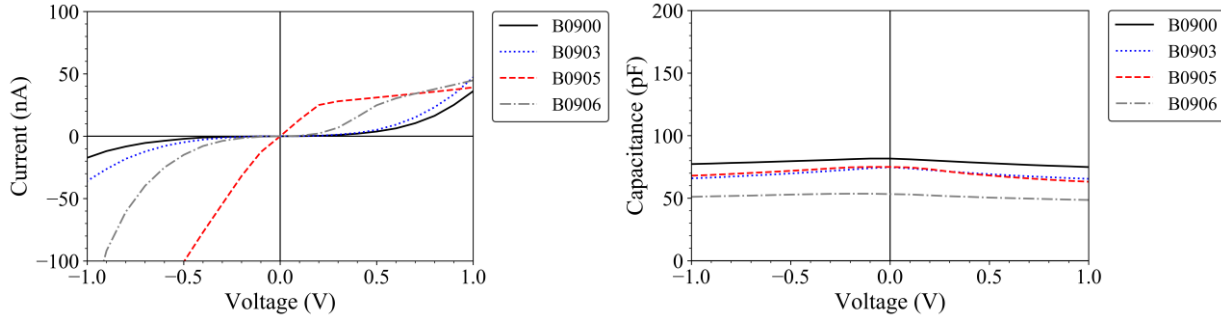


Fig. 5-25. (Left) IV-curve and (Right) CV-curve for 1-mm thick, partial-conformal, pvp-DS-MSNDs.

1.5-mm thick pvp-DS-MSNDs

The IV and CV curves for 1.5-mm thick pvp-DS-MSNDs are shown in Fig. 5-26. The thicker DS-MSNDs were fabricated to allow for deeper trench etching in which more ${}^6\text{LiF}$ conversion material could be backfilled to improve the intrinsic thermal-neutron detection efficiency above the 1-mm thick DS-MSND. Again, the pvp-DS-MSNDs are operated at 0-V applied bias where there is minimal leakage current, because neither *pn*-junction is forward biased. The capacitance for the 1.5-mm thick DS-MSNDs was significantly higher than the 1.5-mm thick DS-MSNDs likely due to increased area of the partial conformal contact extending down the DS-MSND fins. This increased capacitance shifts features in the pulse height spectrum to lower channels. However, the capacitance is still low enough to provide good signal, and high efficiency devices have been fabricated with this doping scheme [29].

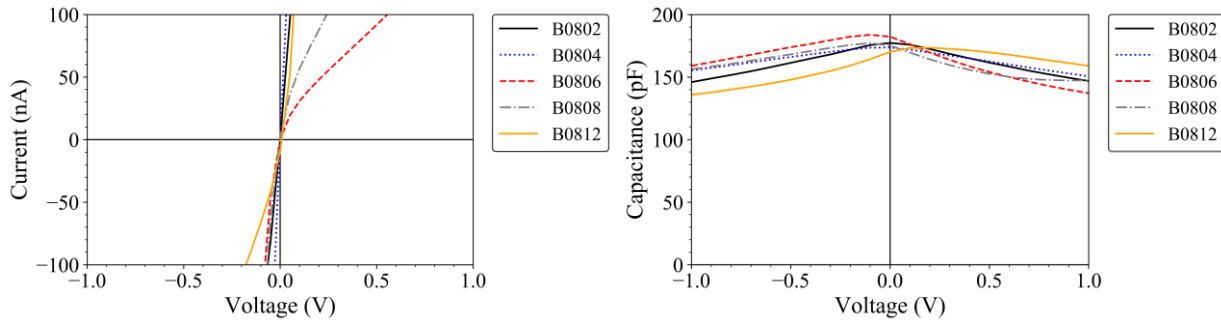


Fig. 5-26. (Left) IV-curve and (Right) CV-curve for 1.5-mm thick, partial-conformal, pvp-DS-MSNDs.

1.5-mm thick *pvp-n-ring* DS-MSNDs

Prototype *pvp-n-ring* DS-MSNDs were fabricated on 1.5-mm thick wafers. Both sets of trenches were doped *p*-type and were electrically connected on the probe station. The bias was applied across the *p*-type regions and a thin *n*-type doped ring encompassing the trenches on one side of the diode. The IV and CV curves for the *pvp-n-ring* DS-MSNDs are plotted in Fig. 5-27. Good rectifying behavior was observed indicating it may be possible to operate the detectors with bias up to about -50 V bias. The capacitance was significantly lower than other DS-MSNDs likely attributed to the small area of the *n*-ring contact.

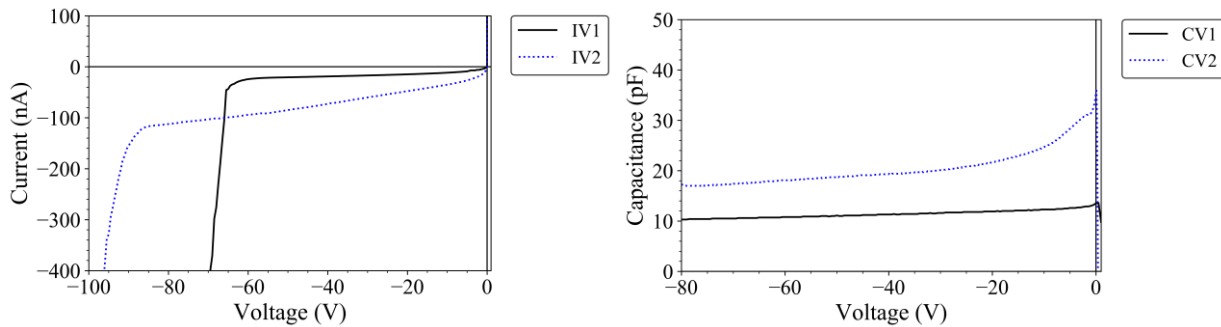


Fig. 5-27. (Left) IV-curve and (Right) CV-curve for 1.5-mm thick, partial-conformal, *pvp-n-ring*-DS-MSNDs.

5.2.2. Radiation Sensitivity

DS-MSNDs that pass the IV and CV measurements are ready for radiation sensitivity testing. The alpha-particle measurements are used to study the charge collection efficiency of non-backfilled DS-MSNDs, and two types of neutron measurements are described that measure intrinsic thermal-neutron detection efficiency.

Alpha-Particle Measurements

Alpha-particle measurements can be performed on empty DS-MSNDs either on a probe station or mounted in a CDB. Shown in Fig. 5-28 is an example of an alpha-particle measurement on a DS-MSND wafer on the probe station. The probed diode is then connected to an Ortec 142A preamplifier and Canberra 2022 amplifier, and the pulse height spectrum is collected with an Ortec Easy-MCA. A bias can be applied through the probe and back-side pedestal contact points across the diode.

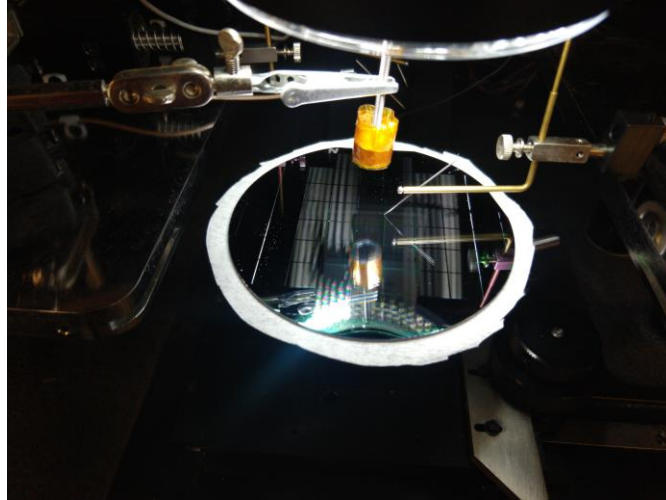


Fig. 5-28. Experiment configuration for alpha-particle charge collection efficiency measurement.

The relative charge collection efficiency for 1-mm thick *pvp*-DS-MSNDs and 1-mm thick *pvn*-DS-MSND was measured with an ^{241}Am alpha-particle source. The alpha particles have short ranges in silicon and will only penetrate a few microns. Therefore, a measurement was performed on one side. Afterwards, the wafer was flipped over and measured again to study the charge collection efficiency of the backside of the diode. The *pvp*-DS-MSND was operated at 0-V bias, and the *pvn*-DS-MSND was operated with -5 V reverse bias. The gain on the amplifier was 100x with a shaping time of 12 μs . The pulse height spectra for the 1-mm *pvp* and *pvn* DS-MSND study are shown in Fig. 5-29. The *p*-type side of the *pvn*-DS-MSND had the best charge collection efficiency with most of the pulses landing in higher energy channels. Conversely, the *n*-type side of the *pvn*-DS-MSND had very poor charge collection efficiency for most interactions. The small peak near channel 650 *pvn*-DS-MSND *n*-side irradiation is likely caused by alpha-particle interactions in the bottoms of the trench nearer to the high-electric field region at the base of the *p*-type side of the DS-MSND. A subsequent measurement was performed where the ^{241}Am source was positioned so the angle of incidence was 45° to ensure all interactions occurred near the tops of the *n*-type fins. The resulting pulse height spectrum is shown in Fig. 5-30, and the higher energy peak was no longer present. These results indicate that the back-side trenches on *pvn*-DS-MSND will be less sensitive to neutron interactions, because much of the signal will get lost in the background noise, which was the same conclusion drawn in prior work [33]. Both sides of the *pvp*-DS-MSND have nearly identical charge collection efficiency. The results of this study indicate that the *pvp*-DS-MSND design will outperform the *pvn*-DS-MSND in intrinsic thermal-neutron

detection efficiency, because the both sides of the detector will be equally sensitive to charged-particle reaction products from neutron. However, as shown by the *p*-side irradiation of the *pvn*-DS-MSND, there is still room for improvement for charge collection efficiency, which would ultimately improve the signal-to-noise ratio of the DS-MSND. The *pvp-n-dot* or *pvp-n-ring* DS-MSND may provide this improvement by allowing for bias to be applied on both sets of *p*-type trenches.

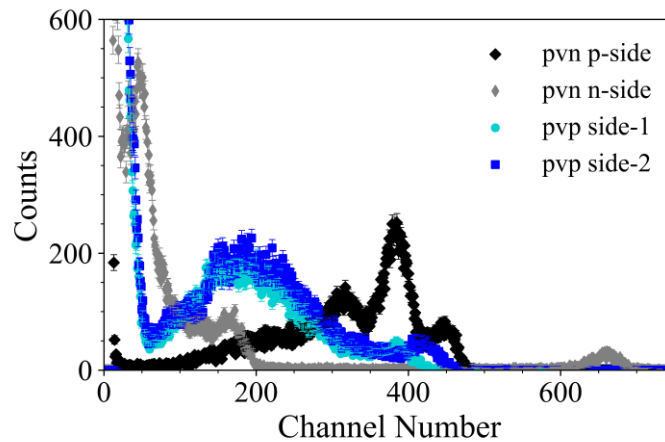


Fig. 5-29. Pulse height spectra from ^{241}Am alpha-particle measurements for 1-mm thick *pvn*-DS-MSNDs and 1-mm thick *pvp*-DS-MSNDs.

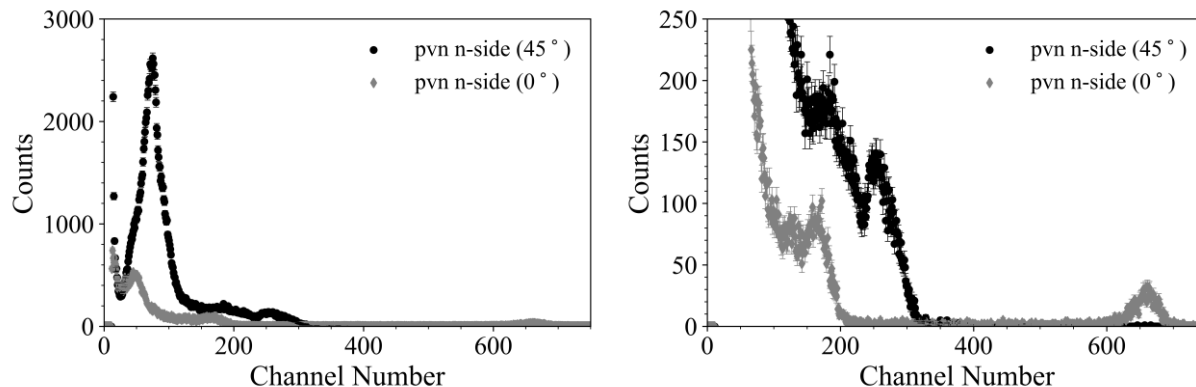


Fig. 5-30. Pulse height spectra for ^{241}Am alpha-particle measurements comparing normal and angled alpha-particle incidence. The y-axis limit is reduced on the right-side plot to show how the high-energy peak for normal incidence is eliminated when the alpha particles intersect the DS-MSND at an angle so that the alpha particle cannot reach the bottoms of the trenches.

Neutron Measurements

One of the most important characteristics of a neutron detector is its intrinsic thermal-neutron detection efficiency. Defined in Eq. 4-8, the intrinsic thermal-neutron detection efficiency is the number of thermal neutrons recorded divided by the number of thermal neutrons incident on the detector. Described in this section are the two methods used in this work to measure the intrinsic thermal-neutron detection efficiency of DS-MSNDs.

Diffacted Neutron Beam Port Measurements

The diffracted thermal-neutron beamport at the KSU TRIGA Mk II nuclear reactor utilizes a pyrolytic graphic monochromator to diffract a collimated beam of 0.0253 eV neutrons from a radial beamport in the reactor [155]. The clean, thermal-neutron beam can then be further collimated by way of a cadmium shutter with variable aperture sizes. An aperture with a 2.5-mm diameter circular hole is used for DS-MSND measurements. Since the diameter of the collimated beam is smaller than the active area of the DS-MSND, the solid angle for the configuration is unity.

The first step to determine the intrinsic thermal-neutron detection efficiency for an unknown detector is to determine the neutron flux exiting the collimator by calibrating against a neutron detector with known detection efficiency. Note the calculation is further simplified if the reference detector also uses a $1/\nu$ absorber like ^3He , ^{10}B , or ^6Li [137]. A 2-in. diameter, 6-in. long, 4-atm, Reuter-Stokes ^3He proportional counter with an intrinsic thermal-neutron detection efficiency of $80.7 \pm 0.5\%$ was used as the calibration detector for the diffracted beamport

measurements. The ^3He detector was positioned in the beamline so that the neutrons were incident on the side of the detector at the detector midpoint to eliminate the need for corrections due to the dead regions at both ends of the ^3He detector caused by the high-voltage insulating standoffs. A 2.5-mm diameter aperture was used so that the fractional solid angle was unity for the ^3He detector and DS-MSNDs.

To start, the reactor is brought up to power, and the net count rate for neutrons in the diffracted beam was determined by subtracting the count rate of the detector with the shutter aperture open to a measurement with aperture closed. The number of thermal neutrons incident on the detector per unit time was then calculated by dividing the net count rate, n , by the known intrinsic thermal-neutron detection efficiency of the calibrated detector, $\varepsilon_{cal,th}$, (Eq. 5-15). Then, the calibrated detector is removed and a DS-MSND was placed in the beam with the beam normally incident on the trenches. A measurement is performed with the shutter open and then repeated with the shutter closed. The intrinsic thermal-neutron detection efficiency of the DS-MSND can then be calculated by dividing the neutron count rate by the number of neutrons incident on the detector per unit time, (Eq. 5-16). Note, a correction factor, C_{lid} , was added to account for neutron attenuation by the plastic lid covering the DS-MSND in the DS-MSND test box. The attenuation of the lid was determined by measuring the relative count rate of a ^3He detector with and without the lid in front of the detector in line with the diffracted neutron beam.

$$\varphi_{th} = \frac{n}{\varepsilon_{cal,th}} \quad \text{Eq. 5-15}$$

$$\varepsilon_{th} = \frac{n}{\varphi_{th} * C_{lid}} \quad \text{Eq. 5-16}$$

Following the breakthrough in improved ^6LiF packing using the ink roller technique, several 1-mm thick, *pvp*-DS-MSNDs were manufactured, and their intrinsic thermal neutron detection efficiencies were measured with the diffracted thermal-neutron beamport. Listed in Table 5-11 is a subset of the detection efficiencies achieved with improved packing fractions up to 55%, and the pulse height spectra for several of the DS-MSNDs are shown in Fig. 5-31. The DS-MSNDs had trench depths between 400-450 μm , trench width of approximately 20 μm , and unit cell width of 30 μm . Coupled with the improved packing fractions these DS-MSNDs were the

first to break the 60% intrinsic thermal-neutron detection efficiency barrier. The pulse height spectra still contained a low valley between the background noise and gamma-ray signals. This valley is critical for setting an LLD wherein gamma rays are discriminated without adversely affecting neutron detection efficiency.

Table 5-11. Results from diffracted beamport measurements to determine intrinsic thermal-neutron detection efficiency for 1-mm thick, pvp-DS-MSNDs.

Device	Source	Time (s)	Counts	Detection Efficiency
³ He	Shutter Open	120	33253	80.70 ± 0.5%
	Shutter Closed	120	7977	
B1	Shutter Open	120	13107	57.2 ± 1.1%
	Shutter Closed	120	216	
B3	Shutter Open	120	14615	63.9 ± 1.2%
	Shutter Closed	120	218	
B4	Shutter Open	120	13596	59.1 ± 1.1%
	Shutter Closed	120	279	
³ He	Shutter Open	300	68660	80.70 ± 0.5%
	Shutter Closed	300	19011	
AVB2.1	Shutter Open	120	10578	58.3 ± 1.1%
	Shutter Closed	120	259	
AVB2.2	Shutter Open	120	10812	59.2 ± 1.1%
	Shutter Closed	120	327	
AVB2.4	Shutter Open	120	11196	61.9 ± 1.1%
	Shutter Closed	120	228	
AVB2.8	Shutter Open	120	11129	61.5 ± 1.1%
	Shutter Closed	120	228	
AVB3.1	Shutter Open	120	10913	58.9 ± 1.1%
	Shutter Closed	120	473	
AVB3.5	Shutter Open	120	11115	60.9 ± 1.1%
	Shutter Closed	120	331	

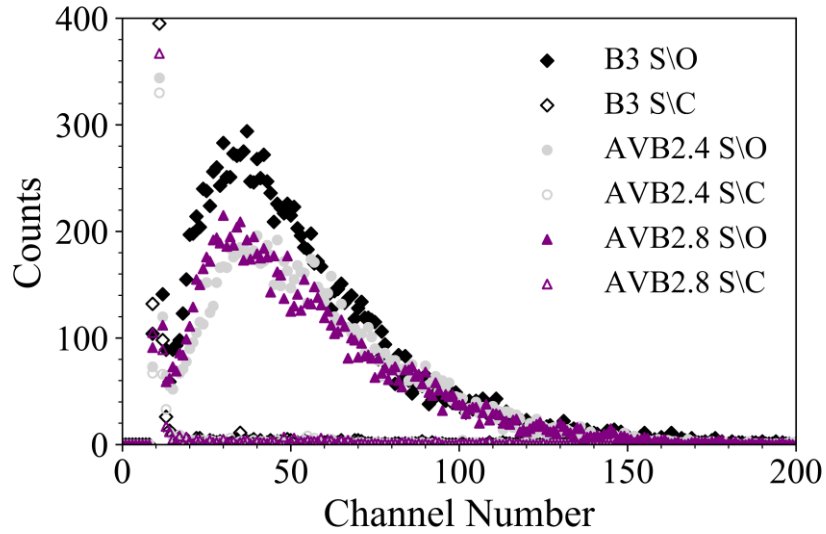


Fig. 5-31. Pulse height spectra for first DS-MSNDs with intrinsic thermal-neutron detection efficiencies greater than 60%. Measurements were performed at the diffracted beamport with a 2.5-mm cadmium wide shutter open (S\O) and shutter closed (S\C).

Moderated ^{252}Cf Measurements

The intrinsic thermal-neutron detection efficiency of DS-MSNDs was also measured by using a moderated ^{252}Cf source and comparing the count rate of the unknown DS-MSND to the count rate of a DS-MSND previously calibrated in the diffracted thermal-neutron beamport. The relationship between the count rates and intrinsic thermal-neutron detection efficiencies are shown in Eq. 5-17 where $n_{unknown}$ and $n_{calibrated}$ are the net count rates for the unknown and calibrated DS-MSNDs, respectively, and $\varepsilon_{unknown}$ and $\varepsilon_{calibrated}$ are the intrinsic thermal-neutron detection efficiencies for the unknown and calibrated DS-MSNDs, respectively [29]. Because both devices are the same size, utilize the same backfill material, and the measurements are performed with the same source-moderator-detector geometry, no additional corrections are required. A diagram of the measurement geometry is shown in Fig. 5-32.

$$\frac{n_{calibrated}}{\varepsilon_{calibrated}} = \frac{n_{unknown}}{\varepsilon_{unknown}} \quad \text{Eq. 5-17}$$

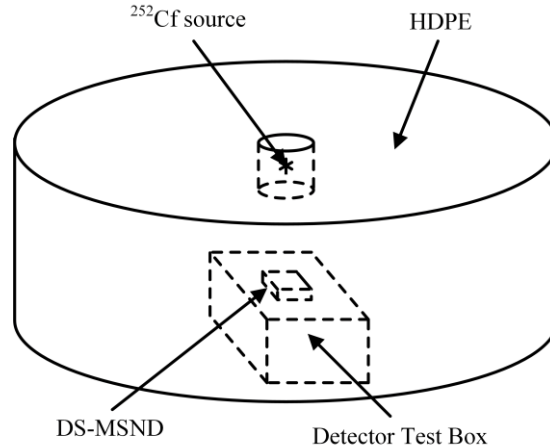


Fig. 5-32. Diagram of test setup for moderated ^{252}Cf measurements. Adapted from [29].

With a new plateau reached in attainable ^6LiF packing density at approximately 50%, the remaining option to improve the neutron detection efficiency of the DS-MSNDs was to etch deeper trenches which required 1.5-mm thick wafers. On the thicker wafers, DS-MSNDs were fabricated with 550- μm deep trenches with trench widths ranging from 20 to 22 μm on a pitch of 30 μm . The ^6LiF packing fraction for these deeper etched devices ranged from 50-55%. The intrinsic thermal-neutron detection efficiency of the thicker DS-MSNDs was determined with a moderated ^{252}Cf source by comparing to a previously calibrated DS-MSND, AVB2.2. The DS-MSNDs were operated at 0-V bias. An Ortec 142A preamplifier was connected to the test box and a Canberra 2022 amplifier. The bipolar output of the amplifier was connected to an MCA to record the pulse height spectra. Recall, the pulse polarity of *pvp*-DS-MSNDs is depend on which side of the DS-MSND the neutron interaction occurs. Thus, bipolar output allows for measurement of both sets of fins simultaneously.

Shown in Table 5-12 are the intrinsic thermal-neutron detection efficiencies of several 1.5-mm thick DS-MSNDs, and the pulse height spectrum for DS-MSND B0812 is shown in Fig. 5-33. The LLD was set in the lowest point between the neutron signal and the background signal. The highest intrinsic thermal-neutron detection efficiency achieved was $69.3 \pm 1.5\%$, which was a new record for neutron detectors of its type. Also, note that all the detectors tested had detection efficiencies greater than 65%. The increased performance is attributed to the deeper trenches and improved ^6LiF backfill density.

Table 5-12. Intrinsic thermal-neutron detection efficiencies of 1.5-mm thick DS-MSND measured with the moderated ^{252}Cf source method.

Device	Source	Time (s)	Counts	Detection Efficiency
AVB 2.8	Mod. ^{252}Cf	300	12799	$61.5 \pm 1.1\%$
	Background	300	6	
B0811	Mod. ^{252}Cf	300	14186	$68.2 \pm 1.5\%$
	Background	300	20	
B0812	Mod. ^{252}Cf	300	14413	$69.3 \pm 1.5\%$
	Background	300	16	
B0814	Mod. ^{252}Cf	300	13537	$65.1 \pm 1.4\%$
	Background	300	2	
B0815	Mod. ^{252}Cf	300	13528	$65.0 \pm 1.4\%$
	Background	300	279	

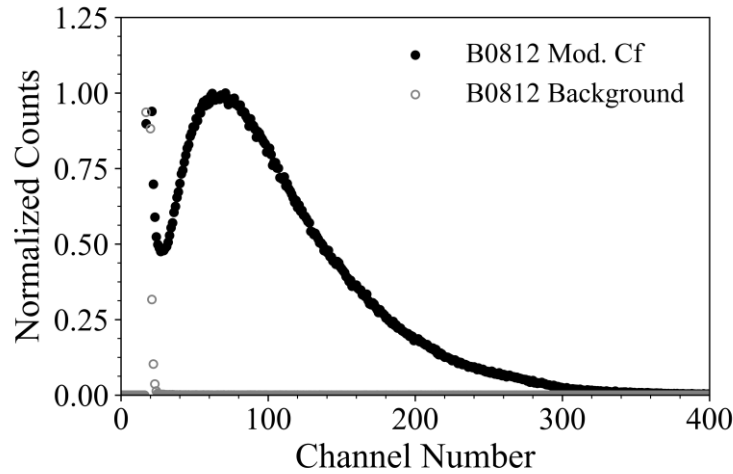


Fig. 5-33. Pulse height spectrum for DS-MSND B0812 which had an intrinsic thermal neutron detection efficiency of $69.3\% \pm 1.5\%$.

Gamma-Ray Measurements

The gamma-ray rejection ratio (GRR) is an important metric for neutron detectors and is defined in Eq. 5-18 where n is the net count rate for gamma rays falsely recorded as neutron counts, A is the source activity, Ω_f is the fractional solid angle, and BR is the branching ratio. In an ideal neutron detector, the GRR would equal zero indicating the neutron detector is not sensitive to gamma rays. For reference, the GRR of commercially available MSNDs is 10^{-7} [28].

$$GRR = \frac{n}{A * \Omega_f * BR} \quad \text{Eq. 5-18}$$

The GRR for the *pvp*-type 1.5-mm thick DS-MSND was measured with a ^{137}Cs gamma-ray source placed directly on top of the test box providing an exposure of approximately 13 mR/hr and was found to be 2.26×10^{-3} when the LLD was set at the lowest point in valley between the neutron signal and background signal. Shown in Fig. 5-34 is the DS-MSND pulse height spectra for a moderated ^{252}Cf and ^{137}Cs source, and the gamma-ray signal intersects the neutron signal significantly. However, if the LLD is increased to achieve a more acceptable GRR of 5.5×10^{-5} , the intrinsic thermal-neutron detection efficiency decreases to approximately 60%.

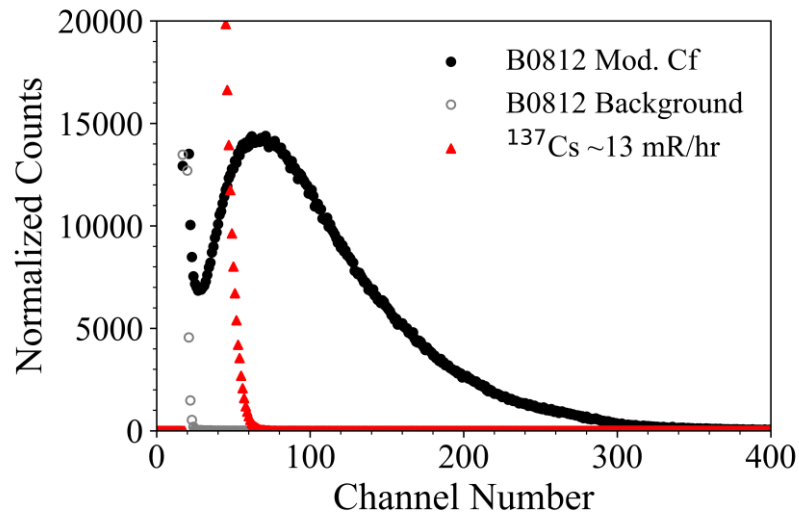


Fig. 5-34. Pulse height spectra from DS-MSND B0812 for background, moderated ^{252}Cf , and ^{137}Cs .

The next generation of DS-MSNDs will focus on shifting the neutron induced signal to higher energy channels by improving charge collection efficiency and re-optimizing the trench geometry. Charge collection efficiency might be improved in the *pvp*-DS-MSND by reducing dopant drive-in time and temperature thereby reducing the volume of dead-region in the fins by limiting dopant depth. Additionally, implementing the *pvp-n-dot* or *pvp-n-ring* design would allow for a bias to be applied across the *p*-type trenches on both sides and the *n*-contact, thereby increasing the electric field in the DS-MSNDs fins, which should improve charge collection efficiency. Also, the trench geometry could be further optimized for better signal-to-noise ratio by

etching deeper and narrower trenches which would result in thicker fins. More reaction-product energy can then be deposited in the fins and measured. The deeper trenches offset losses in neutron absorption efficiency caused by reducing the trench width.

5.3. Other MSND and DS-MSND Variants

Described in the following subsections are efforts made to develop fast charge collection along with MSNDs and other fabrication techniques aimed at improving the signal to noise ratio of DS-MSNDs by adjusting the dopant profile. The results from these experiments were largely unsuccessful but are included in this work for completeness.

5.3.1. *Fast Charge Collection MSNDs*

The charge carrier motion in traditional single-sided MSNDs and *pvp*-DS-MSNDs is largely vertical along the lengths of the fins and requires 10-20 μ s charge integration time to measure most of the reaction product energy. The longer integration time is completely acceptable for the detection scenarios DS-MSNDs have been designed for such as source search and localization, and personnel monitoring. However, if the required charge integration time was reduced, DS-MSNDs could operate in even higher radiation flux environments with limited dead time. The methods used to try to reduce the required charge integration time were to (1) increase the electric field in the device's fins which increases the velocity of the charge carriers and (2) change the path of the charge carriers to the electrodes from being drifted vertical through long fins (400-650 μ m) to being drifted laterally across the width of the fins (8-12 μ m).

Co-Doped MSNDs

Several Co-Doped MSNDs were fabricated which had a planar backside contact, a deep diffused contact in the trenches, and a contact on the tops of the fins of opposite type of the trench contact, see Fig. 5-35. After KOH etching and cleaning, the trench junction was diffused by solid source diffusion while an oxide layer remained on the tops of the fins leaving the tops of the fins undoped. Afterwards, the oxide layer on the top of the fins was removed, and the opposite type dopant was diffused onto the fin tops. The backside planar contact was then diffused. This doping procedure leaves regions of overlapping dopant types at the top corners of the fins hence the name co-doped MSNDs. The anode was attached to the contact on the top of the fins, and the cathode was attached to the backside planar contact with the trench junction left floating. Ideally, the two

different types of dopant on the fin top and sidewalls would create a larger electric field in the fins than standard pvn -MSNDs and promote faster charge collection.

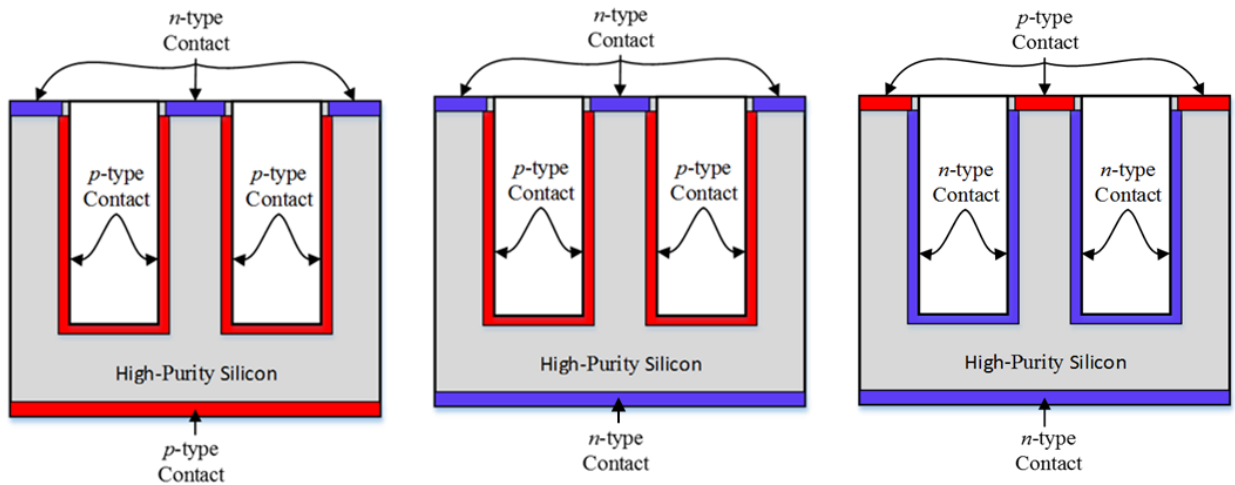


Fig. 5-35. Co-doped Fast-MSND designs. All were fabricated with solid-source diffusion on v -type silicon.

Recall that the depth of the dopant is controlled by the time and temperature of the drive-in step in the diffusion process. A set of npp -, npn -, and pnn -MSNDs were fabricated with deep junctions for all the contacts, and a second set of npp - and npn -MSNDs were produced with a shallow junction on the tops of the fins. Reducing the junction depth should decrease the co-doped areas at the corners at the tops of the fins. Note, the nomenclature for Co-doped MSNDs was top fin contact, trench wall contact, and backside contact. Sample IV curves for each type of Co-Doped MSND are shown in Fig. 5-36. All MSNDs with a deep diffused junction in the fin tops had high leakage current with no rectifying behavior. This was likely caused by junction breakdown in the heavily co-doped regions. Conversely, the MSNDs with shallow-diffused junctions had low leakage current with good rectifying behavior.

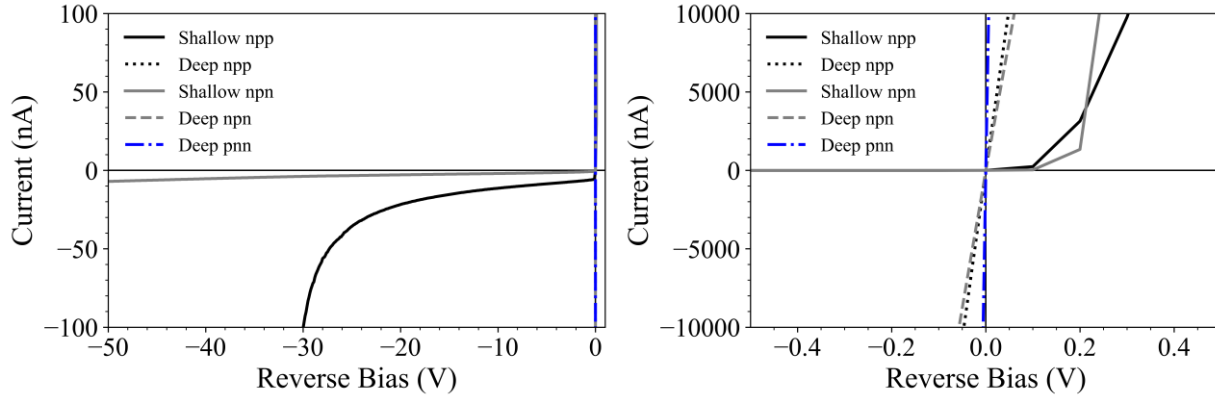


Fig. 5-36. IV curves for Co-Doped MSNDs. The MSNDs with shallow junctions on the tops of the fins showed good rectifying behavior.

The charge collection efficiency of the shallow-junction co-doped MSNDs as a function of amplifier shaping time was estimated using an empty MSND and a collimated ^{241}Am alpha-particle source. In the MSND pulse height spectrum, for a given shaping time, two peaks form if the alpha particles are normally incident on the trenches. A false full energy peak occurs at lower channel numbers and appears from interactions near the tops of the fins. The true full energy peak occurs at higher channel numbers and is from interactions occurring in the bottoms of the trenches. The ratio of the channel number between the false full energy peak and true full energy peak gives an estimate of the charge collection efficiency for that shaping time. This process is described in more detail in the following references [33, 156]. The pulse height spectra for charge collection efficiency measurements for the two shallow-junction co-doped MSNDs and a traditional *pvn*-MSND are shown in Fig. 5-37. The ratio of the full energy peaks (FEPs) for traditional *pvn*-MSND was approximately 90% with a 12- μs shaping time. Conversely, the maximum FEP ratio for the *npn*- and *npp*-co-doped MSNDs was about 0.55 and 0.25, respectively, with 12- μs shaping time. For shaping times less than 1- μs , all designs had suboptimal charge collection efficiency, and therefore, the design was abandoned for fast charge collection MSND designs.

If the design is ever revisited, more complex diffusion masks should be implemented that will allow for an electrode to be attached to the dopant deposited in the trench. The three-terminal design may show improved electric field in the fins if a bias is held across the top of the fins and trench side walls. However, the design may still ultimately fail if the electric field in the co-doped region is higher than silicon's breakdown electric field which could occur at relatively low voltages, because the distance between the electrodes is small.

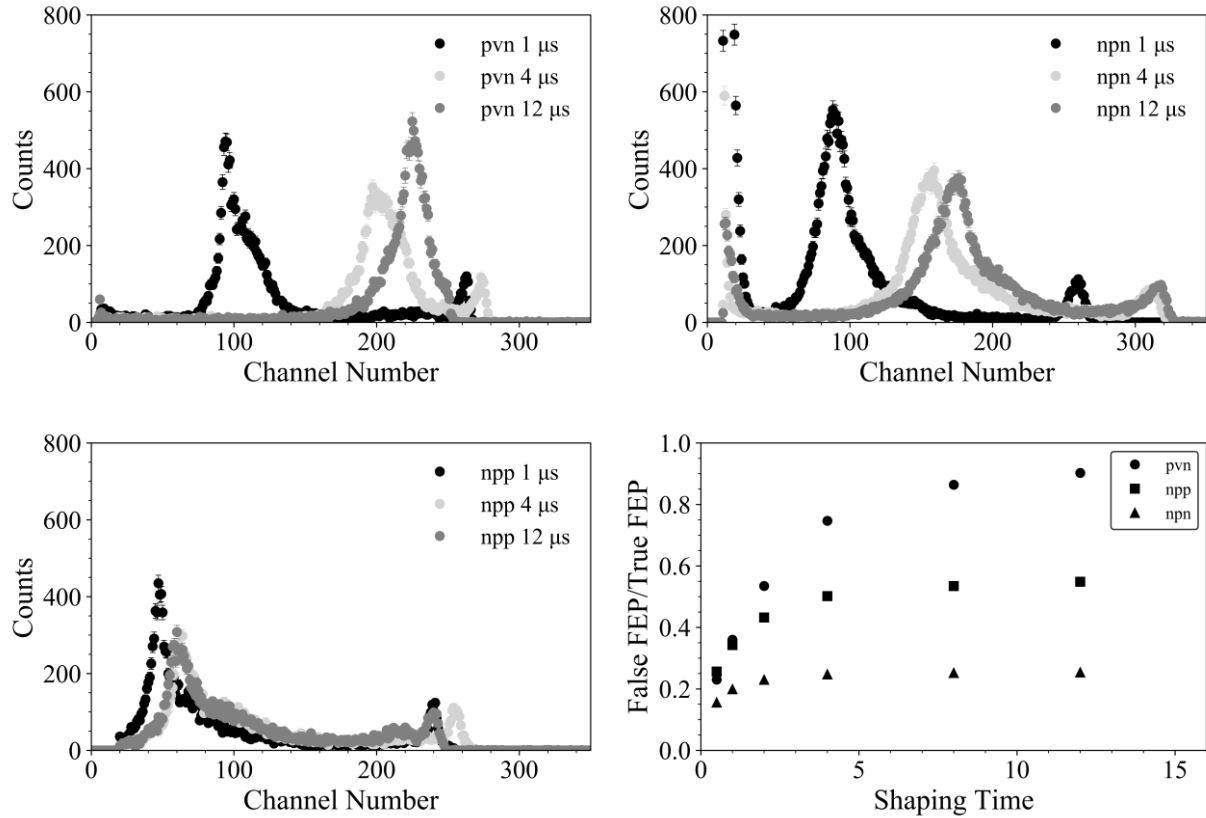


Fig. 5-37. Pulse height spectra for ^{241}Am charge collection efficiency measurements for (Top Left) traditional pvn-MSND, (Top Right) npn-co-doped MSND, and (Bottom Left) npp co-doped MSND. (Bottom Right) Ratio of the false full energy peak (FEP) to true FEP for the three designs shown.

Alternating Trench MSNDs

The alternating trench MSND was designed to have adjacent trenches doped with opposite type material to provide a horizontal electric field where charge carriers are drifted across the width of the fins ($\sim 10\ \mu\text{m}$ maximum) rather than vertically ($400\text{--}600\ \mu\text{m}$ maximum). Shown in Fig. 5-38 is the proposed design where there are two contact fingers on the top surface of the MSNDs, one for the n -type trenches and one for the p -type trenches. Ion implantation was chosen as the junction formation method, because photoresist could be used as an implantation mask on every other trench which eliminated the need for multiple oxide growth steps. Wet and dry oxide growth require high temperatures and significant time to grow. If a dopant was previously deposited and then an oxide growth was performed, the dopants would continue to diffuse deeper into the fins, thereby, increasing the size of the dead region in the fins which ultimately reduces the signal-to-noise ratio. With ion implantation, RTA can be used to activate the dopants with minimal diffusion into the fins.

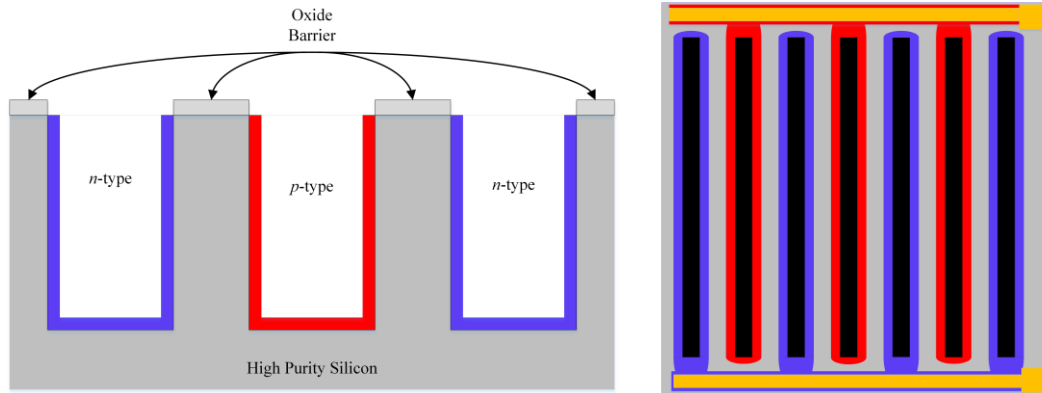


Fig. 5-38. Alternating Trench MSND diffusion profiles. Alternating *n*- and *p*-type trenches will create an intrinsic electric field within the fins causing charge carriers to be swept out laterally. There are no floating contacts in this design.

An abbreviated processing diagram for alternating trench MSND fabrication is shown in Fig. 5-39. After the wafers were etched, a photolithography process was performed to open an implantation window for alternating trenches while protecting the remaining trenches. The wafers were then sent out for *n*-type ion implantation, where half of the trenches would have phosphorus implanted, and the photoresist layer would serve as an implantation mask on the adjacent trenches. The wafers were then sent back to the S.M.A.R.T. Laboratory, and the photoresist was removed, re-applied, and re-patterned for *p*-type ion implantation. Following the *p*-type implantation the wafer was cleaned and annealed, and a final photolithography process was performed to pattern the contact fingers.

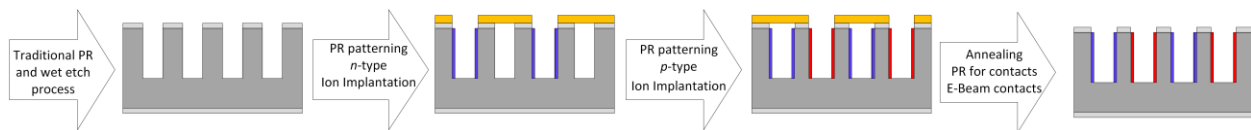


Fig. 5-39. Fabrication process for ion-implanted, alternating trench MSNDs.

A Dry-Film Photoresist (DFPR) processing method was developed to make the implant mask, because spin-on liquid photoresist failed to adequately bridge the high aspect ratio trenches. The DFPR is applied with a heated laminator and then processed like standard photoresist with a soft bake, alignment, UV expose, and development steps. The process was fine-tuned to limit the DFPR extrusion into the trenches such that the photoresist layer was thick enough on the tops of the fins to stop all incident ions during the dopant implant step (see Fig. 5-40).

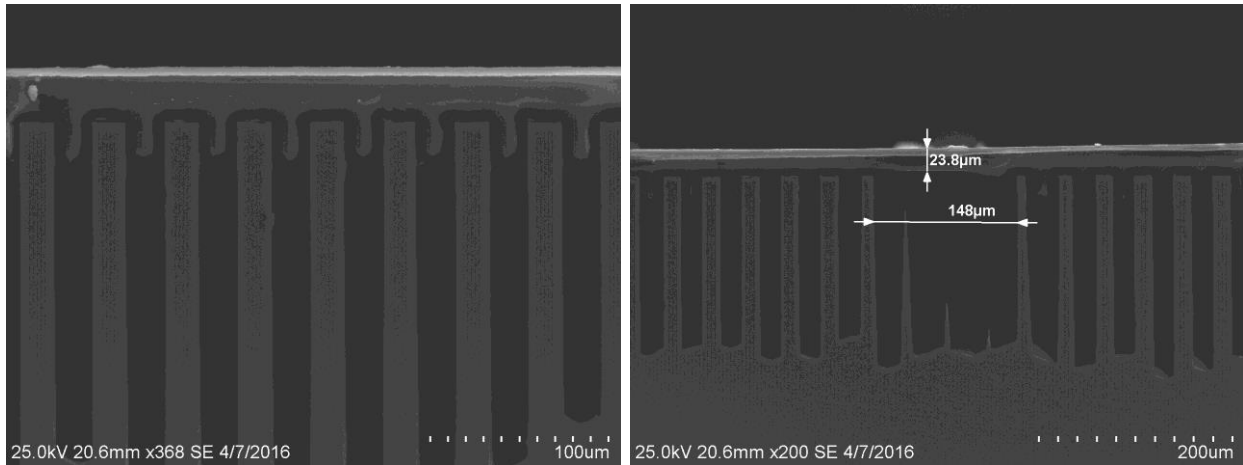


Fig. 5-40. DFPR on an MSND showing minimal extrusion into the trenches and providing an adequate ion implantation mask on the surface.

Boron and phosphorus were used as the *p*-type and *n*-type dopants, respectively. The dopant atoms were implanted at 200 keV to form high-concentration shallow junctions (less than 0.1- μm deep). A dose of approximately 10^{16} cm^{-2} was used. The high dose was required due to the shallow implant angle necessary to implant the entire fin sidewall (see Fig. 5-8). Wafers were patterned and sent to INNOViON for *p*-type implantation. INNOViON started the implant process and performed implants with dose intervals of $5 \times 10^{14} \text{ cm}^{-2}$ to check the ruggedness of the implant mask. After the eighth pass, they noticed severe photoresist liftoff on the edges of the wafer and some liftoff on the diodes (see Fig. 4-40). Three of thirteen wafers had severe delamination on the trenches, four had minimal delamination on the edges, and six had good photoresist adhesion. When the implant masks were reworked, a plasma ashing step was added prior to HMDS application. The final bake time and temperature was also increased to improve adhesion during the implant. The wafers were then returned to complete the implant. After the *p*-type implant was completed, a new implant mask was formed using DFPR for the *n*-type implant. Similar adhesion problems were observed during the *n*-type implantation, and the DFPR mask had to be reprocessed halfway through the implant indicating that the dry film mask was not robust enough to withstand the high dose required. Furthermore, damage to fragile silicon fins was observed and likely caused during transport of the etched wafer to and from the implantation facility.

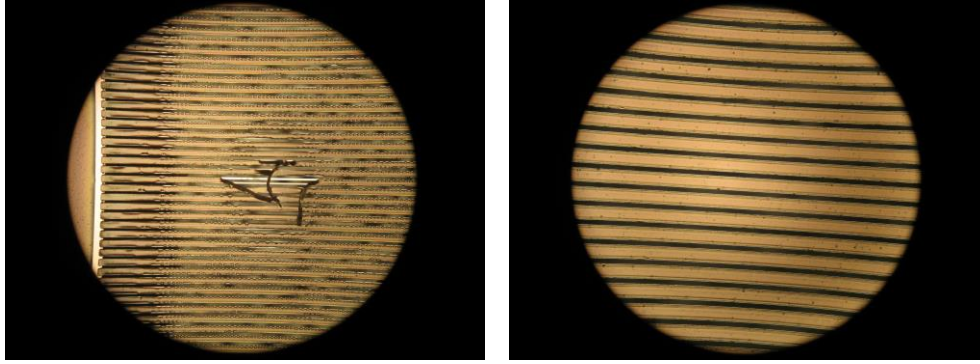


Fig. 5-41. (left) Severe photoresist delamination during ion implantation. Heat and damage incurred during the process degrades photoresist adhesion to the underlying substrate. (right) Example of a dry-film photoresist mask with good adhesion to the substrate.

The IV and CV curves from the best wafer with the alternating trench MSND pattern are shown in Fig. 5-42. The IV curves show characteristics of a rectifying junction, which was not observed for previous Fast-MSND wafers with severe delamination problems. The capacitance of the Fast-MSND diodes ranged from 200-300 pF at 0-V bias. The capacitance is higher than vertically operated *pvn*-MSNDs, which consequently will decrease the signal size. The higher capacitance was expected, because the surface area of the contacts increased and the distance between contacts decreased.

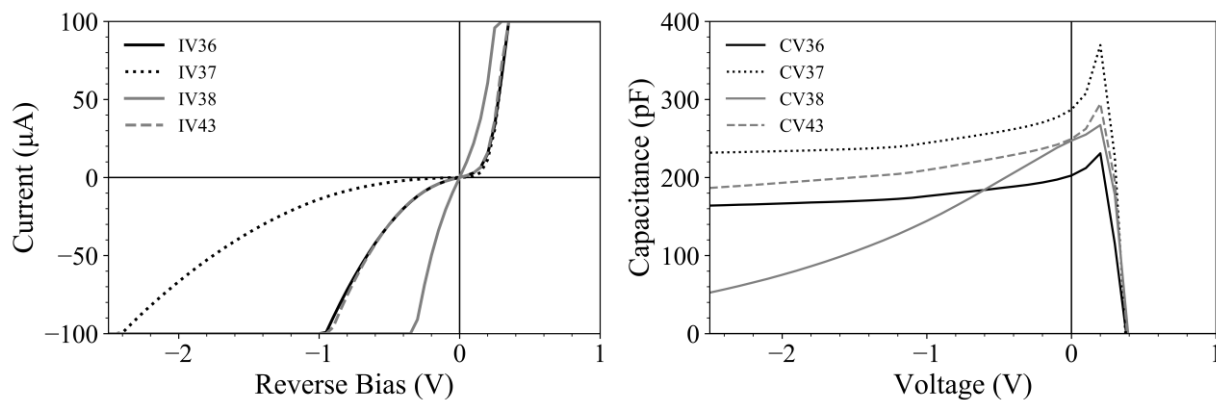


Fig. 5-42. (Left) IV and (Right) CV curves for alternating trench MSND prototype diodes.

The required charge collection time was estimated by performing an alpha-particle charge-collection-efficiency experiment with a normally-incident, collimated ^{241}Am source. The pulse height spectra for shaping times of 0.5, 1, 4, and 12 μs are shown in Fig. 5-43. A distinct full energy peak begins to emerge over the noise floor for shaping times greater than or equal to 1 μs .

The peak continues to shift to higher energy channels as the shaping time increases indicating that charge collection efficiency increases as the charge integration time increases up to at least 4 μs .

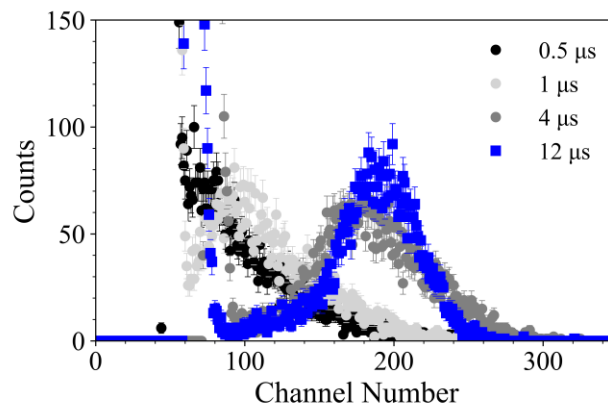


Fig. 5-43. Alpha-particle charge-collection-efficiency experiment for alternating trench MSND prototype wafer. Distinct full-energy peaks were observed for shaping times greater than 1 μs .

The next processing step was to evaporate electrical contacts onto the bond pads, and then, backfill, dice, and mount the diodes into CDBs. Unfortunately, after the contacts were evaporated onto the wafers, the leakage current increased to over 1- μA at 0-V bias which also increased the noise floor and consequently rendered wafers unusable. The alternating trench MSND design was ultimately abandoned due to the high processing costs of implantation and low yield from wafer damage and poor photoresist adhesion.

L-Shaped Doping Profile MSND

An L-shaped MSND diffusion profile was fabricated when photoresist adhesion challenges surfaced during ion implantation processing of Fast-MSND wafers. The L-shaped diffusion profile implements ion-implantation to dope the entirety of one of the fin sidewalls and top of the fins, but unlike the alternating trench diffusion profile, the "L-shape" design does not require a photoresist implantation mask (see Fig. 5-44). After the p -type implant was completed, an n -type contact was diffused onto the backside of the wafer using solid source diffusion. The drive-in stages of the n -type diffusion were used to simultaneously anneal and activate the p -type implantation on the trenched side of wafer.

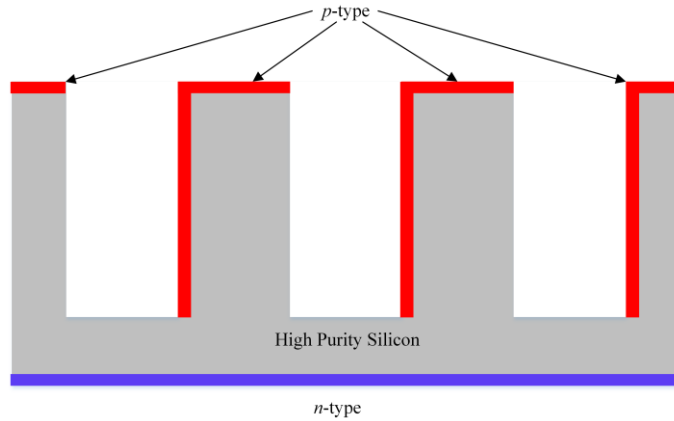


Fig. 5-44. “L-shaped” diffusion profile. This profile was fabricated with a combination of ion implantation (p-type) and solid-source diffusion (n-type). An implantation mask was not required to achieve the desired junction geometry.

IV and CV curves for the L-shaped MSNDs are shown in Fig. 5-45. Next, an alpha-particle charge-collection experiment was performed to estimate the required charge collection time for the MSNDs. Ideally, the location of the peaks on the pulse height spectrum formed from interaction in the tops and fins and bottoms of the fins will be close to each other and be minimally affected by a reduction in shaping time. As shown in the Fig. 5-46, a decreased shaping time from 12 μs to 1 μs significantly shifts the false full energy peak to lower energy channels. This result indicates that the L-shaped diffusion profile may not serve well as Fast-MSND with charge collection times less than 1 μs .

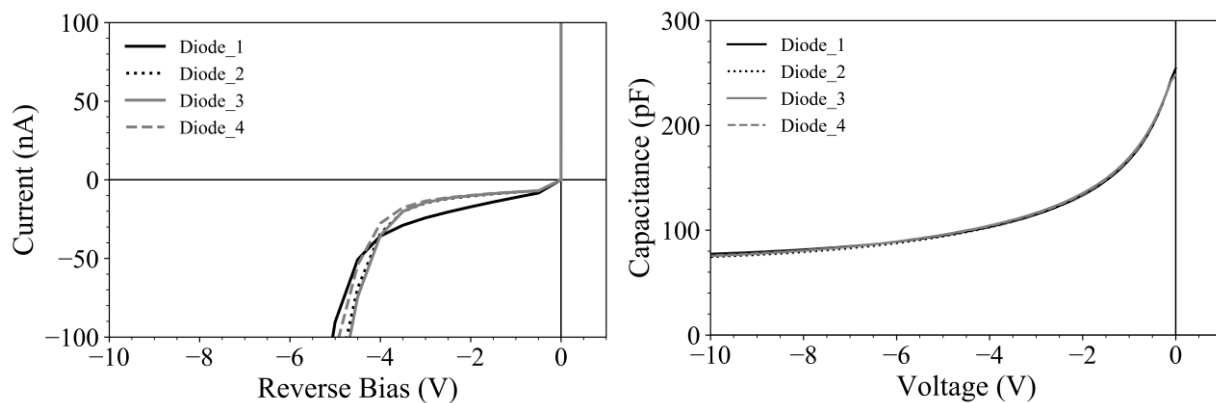


Fig. 5-45. (Left) IV and (Right) CV curves for L-shaped MSND prototypes.

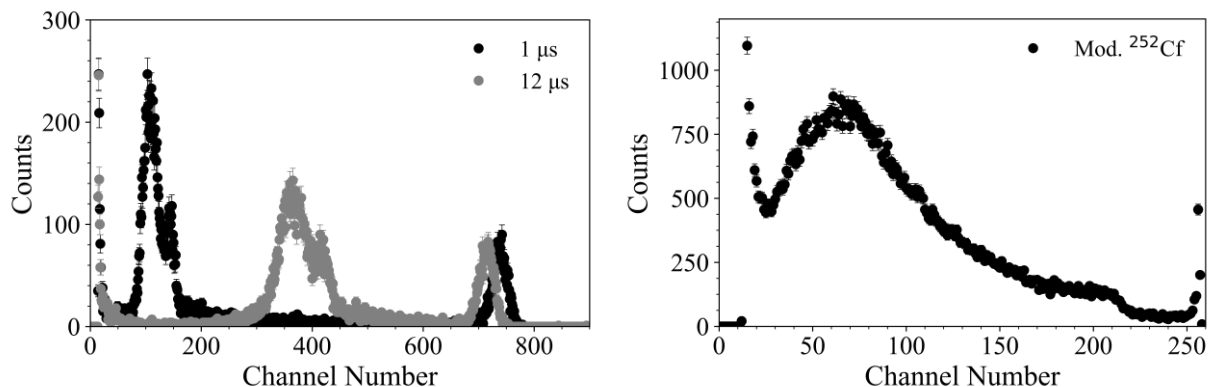


Fig. 5-46. (Left) Alpha-particle charge-collection experiments performed with an ^{241}Am source. The shift in the “false full-energy peak” indicates not all charge was collected for the 1 μs shaping time. The MSND was operated with -2.5 V bias. (Right) Reaction-product spectrum for “L-shaped” MSND measurements with moderated ^{252}Cf . The shaping time for the ^{252}Cf measurement was 12 μs .

The intrinsic thermal-neutron detection efficiency of the L-shaped prototype MSNDs was measured using a moderated Cf-252 source. The theoretical intrinsic thermal-neutron detection efficiency for the MSND and implant geometry was 30%, and the prototype MSNDs measured approximately 25% intrinsic thermal-neutron detection efficiency. The reaction-product pulse-height spectrum (Fig. 5-46) showed a significant valley between the gamma-ray/background noise and neutron signal portions of the spectrum. Although the "L-shape" diffusion profile design was not suitable as a Fast-MSND, it demonstrated a successful implantation method, anneal, and activations of *p*-type dopants.

5.3.2. Other DS-MSND Variants

The following sections describe three DS-MSND variants. The interdigitated DS-MSND was designed to offer fast charge collection times with moderate intrinsic thermal-neutron detection efficiency. The LL-DS-MSND and Spin-on-Dopant DS-MSND were experiments performed to investigate alternatives to solid-source diffusion for junction formation.

Interdigitated DS-MSND

The interdigitated DS-MSND design shown in Fig. 5-47 was investigated to reduce the required charge collection time to less than 1 μs . The dopant profile would not require ion implantation and could be achieved using solid-source diffusion or spin-on-dopant. As with the MSND, the interdigitated DS-MSND should have an intrinsic thermal-neutron detection efficiency of about 30% for normally incident neutrons.

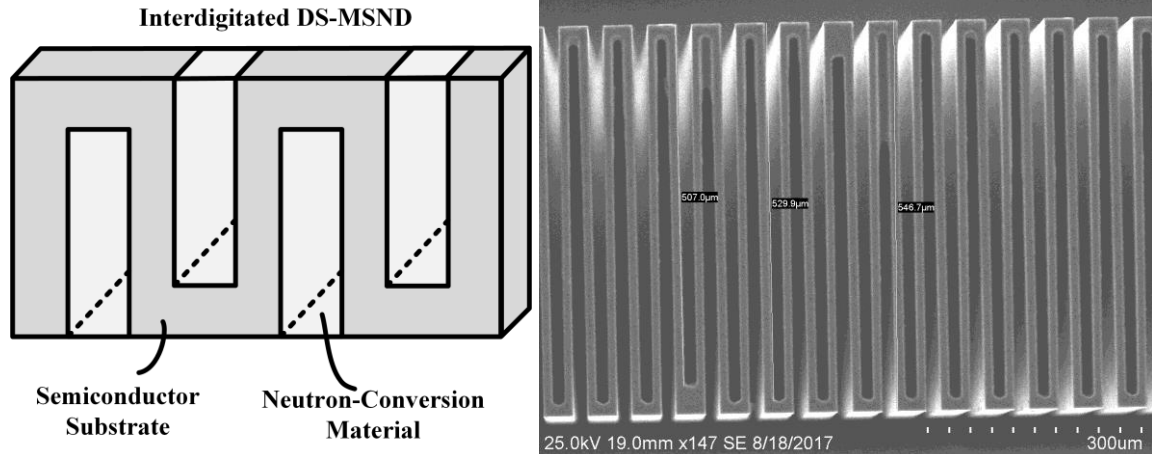


Fig. 5-47. Interdigitated DS-MSND design. One side of the DS-MSND is conformally doped with *p*-type dopant, and the opposite side is doped with *n*-type dopant. Lateral charge carrier movement should be induced with this design and thus sub-microsecond shaping times may be achieved.

Interdigitated DS-MSNDs were processed on 500- μm thick, (110)-orientated silicon wafers. The *p*- and *n*-type junctions were formed using solid source diffusion. Long sourcing and drive-in times were used to try to ensure that the dopant would conformally dope the trench region. After the DS-MSMD was backfilled, IV and CV measurements were performed, and IV curves for seven diodes are show in Fig. 5-48. Rectifying-junction behavior was observed, and the leakage current at 0-V bias was less than 1 nA for six of the seven devices tested. The leakage current then increased rather quickly into the micro-ampere region around -0.2 V applied bias. Zero-volt bias operation was adequate because the fins are narrow and charge is swept laterally. The capacitance of the interdigitated DS-MSND prototype was likely greater than 1.9 nF, which is the maximum capacitance that can be measured with the available CV-meter.

Neutron sensitivity measurements were performed using a moderated ^{252}Cf source, 142 IJ preamplifier, Canberra 2022 amplifier, and an Ortec Easy-MCA. The resulting pulse-height spectra for shaping times of 12 μs , 4 μs , and 2 μs with 0-V bias are shown in Fig. 5-48. Response above background levels was observed for each measurement, but there was not a clear valley typical of the MSND reaction product spectra. The small pulse heights could be attributed to high capacitance and large dead regions from deep junctions. In order for the interdigitated design to be successful, the dopant drive-in times could be reduced to decrease the “dead” volume and the diode active-area must be decreased to reduce the capacitance.

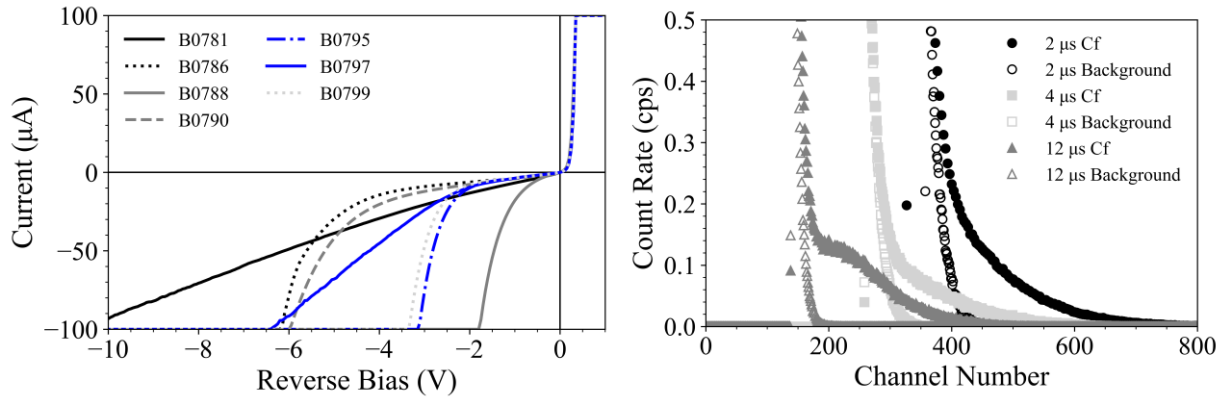


Fig. 5-48. (Left) IV measurements for interdigitated DS-MSNDs. (Right) Reaction product spectra for an interdigitated DS-MSND. Low count rates were likely due to a poor LiF backfill, and the low signal to noise ratio may be attributed to high capacitance.

LL-Shaped Doping Profile DS-MSND

Before discovering that the ${}^6\text{LiF}$ backfill density was the main factor contributing to low intrinsic thermal-neutron detection efficiencies for DS-MSNDs, the leading theory was dead regions within the DS-MSND from solid-source diffusion and less than optimum charge collection efficiency were the main causes for poor detector performance. Thus, ion implantation was considered for the junction formation process, because shallow junctions can be fabricated. Following the success of the ion-implanted L-shaped, single-sided MSND, LL-shaped DS-MSNDs were processed with a similar ion-implantation and RTA process. To minimize costs, the LL-shaped DS-MSND were implanted simultaneously with several of the alternating trench MSNDs. Due to the timing of the implants the LL-Shaped DS-MSND would only be able to receive n -type implants on both sides of the wafer, and therefore, the LL-Shaped DS-MSNDs were processed on 5-kohm-cm, p -type silicon instead of n -type silicon (see Fig. 5-49).

After the n -type (phosphorus) implant, the DS-MSND wafer was cleaned and a thin oxide layer was grown to limit dopant-out diffusion before the wafers was annealed at 1000°C for 1 hour. The pulse height spectrum was measured with a moderated ${}^{252}\text{Cf}$ neutron-source after the DS-MSNDs had been backfilled, diced, and mounted into CDBs. The intrinsic thermal-neutron detection efficiency of the “LL-shape” DS-MSNDs was approximately 31%. High manufacturing cost, increased lead times, and damage to the delicate silicon fins during shipment to and from the implantation facility prohibited further probing into the viability of using ion implantation as means to dope high-efficiency DS-MSNDs.

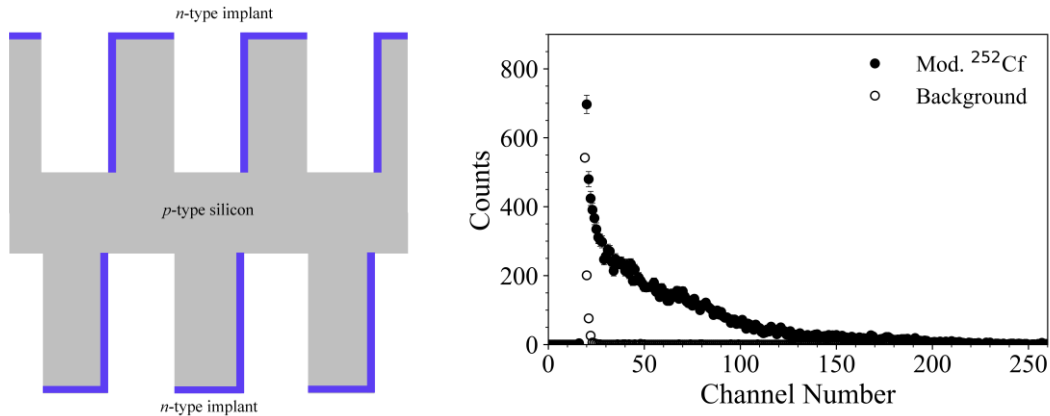


Fig. 5-49. (Left) Drawing of npn-type, LL-shaped, DS-MSND. (Right) Pulse height spectra for a moderated ^{252}Cf source and background. Elevated noise floor and poor packing fraction limits detection efficiency to $\sim 31\%$. The shaping time was $12\ \mu\text{s}$ for both measurements.

Spin-on-Dopant DS-MSND

Spin-on dopant (SOD) was another semiconductor doping method investigated as an alternative doping process to solid-source diffusion. In the SOD process, a solvent-based solution containing p - or n -type dopants is spun onto a wafer, and then, the solvent is baked out leaving only the dopant behind. The wafer is then placed into a high temperature furnace so that the dopants on the surface of the wafer diffuse into the wafer and become electrically active. Spin-on-dopant is relatively inexpensive when compared to ion implantation. Furthermore, SOD can be used to fabricate conformal junction profiles, because it is initially applied to the wafer in liquid form. Several fully conformal pvp -type wafers were fabricated using SOD, and the maximum measured intrinsic thermal-neutron detection efficiency was nearly 45%, close to the maximum achievable detection efficiency at that time of about 53% (see Fig. 5-50).

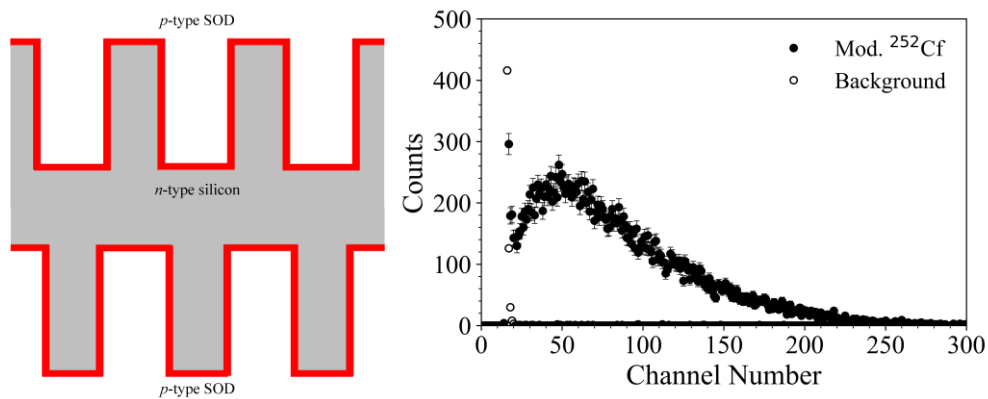


Fig. 5-50. (Left) Schematic of diffusion profile formed from SOD processing. (Right) Pulse height spectrum of pvp -type DS-MSND fabricated with boron-loaded SOD.

Chapter 6 - Microstructured Semiconductor Neutron Detectors

Instruments: Design and Characterization

Recall that the MSND technology was funded to provide an alternative to ^3He for thermal neutron detection and simultaneously provide high-fidelity tools to the warfighter to improve their capabilities to detect, locate, and identify illicit radioactive material. The detection of SNM, which if possessed by rogue entities could be used in a nuclear weapon, is of particular interest because the materials classified as SNM constitute a handful of elements that spontaneously emit neutrons. Therefore, if a detector registers a neutron signature above the background rate an alarm should be triggered, and the nature of the source should be closely investigated. In addition to national security concerns, neutron detectors are commonly used in industrial applications, personal dosimetry, and basic science research including neutron scattering and space exploration. MSND and DS-MSND based instruments were designed to provide affordable, high efficiency, alternatives for neutron detection in all these areas.

When performing a radiation measurement, the relative uncertainty (or precision) in a measured count rate is inversely proportional to the square root of the total number of counts recorded [44, 45, 157]. The total number of counts recorded is a function of (1) the activity of the source and any shielding or moderation around the source, (2) the distance between the source and the detector, (3) the active area of the detector, and (4) the detection efficiency of the detector. In many cases, such as standoff detection or dosimetry, the first two factors cannot be changed by the operator. The size of the detector is usually bound by the mission space. For example, a handheld or wearable detector must be reasonably small and light weight while a radiation portal monitor can span several square meters. The final factor, detection efficiency, is arguably the most important, because improved detection efficiency increases the probability of measuring incident neutrons. Thus, much effort has been concentrated on maximizing the intrinsic thermal-neutron detection efficiency of individual DS-MSNDs. These devices were subsequently implemented into larger arrays for field deployable detectors systems. Introduced in this chapter are the design, simulations, and characterization of the latest iterations of Helium-3 Replacement (HeRep) detectors, Modular Neutron Detectors (MNDs), and Wearable Detectors Devices (WDDs).

6.1. Direct ^3He -Replacement (HeRep) Detectors

Historically, the “gold standard” for thermal-neutron detection was defined by ^3He gas-filled detectors. Decreased availability and increased price has motivated research into alternative neutron detector technologies. MSND technology is compact, rugged, mass-producible, low-power, and can be arrayed to form larger detector systems. Two generations of HeRep detectors were developed based on single sided MSNDs to serve as a drop-in replacement for 2-in. diameter, 4-atm, ^3He neutron detectors [21, 33, 126, 128]. The HeRep Mk II measured 102% and 95% of the count rate of a similarly sized ^3He neutron detector for a bare ^{252}Cf with an without detector moderator, respectively [128].

When DS-MSNDs were developed, the focus on the HeRep instrumentation shifted to provide a replacement for compact, high-pressure, ^3He detectors that could replace legacy detectors in smaller, light weight, handheld detector systems.

6.1.1. HeRep Mk III

The HeRep Mk III was the first detector system to implement DS-MSNDs and was designed as a replacement for 6-atm, 4.5-in. long, 0.75-in. diameter, ^3He neutron detectors [33, 122, 125]. The HeRep MK III comprises 12 *pvp*-type DS-MSNDs with intrinsic thermal-neutron detection efficiencies greater than or equal to 50%, two sets of pulse processing and discrimination electronics, and a TTL-pulse generator that produced pulses when the input pulse was greater than a programmable LLD. No bias circuitry was required, because the *pvp*-DS-MSNDs operate on the built-in potential of the *pn*-junctions in the fins. Two HeRep Mk IIIs were produced, one based entirely on common FR4 circuit board material and one based on Kapton®-based flexible circuit board material (see Fig. 6-1). FR4 is the more widely available and cost-effective option for printed circuit boards, but boron and bromine present within the FR4 board material have relatively large thermal- and fast-neutron absorption cross-sections and can reduce the internal neutron flux without contributing to the reported count rate. However, at the time of development, the cost of Kapton® circuit board was roughly one hundred times that of identical FR4 material. The two HeRep MK III detectors were developed to study how the circuit board material affected the thermal neutron detection efficiency of HeRep detectors.

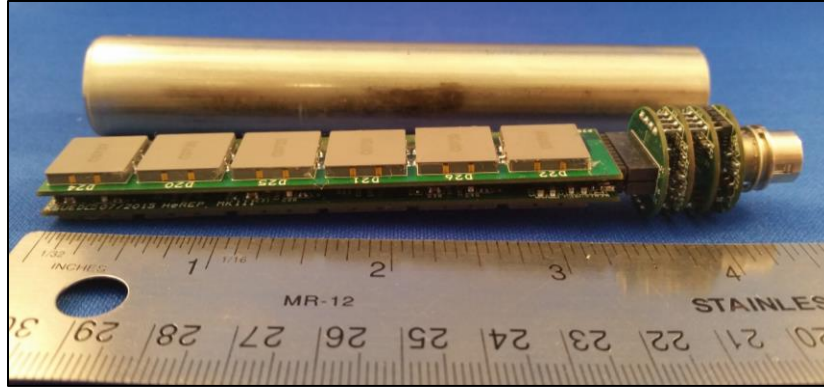


Fig. 6-1. FR4-based HeRep Mk III with 12 DS-MSNDs.

The angular dependence of the HeRep Mk III response to a moderated, 35-ng ^{252}Cf source at 25 cm with and without the HeReps encased in a 3-in. diameter HDPE moderator cask is shown in Fig. 6-2. The count rate for the flexible circuit board HeRep was approximately 15% higher than the FR4 based HeRep when the detectors were placed in the HDPE moderator cask. The depressed count rate of the FR4-based HeRep was mostly likely caused by the ^{10}B content of the FR4 circuit board acting as a thermal neutron sink. The HeReps had the same count rates in the bare source, bare detector configuration. If the cost of flexible circuit board material starts decline as it is implemented more in other industries, the benefit to cost ratio may improve so that mass produced HeRep systems could implement the Kapton-based circuit boards.

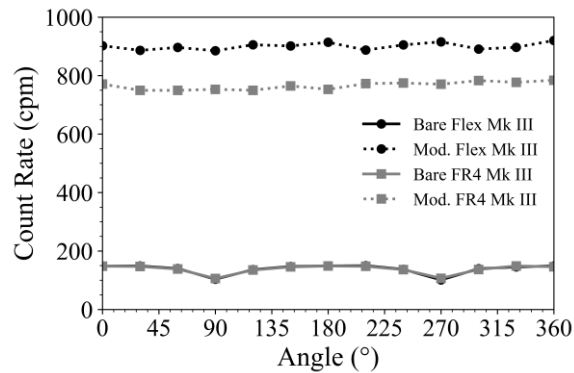


Fig. 6-2. HeRep Mk IV response to moderated ^{252}Cf at 25 cm. The responses for the unmoderated FR4 and unmoderated flexible Kapton based HeReps are nearly identical. The background count rate ranged from 1.5 cps to 3.3 cps for all measurements.

In addition to not needing high voltage insulating standoffs that create dead regions within the detector where neutrons are absorbed but not detected, the option to add moderator to void regions in the interior of the detector case is another advantage solid-state neutron detectors have over gas-filled neutron detectors like ^3He tubes. Small HDPE moderator beads were added to the interior regions of the flexible, Kapton-based HeRep Mk III. The detector response to a moderated

^{252}Cf source was measured and compared to measurements performed without interior moderator beads (see Fig. 6-3). The interior moderator improved the response for the bare detector configuration but had negligible effect in the moderated detector configuration likely due to the relatively small volume of interior moderator compared to the volume of exterior moderator.

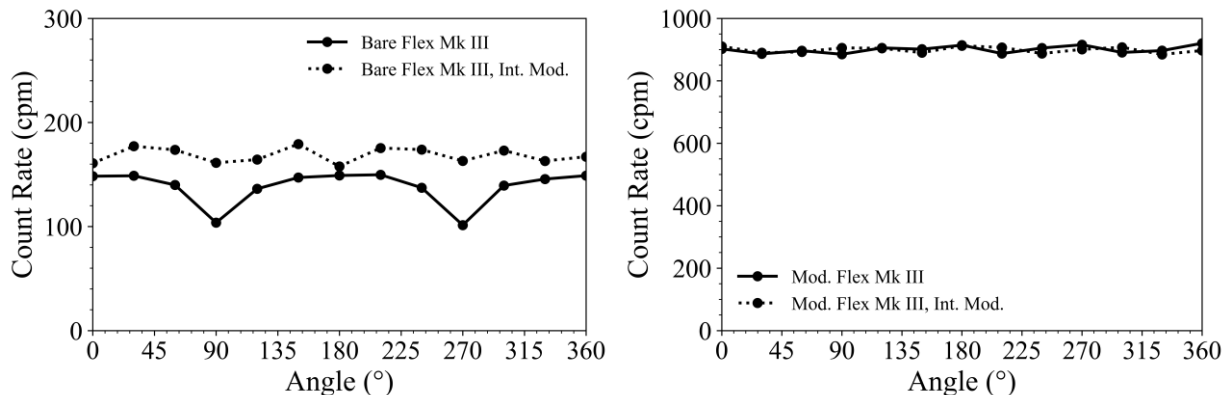


Fig. 6-3. (Left) Bare HeRep Mk III and (Right) Moderated HeRep Mk IV response for the interior moderator and no-interior moderator configurations to moderated ^{252}Cf at 0.25 m.

The HeRep Mk III was directly compared to a 0.75-in. diameter, 3-in. long, 10-atm ^3He detector that had a total length of 4.5-in. when including the SHV connector. Measurements were performed with a moderated ^{252}Cf source at 25 cm with and without the HeRep and ^3He detector in a 3.0-in. diameter by 5.75-in. long HDPE moderator cask. The results are shown in Table 6-1. The HeRep Mk III response ranged from $45.4 \pm 0.2\%$ up to $56.7 \pm 0.2\%$ of the 10-atm ^3He detector depending on the source and detector moderator configuration. Finally, the GRR was 1.5×10^7 for ^{137}Cs at a dose rate of 50 mR/hr.

Table 6-1. Direct comparison to ^3He for a moderated 30-ng ^{252}Cf source at 25 cm.

Detector	Bare Detector		Moderated Detector	
	Net Count Rate (cps)	% of 10-atm ^3He	Net Count Rate (cps)	% of 10-atm ^3He
10-atm ^3He	4.41 ± 0.02	100%	19.97 ± 0.04	100%
HeRep Mk III (No Interior Moderator)	2.09 ± 0.01	$47.4 \pm 0.3\%$	10.88 ± 0.03	$54.4 \pm 0.2\%$
HeRep Mk III (Interior Moderator)	2.00 ± 0.01	$45.4 \pm 0.3\%$	11.33 ± 0.03	$56.7 \pm 0.2\%$

6.1.2. HeRep Mk IV

Two square form factor HeRep Mk IV detector prototypes were fabricated. The square form factor was achieved by attaching the DS-MSNDs perpendicularly to the main motherboard strip instead of using a planar surface mount arrangement and allowed for more efficient utilization of the detector packaging. One HeRep Mk IV had dimensions of 0.75 in. x 0.75 in. x 3.1 in, and the other had dimensions of 0.75 in. x 0.75 in. x 6.1 in. Each design integrated 15 of the 1-cm² DS-MSNDs with intrinsic thermal-neutron detection efficiencies between 50% and 55%. The shorter HeRep Mk IV design implemented the maximum number of DS-MSNDs per unit volume possible, and the larger HeRep Mk IV included interior moderator between adjacent DS-MSNDs and also the electronic boards containing all required signal processing electronics (see Fig. 6-4).

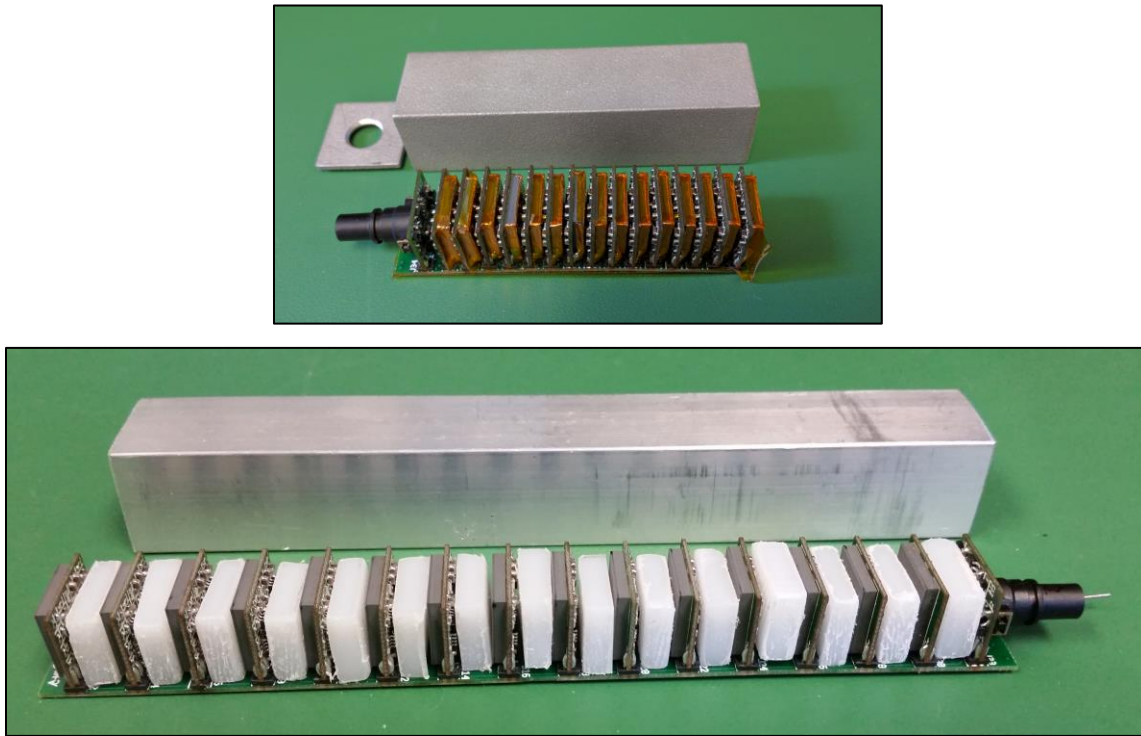


Fig. 6-4. (Top) 0.75-in by 0.75-in by 3.1-in HeRep Mk IV (Bottom) 0.75-in by 0.75-in by 6.1-in HeRep Mk IV. Each were populated with 15 DS-MSNDs and 16 pieces of HDPE moderator placed in void spaces between adjacent detectors and electronics in the longer HeRep Mk IV.

The neutron response of the HeRep Mk IV detector systems were compared to the previously described 10-atm ³He detector, with results shown in Table 6-2. In bare detector configurations, the 3.1-in. HeRep Mk IV measured approximately 93%, 79%, and 117% of the count rate of the 10-atm ³He detector for bare ²⁵²Cf, moderated ²⁵²Cf, and bare AmBe sources, respectively. With the detectors in a 1-in. thick by 3.1-in. tall HDPE moderator cask the 3.1-in.

HeRep Mk IV count rate was about 78% and 82% of the count rate of the ^3He detector for bare ^{252}Cf and moderated ^{252}Cf , respectively. These results indicated that the 3.1-in. HeRep Mk IV responds better when compared to the 10-atm ^3He detector to sources that have a higher-energy neutron spectrum. As the average neutron energy decreases, as in the case for moderated sources and/or moderated detectors, the ^3He response improves over the HeRep Mk IV detector. Therefore, the 3.1-in. HeRep Mk IV may be desirable over a ^3He detector for small detector package applications, where the use of external moderator may be limited by size and weight constraints. Additionally, the 3.1-in. HeRep Mk IV would offer a more cost-effective alternative to ^3He while maintaining nearly 80% of the performance of the ^3He detector if external moderator is used.

The 6.1-in. long HeRep Mk IV was developed to study the effect of interior moderator in the HeRep Mk IV. Fifteen DS-MSNDs were used in the 6.1-in. long HeRep Mk IV, just like the 3.1-in. long Mk IV, but the space between detectors in the 6.1-in. long version was filled with blocks of HDPE. The goal of adding HDPE was to improve the detector response to fast-neutrons and to be able to increase the length of the detector without increasing the number of DS-MSNDs while not significantly increasing the dead regions of the detector not sensitive to neutrons. For the 6.1-in. HeRep Mk IV to have the same intrinsic detection efficiency as the 3.1-in. HeRep Mk IV the count rate of 6.1-in. long detector would have to be approximately twice the 3.1-in. long detector count rate. The longer HeRep Mk IV had higher count rates than its shorter counterpart, but the count rates were not twice as high. This result indicated additional DS-MSNDs would be required to achieve the same intrinsic neutron detection efficiency.

Table 6-2. HeRep Mk IV direct comparison to a 0.75-in diameter by 3.1-in long, 10-atm ³He detector. A 26.5-ng ²⁵²Cf source and an AmBe source emitting 200,000 neutrons per second were used for the measurements. The source-to-detector distance was 25 cm for all measurements.

Detector	Net Count Rate (cpm)	% of 10-atm ³ He
<i>Bare ²⁵²Cf, Bare Detector</i>		
10-atm ³ He	19.0 ± 0.3	
3.1-in HeRep Mk IV	17.6 ± 0.2	92.8 ± 1.8%
6.1-in HeRep Mk IV	20.6 ± 0.3	108.5 ± 2.0%
<i>Moderated ²⁵²Cf, Bare Detector</i>		
10-atm ³ He	208.8 ± 1.4	
3.1-in HeRep Mk IV	165.8 ± 1.2	79.3 ± 0.8%
6.1-in HeRep Mk IV	244.6 ± 1.5	117.1 ± 1.0%
<i>Bare ²⁵²Cf, Moderated Detector</i>		
10-atm ³ He	355 ± 2	
1" thick x 3.1" tall HDPE		
3.1-in HeRep Mk IV	277 ± 2	78.1 ± 0.8%
1" thick x 3.1" tall HDPE		
10-atm ³ He	195 ± 1	
5/8" thick x 6.1" tall HDPE		
6.1-in HeRep Mk IV	255 ± 2	130.4 ± 1.2%
5/8" thick x 6.1" tall HDPE		
<i>Moderated ²⁵²Cf, Moderated Detector</i>		
10-atm ³ He	610 ± 5	
1" thick x 3.1" tall HDPE		
3.1-in HeRep Mk IV	502 ± 4	82.2 ± 0.9%
1" thick x 3.1" tall HDPE		
10-atm ³ He	549 ± 4	
5/8" thick x 6.1" tall HDPE		
6.1-in HeRep Mk IV	625 ± 5	113.8 ± 1.2%
5/8" thick x 6.1" tall HDPE		
<i>Bare AmBe, Bare Detector</i>		
10-atm ³ He	35.3 ± 0.4	
3.1-in HeRep Mk IV	41.2 ± 0.4	116.7 ± 1.7%
6.1-in HeRep Mk IV	41.2 ± 0.4	116.5 ± 1.8%

6.1.3. HeRep Mk V

The HeRep Mk V combined features from the HeRep Mk III and Mk IV designs. It has a rectangular form factor measuring 1-in. x 1-in. x 6-in. and implemented 20 DS-MSNDs with intrinsic thermal-neutron detection efficiency of 50-55% arranged onto two strips. The DS-MSNDs alternate on the front and back side of the circuit board with the accompanying electronics on the opposite side, and the two strips were arranged in an “L-shaped” pattern, see Fig. 6-5. This design limits streaming paths between detectors, which were apparent in the Mk III design, while maximizing active length. As with previous generations, all required signal processing electronics are included within the HeRep package, and the HeRep Mk V interfaces via USB-C to an external measurement monitoring system, i.e. a computer, tablet, or phone. The void space within the detector was filled with an HDPE moderator block. The angular response of the detector to a moderated ^{252}Cf source at 25 cm is shown in Fig. 6-5. The HeRep Mk V exhibits a marked improvement over the previous generation devices when one or both of the detector strips are pointed towards the source. When the HeRep Mk V is rotated 180 degrees, the HeRep Mk V performs similar to the 6.1-in. long HeRep Mk IV. The suppressed response is caused by the HDPE interior moderator reflecting already thermalized neutrons from the moderated ^{252}Cf source. When comparing the area corrected responses of the HeRep Mk III, Mk IV, and Mk V, the 3.1-in Mk IV was the most efficient followed by the Mk V, the 6.1-in. Mk IV, and Mk III.

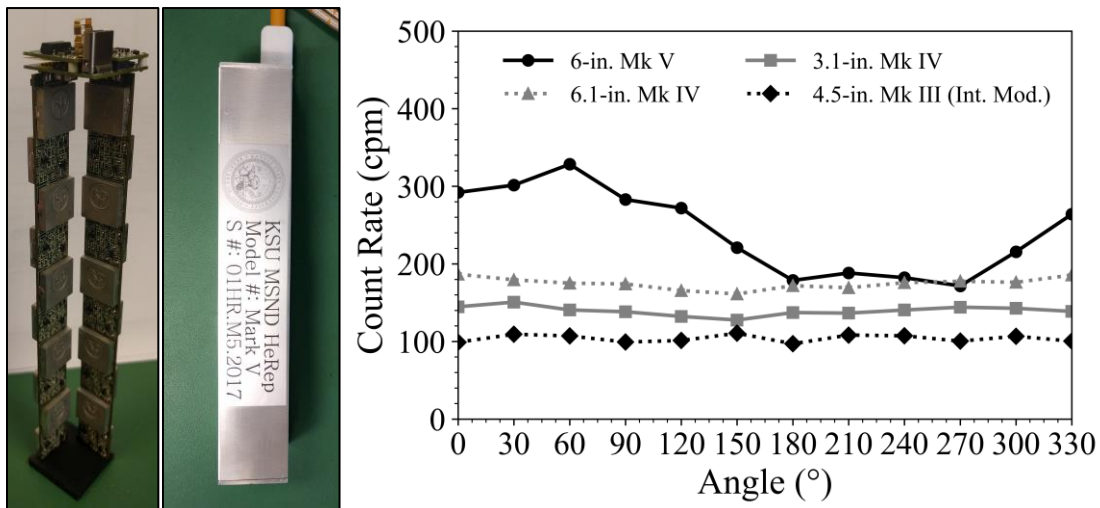


Fig. 6-5. (Left and Middle) HeRep Mk V detector system with 20 DS-MSNDs that have intrinsic thermal-neutron detection efficiencies of at least 50%. (Right) Angular response of the HeRep Mk V compared to both HeRep Mk IV detectors and the HeRep Mk III detector

6.2. Modular Neutron Detectors (MND)

The Modular Neutron Detector (MND) was designed to serve as a compact, lightweight, high-sensitivity neutron detector to fulfill a need for detectors sizes between small arrays like the Domino and larger stationary panel arrays or cumbersome handheld detectors. The first two generations of MNDs developed are described in prior work [33]. The MNDs were designed specifically to be low-profile to allow for covert deployment. This work describes the design and performance of the MSND-based MND Mk III and the design of the MRD Mk I, the first modular detector to implement DS-MSNDs.

6.2.1. *MND Mk III*

The MND Mk III is composed of 24, 1-cm² active area, individually shielded MSNDs with intrinsic thermal-neutron detection efficiencies of approximately 30% and on-board preamplifier, amplifier, discriminator, TTL-pulse generating, and bias electronics (see Fig. 6-6 and Fig. 6-7). Additionally, the MND Mk III could be attached to an on-board battery and connected to a communications dongle for wireless communication to an Android device via Bluetooth Low Energy (LE) to form a fully wireless detector module, or the MND Mk III could be externally connected to a master control board that provides power and a wired communication interface between the sensor and an Android device via low-voltage differential signal (LVDS) communications protocol. Each MND was enclosed in an ABS plastic case. The wireless MND Mk III measured 11.2 cm x 6.1 cm x 1.7 cm, and the dimensions of the wired MND Mk III was 10.4 cm. x 6.4 cm x 1.4 cm. During measurements, the MND accumulates counts on an on-board 8-bit counter when the pulse height was above the programable LLD. The counts are read out from the counter and relayed to the Android readout device at one seconds intervals.



Fig. 6-6. Image of a wireless MND Mk III populated with 24, 1-cm² MSNDs with intrinsic thermal neutron detection efficiencies of 30%.

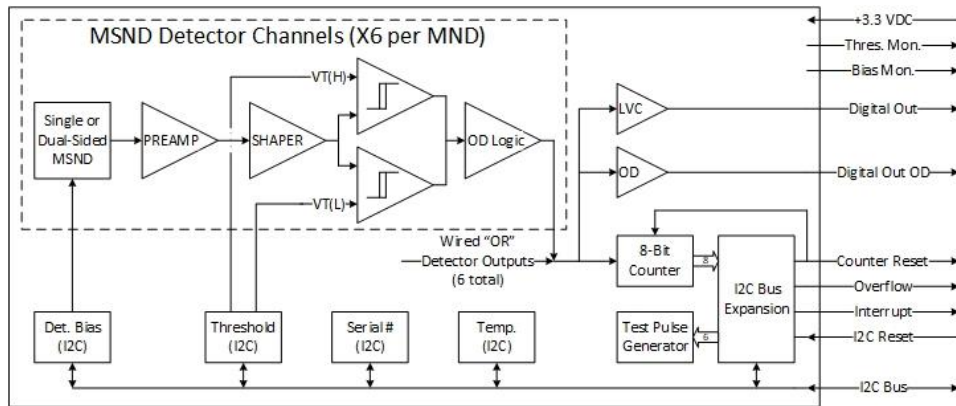


Fig. 6-7. Schematic of MND electronics.

The radiation response of the MND Mk III was modeled in MCNP and compared to measurements with a ²⁵²Cf source. The MCNP MND model included the MSNDs, FR4 electronics boards, CDBs with RF shields, Li-ion battery, and an ABS plastic case as well as an approximation for the concrete walls of the room in which the actual measurements took place to account for room scattering. The simplified MND model is shown in Fig. 6-8, and an example MCNP input card is in Appendix C. Measurements were performed with the MND Mk III for a bare ²⁵²Cf source at 25 cm, a moderated ²⁵²Cf source at 25 cm, and background, and the results are shown in Table 6-3. The source moderator cask was composed of a 0.5-cm radius by 9-cm tall cylindrical void where the source was placed, surrounded by a 0.5-cm thick by 9-cm tall lead cylinder, encased in a 1-cm thick by 10-cm tall steel cylinder all enclosed in a 2.5-cm thick, 13-cm tall HDPE outer cylindrical shell.

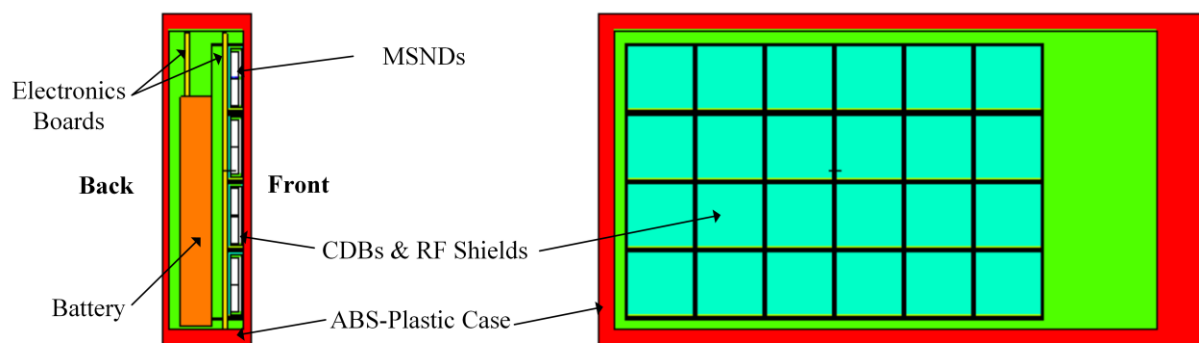


Fig. 6-8. MCNP model of the MND Mk III. The “front” side is nearest the MSNDs, and the “back” side is nearest to the battery.

Table 6-3. Simulation and measurement results for an MND in stand-alone configuration for ^{252}Cf . The source to detector distance was 25 cm.

	MND Mk III Response (cps/ng)			
	Front		Back	
	Simulation	Measured	Simulation	Measured
Bare ^{252}Cf @ 25cm	0.0138 ± 0.0001	0.0175 ± 0.0002	0.0129 ± 0.0001	0.0113 ± 0.0002
Moderated ^{252}Cf @ 25cm	0.1506 ± 0.0002	0.130 ± 0.0012	0.0957 ± 0.0001	0.0823 ± 0.0007
Background (measured)		0.0102 ± 0.0003	cps	

The simulation and experimental measurements showed agreement within a factor of 1.3. The differences between the simulation and measurement were likely caused by simplifications of the battery, discrete electronics in the MND, and the concrete walls of the room. Nevertheless, the simulations served as a good first approximation to estimate performance. The simulations and measurements both showed that the MND operating in a stand-alone configuration has higher response when irradiated from the front side, because the neutrons do not have to travel through the battery and FR4 printed circuit board (PCB) where they can be scattered away or absorbed by ^6Li or ^{10}B present in the battery and PCB, respectively.

Measurements were performed with an MND mounted on the center of the torso of an ANSI phantom to estimate the response of the detector if it were implemented as a personal radiation monitor or used as part of a distributed network of sensors deployed on multiple persons. The response was measured for a 12.3-ng (28,500 n/s) bare and moderated ^{252}Cf source at 25 cm. The results are listed in Table 6-4. As expected, the count rate significantly increased for both

sources over the previously discussed stand-alone operation, because the phantom acts as a large neutron moderator near the detector. The MND performance is comparable to other neutron-sensitive personal radiation detectors commercially available like the Mirion Technologies PDS-100GN/ID which states a neutron response of 3 cps for 28,000 n/s from ^{252}Cf with the detector on a phantom [158].

Table 6-4. Measurement results for one MND Mk III centrally located on a phantom to a 12.3-ng ^{252}Cf source located 25 cm from the detector.

Source	Count Rate (cps)
Bare ^{252}Cf	2.46 ± 0.02
Moderated ^{252}Cf	4.94 ± 0.05
Background	0.0154 ± 0.0005

6.2.2. MRD Mk I

The Modular Radiation Detector (MRD) has been designed as an advanced version of its MND predecessor incorporating high-efficiency DS-MSNDs and a spectroscopic gamma-ray detector within a single package. The critical design criteria included the following:

- Implement DS-MSNDs for increased neutron sensitivity
- Include spectroscopic gamma-ray detector capable of isotope identification
- Reduce size to improve concealability
- Wired and wireless communication available within same package
- Real-time readout and leave behind, monitor, and retrieve operational modes
- Minimum 8-hour mission lifetime

The newly designed *pvp-n-dot* or *pvp-n-ring* DS-MSNDs will be integrated into the MRD providing at least double the intrinsic thermal-neutron detection efficiency over the MND Mk III which included 30% $\varepsilon_{int,th}$ single-sided MSNDs. Recall that the polarity of pulses from the *pvp-n-dot* design is the same regardless of which set of fins the interaction occurs, and therefore, only one set of signal processing electronics is required in the MRD just like the MND. Additionally, a bias supply was also already incorporated into the MND Mk III, so it is likely that only small changes in the neutron pulse processing components will be required.

Simulations were performed with MCNP6.1 to estimate the neutron detection efficiency of the MRD with DS-MSNDs. The neutron response to a thermal-neutron (0.025 eV) beam with the MRD in a stand-alone configuration and the response of an MRD to a bare ^{252}Cf source with the MRD mounted on an ANSI standard phantom was modeled. For initial approximations, the battery, electronics boards, and cases were re-used from the MND Mk III model. MRDs with 4, 6, 8, 12, 16, 20, and 24 DS-MSNDs were considered. The first set of simulations was performed with 1-cm² DS-MSNDs having an intrinsic thermal-neutron detection efficiency of 60% and the simulations were repeated with the intrinsic thermal-neutron detection efficiency increased to 70% to cover the ranges of detection efficiency achievable with the new design.

The results of the simulations are listed in Table 6-5. The simulations serve as a baseline estimate of performance for the MRD based on the number of DS-MSNDs. The results indicate only 12 DS-MSNDs are required to match the performance of the previous generation of MNDs, which is expected because the detection efficiency of the DS-MSNDs is twice the detection efficiency of the MSNDs. Therefore, the MRD can be populated with fewer DS-MSNDs to reduce cost and size of the detector package and to make room for the gamma-ray detector and supporting electronics. The MRD Mk I will likely implement 12 to 16 DS-MSNDs. Finally, note that the neutron count rate of the MRD for a bare ^{252}Cf source with the MRD mounted on a phantom is higher when the DS-MSNDs are facing inwards towards the phantom with the electronics boards and battery between the source and the detectors. Thus, the simulations indicate more neutrons thermalize in the phantom and are scattered back into the MRD than fast neutrons that are lost in the battery and FR4 boards. Additionally, the hydrogen in the FR4 and battery may help moderate fast neutrons before reaching the DS-MSNDs. For moderated or already thermalized neutron sources, the MRD would perform better with the DS-MSNDs facing outwards; however, the detection efficiency for thermal neutron sources is much higher than fast neutron sources. Unfortunately, the nature of the source may be unknown for many search and localization missions. Thus, when worn, the MRD should be orientated with the DS-MSNDs facing inwards toward the body to optimize the performance for the worst-case scenario of searching for an unmoderated fast neutron source, because the MRD will still provide high detection efficiency for moderated sources even if it is slightly less than the theoretical optimum configuration.

Table 6-5. Results of MCNP6 simulations for the MRD implementing 60% and 70% intrinsic thermal-neutron detection efficiency DS-MSNDs. All simulations were run until the relative error of the tally was less than or equal to 0.01.

Num. of DS-MSNDs	Thermal Beam 0.025 eV (cps/nv) _{th}		Bare ²⁵² Cf @ 25cm w/ DS-MSNDs outward on Phantom 20,000 n/s (cps)		Bare ²⁵² Cf @ 25cm w/ DS-MSNDs inward on Phantom 20,000 n/s (cps)	
	60% DS-MSNDs	70% DS-MSNDs	60% DS-MSNDs	70% DS-MSNDs	60% DS-MSNDs	70% DS-MSNDs
4	2.18	2.42	0.41	0.50	0.70	0.81
8	4.36	4.83	0.80	0.96	1.36	1.57
12	6.39	7.12	1.20	1.44	2.01	2.33
16	8.65	9.58	1.60	1.90	2.62	3.06
20	10.84	11.94	2.00	2.36	3.26	3.78
24	12.99	14.37	2.35	2.79	3.86	4.45

The MRD has been designed to include a spectroscopic gamma-ray detector within the package to be used for detection and identification of radioactive sources that decay by emitting gamma rays. A high-resolution gamma-ray spectrometer was desired to allow for separations of the lower energy lines (100-300 keV) found from the decay of SNM. Additionally, the detector needed to be small in order to fit into a wearable detector system, which was the driving force behind the MRD design, and the gamma-ray detector needed to operate at room temperature up to 55°C without external cooling to reduce power consumption.

Scintillation detectors coupled to SiPMs and semiconductor gamma-ray detectors are the two most prominent options for small-size, high-resolution gamma-ray spectroscopy. CdZnTe was briefly considered but was ultimately dismissed due to high cost and high bias voltage requirements. Instead, a system implementing ScintiClear® SrI₂ scintillation gamma-ray detector from CapeSym, Inc., mounted to a silicon photo-multiplier (SiPM) array was chosen for the gamma-ray detector, which has an expected energy resolution of less than 3.5% for 662 keV gamma rays [159]. SiPMs were chosen as the light collection device, because SiPMs are compact and require relatively low bias to operate (typically 25-30 V). Onboard amplifiers and a MCA will be developed for pulse processing and on-board storage spectra storage will be included for the gamma-ray detector. The gamma-ray detector system will be somewhat scintillator agnostic. If the scintillator can be coupled to a SiPM, the scintillation crystal can be swapped out to adjust performance and price of the system. Depicted in Fig. 6-9 is a concept drawing of the MRD capable of simultaneous, dual-mode, neutron and gamma-ray detection.

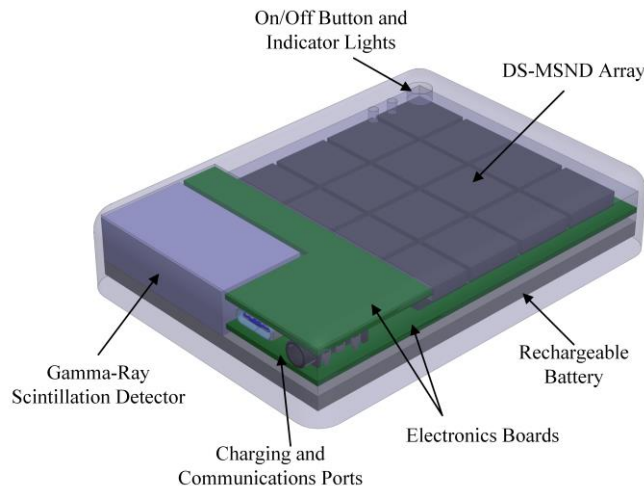


Fig. 6-9. Concept drawing of MRD Mk I with an array of DS-MSNDs and a spectroscopic gamma-ray detector.

Additional ease-of-use functionality will be implemented in the MRD Mk I, including source directionality arrows, automatic isotope identification based on gamma-ray spectroscopy using already developed Gamma Detector Response and Analysis Software (GADRAS), wired and wireless communication options in one package, improved on-board storage, and eventually, real-time neutron and gamma-ray dosimetry. The MND Mk I will ultimately provide a highly versatile neutron and gamma-ray detector system in a compact, cost-effective, power efficient package that can be operated in leave behind or real time operations by itself or integrated into larger detector arrays that can be carried or worn discretely. The enhanced functionality broadens to mission space to include not only search and localization but also personal dosimetry, area monitoring, and space applications where size, weight, and power parameters are of increased importance.

6.3. Wearable Radiation Detectors

The MND and MRD were specifically designed to be integrated into hands-free, low-profile, high-efficiency wearable radiation detector systems. The wearable radiation detectors were developed as a tool for the warfighter to aid in the search and localization of SNM. Neutrons are emitted when SNM decays through fission and detecting the presence of these neutrons is critical for detection of the possibly illicit material. The wearable radiation detectors described herein focus heavily on neutron detection to intercept SNM for the following reasons:

1) Neutrons are highly penetrating and require special shielding usually including a moderator to slow the neutron and an absorber to capture the thermal neutrons.

2) Neutron emitting sources are relatively rare compared to gamma-ray sources. Therefore, a neutron signal above background is good indication further investigation of the radiation source should be performed.

3) Naturally, occurring neutron background levels tend to be low and more constant than gamma-ray background levels [2]. Therefore, the background response for the neutron sensors would need to be less frequently calibrated and can be less susceptible to false alarms.

This section covers the three Wearable Detector Devices (WDDs) that have been designed, fabricated, and characterized utilizing MNDs with MSND technology and the design of a Reconfigurable Wearable Detector (RWD) which integrates MRDs with DS-MSNDs and a spectroscopic gamma-ray detector. All of the wearable detectors were designed to be compact for covert or overt missions, be lightweight to reduce operator fatigue, operate hands-free so the operator can handle additional equipment, and provide reliable radiation source alarming response.

6.3.1. WDD V.1

The first generation WDD comprises 16 MND Mk II's, 16 Controller Area Network (CAN) communications dongles, eight USB-C quad-connector boards, and a master control module [33, 119]. The MNDs were connected to CAN controller boards and then encased in a 12.7-cm x 7.6-cm x 1.5-cm HDPE moderator case (Fig. 6-10). Each MND was then connected to a network of quad-connector boards that were daisy-chained to form the communications backbone linking the MNDs to the master control board within an inconspicuous vest. The master control module housed a battery pack containing three 3400 mAh 18650 rechargeable batteries, power conditioning electronics for the CAN dongles and MNDs, and a communication interface between the detectors and a handheld Android phone or tablet. The schematic of the connections within the vest is shown in Fig. 6-11.

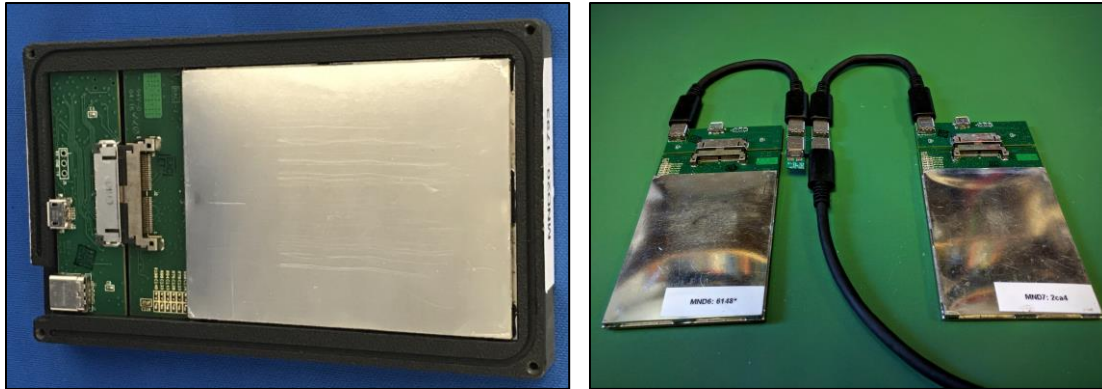


Fig. 6-10. (Left) MND and CAN communications dongle in HDPE moderator case. (Right) Example of MNDs connected to quad-connector boards. One output on the quad-connector board is terminated with a 50-ohm terminator.

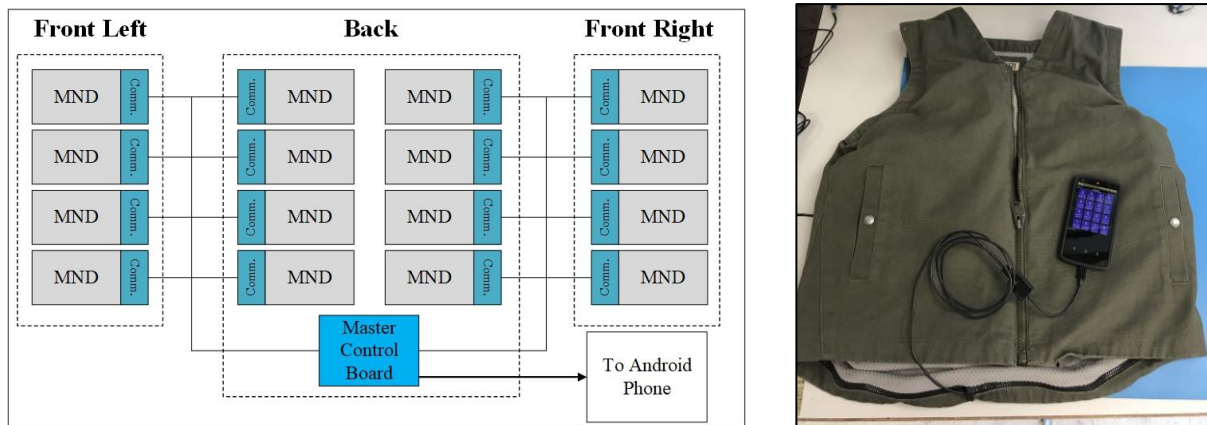


Fig. 6-11. (Left) Schematic of connections in the WDD Mk I [33, 119]. (Right) Image of the WDD Mk I connected to the Android readout device.

As neutrons are detected by the MSNDs on the MND, counts are recorded on an on-board 8-bit counter within the MND. The CAN dongle can read out and reset the 8-bit counter every 0.1-1 second. The Master Control Module then receives the count rate information relayed by the CAN dongle and sends the information to the Android readout device once per second. The Android application displays the real-time count rate, a histogram of count rates with one-second bins over the last 60 seconds of measurement time, or individual count rates for each MND in the system (Fig. 6-12). An audible and haptic alarm is triggered if the neutron count rate surpasses a programmed alarm threshold based on the background count rate.

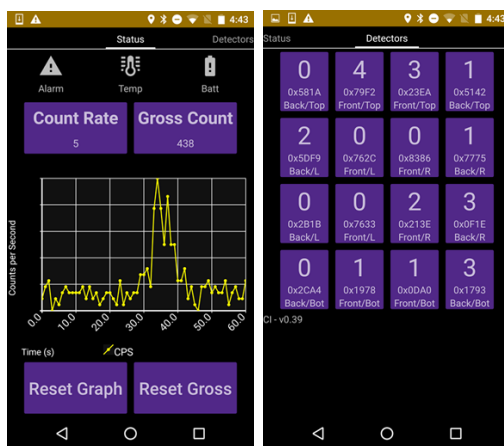


Fig. 6-12. (Left) Real-time neutron count rate of all MNDs in the WDD. (Right) Real-time count rate of individual MNDs in the WDD.

For all neutron response measurements, the WDD was mounted on a phantom described in ANSI 42.51 to provide a standard representation of the moderating properties of an operator's body [160]. The source and center of the moderator was 1-m above the floor for all measurements. The neutron response was measured for bare and moderated ^{252}Cf (21.9 ng: $\sim 50,700$ n/s) and bare AmBe ($\sim 213,000$ n/s) at distances of 0.5, 1.0, 1.5, and 2 m, and the results are shown in Fig. 6-13. The dimension of the moderator cask was 9.7-cm diameter by 12.8-cm tall containing 0.5-cm thick lead, 1-cm thick steel, and 2.5-cm thick HDPE concentric cylinders. Also shown in Fig. 6-13 is the response in units of cps/nv for each source. The flux at the detector location was estimated with MCNP6 simulation by tallying the average flux inside the volume of the phantom without the detectors present. The count rate decreases as distance increases, because the solid angle between the phantom and source also decreases as the distance increases. When the count rate is divided by the incident flux, the detection efficiency is shown to increase as the source to detector distance increases. The increased response is likely caused by a reduction in parallax as distance increases and a softened neutron energy spectrum at increased distances due to additional room and air scatter reducing the average energy of the neutrons before reaching the detector. Finally, as expected, the WDD was most sensitive to moderated ^{252}Cf , followed by bare ^{252}Cf , and least sensitive to bare AmBe, because moderated ^{252}Cf has the lowest energy neutrons and AmBe has highest average energy neutrons. The background count rate was 0.446 ± 0.002 cps.

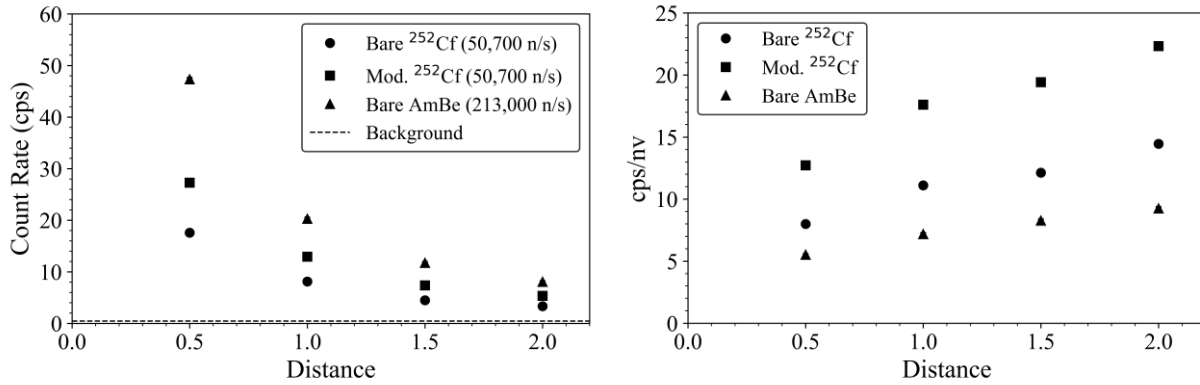


Fig. 6-13. Results of neutron response measurements for WDD V.1. Note the error bars are smaller than the data points.

The angular response of the WDD was measured with a moderated ²⁵²Cf source at 1.5 m in increments of 45°, and the results are shown in Fig. 6-14. The count rate depressions at 90° and 270° are caused by a decreased solid angle during side-on irradiation. Eight of the MNDs were located on the front of the phantom, and the remaining eight MNDs were located on the back of the phantom during the measurements. The angular response could be improved by moving MNDs to the side of torso of the phantom.

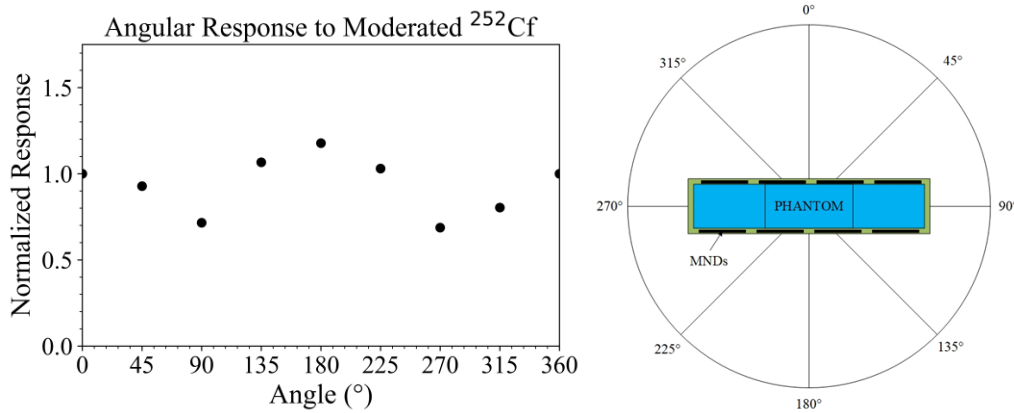


Fig. 6-14. WDD V.1 normalized angular response to moderated ²⁵²Cf at 1.5 m. The error bars on the measurement are smaller than the data points.

Moving source measurements were performed for the bare and moderated ²⁵²Cf source with source speeds of 1.2 m/s and 0.6 m/s. In the measurement, the source started behind a borated HDPE shield and then moved at a constant velocity along a 2.9-m track before stopping behind another borated HDPE shield. The distance of closest approach between the source and WDD on the phantom was 1.5 m. The WDD started logging data at the 30 second mark, and the source started moving at approximately the 70 second mark. The results of the measurements are shown

in Fig. 6-15. The peak from the source passing the WDD in the most challenging detection scenario, bare ^{252}Cf moving at 1.2 m/s, blended into the background signal. As the source speed decreased to 0.6 m/s and the source was moderated, the signal peak became more prominent. However, notice that the background count rate at the source starting and ending location was significantly higher than previous background measurements. This was likely caused by imperfect shielding where neutrons could stream through or scatter around the borated HDPE blocks. Improving the shielding or increasing the length of the track would improve the experiment and likely increase the signal-to-noise ratio as the source passed the WDD for all configurations tested. The signal from the moving source improved when the distance of closest approach was reduced to 1 m (see plots in Appendix D).

Finally, the gamma-ray rejection ratio (GRR) was measured with a ^{137}Cs source at an exposure rate of 10 mR/hr, which matches the exposure rate used in other gamma sensitivity measurements for neutron detectors [161, 162]. The GRR was 1.8×10^{-8} indicating the WDD was largely insensitive to gamma rays. Additional analysis of the WDD V.1 can be found in reference [119].

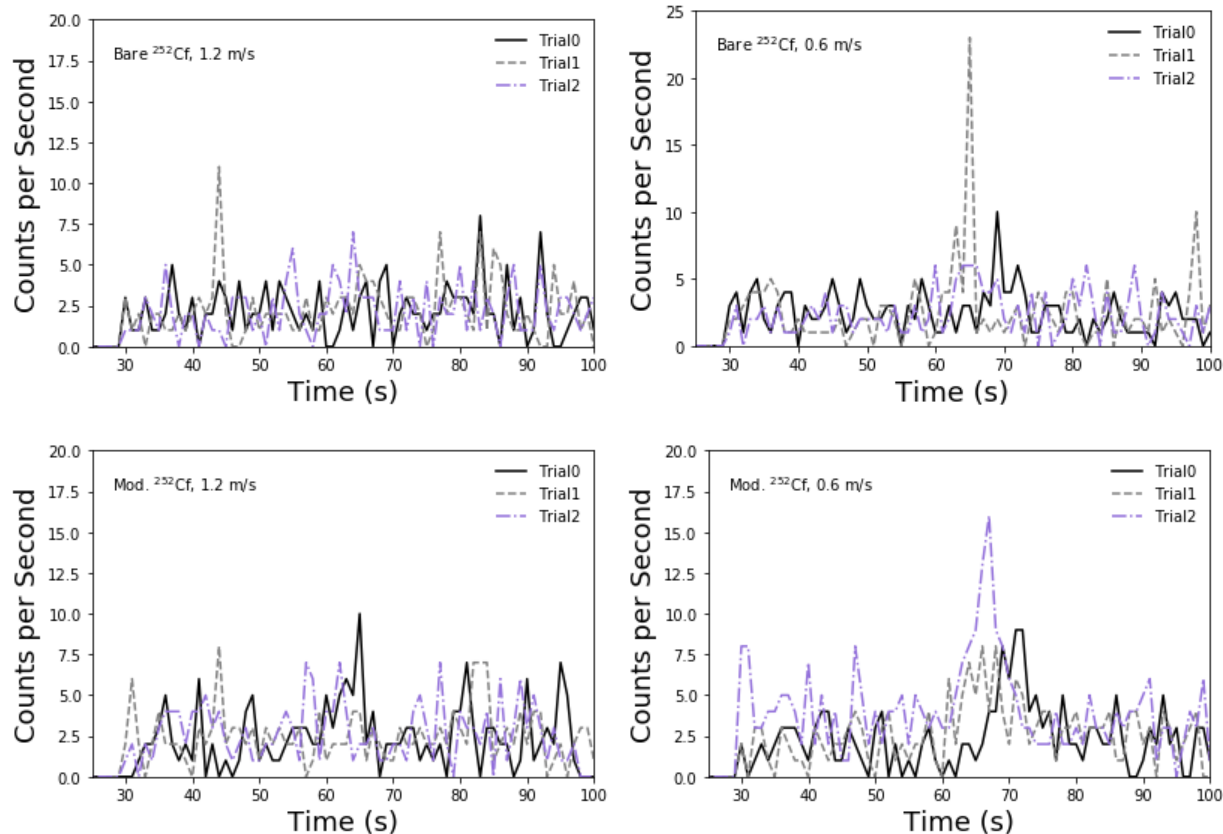


Fig. 6-15. WDD V.1 response to a moving neutron source. The distance of closest approach was 1.5 m and occurred at approximately the 70-second mark. Elevated background at the starting and end location mask the transient signal for some measurements.

6.3.2. Wired WDD V.2

The wired version of the WDD V.2 comprises 16 MND Mk III packages coupled to low-voltage differential signal (LVDS) communication boards that attached to a master control module via 6-pin ribbon cable leads. The MND and LVDS communication dongle were enclosed in a 6.4-cm wide, 10.5-cm long, 1.4-cm thick ABS plastic case, which was more compact and low profile than the previous version (Fig. 6-16). As with the previous WDD, the master control board received the count rate information from the LDVS communication dongles on the MNDs and relayed the data to an Android readout device. Two thin, 3.85 V, 2900 mAh, Li-ion cell phone batteries were used in place of the three bulky 18650 batteries in the master control module to provide power to the control modules, communication dongles, and MNDs. The total weight of the wired WDD V.2 installed in a custom prototype vest was approximately 8 lbs (3.6 kg). The Android readout application remained largely the same with options to display the real-time neutron count rate from all the detectors in the system or monitor the count rate from individual

detectors. Time-stamped count rate information was stored on the Android device for post-mission analysis.

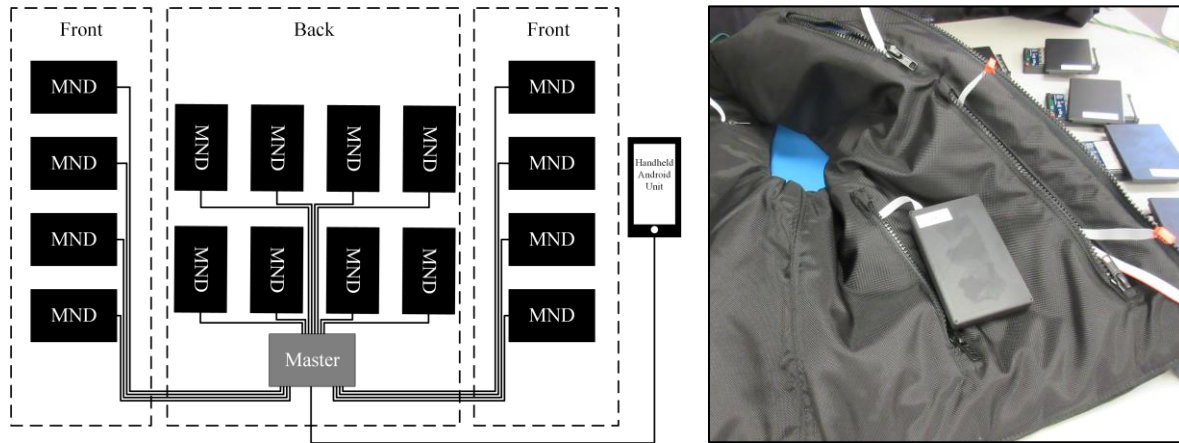


Fig. 6-16. (Left) Diagram of the wired connections in the WDD V.2. (Right) Photo of wired MND installation into a concealed pocket in a prototype garment.

The wired WDD V.2 was mounted onto an ANSI 42.53 phantom, and the neutron sensitivity was measured with a bare ^{252}Cf source, moderated ^{252}Cf source, and bare AmBe source at distances of 0.5, 1.0, 1.5, and 2.0 m. The results for the measurements are shown and compared to the WDD V.1 in Fig. 6-17. When the source was close to the phantom, 1 m or less, the V.1 and V.2 WDDs performed nearly equally. When the source distance was increased past 1 m, the WDD V.2 had better performance, which can likely be attributed to the different case designs. The V.2 cases were thin ABS plastic, and the V.1 cases were made of thicker HDPE. As the source-to-detector distance increases the neutron energy spectrum shifts to lower energies, and the HDPE case on the V.1 WDD may have caused some already thermalized neutrons to scatter away from the detector. The thinner cases in the WDD V.2 scatter away fewer thermal neutrons. For bare sources with shorter source-to-detector distances, the majority of neutron thermalization would occur in the phantom and the effects of the case material would have less impact. The angular response of the WDD to moderated ^{252}Cf is shown in Fig. 6-18. Both versions have the same basic shape with a dip in response for side-on irradiation, which was expected because the layout of the detectors in the prototype garments were nearly identical.

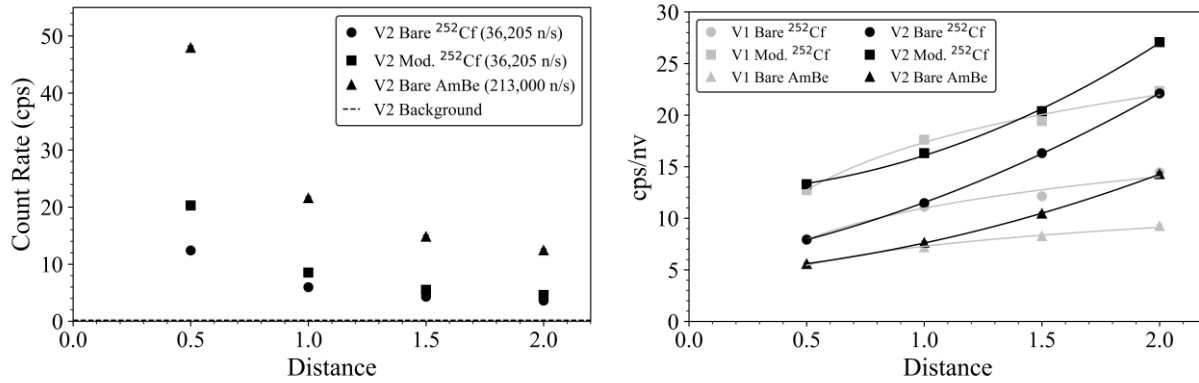


Fig. 6-17. (Left) Count rate as a function of distance for the wired WDD V.2 for bare ²⁵²Cf, moderated ²⁵²Cf, and bare AmBe. (Right) Counts per second per unit flux from the three neutron sources as a function of distance for V.1 and V.2 WDDs. The error bars are within the size of the data point.

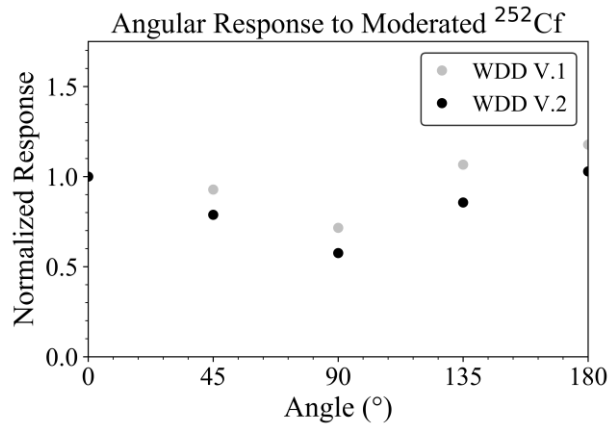


Fig. 6-18. Angular response of WDDs to moderated ²⁵²Cf normalized at 0°.

Measurements with a moving source were performed for bare and moderated ²⁵²Cf moving at 1.2 and 0.6 m/s with a distance of closest approach of 1 m. Screenshots of the Android application readout from these measurements are shown in Fig. 6-19. Again, a peak clearly appears for the moderated ²⁵²Cf measurements. The sensitivity is lower for the fast neutrons from bare ²⁵²Cf and the peak from when the source passes the WDD is harder to distinguish from the elevated background.

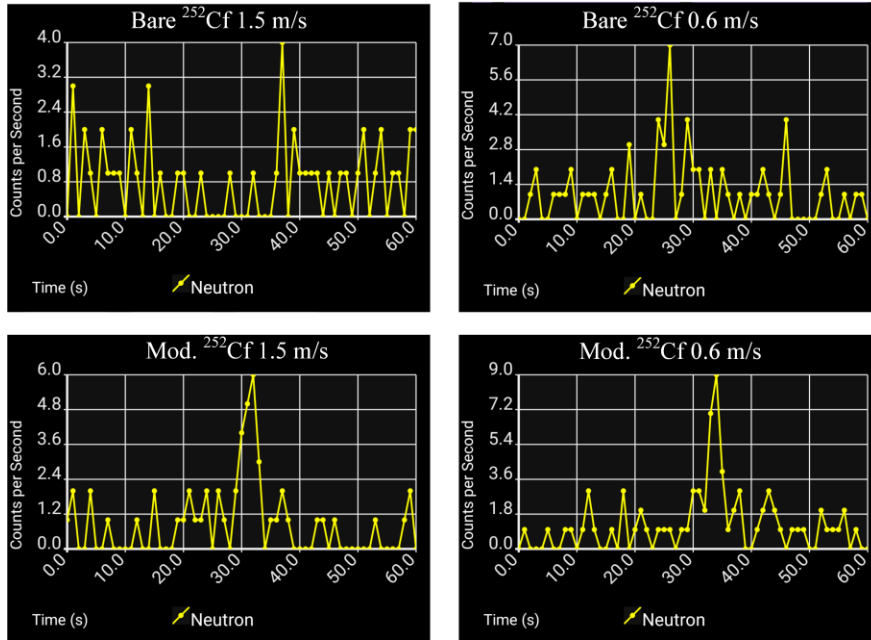


Fig. 6-19. Screenshots of count rate vs time plot from Android application for moving source measurements with the wired WDD V.2. The distance of closest approach was 1 m for all measurements. Statistically significant detection was achieved for all but the bare ^{252}Cf moving at 1.5 m/s scenario.

The GRR was measured with a ^{137}Cs gamma-ray source positioned to provide the phantom with an exposure rate of approximately 10 mR/hr. The net count rate with the gamma-ray source present was 0.0335 ± 0.0006 cps resulting in a GRR of 6.2×10^{-9} . The low gamma-ray sensitivity within the MND is critical for operation in mixed gamma-ray and neutron environments. Because the MNDs are largely insensitive to gamma rays, the operator can be confident a neutron source is present if the MNDs signal an alarm. The wired WDD V.2 was lighter, more compact, and had higher neutron sensitivity than the WDD V.1. Both versions allow for an operator to deploy the system in covert scenarios where RF transmission from WIFI or Bluetooth are not allowed. Additional information on the wired WDD V.2 can be found in the following reference [120].

6.3.3. Wireless WDD V.2

A wireless WDD V.2 was produced utilizing Bluetooth Low Energy (BLE) to transmit data from MND Mk III and Modular Gamma-ray Detector (MGD) packages directly to an Android device eliminating the need for a master control module and central battery pack. The wireless WDD V.2 comprises 16 MND Mk IIIs, two MGDs, and an Android phone. The MNDs and MGDs are each connected to an BLE communications dongle and have an onboard Li-ion battery capable of wireless charging within its ABS plastic case. The dimensions of the wireless MND are 11.2

cm x 6.1 cm x 1.7 cm which was slightly thicker than the wired MND. The wireless MNDs have a continuous operation time of approximately 3 weeks on a single charge.

The MGDs contained seven LND model 713 Geiger-Müller (GM) gamma-ray detectors and accompanying electronics (see Fig. 6-20). High-voltage bias supply and power regulating electronics were also added to the MGD to meet the bias requirements for the GM tube. Although the MGD cannot provide gamma-ray spectroscopy, the count rate alarm will alert the operator to the presence of local gamma-ray sources. The MGD is slightly larger than the wireless MND measuring 10.9 cm x 6.1 cm x 2.1 cm. The wireless capability of the detector modules improves the reconfigurability, because the location of the detectors is not limited by a wiring harness. The operator can load as many or as few detectors as needed into a specialized or standard garment and start their mission. The Android application was also updated to include summed and individual count rates from the MGD detectors. Detailed information on the wireless WDD V.2 system can be found in [163].



Fig. 6-20. Modular Gamma-ray Detector (MGD) with seven LND model 713 Geiger-Müller detectors. The wireless MGD has an onboard rechargeable battery, BLE communications board, and all required signal processing electronics.

The wireless WDD was independently tested at Pacific Northwest National Laboratory (PNNL), and then, the tests were repeated at the KSU S.M.A.R.T. Laboratory. At PNNL, the WDD V.2 was outfitted with 16 wireless MNDs. Eight were positioned on the front of the phantom, and the remaining eight were placed on the back of the phantom. Only eight MNDs were used in the KSU test campaign. The measurements were performed twice at KSU; once performed with the detectors on the front of the phantom, and once with the detectors on the back on the phantom. The results of the two measurements were summed to estimate the count rate of a fully populated, 16 MND, WDD. Also, two MGDs were used in the KSU test campaign. The MGDs were located

on the sides of the phantom for all measurements. The wireless WDD V.2 mounted on a phantom is shown in Fig. 6-21.



Fig. 6-21. Wireless WDD in prototype garment mounted on an ANSI 42.53 phantom.

Measurements were performed with bare ^{252}Cf , moderated ^{252}Cf , and bare AmBe positioned to provide neutron fluxes of 0.1, 1.0, 5.0 and $10 \text{ n cm}^{-2} \text{ s}^{-1}$. The results of the measurements are shown in Fig. 6-22. The results showed good agreement between both testing locations. The slightly higher neutron response at the KSU test facility can be attributed to increased neutron albedo in the testing environment. In all the measurements, the foreground count rate was significantly higher than the background count rate.

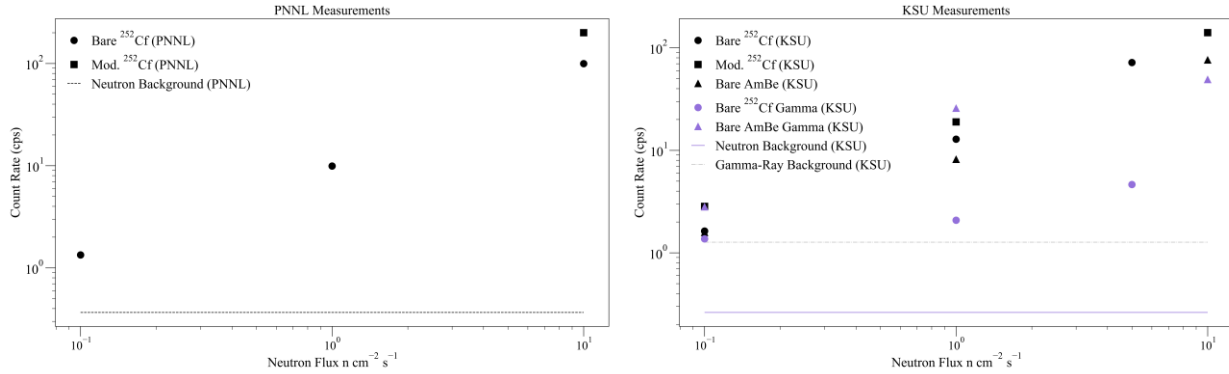


Fig. 6-22. Wireless WDD V.2 response to bare ^{252}Cf , moderated ^{252}Cf , and bare AmBe for neutron fluxes of 0.1, 1, 5, and 10 $\text{n cm}^{-2} \text{s}^{-1}$ from measurements performed at PNNL and KSU. The error bars are smaller than the data point.

The angular response of the wireless WDD V.2 with 16 MNDs and 2 MGDs for bare ^{252}Cf neutrons and gamma rays was measured and is shown in Fig. 6-23. The neutron results show a dip in the response for side-on irradiations as expected. The gamma-ray response peaked when the phantom was irradiated at 90° , because the MGDs were located on the sides of the garment. The decreased gamma-ray signal at 180° (back-side irradiation) was most likely caused, because the MGDs were positioned nearer to the front of the phantom rather than directly on the mid-plane due to the size and construction of the garment.

PNNL measured the Gamma Absolute Rejection Ratio for neutrons (GARR_n). The GARR_n is measured with a bare ^{252}Cf neutron source providing $10 \text{ n cm}^{-2} \text{ s}^{-1}$ flux and a ^{60}Co gamma-ray source providing 10 mR/h exposure. A measurement is performed with both sources present, and then another measurement is performed with only the ^{252}Cf source present. The ratio of the responses is the GARR_n [162]. An ideal GARR_n is 1.0 which indicates that the neutron detectors have no gamma-ray response. The GARR_n for the wireless WDD V.2 with 16 MNDs was 1.02 ± 0.0039 well within the acceptable range of 0.9 to 1.1 [162].

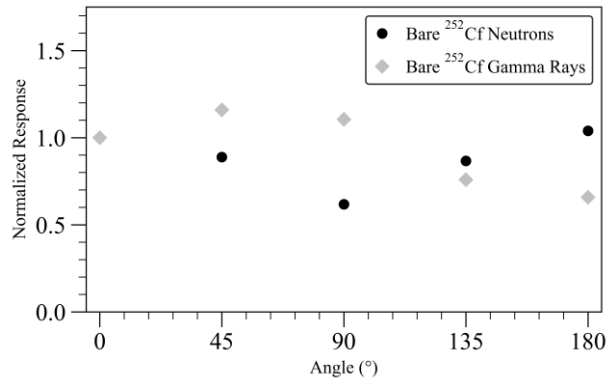


Fig. 6-23. Wireless WDD V.2 angular response to bare ²⁵²Cf. The neutron measurements were performed at PNNL, and the gamma-ray measurements were performed at KSU.

6.3.4. Reconfigurable Wearable Detector (RWD)

The Reconfigurable Wearable Detector (RWD) system has been designed to utilize the newly developed Modular Radiation Detectors (MRDs) implementing DS-MSND technology for neutron detection and a SrI₂(Eu) scintillation detector mounted on SiPMs for gamma-ray detection. The RWD will integrate both wired and wireless transmitters into a single detector package, thereby, allowing the operator to switch freely between the mode of operation as the mission dictates. The features of the MRD were previously described in Section 6.2.2.

When operating in wireless mode, each MRD establishes a WiFi direct connection to the Android readout device for direct communication between the module and phone or tablet. The phone can be used to program bias and discriminator settings for the MRDs, and the MRDs sends gamma-ray and neutron count rates, gamma-ray spectrum, and module temperature information to the readout device. In wired operation, the MRDs are daisy chained together to a single “master” MRD that is connected to the phone with a custom USB-cable. The “master” MRD interfaces directly with the Android device. For operational simplicity, all MRDs are capable of being operated as the “master” MRD.

The application developed for the Android readout device is responsible for processing the neutron and gamma-ray alarms, isotope identification, dose rate, and source directionality functions. The neutron and gamma-ray alarms will be triggered if the average count rate or number of counts measured in a given sample time (1-4 seconds) is statistically higher than the background count rate. The background count rate is calibrated when the system is initialized by performing a measurement at the start of the mission with no sources present for at least one minute. The operator can then decide to use the initial static background for the entire duration of the mission

or utilize a rolling background where the background count rate is continually updated based on the previous 1-10 minutes of operation if no radiation alarms were triggered.

Isotope identification will be performed based on the pulse height spectra measured with the SrI₂(Eu) detectors. The pulse height spectrum from each detector will be sent to the Android device every 1-10 minutes or every time an alarm is triggered. The spectra are then combined and sent to an on-board version of GADRAS which provides the isotope ID algorithms. The temperature of each module is also sent with the spectrum to correct for temperature non-linearities in the output from the scintillation crystal and SiPMs. If matched, the identified isotope is displayed and stored along with the alarm information on the Android application.

By the end of the project, the Android application will also display real-time neutron and gamma-ray dose rates and implement a directionality algorithm that is used to point the operator in the direction of the source. Baseline simulations performed to determine the capabilities of the MRD as a neutron dosimeter and preliminary directional algorithms are presented in this chapter.

RWD MCNP Simulations

The WDDs and RWD developed by the KSU/Alion/RDT team over the past several years [119, 120] have been designed considering the alarming requirements set forth in ANSI N42.53, American National Standard Performance Criteria for Backpack-Based Radiation-Detection Systems Used for Homeland Security [160]. The standard states that the maximum neutron background flux in which standardized measurements can be performed is 200 neutrons m⁻² s⁻¹ (0.02 n cm⁻² s⁻¹). The detector systems are mounted on a standard phantom to emulate the moderation and attenuation characteristics of a human body. Once on the phantom, the detector system has a maximum allowable stabilization time of 15 minutes. The neutron alarming requirement states that the detector system should signal an alarm within two seconds after a bare or moderated ²⁵²Cf source with an emission rate of 20,000 n s⁻¹ moving at 1.2 m s⁻¹ passes the point of closest approach, which is 1.5-m from the phantom. The problem geometry is shown in Fig. 6-24. The detector is then rotated in 45° increments, and the measurements are repeated. The neutron detector system should signal an alarm regardless of source-detector orientation. Per the ANSI specification, a bare ²⁵²Cf source is encased in a spherical pig containing 0.5-cm thick lead and 1-cm thick steel shields. The source and pig is then inserted into a 4-cm thick, spherical HDPE moderator cask for the moderated ²⁵²Cf measurements.

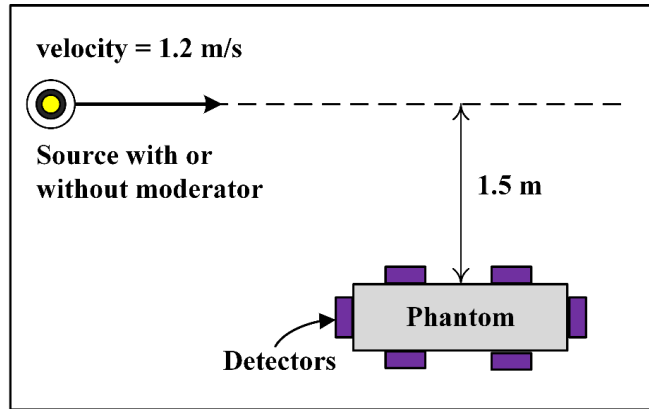


Fig. 6-24. Diagram of moving source and phantom geometry for neutron alarm requirements. The depicted configuration was considered the 0° test case.





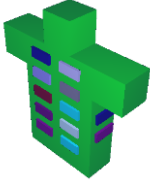
Simulation of RWD with MRDs Utilizing DS-MSND

The DS-MSNDs used in the MRD will have an intrinsic detection efficiency between 60% and 70% for 0.0253-eV neutrons, which is twice the detection efficiency of the MSNDs in previous generation MNDs. MCNP6.1 simulations were performed to optimize the number of MRDs and number of DS-MSNDs in each MRD for the RWD system. In the simulations, each DS-MSND was modeled with the parameters listed in Table 6-6, which corresponds to an intrinsic thermal neutron detection efficiency of 65%. Arrays of 12 and 16 DS-MSNDs were considered to reduce SWAP parameters in the MRDs. RWDs containing up to 24 MRDs were simulated, and the RWD configurations on the phantom used in the simulations are listed in Table 6-7. The MRDs were arranged as symmetrically as possible to keep the angular response uniform and aid in the implementation of source directionality algorithms that can point the operator in the general direction of the source in real time.

Table 6-6. DS-MSND specification for MRD optimization simulations.

Parameter	DS-MSND (Offset)
Microfeature Shape	Straight Trench
Wafer Thickness	1500 μm
Microfeature Depth	550 μm
Unit Cell Width	30 μm
Trench Width	10 μm
Backfill Material	^6LiF
Packing Fraction	35%
Lower Level Discriminator	300 keV
Neutron Source (Isotropic)	^{252}Cf

Table 6-7. MRD locations on phantom for ANSI 42.53 neutron alarming requirement optimization simulations.

Number of MRDs	Locations	Image
8	2 on front, 2 on back, 2 on each side	
12	4 on front, 4 on back, 2 on each side	
16	6 on front, 6 on back, 2 on each side	
20	8 on front, 8 on back, 2 on each side	
24	10 on front, 10 on back, 2 on each side	

The background response for a single MRD with 65% ϵ_{int} DS-MSNDs centrally located on the phantom as specified in ANSI 42.53 was modeled in MCNP. The background source was a volumetric neutron source with a geographically dependent neutron energy spectrum, which is built in feature for MCNP and was implemented using the BN source parameter. The simulated response for neutron background radiation are listed in Table 6-8 along with the expected background count rate calculated with Eq. 6-1 with an assumed background neutron flux of $200 \text{ n m}^{-2} \text{ s}^{-1}$ [160]. It was assumed that each MRD would have the same response to background radiation regardless of the location of the MRD on the phantom, because the background source

field was assumed uniform and isotropic. The expected background count rate for the RWD system was calculated by taking the expected count rate for a single MRD and multiplying by the number of MRDs in the system. It should be noted that in real-world applications detectors near the center of the phantom have be more sensitive to background neutrons, because they are surrounded by more moderator. Also, all simulations were performed with the detectors located on the ANSI standard phantom. The operator’s height, weight, and muscle mass percentage will affect their neutron moderating characteristics and thus the sensitivity of the detector system.

$$b = \varphi \varepsilon_{abs} A \quad \text{Eq. 6-1}$$

b = background count rate

φ = background neutron flux

ε_{abs} = absolute background neutron detection efficiency

A = Area of DSMSNDs in MND

Table 6-8. Simulation results for a single MRD mounted on a phantom in a background neutron flux environment.

Number of DS-MSNDs in the MRD	Absolute Detection Efficiency, ε_{abs}	Predicted Background Count Rate (cps) for 1 MRD
12	$3.56\text{E-}02 \pm 7\text{E-}4$	0.0085 ± 0.0002
16	$4.67\text{E-}02 \pm 9\text{E-}4$	0.0149 ± 0.0003

Prior to starting the mission, a background calibration measurement to determine the baseline neutron flux environment is performed with the RWD. It is assumed that the background neutron flux will not drastically change throughout the duration of the mission, which may be a valid assumption because the background neutron level tends to be low and constant [2]. After the background calibration measurement is completed, the mission can begin. During the mission, the real-time count rate of all the MRDs in the system will be updated to the handled device once per second, and per the ANSI specification, the system needs to alarm to the presence of the neutron source within two seconds after the passing the point of closest approach.

A common method to determine the level on which to set the alarming trigger based on the background radiation level and acceptable detection tolerances is described by Currie [164] and re-iterated in other texts [44, 45, 165]. The critical level, L_C , is the decision point on which to determine if an alarm is triggered and is defined in Eq. 6-2. If the reported count rate is greater

than L_C , then a source is said to be present. If the count rate is lower than L_C , no source is present above the natural background level.

$$L_C = k_\alpha \sigma_0 \quad \text{Eq. 6-2}$$

α = tolerance for error of the first kind (false positive)

k_α = Gaussian probability level corresponding to $1-\alpha$

σ_0 = error for when net count rate is equal to zero

For the RWD, the duration of the background calibration measurement and mission measurements are not equal. Thus, σ_0 takes the form shown in Eq. 6-3 where B_m is the number of background counts recorded during the mission measurement time, t_m , and B_{cal} is the number of background counts recorded during the background calibration measurement time, t_{cal} . The mission measurement time is limited to 1-4 seconds due to the alarming requirements, and the background calibration time is limited to 15 minutes. However, for the simulations presented herein, a two-minute background measurement time was used to reduce long start-up times for real-world deployment

$$\sigma_0 = \sqrt{\frac{B_m}{t_m^2} + \frac{B_{cal}}{t_{cal}^2}} \quad \text{Eq. 6-3}$$

Setting the alarm to trigger on the critical level, L_C , limits the probability of Type I errors to a predefined acceptance level. For example, if k_α is 1.654 the confidence level is 95%. However, L_C does not predict how well the detector system can alarm when a source is indeed present. Thus, the concept of detection limit, L_D , is commonly introduced that indicates the number of counts required to trigger an alarm most of the time (within some confidence level) when an actual source is being measured [44, 45, 164, 165]. Eq. 6-4 shows how the detection limit is determined where β is the tolerance level for Type II errors (false negatives), k_β is the associated confidence level factor based on a Gaussian distribution, and σ_D is the error in the net number of counts recorded during the sample period, which include background and source contribution

$$L_D = L_C + k_\beta \sigma_D \quad \text{Eq. 6-4}$$

For performance predictions, one solves for L_D , the number of counts or average count rate needed in the sample period to be able to repeatably detect a given source with few Type II errors (false negatives). For some net count rate, n , the standard error is shown in Eq. 6-5, where G_m is the gross number of counts in the measurement interval, and N_m is the net number of counts

recorded during the mission measurement interval. L_D in Eq. 6-4 can then be determined by setting σ_n in Eq. 6-5 equal to σ_D , and the result is shown in Eq. 6-6.

$$\sigma_n = \sqrt{\frac{G_m}{t_m^2} + \frac{B_{cal}}{t_{cal}^2}} = \sqrt{\frac{N_m}{t_m^2} + \frac{B_m}{t_m^2} + \frac{B_{cal}}{t_{cal}^2}} \quad \text{Eq. 6-5}$$

$$L_D = \frac{1}{2} \left(\frac{k_\beta \sqrt{k_\beta^2 t_{cal} + 4L_c t_{cal} t_m + 4b t_{cal} t_m + 4b t_m^2}}{t_m \sqrt{t_{cal}}} + \frac{k_\beta^2}{t_m} + 2L_c \right) \quad \text{Eq. 6-6}$$

Shown in Fig. 6-25 are the required average net count rates to trigger an alarm at L_C and the detection limit, L_D , which is the minimum desired count rate for the problem geometry described in ANSI 42.53 to limit the false negative error likelihood to less than 95%. All plots assumed a 2-minute background calibration would be performed. The results for 1, 2, 3, and 4-second long measurement times or decision windows are plotted. To trigger an alarm the average net count rate over the whole decision window must be above L_C for a given number of MRDs deployed in the RWD system.

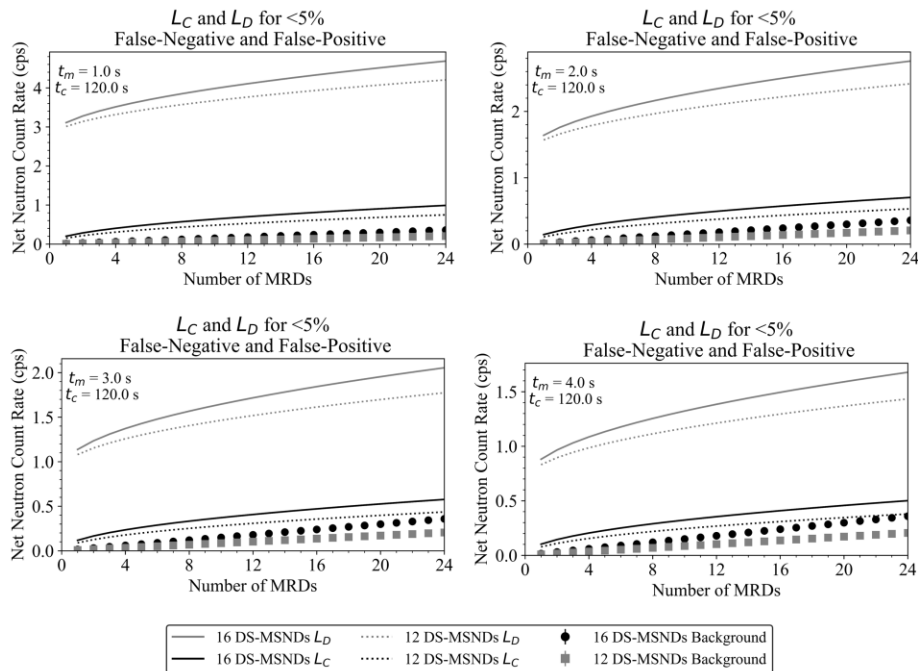


Fig. 6-25. Critical decision level and detection level with 95% confidence for RWDs with up to 24 MRDs containing 16 or 12, 65% ϵ_{int} , DS-MSNDs. An average net count rate over the duration of the decision window above the critical decision level triggers a neutron alarm. The background calibration measurement was 2 minutes and decisions windows of 1, 2, 3, and 4 seconds are shown.

To estimate the response of the RWD to the moving source measurements shown in Fig. 6-24, simulations were performed with the source starting at the centerline of the phantom 1.5 meters away and repeated with the source shifted laterally in 20-cm increments until the source had traveled in a straight line 2.4 m from the source. The simulations were performed for the 0° orientation (y-direction), where the source travels parallel to the torso of the phantom, and the 90° orientation (x-direction), where the source travels parallel to the thin side of the phantom. Because the problem space is symmetrical, the results were mirrored across the 0-cm position indicating what the expected response would be when the source approaches and then passes the RWD. Moderated and bare ^{252}Cf sources were considered with a neutron emission rate of $20,000 \text{ n s}^{-1}$ (see Fig. 6-26).

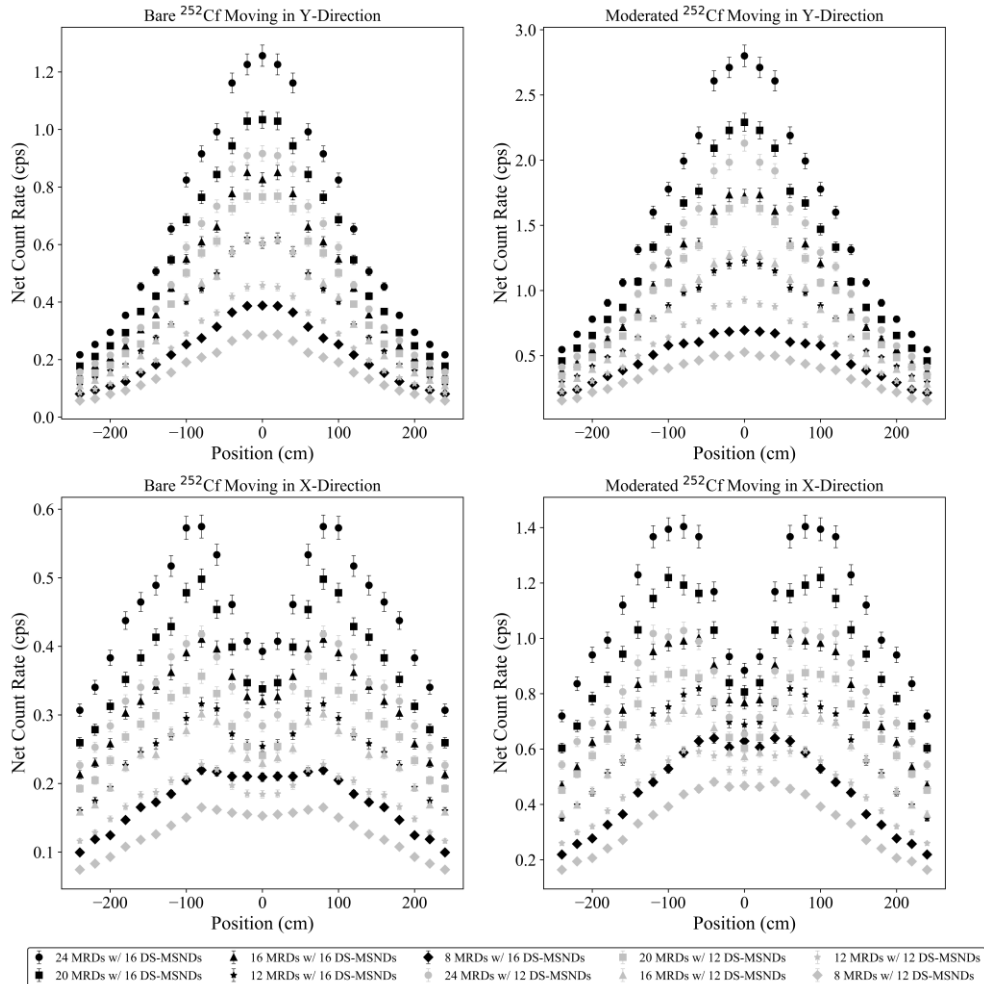


Fig. 6-26. RWD moving source simulation results for bare ^{252}Cf and moderated ^{252}Cf passing by the torso (y-direction), and side of the phantom (x-direction). MRDs with 12 and 16 DS-MSNDs with ϵ_{int} of 65% were modeled. RWDs containing 8 to 24 MRDs were considered, see Table 6-7 for MRD orientation.

The expected average count rates over measurement times of 1, 2, 3, and 4 seconds for the 12 and 16 DS-MSND MRDs plotted against L_C and L_D for 95% and 90% confidence levels are shown in Fig. 6-27 and Fig. 6-28. As expected, as the number of MRDs in the RWD increases, the neutron response increases over the background and over L_C . The simulations indicate two to three second measurement intervals are optimum for maximizing the probability of detecting the source. The worst-case scenario was bare ^{252}Cf moving in the x-direction past the side of the phantom. To improve the probability of detection the operator can load additional MRDs into the RWD to improve the source to detector solid angle or multiple RWDs could be deployed simultaneously on multiple operators that would maneuver around an area together to search for radioactive material. Note that with the source definitions and problem geometries specified in ANSI 42.53, only 228 neutrons per second intersect the entire phantom, and for bare ^{252}Cf the average neutron energy is 2.13 MeV. Additional moderator can be added to the system to increase the neutron response for higher energy neutrons but at the costs of increasing the size and weight of the modules, which were designed to be concealable. Using pre-mission intelligence, slower patrol speeds, and optimized patrol search patterns will help to mitigate any false negatives that could occur when looking for very small sources. If the size of the source in question is somewhat known beforehand, additional or fewer MRDs can be loaded into the RWD to more accurately fulfil the mission needs.

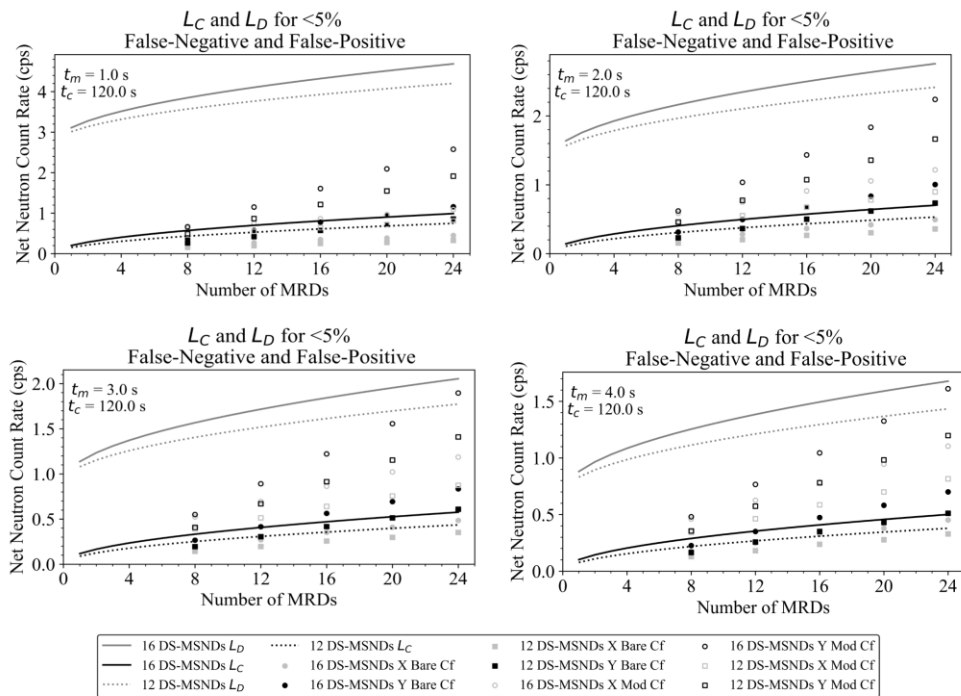


Fig. 6-27. Expected average count rate of RWD during 1, 2, 3, and 4 second measurements for moving bare and moderated ^{252}Cf sources compared to 95% confidence L_C and L_D thresholds.

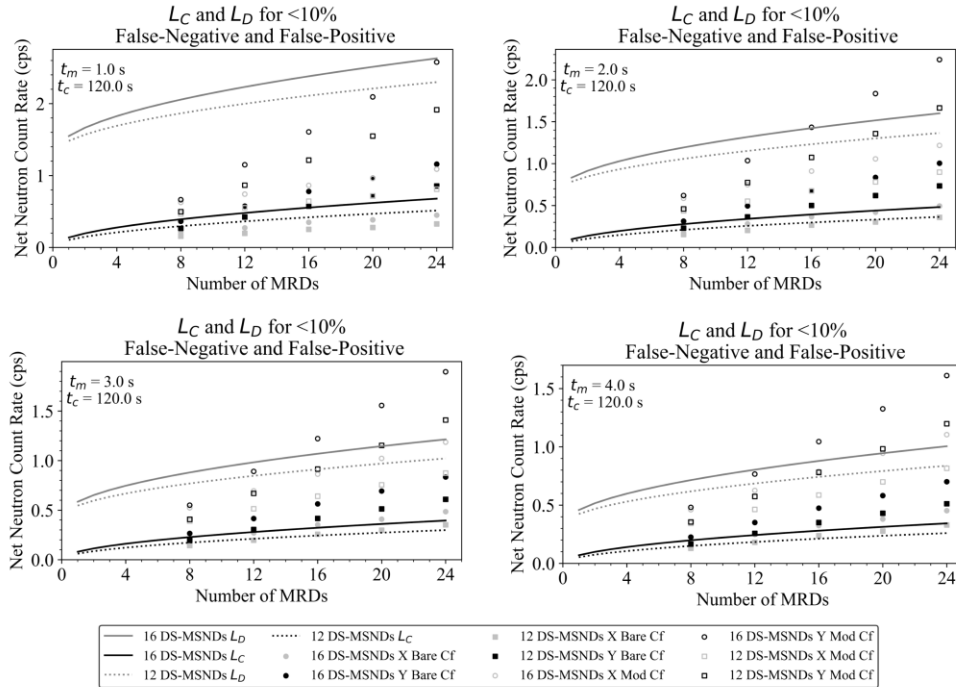


Fig. 6-28. Expected average count rate of RWD during 1, 2, 3, and 4 second measurements for moving bare and moderated ^{252}Cf sources compared to 90% confidence L_C and L_D thresholds.

Point Source Localization

The utility of the RWD can be further enhanced by implementing a point source localization algorithm. One possible method to determine the direction of a point neutron source relative to the detector operator is to compare the count rates of all the detectors in the system and define a directional vector based the relative count rates. A simple algorithm to roughly determine the direction of the source relative to the operator is described below.

1. Each detector is assigned a physical location (i,j,k). This step would be performed when the detector system is initialized. It may be possible to adjust the magnitude of the vector based on common body size parameters, i.e. height, weight, BMI. An example numbering scheme is shown in Fig. 6-29.
2. Calculate weighting parameter, w , for each MND

$$w_i = \frac{\text{Counts}_{MRD,i}}{\text{Total Counts from all MRDs}}$$

3. Calculate directional vector, V . v_i is directional vector pointing from the center of the phantom to the MRD location.

$$V = \sum_{i=1}^{\# \text{MNDs}} w_i v_i$$

- If the magnitude of the directional vector is larger than a threshold directional vector calibrated to background radiation, a point neutron source is likely present.

Shown in Fig. 6-30 are the components of the directional vector from simulations of a moderated ^{252}Cf source revolved 360° around the detector. Note that the same source location algorithm can be simultaneously applied with the gamma-ray detectors in the MRDs.

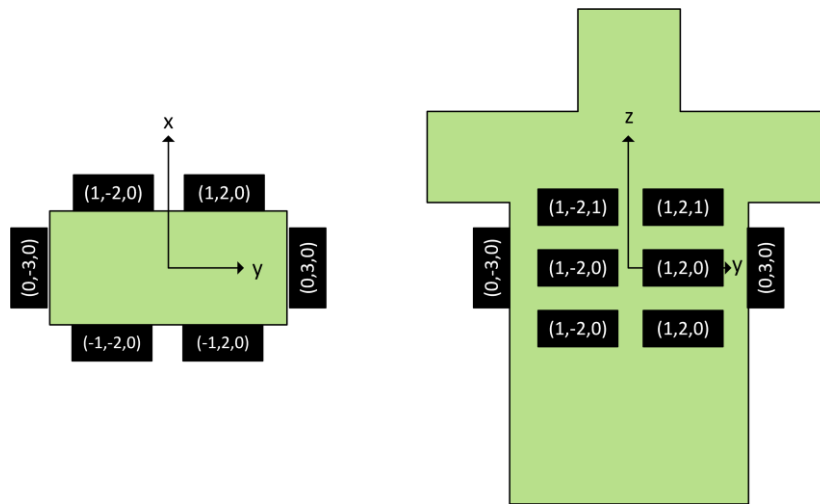


Fig. 6-29. Detector configuration and location identification for 14 MRD RWD system.

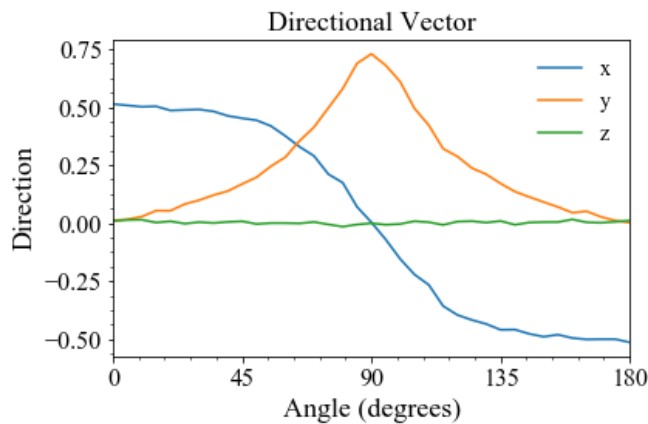


Fig. 6-30. x , y , and z components of directional vector as a moderated ^{252}Cf is rotated around the phantom.

6.3.5. Neutron Dosimetry Capabilities of the RWD

Simulations were performed to determine the feasibility of using the MNDs or MRDs in the wearable detectors as neutron dosimeters. The following subsections give a concise overview

of neutron dosimetry followed by the simulations results of the RWD's neutron dosimetry capabilities.

Neutron Dosimetry Overview

In the field of radiation dosimetry, radiation detectors are used to correlate the local radiation environment to real radiation induced effects on humans. This measurement process is different than the previous sections where the focus was simply indicating the presence of a neutron source. The most basic measure of the effect radiation has on matter is the absorbed dose. Absorbed dose, D , is the average energy absorbed from any type of radiation per unit mass of the absorber [45, 46]. The dose equivalent, H , was defined to reflect the biological effectiveness of the ionization density of charged particle tracks from the ionizing radiation at a point in tissue² [166]. Dose equivalent is the product of the absorbed dose and quality factor, Q , at a point in tissue. The quality factor is a function of the linear energy transfer radiation in water and converts dose to dose equivalent by the following equation [166]

$$H = DQ(L) . \quad \text{Eq. 6-7}$$

The quality factor is higher (~20) for radiation with high ionization density tracks (alpha particles, fission fragments) and lower (1) for radiation with low ionization density tracks (electrons, gamma rays). For neutrons, the quality factor ranges from one to about twenty because the primary interaction mechanism changes as a function of neutron energy. The dose equivalent is classified as a protection quantity, which is used to quantify the extent of exposure of the human body to ionizing radiation [167]. This can then be used to predict deterministic and stochastic health effects related to radiation exposure. However, it is not possible to directly measure the dose equivalent. Thus, operational quantities like the ambient dose equivalent were defined that can be practically measured with calibrated radiation detectors and correlated to the effective dose or dose equivalent [167].

The ambient dose equivalent, $H^*(10)$, was defined by the International Committee on Radiation Units and Measurements (ICRU) as an operational dose quantity to determine the dose equivalent for a person based on the radiation fluence. Formally, as defined by the International

² Dose equivalent is a legacy term originally defined in ICRP Publication 26 and has since be replaced by equivalent dose in ICRP 60.

Committee on Radiation Protection (ICRP), the “ambient dose equivalent $H^*(d)$, at a point in a radiation field is the dose equivalent that would be produced by the corresponding expanded and aligned field in the ICRU sphere at a depth, d , on the radius opposing the direction of the aligned field. The unit of ambient dose equivalent is joule per kilogram ($J\ kg^{-1}$) and its special name is Sievert (Sv)” [168]. A depth of 10 mm is commonly used for highly penetrating radiation such as neutrons. This depth in the ICRU sphere is used because the ambient dose equivalent (operational quantity) gives a conservative estimate of the effective dose (protection quantity) a person would receive for neutrons with energies between 50 keV and 2.5 MeV. Outside this range, the effective dose can be higher than the ambient dose equivalent, but for typical broad neutron spectra found at many radiation facilities, the ambient dose equivalent is conservative [169]. Ambient dose equivalent is still a commonly used measure for radiation area monitoring, and common rem meters are the Andersson-Braun rem counter, Hankins rem ball, or PRESCILA dosimeter [48, 170, 171].

In a monoenergetic neutron field, the ambient dose equivalent can be calculated with Eq. 6-8, where $h_{cc,e}$ is the energy dependent fluence to ambient dose equivalent conversion coefficient (see Fig. 6-31), and Φ is the monoenergetic neutron fluence. However, most real-world neutron environments are not monoenergetic, and Eq. 6-8 takes the form of Eq. 6-9 where contributions from all neutron energies are considered [129].

$$H^*(10) = h_{cc,e} * \Phi \tag{Eq. 6-8}$$

$$H^*(10) = \int_0^\infty h_{cc}(E)\Phi(E)dE \tag{Eq. 6-9}$$

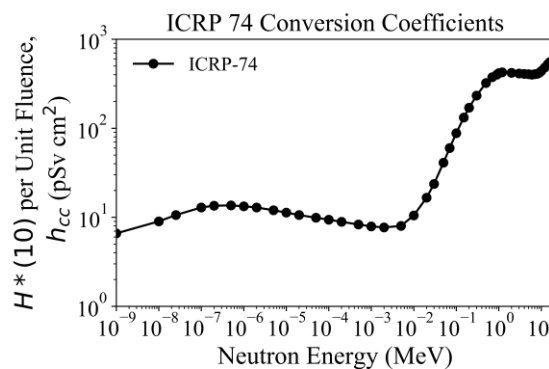


Fig. 6-31. ICRP 74 neutron fluence to ambient dose conversion coefficients. The detector response function of rem meters is tailored to try match the shape of $H^*(10)/\Phi$ curve [168].

It is required to know the energy dependent neutron fluence, $\Phi(E)$, to calculate the ambient dose equivalent using Eq. 6-9. While the energy dependent fluence can be indirectly measured and unfolded [172, 173], it is common to try to match the response function of a detector to the fluence to dose conversion factor for real time dose monitoring. The energy dependent response function for a neutron detector can be expressed with Eq. 6-10, where d_{cc} is the fluence to counts conversion coefficient, and C is a count to dose calibration constant with units of Sv per count [170]. If the detector response function matches the fluence to dose conversion coefficients, the ambient dose equivalent can be accurately measured without knowledge of the energy distribution of the local neutron radiation environment [170]

$$R = \int_0^{\infty} C d_{cc}(E) \Phi(E) dE . \quad \text{Eq. 6-10}$$

A metric used to quantify the performance of a dose monitor is the relative response per unit dose, which is the ratio of the energy dependent detector response function to the ambient dose equivalent conversion coefficients, $d_{cc}(E)/h_{cc}(E)$, or the ratio of Eq. 6-10/Eq. 6-9 normalized at some neutron energy. An ideal ambient dose equivalent rem meter would have a relative response per unit dose equal to one for all energies, meaning it exactly matches the fluence to dose conversion coefficients. The relative response per unit fluence is related to the sensitivity of detector, and if the shape of the response function matches the shape of the conversion coefficients curve, higher response per unit fluence is desired. The relative response per unit fluence for some common dose meters is shown in Fig. 6-32.

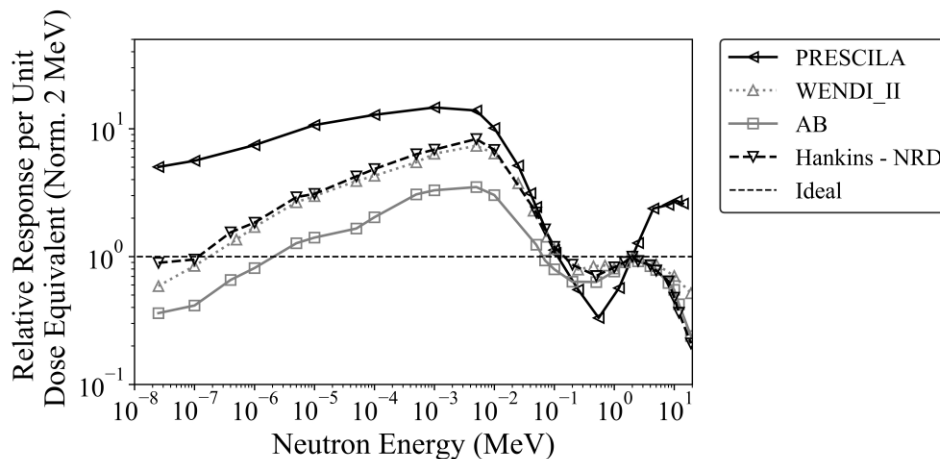


Fig. 6-32. Relative response per unit dose equivalent for the PRESCILA, WENDI-II, Anderson-Braun (AB), and Hankins-NRD dose meters as a function of neutron energy. Calculated from data presented in [48].

Many of the commonly available dose meters tend to overestimate the ambient dose equivalent for thermal and epithermal neutrons and underestimate the dose from high energy neutrons. More advanced neutron dose meters include multiple detectors, moderators, and absorber layers within a single detector system. The responses of the detectors at different locations in the detector system can be placed into relative neutron energy bins thereby forming a real time neutron energy spectrometer [123, 127, 129]. The detector system response can then be more closely calibrated to match the ambient dose equivalent conversion coefficients. However, the more advanced system is still a handheld device. A rem meter that can be worn by the operator and operated hands-free may be beneficial in some applications and has been previously suggested as an alternative to handhelds [174]. In addition to the weight of the detector system being distributed across the operator's shoulders instead of on one arm, constantly wearing the dosimeter may provide a more accurate recorded dose equivalent. The weight of the detector system will also be reduced, because the wearable dose meter could use the body as the neutron moderator instead of relying on external moderator. Thus, a feasibility study was performed to determine if the RWD could also be deployed as a neutron dose monitor.

Single Channel RWD Neutron Dosimeter

First, the energy dependent neutron response function was determined by MCNP6 simulation for an MRD centrally located on an ANSI N42.53 phantom. The entire phantom was irradiated by a monodirectional, monoenergetic neutron beam, and the number of counts recorded by the MND was tallied and normalized per source particle (see sample Python script in Appendix C). Shown in Fig. 6-33 is a diagram of the problem geometry. The MRDs in this study had 24, 1-cm² DS-MSNDs with intrinsic thermal-neutron (0.025 eV) detection efficiency of 69%. The simulation was performed for neutron energies ranging from 10⁻⁰⁹ MeV to 20 MeV. The same set of simulations was then repeated with the phantom irradiated from the back side to estimate the response of single MND located on the opposite side of the phantom. The detector response per unit fluence was calculated by dividing the response per source-particle tally by the results of a cell fluence tally in the phantom for a problem geometry composed of all void regions. The relative response per unit dose was calculated by determining the ratio of the energy dependent detector response function, $d_{cc}(E)$, to the ICRP 74 energy dependent fluence to ambient dose equivalent conversion coefficients, $h_{cc}(E)$, and normalizing to a single neutron energy (Fig. 6-34) [168].

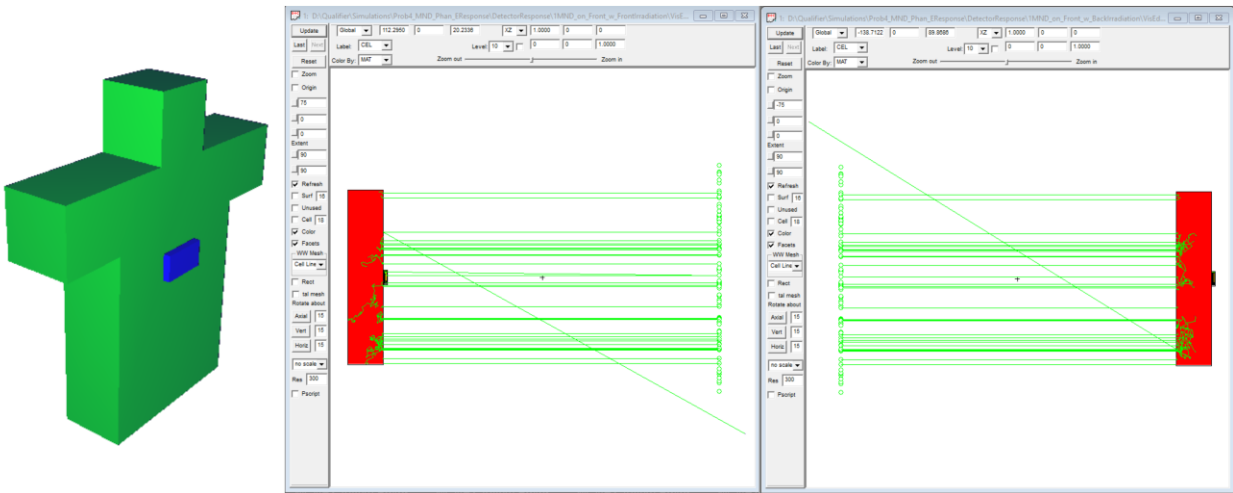


Fig. 6-33. (Left) 3D model of MRD centrally located on ANSI 42.53 phantom. (Middle and Right) Visualizations of neutron irradiation on front side and back side of phantom by a mono-energetic, mono-directional neutron beam with beam diameter of 1 meter.

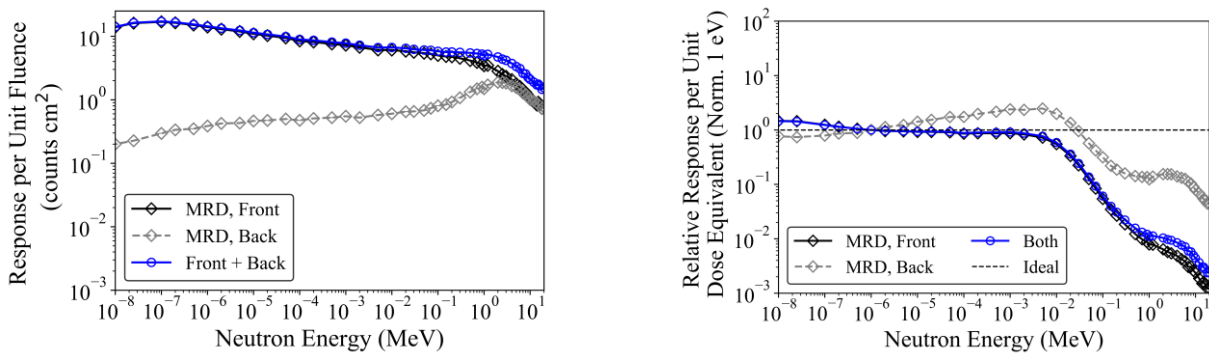


Fig. 6-34. (Left) MRD energy dependent response per unit fluence. (Right) Relative response per unit flux for a single MRD on a phantom normalized to 1 eV.

As expected, the response per unit fluence for the front MRD was relatively high compared to the Andersson-Braun, Hankins, or PRESCILA rem meters up to neutron energies of about 1 MeV, because the MRD was designed to have high detection efficiency for thermal neutrons, and the phantom increases the response rate for epithermal neutrons through moderation and backscattering. The shape of the response function of the front-side MRD matches very well with the ICRP74 dose equivalent conversion coefficients [168] for neutrons with energies up to approximately 10 keV and then sharply declines. The response function from the MRD when the phantom was irradiated from the backside more closely matches the shape $H^*(10)$ conversion coefficients and looks similar to the response function from an Andersson-Braun or Hankins rem meter. Geometrically, the detector-source configuration is similar for all three, since there is a large moderating medium between the detector and source. For the Andersson-Braun and Hankins

rem meter the moderator is the HDPE cask, and the moderating medium is the phantom for the MRD. Adding additional MRDs to the system increases the response per unit flux but does not change the shape of the response function.

Multi-Channel RWD Neutron Dosimeter

An RWD with unmodified MRDs would be a high accuracy dose meter in a neutron environment containing only thermal neutrons; however, it would be inaccurate to assume only thermal neutrons exist in many real-world applications. Also, thermal neutrons contribute to only a small fraction of an operators dose. Therefore, simulations were performed to determine if the response function could be improved by adding neutron absorbers around the MRDs and modifying the backfill material.

Three modifications were made to the MRD design to try to separate the detector response function into thermal, epithermal, and fast neutron bins. To form the thermal neutron channel, a 1-mm thick Cd sheet was position between the phantom and the MRD. Cadmium has a large neutron capture cross section for neutron energies less than about 0.5 eV, and therefore, the Cd sheet should absorb any neutrons that scatter back toward the MND after being moderated in the phantom. Ideally, the thermal MRD should only detect neutrons that are emitted from the neutron source with near thermal energy, because epithermal and fast neutrons will have to be thermalized in phantom before they are detected. A 1-mm thick Cd case was wrapped around the outside of an MRD to form the epithermal MRD. Opposite of the thermal MRD, the epithermal MRD should not be sensitive to thermal neutrons emitted from the source and can only detect neutrons that have scattered in the phantom. The Cd absorber may require additional shielding to protect the user from dose from capture gamma rays. Alternatively, ${}^6\text{Li}$ -loaded material could be used as the absorbing shield which doesn't emit capture gamma rays for thermal neutron absorptions, but the absorber thickness would need to be increased to offset the lower neutron capture cross section. The fast MRD was made by replacing the ${}^6\text{LiF}$ -backfilled DS-MSNDs with wax-backfilled DS-MSNDs. The fast MRD relies on proton recoil from high energy neutron scattering events in the hydrogenous wax to deposit energy in the silicon substrate and subsequently be detected. Images of each detector are shown in Fig. 6-35. The trench geometry for the wax-backfilled DS-MSNDs was not changed from the ${}^6\text{LiF}$ -backfilled DS-MSNDs. Additional optimization could be performed to improve the fast-neutron response.

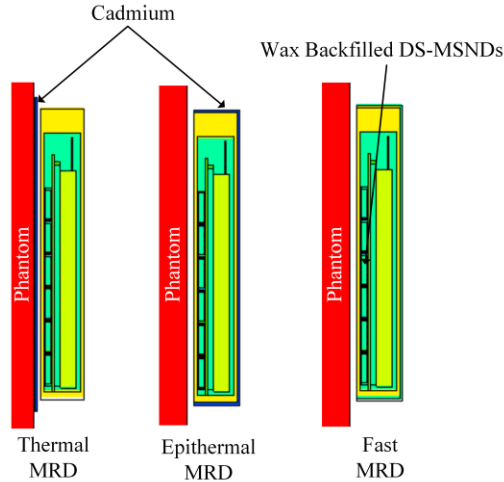


Fig. 6-35. Thermal, epithermal, and fast sensitive MRDs. Cadmium absorbers were positioned to either absorb initially thermal neutrons or absorb neutrons thermalized in the phantom. The fast-neutron sensitive MRD replaces ${}^6\text{LiF}$ convertor material with hydrogenous wax that relies on proton recoil to produce a charged-particle reaction product that interacts in the adjacent silicon microfeatures.

Simulations were performed for an MRD-based rem meter containing one fast-, one epithermal-, and one thermal-neutron sensitive MRD on each side of the phantom, and the response for each MRD was recorded individually. The total response function of the system can now be represented by Eq. 6-11, and calibration coefficients for each MRD channel can be tailored so that the total response matches more closely to the ambient dose equivalent conversion coefficients. The *th*, *epi*, and *fast* subscripts differentiate the calibration coefficients and response functions for thermal, epithermal, and fast neutron sensitive MRDs, respectively

$$R = \int_0^{\infty} (C_{th}d_{th}(E) + C_{epi}d_{epi}(E) + C_{fast}d_{fast}(E))\Phi(E)dE . \quad \text{Eq. 6-11}$$

The response function per unit fluence and relative response per unit dose equivalent are shown in Fig. 6-36. The response per unit fluence for the RWD rem meter is significantly higher than that for the commercial rem meters at low neutron energies, but at high neutron energies the response per unit fluence for the RWD rem meters is significantly lower than PRESCILA and WENDI-II and about the same magnitude as Andersson-Braun and Hankins rem meters. The relative response per unit dose with for the three-channel MRD system matches much more closely to the fluence to dose conversion coefficients when each channel of the MRD is calibrated separately compared to summing the responses from all MRDs and trying to set a single calibration coefficient. When compared to the commercial rem meters, the three-channel MND rem meter responds more closely to ICRP74 for neutron energies less than about 10 keV, and then performs about as well as the commercial detectors between 1 MeV and 20 MeV. For neutron energies

between 10 keV and 1 MeV, the three-channel MND system significantly underestimates the dose equivalent. It may be possible to fine tune the calibration coefficients for the thermal and epithermal MNDs to overestimate the dose at lower neutron energies in a way that makes up for the underestimation between 10 keV and 1 MeV.

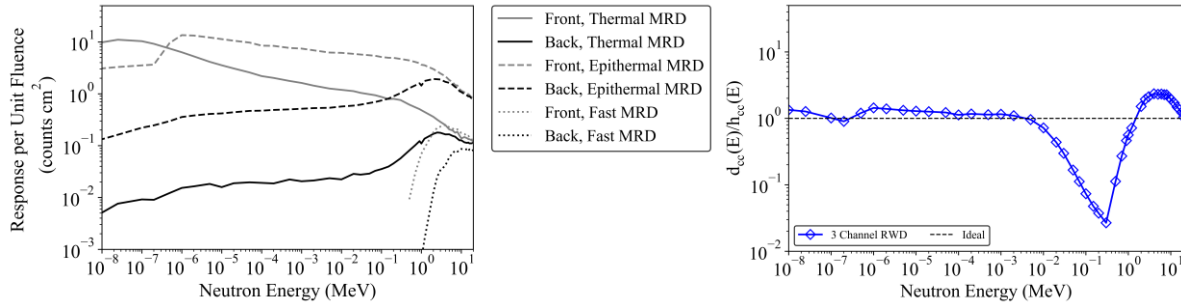


Fig. 6-36. (Left) Detector response per unit fluence for all six MRDs in the three-channel RWD dosimeter system. (Right) Response per unit ambient dose equivalent for the three-channel system using calibration coefficients of the form shown in Eq. 6-11.

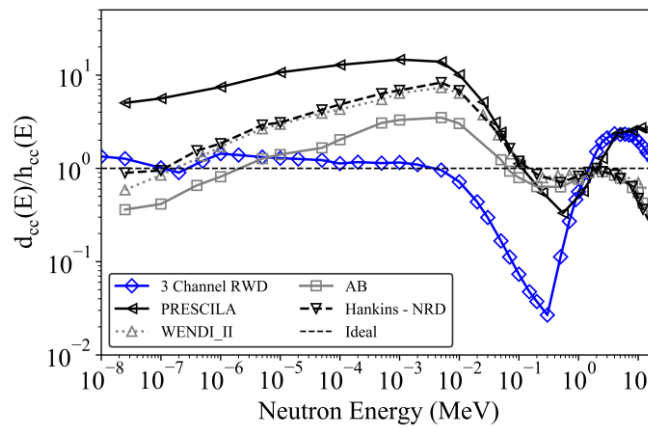


Fig. 6-37. Comparison of the three-channel RWD dosimeter to other common commercial dose monitors.

Chapter 7 - Conclusions

A need has persisted for low-cost, high efficiency, thermal neutron detectors to replace expensive ^3He gas-filled detectors. Single-sided MSNDs were developed as an early solution offering moderate intrinsic thermal-neutron detection efficiency ($\sim 30\%$) and are compact, low-power, inexpensive, mass-producible, and rugged [20, 21, 25, 26, 28]. The single-sided MSNDs could be stacked and integrated to increase the neutron detection efficiency to up to 42% [22]; however, macroscopically aligning microscopic trenches to eliminate neutron free streaming paths was unreliable. DS-MSNDs were then developed as a means to reliably increase the neutron detection efficiency to greater than 50% for 1-mm thick, 1-cm² active area detectors by using VLSI processing to efficiently align and etch offset trenches on both sides of a silicon diode [30-33]. Unfortunately, the highest measured intrinsic-thermal neutron detection efficiency for these DS-MSNDs was $53.5 \pm 0.6\%$, which fell short of the theoretical maximum intrinsic thermal-neutron detection efficiency of approximately 80% [33]. This work showed that the main factor limiting the detection efficiency for DS-MSNDs was the ^6LiF backfill packing density within the DS-MSND trenches. Improved backfilling methods were developed and coupled with increased trench depth etching processes on 1.5-mm thick silicon wafers, a record breaking intrinsic thermal-neutron detection efficiency of $69.3 \pm 1.5\%$ was achieved truly rivaling the detection efficiency of expensive, small-diameter, high-pressure ^3He detectors.

Previously, the ^6LiF backfill packing fraction was assumed to be 90-95% based on qualitative assessments of SEM images. The high packing fraction assumption was then used in MCNP simulations to predict the theoretical limits of neutron detection efficiency. Recently, three methods were used to quantitatively evaluate the ^6LiF packing fraction of DS-MSNDs, and the true packing fraction was revealed to be approximately 30-35%. Subsequently, an in-depth study of powder packing methodologies was performed, and new backfilling methods were developed for DS-MSNDs that yielded ^6LiF -packing fractions as high as 55%. MCNP optimization simulations were performed with the updated packing fraction information, and the new simulations showed that intrinsic thermal-neutron detection efficiencies greater than 75% could still be achieved by etching deeper microfeatures. Thus, *pvp*-type DS-MSNDs were fabricated on 1.5-mm thick wafers with 20- μm wide by 600- μm deep trenches with a 30- μm unit cell width. The

thicker DS-MSND surpassed the previous detection efficiency ceiling of 50-55% and regularly achieved intrinsic thermal-neutron detection efficiencies ranging between 60-69%.

The *pvp*-type DS-MSNDs were mass-producible, rugged, compact, and were operated at 0-V bias, which eliminated the need for bias electronics in detector packages further reducing detector cost. However, to achieve the ultra-high detection efficiency, the lower level discriminator was set in the valley of the pulse height spectrum which was shifted to lower energy channels due to the weaker electric field in the deeper trenches. The neutron signal began to overlap with the background gamma-ray signal, and the gamma-ray rejection ratio was 2.26×10^{-03} when the LLD was set in the valley of the pulse height spectrum. Nevertheless, the LLD could be increased such that the GRR was improved to 5.5×10^{-5} , and the intrinsic thermal-neutron detection efficiency only reduced to approximately 60%, showing that the *pvp*-type DS-MSND can still satisfy the need for detectors with high neutron detection efficiency and limited gamma-ray sensitivity.

Models of alternative doping schemes for DS-MSNDs presented herein indicate that the charge collection efficiency can be improved by implementing a *pvp-n*-ring doping profile where a bias can be applied across the *p*-type doped trenches and an *n*-type doped ring on the perimeter of the trenches. Early prototypes of this design were produced and showed good rectifying behavior and low capacitance in the IV and CV curves, respectively. Further investigation into the advanced doping profile could yield DS-MSNDs with even higher neutron detection efficiencies and superior gamma-ray discrimination with only 10-50 V reverse bias required.

Several prototype detector systems were fabricated implementing MSND and DS-MSND technology. The HeReps were designed as drop-in replacements for high-pressure, small-diameter ^3He detectors commonly implemented in handheld detector systems. The performance of the HeRep Mk IV nearly matched or outperformed a similarly sized 10-atm ^3He detector depending on the neutron source energy spectrum. Several iterations of MNDs were fabricated with single sided MSNDs and implemented into inconspicuous wearable detector systems. The wearable detectors offer a high sensitivity solution for search and localization of SNM through passive neutron detection that is also ergonomic and allows the operator to keep both hands free for other mission critical actions. Prototype Modular Radiation Detectors have been designed as an upgrade on the MND package implementing DS-MSNDs and a spectroscopic gamma-ray detector. In future years, other detector packages could realize benefits by upgrading to the DS-MSND platform such as the RDT Domino® [124, 175], neutron spectrometers [123, 127, 129] and

position sensitive neutron detectors [176]. These DS-MSND based detector systems will provide high-fidelity solutions for many applications where neutron detection is required, including national security, radiation dosimetry, neutron scattering measurements, and space exploration.

References

- [1] R. T. Kouzes, "The ^3He Supply Problem," United States, 2009-05-01 2009. [Online]. Available: <https://www.osti.gov/servlets/purl/956899>
- [2] M. S. Gordon *et al.*, "Measurement of the flux and energy spectrum of cosmic-ray induced neutrons on the ground," *IEEE Trans. Nucl. Sci.*, vol. 51, pp. 3427-3434, 2004, doi: 10.1109/TNS.2004.839134.
- [3] T. J. Aucott, M. S. Bandstra, V. Negut, D. H. Chivers, R. J. Cooper, and K. Vetter, "Routine Surveys for Gamma-Ray Background Characterization," *IEEE Trans. Nucl. Sci.*, vol. 60, pp. 1147-1150, 2013, doi: 10.1109/TNS.2013.2251355.
- [4] L. J. Mitchell, B. F. Philips, E. A. Wulf, A. L. Hutcheson, and B. E. Leas. Cross country background measurements with high purity germanium. Available: <https://ieeexplore.ieee.org/ielx5/6144196/6152483/06154508.pdf?tp=&arnumber=6154508&isnumber=6152483>.
- [5] B. Feigl and H. Rauch, "Der Gd-neutronenzähler," *Nucl. Instrum. Methods*, vol. 61, no. 3, pp. 349-356, 15 May 1968 1968, doi: 10.1016/0029-554X(68)90250-4.
- [6] D. S. McGregor, M. D. Hammig, Y.-H. Yang, H. K. Gersch, and R. T. Klann, "Design considerations for thin film coated semiconductor thermal neutron detectors—I: basics regarding alpha particle emitting neutron reactive films," *Nucl. Instrum. Meth. A*, vol. 500, pp. 272-308, 2003, doi: 10.1016/S0168-9002(02)02078-8.
- [7] A. Miresghi *et al.*, "High efficiency neutron sensitive amorphous silicon pixel detectors," *IEEE Trans. Nucl. Sci.*, vol. 41, no. 4, pp. 915-921, 1994, doi: 10.1109/23.322831.
- [8] T. Aoyama, Y. Oka, K. Honda, and C. Mori, "A neutron detector using silicon PIN photodiodes for personal neutron dosimetry," *Nucl. Instrum. Meth. A*, vol. 314, no. 3, pp. 590-594, 1992/05/10/ 1992, doi: [https://doi.org/10.1016/0168-9002\(92\)90253-Z](https://doi.org/10.1016/0168-9002(92)90253-Z).
- [9] D. S. McGregor, S. M. Vernon, H. K. Gersch, S. M. Markham, S. J. Wojtczuk, and D. K. Wehe, "Self-biased boron-10 coated high-purity epitaxial GaAs thermal neutron detectors," *IEEE Trans. Nucl. Sci.*, vol. 47, no. 4, pp. 1364-1370, 2000, doi: 10.1109/23.872979.
- [10] D. S. McGregor, J. T. Lindsay, C. C. Brannon, and R. W. Olsen, "Semi-insulating bulk GaAs thermal neutron imaging arrays," *IEEE Trans. Nucl. Sci.*, vol. 43, no. 3, pp. 1357-1364, 1996, doi: 10.1109/23.507065.
- [11] S. Pospisil *et al.*, "Si Diode as a Small Detector of Slow Neutrons," *Radiat. Prot. Dosim.*, vol. 46, pp. 115-118, 1993, doi: 10.1093/oxfordjournals.rpd.a081664.
- [12] A. Rose, "Sputtered boron films on silicon surface barrier detectors," *Nucl. Instrum. Methods*, vol. 52, no. 1, pp. 166-170, 1 June 1967 1967, doi: 10.1016/0029-554X(67)90576-9.
- [13] D. S. McGregor, R. T. Klann, H. K. Gersch, and Y. H. Yang, "Thin-film-coated bulk GaAs detectors for thermal and fast neutron measurements," *Nuclear Instruments and Methods in Physics Research Section A: Accelerators, Spectrometers, Detectors and Associated Equipment*, vol. 466, pp. 126-141, 2001, doi: 10.1016/S0168-9002(01)00835-X.
- [14] D. S. McGregor, R. T. Klann, H. K. Gersch, and Y. H. Yang, "Thin-film-coated bulk GaAs detectors for thermal and fast neutron measurements," *Nucl. Instrum. Meth. A*, vol.

- 466, no. 1, pp. 126-141, 2001/06/21/ 2001, doi: [https://doi.org/10.1016/S0168-9002\(01\)00835-X](https://doi.org/10.1016/S0168-9002(01)00835-X).
- [15] D. S. McGregor, R. T. Klann, H. K. Gersch, E. Ariesanti, J. D. Sanders, and B. VanDerElzen, "New surface morphology for low stress thin-film-coated thermal neutron detectors," *IEEE Trans. Nucl. Sci.*, vol. 49, pp. 1999-2004, 2002, doi: 10.1109/TNS.2002.801697.
- [16] D. S. McGregor, S. L. Bellinger, W. J. McNeil, and T. C. Unruh, "Micro-structured high-efficiency semiconductor neutron detectors," in *2008 IEEE Nucl. Sci. Symp.*, Dresden, Germany, 19-25 Oct. 2008 2008, pp. 446-448, doi: 10.1109/NSSMIC.2008.4775204. [Online]. Available: <https://ieeexplore.ieee.org/ielx5/4747668/4774073/04775204.pdf?tp=&arnumber=4775204&isnumber=4774073>
- [17] D. S. McGregor, W. J. McNeil, S. L. Bellinger, T. C. Unruh, and J. K. Shultis, "Microstructured semiconductor neutron detectors," *Nucl. Instrum. Meth. A*, vol. 608, pp. 125-131, 2009, doi: 10.1016/j.nima.2009.06.031.
- [18] J. K. Shultis and D. S. McGregor, "Design and performance considerations for perforated semiconductor thermal-neutron detectors," *Nucl. Instrum. Meth. A*, vol. 606, pp. 608-636, 2009, doi: 10.1016/j.nima.2009.02.033.
- [19] S. L. Bellinger, R. G. Fronk, W. J. McNeil, J. K. Shultis, T. J. Sobering, and D. S. McGregor, "Characteristics of the stacked microstructured solid state neutron detector," presented at the SPIE Hard X-ray, Gamma-ray, and Neutron Detector Physics XII, San Diego, CA USA, 2010. [Online]. Available: <https://www.spiedigitallibrary.org/conference-proceedings-of-spie/7805/1/Characteristics-of-the-stacked-microstructured-solid-state-neutron-detector/10.1117/12.863603.short?SSO=1>.
- [20] W. J. McNeil, "Perforated Didoe Neutron Sensors," Doctor of Philosophy Dissertation, Nuclear Engineering, Kansas State University, 2010.
- [21] S. L. Bellinger, "Advanced microstructured semiconductor neutron detectors: design, fabrication, and performance," Doctor of Philosophy Dissertation, Nuclear Engineering, Kansas State University, 2011.
- [22] S. L. Bellinger, R. G. Fronk, W. J. McNeil, T. J. Sobering, and D. S. McGregor, "Improved High Efficiency Stacked Microstructured Neutron Detectors Backfilled With Nanoparticle LiF," *IEEE Trans. Nucl. Sci.*, vol. 59, 2012, doi: 10.1109/TNS.2011.2175749.
- [23] D. S. McGregor, S. L. Bellinger, and J. K. Shultis, "Present status of microstructured semiconductor neutron detectors," *J. Cryst. Growth*, vol. 379, pp. 99-110, 2013, doi: 10.1016/j.jcrysgro.2012.10.061.
- [24] S. L. Bellinger *et al.*, "Characterization of microstructured semiconductor neutron detectors," presented at the 2013 IEEE Nucl. Sci. Symp. (2013 NSS/MIC), Seoul, South Korea, 2014. [Online]. Available: <https://ieeexplore.ieee.org/ielx7/6819718/6829008/06829849.pdf?tp=&arnumber=6829849&isnumber=6829008>.
- [25] S. L. Bellinger, R. G. Fronk, and D. S. McGregor, "Method of fabricating a neutron detector such as a microstructured semiconductor neutron detector," United States, 2014.

- [26] D. S. McGregor *et al.*, "Development of compact high efficiency microstructured semiconductor neutron detectors," *Radiat. Phys. Chem.*, vol. 116, pp. 32-37, 2015, doi: 10.1016/j.radphyschem.2015.05.025.
- [27] T. R. Ochs *et al.*, "Fabrication of present-generation microstructured semiconductor neutron detectors," presented at the 2014 IEEE Nucl. Sci. Symp. (NSS/MIC 2014), Seattle, WA, USA, 2016. [Online]. Available: <https://ieeexplore.ieee.org/ielx7/7422433/7430744/07431177.pdf?tp=&arnumber=7431177&isnumber=7430744>.
- [28] "MSND® Tile | RDT." Radiation Detection Technologies Inc. http://radectech.com/content/Domino_V5.40_general_spec_sheet_30percent-rev1.pdf (accessed 5/8/2019).
- [29] T. R. Ochs, S. L. Bellinger, R. G. Fronk, L. C. Henson, R. M. Hutchins, and D. S. McGregor, "Improved manufacturing and performance of the dual-sided microstructured semiconductor neutron detector (DS-MSND)," *Nucl. Instrum. Meth. A*, 2018, doi: <https://doi.org/10.1016/j.nima.2018.12.011>.
- [30] R. G. Fronk *et al.*, "Dual-sided microstructured semiconductor neutron detectors (DSMSNDs)," *Nucl. Instrum. Meth. A*, vol. 804, pp. 201-206, 2015, doi: 10.1016/j.nima.2015.09.040.
- [31] R. G. Fronk *et al.*, "Development of the dual-sided microstructured semiconductor neutron detector," presented at the 2014 IEEE Nucl. Sci. Symp. (NSS/MIC), Seattle, WA, USA, 2016. [Online]. Available: <https://ieeexplore.ieee.org/ielx7/7422433/7430744/07431247.pdf?tp=&arnumber=7431247&isnumber=7430744>.
- [32] R. G. Fronk *et al.*, "Advancements on dual-sided microstructured semiconductor neutron detectors (DSMSNDs)," presented at the 2015 IEEE Nucl. Sci. Symp. (NSS/MIC), San Diego, CA USA, 2016. [Online]. Available: <https://ieeexplore.ieee.org/ielx7/7572833/7581238/07582287.pdf?tp=&arnumber=7582287&isnumber=7581238>.
- [33] R. G. Fronk, "Dual-side etched microstructured semiconductor neutron detectors," Doctor of Philosophy Dissertation, Nuclear Engineering, Kansas State University, 2017.
- [34] W. C. Rontgen, "On a New Kind of Rays," *Nature*, vol. 53, no. 1369, pp. 274-276, 1896/01/01 1896, doi: 10.1038/053274b0.
- [35] E. Rutherford, "VIII. Uranium radiation and the electrical conduction produced by it," *The London, Edinburgh, and Dublin Philosophical Magazine and Journal of Science*, vol. 47, no. 284, pp. 109-163, 1899/01/01 1899, doi: 10.1080/14786449908621245.
- [36] E. Rutherford, "XV. The magnetic and electric deviation of the easily absorbed rays from radium," *The London, Edinburgh, and Dublin Philosophical Magazine and Journal of Science*, vol. 5, no. 26, pp. 177-187, 1903/02/01 1903, doi: 10.1080/14786440309462912.
- [37] P. Villard, "Sur la réflexion et la réfraction des rayons cathodiques et des rayons déviés du radium," *Comptes rendus*, vol. 130, pp. 1010-1012, 1900.
- [38] J. Chadwick, "Possible Existence of a Neutron," *Nature*, vol. 129, no. 3252, pp. 312-312, 1932/02/01 1932, doi: 10.1038/129312a0.
- [39] J. Chadwick, "The existence of a neutron," *Proc. SPIE Int. Soc. Opt. Eng.*, vol. 136, no. 830, pp. 692-708, 1932, doi: 10.1098/rspa.1932.0112.

- [40] E. Rutherford, "Bakerian Lecture. Nuclear Constitution of Atoms," *Proc. R. Soc. London, Ser. A*, vol. 97, no. 686, pp. 374-400, 1920. [Online]. Available: <http://www.jstor.org/stable/93888>.
- [41] S. H. Jiang *et al.*, "A study on natural background neutron dose," *IEEE Trans. Nucl. Sci.*, vol. 41, pp. 993-998, 1994, doi: 10.1109/23.322846.
- [42] W. L. Dunn and J. K. Shultis, *Exploring Monte Carlo Methods*. Amsterdam, Netherlands: Elsevier, 2012.
- [43] J. K. Shultis and R. E. Faw, *Fundamentals of Nuclear Science and Engineering*, 2nd ed. Boca Raton, FL: Taylor & Francis Group, LLC, 2008.
- [44] N. Tsoulfanidis and S. Landsberger, *Measurement and Detection of Radiation*, 3rd ed. Boca Raton, FL: CRC Press, 2011.
- [45] G. F. Knoll, *Radiation Detection and Measurement*, 4th ed. Hoboken, NJ: John Wiley & Sons, 2010.
- [46] J. K. Shultis and R. E. Faw, *Radiation Shielding*. La Grange Park, IL: American Nuclear Society, 2000.
- [47] D. A. Brown *et al.*, "ENDF/B-VIII.0: The 8th Major Release of the Nuclear Reaction Data Library with CIELO-project Cross Sections, New Standards and Thermal Scattering Data," *Nucl. Data Sheets*, vol. 148, pp. 1-142, 2018/02/01/ 2018, doi: <https://doi.org/10.1016/j.nds.2018.02.001>.
- [48] R. H. Olsher *et al.*, "PRESCILA: A new, lightweight neutron rem meter," *Health Physics*, vol. 86, pp. 603-612, 2004.
- [49] W. Crookes, "Certain Properties of the Emanations of Radium," *Druggists' Circular and Chemical Gazette (1866-1906)*, vol. 47, no. 8, p. 165, 1903.
- [50] E. Rutherford, *Radioactive substances and their radiations*. Cambridge [Eng.] New York Cambridge [Eng.]: Cambridge Eng. University Press; New York, G. P. Putnam's sons, 1913.
- [51] N. S. Edwards *et al.*, "Lithium foil gas-filled neutron detector using microstrip electrodes," vol. 2017-, ed, 2017, p. <xocs:firstpage xmlns:xocs=""/>.
- [52] N. S. Edwards *et al.*, "Neutron sensitivity of 6 Li-based suspended foil microstrip neutron detectors using Schott Borofloat® 33 microstrip electrodes," *Radiat. Phys. Chem.*, vol. 147, pp. 70-76, 2018, doi: 10.1016/j.radphyschem.2018.02.013.
- [53] K. A. Nelson *et al.*, "Investigation of a lithium foil multi-wire proportional counter for potential 3 He replacement," *Nucl. Instrum. Meth. A*, vol. 669, pp. 79-84, 2012, doi: 10.1016/j.nima.2011.12.003.
- [54] K. A. Nelson *et al.*, "Investigation of aerogel, saturated foam, and foil for thermal neutron detection," ed, 2012, pp. 1026-1029.
- [55] K. A. Nelson, S. R. Bolding, A. J. Schmidt, J. K. Shultis, C. D. Wayant, and D. S. McGregor, "A simulation of a layered 6 Li foil multi-wire proportional counter," ed, 2012, pp. 207-210.
- [56] K. A. Nelson, N. S. Edwards, N. J. Hinson, C. D. Wayant, and D. S. McGregor, "A suspended boron foil multi-wire proportional counter neutron detector," *Nucl. Instrum. Meth. A*, vol. 767, no. C, pp. 14-18, 2014, doi: 10.1016/j.nima.2014.08.007.
- [57] K. A. Nelson *et al.*, "A modular large-area lithium foil multi-wire proportional counter neutron detector," *Radiat. Phys. Chem.*, vol. 116, pp. 165-169, 2015, doi: 10.1016/j.radphyschem.2015.03.044.

- [58] K. A. Nelson *et al.*, "Characterization of a mid-sized Li foil multi-wire proportional counter neutron detector," *Nucl. Instrum. Meth. A*, vol. 762, no. C, pp. 119-124, 2014, doi: 10.1016/j.nima.2014.05.078.
- [59] K. A. Nelson, B. W. Montag, A. J. Schmidt, C. D. Wayant, and D. S. McGregor, "A layered 6 Li foil multi-wire proportional counter," ed, 2012, pp. 597-599.
- [60] B. W. Montag *et al.*, "Recent progress in the commercialization of the Li Foil multi-wire proportional counter neutron detectors," *Radiat. Phys. Chem.*, 2018, doi: 10.1016/J.RADPHYSHEM.2018.08.003.
- [61] D. S. McGregor, S. L. Bellinger, and K. A. Nelson, "Gas-filled neutron detectors and imaging system and array of such detectors," United States of America Patent US 9,817,138 B2 Patent Appl. 13/773,831, 2017.
- [62] D. S. McGregor, S. L. Bellinger, W. J. McNeil, M. F. Ohmes, and K. A. Nelson, "Gas-filled neutron detectors having improved detection efficiency," United States of America Patent US 8,519,350 B2 Patent Appl. 13/404,751, Aug. 27, 2013, 2013.
- [63] K. Ahmed, R. Dahal, A. Weltz, J. J. Q. Lu, Y. Danon, and I. B. Bhat, "Solid-state neutron detectors based on thickness scalable hexagonal boron nitride," *Appl. Phys. Lett.*, vol. 110, no. 2, p. 023503, 2017/01/09 2017, doi: 10.1063/1.4973927.
- [64] A. G. Beyerle and K. L. Hull, "Neutron detection with mercuric iodide detectors," *Nucl. Instrum. Meth. A*, vol. 256, pp. 377-380, 1987, doi: 10.1016/0168-9002(87)90236-1.
- [65] D. S. McGregor, J. T. Lindsay, and R. W. Olsen, "Thermal neutron detection with cadmium_{1-x} zinc_x telluride semiconductor detectors," *Nucl. Instrum. Meth. A*, vol. 381, pp. 498-501, 1996, doi: 10.1016/S0168-9002(96)00580-3.
- [66] B. W. Montag, P. B. Ugorowski, K. A. Nelson, N. S. Edwards, and D. S. McGregor, "Device fabrication, characterization, and thermal neutron detection response of LiZnP and LiZnAs semiconductor devices," *Nucl. Instrum. Meth. A*, vol. 836, pp. 30-36, 2016, doi: 10.1016/j.nima.2016.08.037.
- [67] E. Tupitsyn *et al.*, "Lithium containing chalcogenide single crystals for neutron detection," *J. Cryst. Growth*, vol. 393, pp. 23-27, 2014, doi: 10.1016/j.jcrysgro.2013.10.054.
- [68] E. Tupitsyn *et al.*, "Single crystal of LiInSe₂ semiconductor for neutron detector," *Appl. Phys. Lett.*, vol. 101, p. 202101, 2012, doi: 10.1063/1.4762002.
- [69] R. A. Muminov and L. D. Tsvang, "High-efficiency semiconductor thermal-neutron detectors," *Soviet Atomic Energy*, vol. 62, pp. 316-319, 1987, doi: 10.1007/BF01123372.
- [70] J. Schelten, M. Balzhäuser, F. Höngesberg, R. Engels, and R. Reinartz, "A new neutron detector development based on silicon semiconductor and ⁶LiF converter," *Physica B: Condensed Matter*, vol. 234-236, pp. 1084-1086, 1997, doi: 10.1016/S0921-4526(97)00024-0.
- [71] D. S. McGregor, R. T. Klann, H. K. Gersch, E. Ariesanti, J. D. Sanders, and B. VanDerElzen, "New surface morphology for low stress thin-film-coated thermal neutron detectors," in *2001 IEEE Nucl. Sci. Symp.*, San diego, CA, USA, 4-10, Nov. 2001, vol. 4: IEEE, pp. 2401-2405, doi: 10.1109/NSSMIC.2001.1009304. [Online]. Available: <https://ieeexplore.ieee.org/ielx5/7884/21759/01009304.pdf?tp=&arnumber=1009304&isnumber=21759>
- [72] Y. Danon *et al.*, "Towards high efficiency solid-state thermal and fast neutron detectors," *J. Instrum.*, vol. 7, pp. C03014-C03014, 2012, doi: 10.1088/1748-0221/7/03/C03014.

- [73] K.-C. Huang, R. Dahal, J. J-Q Lu, Y. Danon, and I. B. Bhat, "High detection efficiency micro-structured solid-state neutron detector with extremely low leakage current fabricated with continuous p-n junction," *Appl. Phys. Lett.*, vol. 102, p. 152107, 2013, doi: 10.1063/1.4802204.
- [74] R. J. Nikolic *et al.*, "Fabrication of Pillar-structured thermal neutron detectors," in *2007 IEEE Nucl. Sci. Symp.*, Honolulu, HI, USA, 2007: IEEE, pp. 1577-1580, doi: 10.1109/NSSMIC.2007.4437299. [Online]. Available: <https://ieeexplore.ieee.org/ielx5/4436263/4437154/04437299.pdf?tp=&arnumber=4437299&isnumber=4437154>
- [75] R. J. Nikolić *et al.*, "6:1 aspect ratio silicon pillar based thermal neutron detector filled with B10," *Appl. Phys. Lett.*, vol. 93, p. 133502, 2008, doi: 10.1063/1.2985817.
- [76] J. Uher *et al.*, "Characterization of 3D thermal neutron semiconductor detectors," *Nucl. Instrum. Meth. A*, vol. 576, pp. 32-37, 2007, doi: 10.1016/j.nima.2007.01.115.
- [77] W. Jentschke, "The Crystal Counter," *Physical Review*, vol. 73, no. 1, pp. 77-78, 1948, doi: 10.1103/PhysRev.73.77.2.
- [78] R. Frerichs and R. Warminsky, "Die Messung von β - und γ -Strahlen durch inneren Photoeffekt in Kristallphosphoren," *Naturwissenschaften*, vol. 33, no. 8, pp. 251-251, 1946, doi: 10.1007/BF01204482.
- [79] D. E. Wooldridge, A. J. Ahearn, and J. A. Burton, "Conductivity pulses induced in diamond by alpha-particles [12]," *Physical Review*, vol. 71, no. 12, p. 913, 1947, doi: 10.1103/PhysRev.71.913.
- [80] K. G. McKay, "Electron-hole production in germanium by alpha-particles," *Physical Review (U.S.) Superseded in part by Phys. Rev. A, Phys. Rev. B: Solid State, Phys. Rev. C, and Phys. Rev. D*, vol. 84, no. 4, 1951, doi: 10.1103/PhysRev.84.829.
- [81] E. M. Pell, "Solubility of lithium in silicon," *J. Phys. Chem. Solids*, vol. 3, no. 1, pp. 77-81, 1957, doi: 10.1016/0022-3697(57)90051-3.
- [82] E. M. Pell, "Solubility of Lithium in germanium," *J. Phys. Chem. Solids*, vol. 3, no. 1, pp. 74-76, 1957, doi: 10.1016/0022-3697(57)90050-1.
- [83] W. D. Davis, "Silicon Crystal Counters," *J. Appl. Phys.*, vol. 29, no. 2, pp. 231-232, 1958, doi: 10.1063/1.1723082.
- [84] J. W. Mayer, "Performance of Germanium and Silicon Surface Barrier Diodes as Alpha-Particle Spectrometers," *J. Appl. Phys.*, vol. 30, no. 12, p. 1937, 1959, doi: 10.1063/1.1735093.
- [85] W. R. Harding, C. Hilsum, M. E. Moncaster, D. C. Northrop, and O. Simpson, "Gallium arsenide for gamma-ray spectroscopy," *Nature*, vol. 187, no. 4735, 1960, doi: 10.1038/187405a0.
- [86] E. M. Pell, "Ion Drift in an n-p Junction," *J. Appl. Phys.*, vol. 31, no. 2, pp. 291-302, 1960, doi: 10.1063/1.1735561.
- [87] E. M. Pell, "Diffusion of Li In Si at high T and the isotope effect," *Physical Review (U.S.) Superseded in part by Phys. Rev. A, Phys. Rev. B: Solid State, Phys. Rev. C, and Phys. Rev. D*, vol. 119, no. 3, 1960, doi: 10.1103/PhysRev.119.1014.
- [88] W. Akutagawa, K. Zanio, and J. W. Mayer, "CdTe as a Gamma Detector," *Nucl. Instrum. Methods*, 55: 383-5(Oct. 1967), vol. 55, no. C, 1967, doi: 10.1016/0029-554X(67)90147-4.

- [89] K. Zanio, W. Akutagawa, and J. W. Mayer, "Transport Properties of Semi-insulating CdTe using nuclear particles," *Appl. Phys. Lett.*, vol. 11, no. 1, pp. 5-7, 1967, doi: 10.1063/1.1754949.
- [90] R. N. Hall, R. D. Baertsch, and T. J. Soltys, "High-purity germanium for gamma detectors. Annual Report No. 1, June 1967- -April 1968," S. N. Y. R. a. D. C. General Electric Co, Ed., ed. United States: United States, 1968.
- [91] J. E. Eberhardt, R. D. Ryan, and A. J. Tavendale, "High-resolution nuclear radiation detectors from epitaxial n-GaAs," *Appl. Phys. Lett.*, vol. 17, no. 10, pp. 427-429, 1970, doi: 10.1063/1.1653257.
- [92] S. Roth and W. R. Willig, "Lead iodide nuclear particle detectors," *Appl. Phys. Lett.*, vol. 18, no. 8, pp. 328-330, 1971, doi: 10.1063/1.1653682.
- [93] W. R. Willig, "Mercury iodide as a gamma spectrometer," *Nucl. Instrum. Methods*, vol. 96, no. 4, pp. 615-616, 1971, doi: 10.1016/0029-554X(71)90182-0.
- [94] J. F. Butler, F. P. Doty, and C. Lingren, "Cadmium zinc telluride detectors for industrial radiation measurement," vol. 65:1, ed. United States, 1992.
- [95] J. F. Butler, F. P. Doty, and C. L. Lingren, "Recent developments in CdZnTe gamma-ray detector technology," vol. 1734, ed, 1992, pp. 131-139.
- [96] J. F. Butler, C. L. Lingren, and F. P. Doty, "Cd/sub 1-x/Zn/sub x/Te gamma ray detectors," *IEEE Trans. Nucl. Sci.*, vol. 39, no. 4, pp. 605-609, 1992, doi: 10.1109/23.159673.
- [97] J. D. Eskin, H. H. Barrett, and H. B. Barber, "Recovery of spectral information from an imperfect detector using the expectation maximization algorithm," vol. 1, ed, 1994, pp. 150-154 vol.1.
- [98] P. N. Luke, "Single-polarity charge sensing in ionization detectors using coplanar electrodes," *Appl. Phys. Lett.*, vol. 65, no. 22, pp. 2884-2886, 1994, doi: 10.1063/1.112523.
- [99] M. Schieber *et al.*, "State of the art of wide-bandgap semiconductor nuclear radiation detectors," *Il Nuovo Cimento A (1965-1970)*, vol. 109, no. 9, pp. 1253-1260, 1996, doi: 10.1007/BF02773511.
- [100] D. S. McGregor, Z. He, H. A. Seifert, D. K. Wehe, and R. A. Rojas, "Single charge carrier type sensing with a parallel strip pseudo-Frisch-grid CdZnTe semiconductor radiation detector," *Appl. Phys. Lett.*, vol. 72, no. 7, pp. 792-794, 1998, doi: 10.1063/1.120895.
- [101] S. P. D. M. Douglas and A. R. Ronald, "High-resolution ionization detector and array of such detectors," ed, 1999.
- [102] W. J. McNeil, D. S. McGregor, A. E. Bolotnikov, G. W. Wright, and R. B. James, "Single-charge-carrier-type sensing with an insulated Frisch ring CdZnTe semiconductor radiation detector," *Appl. Phys. Lett.*, vol. 84, no. 11, pp. 1988-1990, 2004, doi: 10.1063/1.1668332.
- [103] P. Ugorowski, A. Ariesanti, D. S. McGregor, and A. Kargar, "Compact, inexpensive, high-energy-resolution, room-temperature-operated, semiconductor gamma-ray detectors for isotope identification," ed, 2010, pp. 385-390.
- [104] E. Ariesanti, A. Kargar, and D. S. McGregor, "Mercuric iodide crystal growth and frisch collar detector fabrication," *Nucl. Technol.*, vol. 175, no. 1, pp. 124-130, 2011, doi: 10.13182/NT11-A12280.

- [105] A. Kargar, E. Ariesanti, and D. S. McGregor, "A comparison between spectroscopic performance of HgI₂ and CdZnTe frisch collar detectors," *Nucl. Technol.*, vol. 175, no. 1, pp. 131-137, 2011, doi: 10.13182/NT11-A12281.
- [106] K. Nelson, J. Neihart, T. Riedel, R. Rojeski, and D. McGregor, "CdZnTe electro-optic neutron detector response to nuclear reactor pulses and transient rod pulls," *Abstr. Pap. Am. Chem. Soc.*, vol. 242, 2011.
- [107] P. B. Ugorowski, A. C. Brooks, R. D. Taylor, T. J. Sobering, and D. S. McGregor, "Preliminary results of KSU Frisch-collar CZT array," ed, 2011, pp. 4674-4676.
- [108] S. M. Sze, *Semiconductor Devices, Physics and Technology*, 2nd. Ed. ed. Hoboken, New Jersey: John Wiley & Sons, Inc., 2002.
- [109] G. Lutz, *Semiconductor Radiation Detectors Device Physics*. Springer, 2007.
- [110] R. F. Pierret, *Semiconductor Fundamentals*, 2nd ed. (Modular Series on Solid State Devices). Reading, Massachusetts: Addison-Wesley Publishing Company, 1988.
- [111] R. F. Pierret, *Advanced Semiconductor Fundamentals*, 2nd ed. (Modular Series on Solid State Devices). Upper Saddle River, New Jersey: Prentice Hall, 2003.
- [112] S. M. Sze, *Physics of Semiconductor Devices*, 2nd ed. Murray Hill, NJ: John Wiley & Sons, 1981.
- [113] G. W. Neudeck, *The PN Junction Diode*, 2nd ed. (Modular Series on Solid State Devices). Reading, Massachusetts: Addison-Wesley Publishing Company, 1989.
- [114] H. Spieler, *Semiconductor detector systems*. Oxford, New York: Oxford ; New York : Oxford University Press, 2005.
- [115] R. V. Babcock, R. E. Davis, S. L. Ruby, K. H. Sun, and E. D. Wolley, "Coated semiconductor is a tiny neutron detector," (in English), 1959-04-01 1959. [Online]. Available: <https://www.osti.gov/servlets/purl/4268072>.
- [116] M. Wielunski *et al.*, "Study of the sensitivity of neutron sensors consisting of a converter plus Si charged-particle detector," *Nucl. Instrum. Meth. A*, vol. 517, pp. 240-253, 2004, doi: 10.1016/j.nima.2003.07.032.
- [117] J. W. Wu, "Low-cost fabrication of high efficiency solid-state neutron detectors," *Proceedings of SPIE - The International Society for Optical Engineering*, vol. 9824, 2016, doi: 10.1117/12.2224050.
- [118] Q. Shao *et al.*, "Experimental determination of gamma-ray discrimination in pillar-structured thermal neutron detectors under high gamma-ray flux," *Nucl. Instrum. Meth. A*, vol. 799, pp. 203-206, 2015, doi: 10.1016/J.NIMA.2015.07.045.
- [119] T. R. Ochs *et al.*, "Wearable detector device utilizing microstructured semiconductor neutron detector technology," *Radiat. Phys. Chem.*, vol. 155, pp. 164-172, 2019/02/01/ 2019, doi: <https://doi.org/10.1016/j.radphyschem.2018.08.028>.
- [120] T. R. Ochs *et al.*, "Wearable neutron detector for dosimetry and nuclear non-proliferation," presented at the International Conference on the Security of Radioactive Material: The Way Forward for Prevention and Detection, Vienna, Austria, 2018.
- [121] T. R. Ochs *et al.*, "Fourth-generation microstructured semiconductor neutron detector (MSND)-based ³He replacement (HeRep) for high pressure ³He detectors," presented at the 2016 IEEE Nucl. Sci. Symp. (NSS/MIC), Strasbourg, France, 2017. [Online]. Available: <https://ieeexplore.ieee.org/ielx7/8062961/8069358/08069930.pdf?tp=&arnumber=8069930&isnumber=8069358>.

- [122] T. R. Ochs *et al.*, "Present status of the microstructured semiconductor neutron detector-based direct helium-3 replacement," *IEEE Trans. Nucl. Sci.*, vol. 64, pp. 1846-1850, 2017, doi: 10.1109/TNS.2017.2653719.
- [123] C. B. Hoshor *et al.*, "Real-time neutron source localization and identification with a hand-held, volumetrically-sensitive, moderating-type neutron spectrometer," *Nucl. Instrum. Meth. A*, vol. 866, pp. 252-264, 2017, doi: 10.1016/J.NIMA.2017.05.033.
- [124] R. G. Fronk *et al.*, "Improved low power, modular thermal neutron counter based on microstructured semiconductor neutron detectors (MSND)," presented at the 2016 IEEE Nucl. Sci. Symp. (NSS/MIC/RTSD 2016), Strasbourg, France, 2017. [Online]. Available: <https://ieeexplore.ieee.org/ielx7/8062961/8069358/08069791.pdf?tp=&arnumber=8069791&isnumber=8069358>.
- [125] R. G. Fronk *et al.*, "Advancements in microstructured semiconductor neutron detector (MSND)-based instruments," presented at the 2015 IEEE Nucl. Sci. Symp. (NSS/MIC 2015), San Diego, CA USA, 2016. [Online]. Available: <https://ieeexplore.ieee.org/ielx7/7572833/7581238/07581971.pdf?tp=&arnumber=7581971&isnumber=7581238>.
- [126] S. L. Bellinger, R. G. Fronk, L. C. Henson, T. R. Ochs, T. J. Sobering, and D. S. McGregor, "Microstructured semiconductor neutron detector (MSND)-based Helium-3 Replacement technology," presented at the 2014 IEEE Nucl. Sci. Symp. (NSS/MIC 2014), Seattle, WA, USA, 2016. [Online]. Available: <https://ieeexplore.ieee.org/ielx7/7422433/7430744/07430745.pdf?tp=&arnumber=7430745&isnumber=7430744>.
- [127] C. B. Hoshor *et al.*, "A portable and wide energy range semiconductor-based neutron spectrometer," *Nucl. Instrum. Meth. A*, vol. 803, pp. 68-81, 2015, doi: 10.1016/J.NIMA.2015.08.077.
- [128] R. G. Fronk *et al.*, "High-efficiency microstructured semiconductor neutron detectors for direct ^3He replacement," *Nucl. Instrum. Meth. A*, vol. 779, pp. 25-32, 2015, doi: 10.1016/j.nima.2015.01.041.
- [129] T. M. Oakes *et al.*, "An accurate and portable solid state neutron rem meter," *Nucl. Instrum. Meth. A*, vol. 719, pp. 6-12, 2013, doi: 10.1016/j.nima.2013.03.060.
- [130] S. R. Bolding, "Design of a Neutron Spectrometer and Simulations of Neutron Multiplicity Experiments with Nuclear Data Perturbations," Master of Science Master's Thesis, Nuclear Engineering, Kansas State University, 2013.
- [131] T. R. Ochs, R. G. Fronk, S. L. Bellinger, and D. S. McGregor, "Design and Performance Considerations for Dual-Sided Microstructured Semiconductor Neutron Detectors " *Nucl. Instrum. Methods Phys. Res. A*, 2019, in press.
- [132] M. J. Berger *et al.* XCOM: Photon Cross Section Database (version 1.5) [Online] Available: <https://www.nist.gov/pml/xcom-photon-cross-sections-database>
- [133] *TCAD Software*. Accessed: March 2019. [Online]. Available: www.silvaco.com
- [134] S. A. Campbell, *Fabrication engineering at the micro- and nanoscale*, 3rd ed. New York, New York: Oxford University Press, Inc., 2008.
- [135] B. V. Zeghbrock, "Principles of Semiconductor Devices," 2011, ch. 3. Unipolar Devices.
- [136] J. T. Goorley *et al.*, "MCNP6 User's Manual," pp. LA-CP-13-00634, 2013.

- [137] D. S. McGregor and J. Kenneth Shultis, "Reporting detection efficiency for semiconductor neutron detectors: A need for a standard," *Nucl. Instrum. Meth. A*, vol. 632, pp. 167-174, 2011, doi: 10.1016/j.nima.2010.12.084.
- [138] W. Fu, R. G. Fronk, D. S. McGregor, and J. A. Roberts, "Numerical evaluation of fast-sensitive microstructured semiconductor neutron detectors for TREAT hodoscope," *Nucl. Instrum. Meth. A*, 2018, doi: 10.1016/J.NIMA.2018.09.080.
- [139] L. F. Voss *et al.*, "Planarization of high aspect ratio p-i-n diode pillar arrays for blanket electrical contacts," *J. Vac. Sci. Technol., B*, vol. 28, pp. 916-920, 2010, doi: 10.1116/1.3478306.
- [140] J.-W. Wu *et al.*, "Boron-10 nanoparticles filled silicon trenches for thermal neutron detection application," *Appl. Phys. Lett.*, vol. 110, p. 192105, 2017, doi: 10.1063/1.4983289.
- [141] J. W. Murphy *et al.*, "Pillar-structured neutron detector based multiplicity system," *Nucl. Instrum. Meth. A*, vol. 877, pp. 355-358, 2018, doi: 10.1016/J.NIMA.2017.09.060.
- [142] B. L. Wall *et al.*, "Dead layer on silicon p-i-n diode charged-particle detectors," *Nucl. Instrum. Meth. A*, vol. 744, 2014, doi: 10.1016/j.nima.2013.12.048.
- [143] S. M. Sze, *VLSI Technology*. Murray Hill, NJ: McGraw-Hill, 1988.
- [144] S. Van Havereke, I. Teirlinck, C. Vinckier, G. Stevens, and M. Heyns, "The etching mechanisms of SiO₂ in Hydrofluoric acid," *J. Electrochem. Soc.*, vol. 141, p. 2852, 1994.
- [145] H. Seidel, L. Csepregi, A. Heuberger, and H. Baumgärtel, "Anisotropic Etching of Crystalline Silicon in Alkaline Solutions: I. Orientation Dependence and Behavior of Passivation Layers," *J. Electrochem. Soc.*, vol. 137, no. 11, pp. 3612-3626, 1990. [Online]. Available: <http://jes.ecsdl.org/content/137/11/3612.abstract>.
- [146] M. Elwenspoek, "On the Mechanism of Anisotropic Etching of Silicon," *J. Electrochem. Soc.*, vol. 140, no. 7, pp. 2075-2080, 1993, doi: 10.1149/1.2220767.
- [147] Microchemicals. "Wet-Chemical Etching of Silicon." https://www.seas.upenn.edu/~nanosop/documents/silicon_etching.pdf (accessed 3/3/2020).
- [148] S. Dutta, M. Imran, P. Kumar, R. Pal, P. Datta, and R. Chatterjee, "Comparison of etch characteristics of KOH, TMAH and EDP for bulk micromachining of silicon (110)," *Microsyst. Technol.*, vol. 17, no. 10, p. 1621, 2011/09/21 2011, doi: 10.1007/s00542-011-1351-6.
- [149] M. Pace. "KOH Silicon Etch Calculator." <http://lelandstanfordjunior.com/KOHcalcfaq.html> (accessed June 19th, 2019).
- [150] W. Kern, "The evolution of silicon wafer cleaning technology," *J. Electrochem. Soc.*, vol. 137, no. 6, pp. 1887-1891, 1990. [Online]. Available: http://inis.iaea.org/search/search.aspx?orig_q=RN:22002871.
- [151] W. Kern and D. A. Puotinen, "Cleaning solutions based on hydrogen for use in silicon semiconductor technology," *R.C.A. Review*, vol. 31, no. 2, pp. 187-206, 1970.
- [152] Saint-Gobain. "PDS Solid Diffusion Sources | Saint-Gobain Boron Nitride." <https://www.bn.saint-gobain.com/products/pds-products> (accessed June, 2019).
- [153] R. M. German, *Particle packing characteristics*. Princeton, N.J.: Metal Powder Industries Federation, 1989.
- [154] Z. Xie, X. An, Y. Wu, L. Wang, Q. Qian, and X. Yang, "Experimental study on the packing of cubic particles under three-dimensional vibration," *Powder Technol.*, vol. 317, pp. 13-22, 2017/07/15/ 2017, doi: <https://doi.org/10.1016/j.powtec.2017.04.037>.

- [155] T. C. Unruh, "Development of a neutron diffraction system and neutron imaging system for beamport characterization," Master of Science Master's Thesis Nuclear Engineering, Kansas State University, 2009.
- [156] R. G. Fronk *et al.*, "Method for determination of charge transport in microstructured semiconductor neutron detectors (MSNDs)," *Nucl. Instrum. Meth. A*, 2019, submitted for review.
- [157] J. R. Taylor, *An Introduction to Error Analysis: The Study of Uncertainties in Physical Measurements*, 2nd ed. Mill Valley, CA: University Science Books, 1997.
- [158] "Neutron-Detecting Personal Radiation Detectors (PRDs) and Spectroscopic PRDs Market Survey Report," National Urban Security Technology Laboratory, 2015. Accessed: 8/30/2019. [Online]. Available: https://www.dhs.gov/sites/default/files/publications/ND-PRD-MSR_0215-508_0.pdf
- [159] "CapeSym | Scinticlear." CapeSym Inc. <http://capesym.com/sri2.html> (accessed 8/19/2019, 2019).
- [160] *American National Standard Performance Criteria for Backpack-Based Radiation-Detection Systems Used for Homeland Security*, ANSI N42.53-2013, ANSI, 2013.
- [161] R. T. Kouzes, J. H. Ely, A. T. Linteur, E. K. Mace, D. L. Stephens, and M. L. Woodring, "Neutron detection gamma ray sensitivity criteria," 2011, doi: 10.1016/j.nima.2011.07.030.
- [162] R. T. Kouzes, J. R. Ely, A. T. Linteur, and D. L. Stephens, "Neutron Detector Gamma Insensitivity Criteria," Pacific Northwest National Laboratory, October 28, 2009 2009.
- [163] T. R. Ochs *et al.*, "Wearable Neutron Detector Device with Wireless Modular Neutron Detectors and Modular Gamma-Ray Detectors " in *2018 IEEE Nuclear Science Symposium and Medical Imaging Conference*, Sydney, Australia, Nov. 10-17, 2018 2018, submitted.
- [164] L. A. Currie, "Limits for qualitative detection and quantitative determination. Application to radiochemistry," *Analytical Chemistry*, vol. 40, no. 3, pp. 586-593, 1968/03/01 1968, doi: 10.1021/ac60259a007.
- [165] *A Handbook of Radioactivity Measurement Procedures*, 2nd Ed. ed. (NCRP Report No. 58). Bethesda, MD: National Council on Radiation Protection and Measurements, 1985.
- [166] *Conversion Coefficients for Radiological Protection Quantities for External Radiation Exposures*, 0146-6453, ICRP, 2010.
- [167] *The 2007 Recommendations of the International Commission on Radiological Protection*, ICRP, 2007.
- [168] *Conversion coefficients for use in radiological protection against external radiation*, ICRP, 1996.
- [169] *Relative Biological Effectiveness (RBE), Quality Factor (Q), and Radiation Weighting Factor (w_R)*, ICRP, 2003.
- [170] R. H. Olsher *et al.*, "WENDI: An improved neutron rem meter," *Health Physics*, vol. 79, pp. 170-181, 2000.
- [171] CardinalHealth. "Portable Neutron Survey Meter Victoreen® Model 190N." <https://www.flukebiomedical.com/products/biomedical-test-equipment/190n-portable-neutron-survey-meter> (accessed 02/10/2018).
- [172] M. Awschalom and R. S. Sanna, "Applications of Bonner Sphere Detectors in Neutron Field Dosimetry," *Radiat. Prot. Dosim.*, vol. 10, no. 1-4, pp. 89-101, 1985, doi: 10.1093/oxfordjournals.rpd.a079413.

- [173] R. L. Bramblett, R. I. Ewing, and T. W. Bonner, "A new type of neutron spectrometer," *Nucl. Instrum. Methods*, vol. 9, no. 1, pp. 1-12, 1960/10/01/ 1960, doi: [https://doi.org/10.1016/0029-554X\(60\)90043-4](https://doi.org/10.1016/0029-554X(60)90043-4).
- [174] J. W. Leake, "A spherical dose equivalent neutron detector," *Nucl. Instrum. Methods*, vol. 45, no. 1, pp. 151-156, 1966/11/01/ 1966, doi: [https://doi.org/10.1016/0029-554X\(66\)90420-4](https://doi.org/10.1016/0029-554X(66)90420-4).
- [175] "RDT Domino V5.4 Neutron Detector." Radiation Detection Technologies, Inc. <http://radectech.com/products/rdt-domino-v5-4> (accessed 11/5/2019, 2019).
- [176] W. J. McNeil *et al.*, "1-D array of perforated diode neutron detectors," *Nucl. Instrum. Meth. A*, vol. 604, no. 1-2, pp. 127-129, 2009, doi: 10.1016/j.nima.2009.01.054.
- [177] G. Adamo *et al.*, "Responsivity measurements of silicon carbide schottky photodiodes in the UV range."

List of Publications (as of March 2020)

Peer Reviewed

T. R. Ochs, R. G. Fronk, S. L. Bellinger, and D. S. McGregor, "Design and performance considerations for dual-sided microstructured semiconductor neutron detectors," *Nucl. Instrum. Meth. A*, vol. 951, p. 163006, 2020.

T. R. Ochs, S. L. Bellinger, R. G. Fronk, L. C. Henson, R. M. Hutchins, and D. S. McGregor, "Improved manufacturing and performance of the dual-sided microstructured semiconductor neutron detector (DS-MSND)," *Nucl. Instrum. Meth. A*, vol. 954, p. 161696, 2020.

T. R. Ochs *et al.*, "Wearable detector device utilizing microstructured semiconductor neutron detector technology," *Radiat. Phys. Chem.*, vol. 155, pp. 164-172, 2019.

T. R. Ochs *et al.*, "Wearable Detector Device Utilizing Microstructured Semiconductor Neutron Detectors," *Transactions of the American Nuclear Society*, vol. 119, pp. 188-191, Orlando, Florida, Nov. 11-15, 2018.

T. R. Ochs *et al.*, "Present status of the microstructured semiconductor neutron detector-based direct helium-3 replacement," *IEEE Trans. Nucl. Sci.*, vol. 64, pp. 1846-1850, 2017.

D. S. McGregor *et al.*, "Development of compact high efficiency microstructured semiconductor neutron detectors," *Radiat. Phys. Chem.*, vol. 116, pp. 32-37, 2015.

R. G. Fronk *et al.*, "Dual-sided microstructured semiconductor neutron detectors (DSMSNDs)," *Nucl. Instrum. Meth. A*, vol. 804, pp. 201-206, 2015.

R. G. Fronk *et al.*, "High-efficiency microstructured semiconductor neutron detectors for direct ^3He replacement," *Nucl. Instrum. Meth. A*, vol. 779, pp. 25-32, 2015.

Conference Proceedings

T. R. Ochs *et al.*, "Present Status of the Dual-Sided Microstructured Semiconductor Neutron Detector (DS-MSND) and Instrumentation," presented at the 2019 IEEE Nucl. Sci. Symp. (NSS/MIC), Manchester, United Kingdom, Oct. 26 – Nov. 7, 2019.

B. W. Montag *et al.*, "Commercialization of the Li-Foil Multi-Wire Proportional Counter Neutron Detector, a Backpack Radiation Detector Design," presented at the 2019 IEEE Nucl. Sci. Symp. (NSS/MIC), Manchester, United Kingdom, Oct. 26 – Nov. 7, 2019.

D.M. Nichols *et al.*, "Reactor Pulse Tracking using Micro-Pocket Fission Detectors in Research Reactors," presented at the 2019 IEEE Nucl. Sci. Symp. (NSS/MIC), United Kingdom, Oct. 26 – Nov. 7, 2019.

T. R. Ochs *et al.*, "Wearable neutron detector for dosimetry and nuclear non-proliferation," presented at the International Conference on the Security of Radioactive Material: The Way Forward for Prevention and Detection, Vienna, Austria, 2018.

T. R. Ochs *et al.*, "Wearable detector device with wireless modular neutron detectors and modular gamma-ray detectors," presented at the 2018 IEEE Nucl. Sci. Symp. (NSS/MIC), Sydney, Australia, 10-17 Nov. 2018.

B. W. Montag *et al.*, "Technology Readiness and Device Design of the Li Foil Multi-Wire Proportional Counter Neutron Detector," presented at the 2018 IEEE Nucl. Sci. Symp. (NSS/MIC), Sydney, Australia, 10-17 Nov. 2018.

T. R. Ochs *et al.*, "Fourth-generation microstructured semiconductor neutron detector (MSND)-based ^3He replacement (HeRep) for high pressure ^3He detectors," presented at the 2016 IEEE Nucl. Sci. Symp. (NSS/MIC), Strasbourg, France, 2017.

R. G. Fronk *et al.*, "Improved low power, modular thermal neutron counter based on microstructured semiconductor neutron detectors (MSND)," presented at the 2016 IEEE Nucl. Sci. Symp. (NSS/MIC/RTSD 2016), Strasbourg, France, 2017.

R. G. Fronk *et al.*, "Advancements on dual-sided microstructured semiconductor neutron detectors (DSMSNDs)," presented at the 2015 IEEE Nucl. Sci. Symp. (NSS/MIC), San Diego, CA USA, 2016.

R. G. Fronk *et al.*, "Advancements in microstructured semiconductor neutron detector (MSND)-based instruments," presented at the 2015 IEEE Nucl. Sci. Symp. (NSS/MIC 2015), San Diego, CA USA, 2016.

R. G. Fronk *et al.*, "Development of the dual-sided microstructured semiconductor neutron detector," presented at the 2014 IEEE Nucl. Sci. Symp. (NSS/MIC), Seattle, WA, USA, 2016.

T. R. Ochs *et al.*, "Fabrication of present-generation microstructured semiconductor neutron detectors," presented at the 2014 IEEE Nucl. Sci. Symp. (NSS/MIC 2014), Seattle, WA, USA, 2016.

S. L. Bellinger, R. G. Fronk, L. C. Henson, T. R. Ochs, T. J. Sobering, and D. S. McGregor, "Microstructured semiconductor neutron detector (MSND)-based Helium-3 Replacement technology," presented at the 2014 IEEE Nucl. Sci. Symp. (NSS/MIC 2014), Seattle, WA, USA, 2016.

S. L. Bellinger *et al.*, "Characterization of microstructured semiconductor neutron detectors," presented at the 2013 IEEE Nucl. Sci. Symp. (2013 NSS/MIC), Seoul, South Korea, 2014.

Appendix A - TCAD Simulations

Example TCAD Command File Partial Conformal *pvp*-DS-MSND with *n*-ring

The contents of the command file built by Silvaco's Devedit program for the partial-conformal *pvp*-DS-MSND with *n*-ring are shown below. The file describes the geometry of the device and is used as input into the Atlas program to calculate the device's electrical properties and transient signals.

```
DevEdit version=2.8.26.R # file written Mon Apr 22 2019 14:08:50 GMT-5 (CDT)
```

```
work.area x1=-1000 y1=-2 x2=20 y2=1502
# devedit 2.8.26.R (Tue Jan 26 05:23:40 PST 2016)
# libMeshBuild 1.24.23 (Tue Jan 26 05:22:55 PST 2016)
# libSSS 2.8.14 (Tue Jan 19 16:38:10 PST 2016)
# libSVC_Misc 1.28.13 (Tue Jan 19 16:37:06 PST 2016)
# libsflm 7.10.1 (Tue May 19 19:52:32 PDT 2015)
# libSDB 1.12.36 (Wed Jan 13 04:01:54 PST 2016)
# libGeometry 1.30.16 (Tue May 19 19:51:51 PDT 2015)
# libCardDeck 1.32.22 (Fri Jan 22 18:42:45 PST 2016)
# libDW_Set 1.28.13 (Tue Jan 19 16:36:26 PST 2016)
# libSvcFile 1.14.19 (Tue May 19 19:51:56 PDT 2015)
# libsstl 1.10.11 (Tue May 19 19:51:57 PDT 2015)
# libDW_Misc 1.40.20 (Tue Jan 19 16:14:10 PST 2016)
# libQSilCore 1.2.8 (Wed May 13 18:39:12 PDT 2015)
# libDW_crypt 3.0.0 (Mon May 18 04:43:00 PDT 2015)
# libDW_Version 3.8.0 (Fri Oct 3 16:08:41 PDT 2014)
region reg=1 mat=Silicon color=0xffcc00 pattern=0x4 \
    polygon="5,0 5,600 20,600 20,1500 10,1500 10,900 -10,900 -10,1500 -20,1500 -20,600 "\
    "-5,600 -5,0"
#
impurity id=1 region.id=1 imp=Phosphorus \
    peak.value=900000000000 ref.value=1000000000000 comb.func=Multiply
#
constr.mesh region=1 default max.height=10 max.width=0.5

region reg=2 name=anode mat=Gold elec.id=1 work.func=0 color=0x595959 pattern=0xb \
    polygon="-5,-1 5,-1 5,0 -5,0"
#
constr.mesh region=2 default

region reg=4 name=anode mat=Gold elec.id=3 work.func=0 color=0x595959 pattern=0xb \
    polygon="20,1500 20,1501 10,1501 10,1500"
#
constr.mesh region=4 default
```

```

region reg=5 mat=Silicon color=0xffcc00 pattern=0x4 \
    polygon="-810,0 -20,0 -20,600 -20,1500 -1000,1500 -1000,0 -820,0 -820,1 -810,1"
#
impurity id=1 region.id=5 imp=Phosphorus \
    peak.value=820000000000 ref.value=1000000000000 comb.func=Multiply
#
constr.mesh region=5 default

region reg=6 name=cathode mat=Gold elec.id=4 work.func=0 color=0x595959 pattern=0xb \
    polygon="-810,1 -820,1 -820,0 -810,0"
#
constr.mesh region=6 default

impurity id=1 imp=Boron color=0x8c5d00 \
    peak.value=6.2e+19 ref.value=3000000000000 comb.func=Multiply \
    y1=0 y2=0 rolloff.y=both conc.func.y="Gaussian (Dist)" conc.param.y=0.75 \
    x1=-5 x2=5 rolloff.x=both conc.func.x="Gaussian (Dist)" conc.param.x=0.75
impurity id=2 imp=Boron color=0x8c5d00 \
    peak.value=6.2e+19 ref.value=3000000000000 comb.func=Multiply \
    y1=0 y2=20 rolloff.y=both conc.func.y="Gaussian (Dist)" conc.param.y=400 \
    x1=-5 x2=-5 rolloff.x=both conc.func.x="Gaussian (Dist)" conc.param.x=0.75
impurity id=3 imp=Boron color=0x8c5d00 \
    peak.value=6.2e+19 ref.value=3000000000000 comb.func=Multiply \
    y1=0 y2=20 rolloff.y=both conc.func.y="Gaussian (Dist)" conc.param.y=400 \
    x1=5 x2=5 rolloff.x=both conc.func.x="Gaussian (Dist)" conc.param.x=0.75
impurity id=8 imp=Boron color=0x8c5d00 \
    peak.value=6.2e+19 ref.value=3000000000000 comb.func=Multiply \
    y1=1480 y2=1500 rolloff.y=both conc.func.y="Gaussian (Dist)" conc.param.y=400 \
    x1=10 x2=10 rolloff.x=both conc.func.x="Gaussian (Dist)" conc.param.x=0.75
impurity id=9 imp=Boron color=0x8c5d00 \
    peak.value=6.2e+19 ref.value=3000000000000 comb.func=Multiply \
    y1=1500 y2=1500 rolloff.y=both conc.func.y="Gaussian (Dist)" conc.param.y=0.75 \
    x1=10 x2=20 rolloff.x=both conc.func.x="Gaussian (Dist)" conc.param.x=0.75
impurity id=10 imp=Boron color=0x8c5d00 \
    peak.value=6.2e+19 ref.value=3000000000000 comb.func=Multiply \
    y1=1480 y2=1500 rolloff.y=both conc.func.y="Gaussian (Dist)" conc.param.y=400 \
    x1=20 x2=20 rolloff.x=both conc.func.x="Gaussian (Dist)" conc.param.x=0.75

# Set Meshing Parameters
#
base.mesh height=15 width=10
#
bound.cond !apply max.slope=30 max.ratio=100 rnd.unit=0.001 line.straightening=1 align.points
when=automatic
#
imp.refine imp=Phosphorus scale=log

```

```
imp.refine imp=Boron scale=log
imp.refine min.spacing=0.02
#
constr.mesh max.angle=90 max.ratio=300 max.height=1000 \
    max.width=1000 min.height=0.0001 min.width=0.0001
#
constr.mesh type=Semiconductor default
#
constr.mesh type=Insulator default
#
constr.mesh type=Metal default
#
constr.mesh type=Other default
#
constr.mesh region=1 default max.height=10 max.width=0.5
#
constr.mesh region=2 default
#
constr.mesh region=4 default
#
constr.mesh region=5 default
#
constr.mesh region=6 default

base.mesh height=15 width=10

bound.cond !apply max.slope=30 max.ratio=100 rnd.unit=0.001 line.straightening=1 align.Points
when=automatic
```


Example TCAD input file to calculate internal potential and electric field

The following code is was built and executed in Silvaco's Deckbuild program. The program reads a .str file defining the diode geometry and solves for the diode's steady state electrical characteristics for the user-defined biasing schemes. The charge carrier lifetimes are also defined in this file.

```
go atlas simflags="-P 3"
mesh infile=pvp_partialconformal_NoN_NoLast.str
contact all neutral

#solving method
models fermi analytic cvt conmob fldmob consrh auger bbt.std print
MATERIAL MATERIAL=Silicon TAUN0=1e-3 TAUP0=1e-3
method newton autonr carriers=2 climit=1e-4

#Initializing Solve
solve initial
solve previous
log outfile=MSND_Vconformal.log

solve vanode=0 vcathode=0
save outfile=no0vBias.str

solve vanode=-0.1 vcathode=0
save outfile=neg_point1V.str

solve vcathode=0 vanode=-0.2 vstep=-0.1 vfinal=-1.0 name=anode
save outfile=neg1Vbias.str

solve vcathode=0 vanode=-1.1 vstep=-0.1 vfinal=-2.7 name=anode
save outfile=neg2point7Vbias.str

solve vcathode=0 vanode=-2.8 vstep=-0.2 vfinal=-5.0 name=anode
save outfile=neg5Vbias.str

solve vcathode=0 vanode=-5.2 vstep=-0.2 vfinal=-10.0 name=anode
save outfile=neg10Vbias.str

solve vcathode=0 vanode=-10.5 vstep=-0.5 vfinal=-20.0 name=anode
save outfile=neg20Vbias.str

solve vcathode=0 vanode=-21.0 vstep=-1.0 vfinal=-30.0 name=anode
save outfile=neg30Vbias.str

solve vcathode=0 vanode=-31.0 vstep=-1.0 vfinal=-40.0 name=anode
```

```
save outfile=neg40Vbias.str
```

```
solve vcathode=0 vanode=-41.0 vstep=-1.0 vfinal=-50.0 name=anode  
save outfile=neg50Vbias.str
```

```
solve vcathode=0 vanode=-55.0 vstep=-5.0 vfinal=-75.0 name=anode  
save outfile=neg75Vbias.str
```

```
solve vcathode=0 vanode=-80.0 vstep=-5.0 vfinal=-100.0 name=anode  
save outfile=neg100Vbias.str
```

```
quit
```

Example TCAD input file to calculate current from single event upset in DS-MSND

The code shown below was used to simulate the signal current from a single event upset in the silicon fin. The program reads in the diode structure file and the previous calculated electrical properties for a given bias. The steady state current is then calculated. Next, the SEU charge-particle track is defined. Finally, the transient analysis is performed at the defined time step with snapshots of the device properties saved at defined intervals.

```
go atlas simflags="-P 3"
mesh infile=pvp_part_conf_nondot.str
load infile=pvp_part_conf_nondot_10V.str MASTER

#solving method
models fermi fldmob bbt.std consrh
MATERIAL MATERIAL=Silicon TAUN0=1e-3 TAUP0=1e-3
method newton autonr carriers=2 climit=1e-3

# -----
method halfimpl dt.min=1.e-12
log outf=pvp_part_conf_nondot.str_1350seu.log
# Solving Initial
solve tfinal=1e-7 tstep=5e-8
save outfile=pvp_part_conf_nondot.str_1350um_Initial.str

# Specify Charge Track
singleeventupset entry ="10,1350" exit="20,1350", radius=5.0 density=2e14

solve tfinal=1.1e-7 tstep=1e-8
save outfile=pvp_part_conf_nondot.str_1350um_JustAfterSEU.str
solve tfinal=2.5e-7 tstep=1.e-7
save outfile=pvp_part_conf_nondot.str_1350um_seu_250ns.str
solve tfinal=5.e-7 tstep=1.e-7
save outfile=pvp_part_conf_nondot.str_1350um_seu_500ns.str
solve tfinal=7.5e-7 tstep=1.e-7
save outfile=pvp_part_conf_nondot.str_1350um_seu_750ns.str
solve tfinal=1.e-6 tstep=1.e-7
save outfile=pvp_part_conf_nondot.str_1350um_seu_1.str
solve tfinal=2.e-6 tstep=1.e-7
save outfile=pvp_part_conf_nondot.str_1350um_seu_2.str
solve tfinal=3.e-6 tstep=1.e-7
save outfile=pvp_part_conf_nondot.str_1350um_seu_3.str
solve tfinal=4.e-6 tstep=1.e-7
save outfile=pvp_part_conf_nondot.str_1350um_seu_4.str
solve tfinal=5.e-6 tstep=1.e-7
save outfile=pvp_part_conf_nondot.str_1350um_seu_5.str
solve tfinal=6.e-6 tstep=1.e-7
```

```
save outfile=pvp_part_conf_nondot.str_1350um_seu_6.str
solve tfinal=7.e-6 tstep=1.e-7
save outfile=pvp_part_conf_nondot.str_1350um_seu_7.str
solve tfinal=8.e-6 tstep=1.e-7
save outfile=pvp_part_conf_nondot.str_1350um_seu_8.str
solve tfinal=9.e-6 tstep=1.e-7
save outfile=pvp_part_conf_nondot.str_1350um_seu_9.str
solve tfinal=1.e-5 tstep=1.e-7
save outfile=pvp_part_conf_nondot.str_1350um_seu_10.str
solve tfinal=1.5e-5 tstep=1.e-7
save outfile=pvp_part_conf_nondot.str_1350um_seu_15.str
solve tfinal=2.e-5 tstep=1.e-7
save outfile=pvp_part_conf_nondot.str_1350um_seu_20.str
solve tfinal=3.e-5 tstep=1.e-7
save outfile=pvp_part_conf_nondot.str_1350um_seu_30.str
solve tfinal=4.e-5 tstep=1.e-6
save outfile=pvp_part_conf_nondot.str_1350um_seu_40.str
solve tfinal=5.e-5 tstep=1.e-6
save outfile=pvp_part_conf_nondot.str_1350um_seu_50.str
solve tfinal=7.e-5 tstep=1.e-5
save outfile=pvp_part_conf_nondot.str_1350um_seu_70.str
solve tfinal=1.e-4 tstep=1.e-5
save outfile=pvp_part_conf_nondot.str_1350um_seu_100.str
solve tfinal=1.5e-4 tstep=1.e-5
save outfile=pvp_part_conf_nondot.str_1350um_seu_150.str
```

Appendix B - DS-MSND Simulations

MCNP Input Card Examples

The following MCNP input card was used to estimate the intrinsic thermal neutron detection efficiency for ^{10}B -backfilled, offset, circular pillar DS-MSNDs with a packing fraction of 50%. The example input was for 4- μm diameter, 80- μm tall pillars with 8- μm unit cell width.

```
B DS-MSND Offset, 0.0253 eV neutron beam, 0.5
C =====
C -----CELL CARD-----
C =====
C DSMSND
  10 2 -2.329 -10          u=1 $ Front Si
  11 1 -1.273  10          u=1 $ Front Hole, Converter
  12 0  -11      lat=1 fill=1 u=2 $ Front Unit Cell
  13 0  -12          fill=2     $ Front Diode
  14 2 -2.329 -13 12 14    $ Middle Of Diode
  15 2 -2.329 -16          u=3 $ Back Si
  16 1 -1.273  16          u=3 $ Backside Hole
  17 0  -15      lat=1 fill=3 u=4 $ Backside Unit Cell
  18 0  -14          fill=4     $ Backside Diode
C World
  100 0 #13 #14 #18 -100   $ AIR IN WORLD
  101 0 100                $ OUTSIDE WORLD

C =====
C -----SURFACE CARDS-----
C =====
C DSMSND
  10 RCC  0 0 0 0.008 0 0 0.00020          $ Front Pillar
  11 RPP  0 0.008 -0.00040 0.00040 -0.00040 0.00040 $ Front Unit Cell
  12 RPP  0 0.008 -0.5 0.5 -0.5 0.5          $ Front Diode
  13 RPP  0.008 0.04200 -0.5 0.5 -0.5 0.5    $ Middle of Diode
  14 RPP  0.04200 0.05 -0.5 0.5 -0.5 0.5    $ Back Diode
  15 RPP  0.04200 0.05 0 0.0008 0 0.0008    $ Backside Unit Cell
  16 RCC  0.04200 0.00040 0.00040 0.008 0 0 0.00020 $ Backside Pillar
C
  100 so 50 $ universe

C =====
C -----DATA CARDS-----
C =====
C
C =====
C PHYSICS/CUT OFF
C =====
MODE N # A
IMP:N 1 9R 0
IMP:# 1 8R 0 0
```

```

IMP:A 1 8R 0 0
PHYS:N 6J 5 $ NCIA, 5=ions are from neutron capture
CUT:N 2J 0
CUT:# J 0.01 0 $ 10keV Energy Cut-off
CUT:A J 0.01 0 $ 10keV Energy Cut-off
C =====
C MATERIALS
C =====
M1 $ 10-Boron RHO = 2.206 (Crystalline 95% Enriched)
    5010.70c 0.95 $ 10-B
    5011.70c 0.05 $ 11-B
C
M2 $ NATURAL SILICON, RHO = 2.3290
    14028.70c -9.2223E-01 $ 28-Si
    14029.70c -4.6850E-02 $ 29-Si
    14030.70c -3.0920E-02 $ 30-Si
C
C =====
C SOURCE - COLL. 0.5mm DISK 0.0253eV ALONG THE X-AXIS.
C =====
SDEF POS= 1.0 0 0.0 PAR= N ERG= 0.0253E-6
    VEC= -1.0 0 -0.0 DIR= 1
    RAD= D1 AXS= -1.0 0 -0.0 EXT= 0
constant. in most problems it is a variable.
SI1 0 0.25 $ 0.25 cm radius (0.5mm diameter )
SP1 -21 1 $ Radial Sampling
C =====
C TALLY
C =====
C --- SPECTRUM -----
F8:A,# (10 14 15)
E8 0 100i 5
C --- EFFICIENCY -----
F18:A,# (10 14 15)
E18 0 0.3 5
C =====
C Problem Stuff
C =====
nps 2E6

```

The following MCNP input card was used to estimate the intrinsic thermal neutron detection efficiency for ${}^6\text{LiF}$ -backfilled, offset, straight trench DS-MSNDs with a packing fraction of 50%. The example input was for 24- μm wide, 500- μm deep trenches with 40- μm unit cell width.

LiF DS-MSND Offset, 0.0253 eV neutron beam, 0.5 or 0.67 packing fraction

C =====

C -----CELL CARD-----

C =====

C DSMSND

```

10 2 -2.329 -10          u=1 $ Front Sidewall
11 1 -1.273 10          u=1 $ Front Trench, LiF
12 0   -11   lat=1 fill=1 u=2 $ Front Unit Cell
13 0   -12           fill=2   $ Front Diode
14 2 -2.329 -13 12 14          $ Middle of Diode
15 2 -2.329 -16          u=3 $ Backside Sidewall
16 1 -1.273 16          u=3 $ Backside Trench, LiF
17 0   -15   lat=1 fill=3 u=4 $ Backside Unit Cell
18 0   -14           fill=4   $ Backside Diode

```

C World

```

100 0 #13 #14 #18 -100    $ VOID IN WORLD
101 0 100                 $ OUTSIDE WORLD

```

C =====

C -----SURFACE CARDS-----

C =====

C DSMSND

```

10 RPP 0.0000 0.05 -0.5 0.5 -0.00080 0.00080 $ Front Sidewall
11 RPP 0.0000 0.05 -0.5 0.5 -0.00200 0.00200 $ Front Unit Cell
12 RPP 0.0000 0.05 -0.5 0.5 -0.5 0.5          $ Front Diode
13 RPP 0.05 0.10000 -0.5 0.5 -0.5 0.5          $ Middle of Diode
14 RPP 0.10000 0.15 -0.5 0.5 -0.5 0.5          $ Backside Diode
15 RPP 0.10000 0.15 -0.5 0.5 0 0.004          $ Backside Unit Cell
16 RPP 0.10000 0.15 -0.5 0.5 0.00120 0.00280 $ Backside Sidewall

```

C

100 so 50 \$ universe

C =====

C -----DATA CARDS-----

C =====

C

C =====

C PHYSICS/CUT OFF

C =====

MODE N T A

IMP:N 1 9R 0

IMP:T 1 8R 0 0

IMP:A 1 8R 0 0

PHYS:N 6J 5 \$ NCIA, 5=ions are from neutron capture

CUT:N 2J 0

```

CUT:T J 0.01 0 $ 10keV Energy Cut-off
CUT:A J 0.01 0 $ 10keV Energy Cut-off
C =====
C MATERIALS
C =====
M1 $ 6-Lithium Fluoride RHO = 2.55 (Crystalline 95% Enriched)
    3006.70c -0.227995 $ 6-Li
    3007.70c -0.013996 $ 7-Li
    9019.70c -0.758009 $ 19-F
C
M2 $ NATURAL SILICON, RHO = 2.3290
    14028.70c -9.2223E-01 $ 28-Si
    14029.70c -4.6850E-02 $ 29-Si
    14030.70c -3.0920E-02 $ 30-Si
C
C =====
C SOURCE - COLL. 0.5cm DISK 0.0253eV ALONG THE X-AXIS.
C =====
SDEF POS= 1.0 0 0.0 PAR= N ERG= 0.0253E-6
    VEC= -1.0 0 -0.0 DIR= 1
    RAD= D1 AXS= -1.0 0 -0.0 EXT= 0
constant. in most problems it is a variable.
SI1 0 0.25 $ 0.25 cm radius (0.5 cm diameter )
SP1 -21 1 $ Radial Sampling
C =====
C TALLY
C =====
C --- SPECTRUM -----
F8:A,T (10 14 15)
E8 0 100i 5
C --- EFFICIENCY -----
F18:A,T (10 14 15)
E18 0 0.3 5
C =====
C Problem Stuff
C =====
nps 2E6

```


MCNP Simulation Results

The following tables show the results from MCNP6 simulations to determine the intrinsic thermal-neutron detection efficiencies for offset and opaque DS-MSNDs backfilled with ${}^6\text{LiF}$ of ${}^{10}\text{B}$. DS-MSNDs with circular holes, circular pillars, and straight trenches were considered in the study.

Table B-1. Theoretical intrinsic thermal-neutron detection efficiency MCNP simulation results for offset, straight-trench DS-MSNDs with conversion material density set at half of the enriched crystalline density of the material to simulate a 50% packing fraction for the powder backfill.

Offset Dual-Sided MSND, Straight Trench, ⁶ LiF						Offset Dual-Sided MSND, Straight Trench, ¹⁰ B					
<i>T/W_{Cell}</i>	<i>Unit Cell Width, W_{Cell} (μm)</i>					<i>T/W_{Cell}</i>	<i>Unit Cell Width, W_{Cell} (μm)</i>				
	20	40	60	80	100		4	6	8	10	12
<i>Trench depth H = 175 μm</i>						<i>Trench depth H = 20 μm</i>					
0.10	7.7%	7.5%	7.4%	7.3%	7.2%	0.10	7.4%	7.3%	7.2%	7.1%	7.1%
0.20	15.0%	14.5%	14.0%	13.6%	13.1%	0.20	14.5%	14.1%	13.8%	13.4%	13.1%
0.30	22.1%	21.0%	20.0%	19.0%	18.0%	0.30	21.2%	20.4%	19.6%	18.8%	18.2%
0.40	29.0%	27.1%	25.3%	23.6%	22.0%	0.40	27.5%	26.2%	24.8%	23.4%	22.2%
0.50	35.5%	32.6%	30.0%	27.5%	24.9%	0.50	33.5%	31.4%	29.3%	27.3%	25.4%
0.60	39.1%	35.3%	31.7%	28.2%	24.8%	0.60	36.5%	33.6%	30.7%	27.9%	25.3%
0.70	42.7%	37.8%	33.3%	28.9%	24.4%	0.70	39.4%	35.7%	32.1%	28.6%	25.2%
0.80	46.0%	40.2%	34.6%	29.0%	24.1%	0.80	41.9%	37.7%	33.2%	28.9%	24.6%
0.90	44.5%	35.2%	34.9%	28.8%	24.0%	0.90	27.3%	23.7%	23.0%	23.2%	23.8%
<i>Trench depth H = 350 μm</i>						<i>Trench depth H = 40 μm</i>					
0.10	12.4%	12.2%	12.0%	11.8%	11.6%	0.10	12.0%	11.9%	11.7%	11.6%	11.4%
0.20	24.3%	23.6%	22.8%	22.0%	21.3%	0.20	23.5%	22.9%	22.3%	21.8%	21.2%
0.30	35.8%	34.0%	32.4%	30.7%	29.1%	0.30	34.3%	33.1%	31.8%	30.4%	29.3%
0.40	46.8%	43.8%	40.8%	38.0%	35.3%	0.40	44.6%	42.3%	40.0%	37.8%	35.6%
0.50	57.4%	52.8%	48.3%	43.9%	39.7%	0.50	54.3%	50.7%	47.2%	43.8%	40.4%
0.60	60.5%	54.3%	48.4%	42.6%	36.8%	0.60	56.3%	51.5%	46.8%	42.1%	37.5%
0.70	63.7%	56.1%	48.8%	41.7%	34.5%	0.70	58.6%	52.7%	46.8%	41.1%	35.4%
0.80	66.5%	57.6%	48.9%	40.3%	32.6%	0.80	60.6%	53.7%	46.8%	39.8%	33.0%
0.90	62.4%	48.4%	47.9%	38.5%	31.2%	0.90	36.3%	30.6%	29.6%	29.9%	30.6%
<i>Trench depth H = 500 μm</i>						<i>Trench depth H = 60 μm</i>					
0.10	15.0%	14.8%	14.6%	14.3%	14.1%	0.10	14.9%	14.7%	14.5%	14.3%	14.1%
0.20	29.4%	28.5%	27.5%	26.6%	25.8%	0.20	29.0%	28.3%	27.6%	26.9%	26.2%
0.30	43.2%	41.1%	39.1%	37.1%	35.2%	0.30	42.4%	40.8%	39.2%	37.6%	36.1%
0.40	56.5%	52.9%	49.3%	45.8%	42.5%	0.40	55.1%	52.3%	49.4%	46.6%	43.9%
0.50	69.3%	63.7%	58.3%	52.9%	47.6%	0.50	67.1%	62.6%	58.2%	53.9%	49.6%
0.60	71.2%	63.8%	56.6%	49.6%	42.6%	0.60	67.5%	61.6%	55.7%	49.8%	44.1%
0.70	73.3%	64.4%	55.9%	47.4%	38.9%	0.70	68.5%	61.3%	54.2%	47.2%	40.2%
0.80	75.1%	64.9%	54.8%	44.8%	35.8%	0.80	69.3%	61.1%	52.9%	44.6%	36.6%
0.90	69.1%	53.2%	52.6%	42.0%	33.6%	0.90	39.8%	32.9%	31.8%	32.2%	33.0%
<i>Trench depth H = 650 μm</i>						<i>Trench depth H = 80 μm</i>					
0.10	16.8%	16.5%	16.3%	16.0%	15.7%	0.10	16.7%	16.5%	16.2%	16.0%	15.8%
0.20	32.8%	31.8%	30.7%	29.7%	28.7%	0.20	32.4%	31.6%	30.9%	30.1%	29.3%
0.30	48.1%	45.8%	43.6%	41.3%	39.1%	0.30	47.4%	45.6%	43.9%	42.0%	40.4%
0.40	62.9%	58.9%	54.9%	51.0%	47.2%	0.40	61.6%	58.4%	55.2%	52.1%	49.0%
0.50	77.1%	70.9%	64.8%	58.8%	52.9%	0.50	75.0%	70.0%	65.0%	60.2%	55.3%
0.60	77.9%	69.7%	61.8%	54.0%	46.2%	0.60	74.1%	67.4%	60.9%	54.3%	47.9%
0.70	79.0%	69.3%	60.0%	50.7%	41.4%	0.70	73.8%	66.0%	58.2%	50.4%	42.8%
0.80	79.9%	68.8%	58.0%	47.2%	37.5%	0.80	73.6%	64.7%	55.8%	46.8%	38.2%
0.90	72.4%	55.5%	54.9%	43.5%	34.7%	0.90	41.1%	33.7%	32.6%	33.0%	33.8%

Table B-2. Theoretical intrinsic thermal-neutron detection efficiency MCNP simulation results for offset, circular hole DS-MSNDs with conversion material density set at half of the enriched crystalline density of the material to simulate a 50% packing fraction for the powder backfill.

Offset Dual-Sided MSND, Circular Hole, ⁶ LiF						Offset Dual-Sided MSND, Circular Hole, ¹⁰ B					
D/W_{Cell}	Unit Cell Width, W_{Cell} (μm)					D/W_{Cell}	Unit Cell Width, W_{Cell} (μm)				
	20	40	60	80	100		4	6	8	10	12
Trench depth $H = 175 \mu\text{m}$						Trench depth $H = 20 \mu\text{m}$					
0.10	0.6%	0.6%	0.6%	0.6%	0.6%	0.10	0.6%	0.6%	0.6%	0.6%	0.6%
0.20	2.4%	2.4%	2.4%	2.4%	2.4%	0.20	2.4%	2.4%	2.4%	2.4%	2.4%
0.30	5.5%	5.4%	5.4%	5.3%	5.3%	0.30	5.4%	5.4%	5.3%	5.3%	5.2%
0.40	9.7%	9.6%	9.5%	9.3%	9.2%	0.40	9.5%	9.5%	9.4%	9.2%	9.1%
0.50	15.1%	14.8%	14.6%	14.3%	13.9%	0.50	14.8%	14.7%	14.4%	14.1%	13.8%
0.60	21.7%	21.2%	20.7%	20.1%	19.1%	0.60	21.2%	20.9%	20.4%	19.9%	19.2%
0.70	29.3%	28.6%	27.7%	26.5%	24.6%	0.70	28.7%	28.1%	27.3%	26.3%	25.0%
0.80	36.7%	35.6%	34.2%	32.0%	28.3%	0.80	35.9%	34.9%	33.5%	31.9%	29.1%
0.90	43.5%	41.1%	39.9%	36.2%	31.0%	0.90	41.1%	38.1%	36.0%	35.0%	31.4%
Trench depth $H = 350 \mu\text{m}$						Trench depth $H = 40 \mu\text{m}$					
0.10	1.0%	1.0%	1.0%	1.0%	1.0%	0.10	1.0%	1.0%	1.0%	1.0%	1.0%
0.20	4.0%	4.0%	4.0%	3.9%	3.9%	0.20	3.9%	3.9%	3.9%	3.9%	3.9%
0.30	8.9%	8.9%	8.8%	8.7%	8.6%	0.30	8.7%	8.7%	8.6%	8.6%	8.5%
0.40	15.8%	15.6%	15.4%	15.2%	15.0%	0.40	15.5%	15.4%	15.2%	15.0%	14.9%
0.50	24.6%	24.2%	23.8%	23.3%	22.6%	0.50	24.1%	23.8%	23.5%	23.0%	22.5%
0.60	35.1%	34.5%	33.7%	32.7%	31.1%	0.60	34.5%	34.0%	33.3%	32.4%	31.3%
0.70	47.5%	46.5%	45.0%	43.1%	39.7%	0.70	46.7%	45.7%	44.4%	42.8%	40.6%
0.80	58.2%	56.7%	54.2%	50.6%	44.1%	0.80	57.1%	55.5%	53.3%	50.5%	45.7%
0.90	66.4%	62.7%	60.7%	54.5%	46.0%	0.90	62.9%	57.9%	54.5%	52.6%	46.6%
Trench depth $H = 500 \mu\text{m}$						Trench depth $H = 60 \mu\text{m}$					
0.10	1.2%	1.2%	1.2%	1.2%	1.2%	0.10	1.2%	1.2%	1.2%	1.2%	1.2%
0.20	4.8%	4.8%	4.8%	4.8%	4.8%	0.20	4.8%	4.8%	4.8%	4.8%	4.8%
0.30	10.8%	10.8%	10.7%	10.6%	10.5%	0.30	10.8%	10.8%	10.7%	10.7%	10.6%
0.40	19.1%	18.9%	18.7%	18.5%	18.1%	0.40	19.2%	19.1%	18.9%	18.6%	18.4%
0.50	29.7%	29.3%	28.8%	28.2%	27.4%	0.50	29.8%	29.5%	29.1%	28.6%	28.0%
0.60	42.5%	41.7%	40.8%	39.5%	37.6%	0.60	42.7%	42.1%	41.2%	40.1%	38.7%
0.70	57.4%	56.2%	54.5%	52.1%	48.0%	0.70	57.8%	56.6%	55.1%	53.0%	50.2%
0.80	69.4%	67.6%	64.6%	60.2%	52.3%	0.80	69.6%	67.7%	65.1%	61.4%	55.3%
0.90	77.4%	73.1%	70.7%	63.3%	53.1%	0.90	74.7%	68.5%	64.4%	62.0%	54.6%
Trench depth $H = 650 \mu\text{m}$						Trench depth $H = 80 \mu\text{m}$					
0.10	1.4%	1.4%	1.4%	1.4%	1.3%	0.10	1.4%	1.4%	1.4%	1.4%	1.4%
0.20	5.4%	5.4%	5.4%	5.3%	5.3%	0.20	5.4%	5.4%	5.4%	5.4%	5.4%
0.30	12.1%	12.0%	11.9%	11.8%	11.7%	0.30	12.1%	12.1%	12.0%	11.9%	11.9%
0.40	21.3%	21.1%	20.9%	20.6%	20.3%	0.40	21.4%	21.3%	21.1%	20.9%	20.6%
0.50	33.1%	32.6%	32.1%	31.5%	30.5%	0.50	33.3%	33.0%	32.6%	32.0%	31.3%
0.60	47.3%	46.5%	45.5%	44.1%	41.9%	0.60	47.8%	47.1%	46.2%	44.9%	43.4%
0.70	63.9%	62.7%	60.7%	58.0%	53.4%	0.70	64.7%	63.4%	61.6%	59.3%	56.1%
0.80	76.6%	74.6%	71.4%	66.4%	57.6%	0.80	77.1%	75.1%	72.1%	68.0%	61.2%
0.90	84.2%	79.4%	76.8%	68.6%	57.3%	0.90	81.4%	74.5%	69.9%	67.2%	59.0%

Table B-3. Theoretical intrinsic thermal-neutron detection efficiency MCNP simulation results for offset, circular pillar DS-MSNDs with conversion material density set at half of the enriched crystalline density of the material to simulate a 50% packing fraction for the powder backfill.

Offset Dual-Sided MSND, Circular Pillar, ${}^6\text{LiF}$						Offset Dual-Sided MSND, Circular Pillar, ${}^{10}\text{B}$					
D/W_{Cell}	Unit Cell Width, W_{Cell} (μm)					D/W_{Cell}	Unit Cell Width, W_{Cell} (μm)				
	20	40	60	80	100		4	6	8	10	12
Trench depth $H = 175 \mu\text{m}$						Trench depth $H = 20 \mu\text{m}$					
0.10	8.0%	8.3%	8.9%	8.8%	8.3%	0.10	5.9%	5.9%	6.3%	6.6%	7.1%
0.20	16.5%	17.3%	14.5%	12.6%	11.3%	0.20	9.2%	9.2%	12.1%	11.4%	10.6%
0.30	30.7%	23.9%	19.1%	16.2%	14.1%	0.30	19.2%	19.2%	16.8%	15.0%	13.5%
0.40	39.8%	29.0%	23.3%	19.5%	16.9%	0.40	29.3%	29.3%	21.0%	18.4%	16.3%
0.50	42.7%	32.9%	26.7%	22.6%	19.6%	0.50	35.5%	35.5%	24.8%	21.5%	19.1%
0.60	42.4%	35.3%	29.3%	25.2%	21.9%	0.60	38.9%	38.9%	28.0%	24.3%	21.6%
0.70	40.3%	35.7%	30.7%	27.2%	24.0%	0.70	39.7%	39.7%	30.7%	27.2%	24.2%
0.80	35.1%	32.5%	29.4%	27.1%	24.5%	0.80	36.2%	36.2%	30.4%	27.9%	25.3%
0.90	27.1%	26.0%	24.5%	23.3%	21.9%	0.90	28.8%	28.8%	26.1%	24.8%	23.2%
Trench depth $H = 350 \mu\text{m}$						Trench depth $H = 40 \mu\text{m}$					
0.10	6.8%	7.3%	8.3%	8.1%	7.4%	0.10	3.5%	3.8%	4.2%	4.6%	5.3%
0.20	19.8%	20.8%	16.7%	13.9%	11.8%	0.20	8.4%	11.7%	12.5%	11.4%	10.4%
0.30	41.3%	30.8%	23.8%	19.5%	16.2%	0.30	23.0%	22.8%	19.5%	16.8%	14.6%
0.40	55.6%	39.2%	30.6%	24.9%	20.8%	0.40	38.0%	31.1%	26.0%	22.1%	19.0%
0.50	61.3%	46.2%	36.7%	30.3%	25.6%	0.50	48.3%	38.4%	32.4%	27.3%	23.7%
0.60	62.8%	51.5%	42.0%	35.6%	30.3%	0.60	55.3%	44.9%	38.6%	32.7%	28.5%
0.70	62.0%	54.7%	46.5%	40.9%	35.4%	0.70	59.1%	50.5%	44.9%	39.3%	34.3%
0.80	55.5%	51.4%	46.4%	42.4%	38.1%	0.80	55.7%	50.5%	46.6%	42.5%	38.1%
0.90	43.5%	41.8%	39.5%	37.4%	35.1%	0.90	45.1%	42.8%	40.8%	38.7%	36.1%
Trench depth $H = 500 \mu\text{m}$						Trench depth $H = 60 \mu\text{m}$					
0.10	6.0%	6.6%	7.7%	7.4%	6.6%	0.10	2.1%	2.4%	2.9%	3.4%	4.1%
0.20	20.6%	21.7%	17.0%	13.9%	11.6%	0.20	7.6%	11.3%	12.2%	10.9%	9.8%
0.30	45.0%	33.1%	25.2%	20.3%	16.6%	0.30	24.0%	23.8%	20.1%	17.0%	14.5%
0.40	61.7%	43.0%	33.1%	26.8%	22.0%	0.40	41.1%	33.4%	27.6%	23.1%	19.6%
0.50	69.0%	51.5%	40.6%	33.4%	27.8%	0.50	53.6%	42.2%	35.4%	29.4%	25.1%
0.60	72.0%	58.7%	47.5%	40.1%	33.9%	0.60	62.8%	50.7%	43.4%	36.3%	31.3%
0.70	72.7%	64.0%	54.3%	47.6%	41.0%	0.70	69.2%	58.9%	52.3%	45.5%	39.4%
0.80	66.2%	61.3%	55.2%	50.5%	45.1%	0.80	66.4%	60.1%	55.4%	50.5%	45.1%
0.90	52.4%	50.3%	47.5%	45.0%	42.2%	0.90	54.3%	51.6%	49.1%	46.5%	43.4%
Trench depth $H = 650 \mu\text{m}$						Trench depth $H = 80 \mu\text{m}$					
0.10	5.4%	6.1%	7.2%	6.8%	6.0%	0.10	1.3%	1.7%	2.2%	2.7%	3.4%
0.20	20.8%	21.9%	17.0%	13.7%	11.3%	0.20	7.0%	10.9%	11.8%	10.5%	9.3%
0.30	46.6%	34.0%	25.7%	20.5%	16.6%	0.30	24.1%	23.9%	20.1%	16.8%	14.2%
0.40	64.7%	44.8%	34.3%	27.5%	22.5%	0.40	42.3%	34.2%	28.1%	23.3%	19.6%
0.50	73.3%	54.3%	42.6%	34.9%	28.8%	0.50	55.9%	43.8%	36.6%	30.2%	25.6%
0.60	77.4%	62.9%	50.7%	42.7%	35.9%	0.60	66.6%	53.5%	45.7%	38.0%	32.5%
0.70	79.4%	69.8%	59.0%	51.7%	44.4%	0.70	74.7%	63.4%	56.3%	48.8%	42.1%
0.80	73.1%	67.7%	60.9%	55.7%	49.7%	0.80	72.5%	65.5%	60.5%	55.0%	49.0%
0.90	58.2%	55.9%	52.8%	50.0%	46.8%	0.90	59.6%	56.6%	53.9%	51.0%	47.5%

Table B-4. Theoretical intrinsic thermal-neutron detection efficiency MCNP simulation results for opaque, straight trench DS-MSNDs with conversion material density set at half of the enriched crystalline density of the material to simulate a 50% packing fraction for the powder backfill.

Opaque Dual-Sided MSND, Straight Trench, ⁶ LiF						Opaque Dual-Sided MSND, Straight Trench, ¹⁰ B					
T/W _{Cell}	Unit Cell Width, W _{Cell} (μm)					T/W _{Cell}	Unit Cell Width, W _{Cell} (μm)				
	20	40	60	80	100		4	6	8	10	12
Trench depth H = 175 μm						Trench depth H = 20 μm					
0.10	30.5%	24.9%	24.5%	20.7%	17.8%	0.10	19.7%	17.7%	17.2%	17.3%	17.6%
0.20	34.3%	30.6%	27.1%	23.6%	20.5%	0.20	31.6%	28.9%	26.1%	23.4%	20.8%
0.30	35.0%	31.7%	28.6%	25.6%	22.7%	0.30	32.7%	30.2%	27.8%	25.5%	23.2%
0.40	35.4%	32.4%	29.6%	26.9%	24.3%	0.40	33.3%	31.1%	28.8%	26.8%	24.7%
0.50	35.5%	32.6%	30.0%	27.5%	24.9%	0.50	33.5%	31.4%	29.3%	27.3%	25.4%
0.60	35.4%	32.5%	29.8%	27.2%	24.6%	0.60	33.5%	31.3%	29.1%	27.0%	25.0%
0.70	35.1%	32.0%	29.0%	26.1%	23.2%	0.70	33.0%	30.7%	28.3%	26.0%	23.8%
0.80	34.5%	31.0%	27.6%	24.2%	21.2%	0.80	32.1%	29.6%	26.9%	24.2%	21.6%
0.90	31.0%	25.5%	25.2%	21.6%	18.7%	0.90	21.0%	18.9%	18.4%	18.4%	18.7%
Trench depth H = 350 μm						Trench depth H = 40 μm					
0.10	49.1%	39.5%	38.7%	32.2%	27.1%	0.10	30.6%	27.1%	26.2%	26.4%	26.9%
0.20	55.4%	49.2%	43.1%	37.1%	31.9%	0.20	51.1%	46.4%	41.6%	36.9%	32.3%
0.30	56.5%	51.1%	45.9%	40.8%	35.7%	0.30	52.8%	48.6%	44.6%	40.6%	36.6%
0.40	57.1%	52.2%	47.6%	43.0%	38.5%	0.40	53.8%	50.1%	46.5%	42.8%	39.3%
0.50	57.4%	52.8%	48.3%	43.9%	39.7%	0.50	54.3%	50.7%	47.2%	43.8%	40.4%
0.60	57.3%	52.6%	48.0%	43.5%	39.1%	0.60	54.2%	50.5%	46.9%	43.3%	39.9%
0.70	56.8%	51.7%	46.7%	41.6%	36.7%	0.70	53.4%	49.5%	45.5%	41.5%	37.7%
0.80	55.9%	50.1%	44.2%	38.4%	33.3%	0.80	52.1%	47.6%	43.0%	38.4%	33.9%
0.90	50.2%	40.8%	40.2%	33.8%	28.9%	0.90	32.9%	29.2%	28.3%	28.4%	28.9%
Trench depth H = 500 μm						Trench depth H = 60 μm					
0.10	59.2%	47.4%	46.4%	38.4%	32.2%	0.10	37.3%	32.8%	31.8%	32.0%	32.6%
0.20	66.8%	59.2%	51.8%	44.4%	38.0%	0.20	63.1%	57.2%	51.2%	45.2%	39.4%
0.30	68.2%	61.6%	55.2%	48.9%	42.8%	0.30	65.2%	60.0%	54.9%	49.8%	44.8%
0.40	68.9%	63.0%	57.4%	51.7%	46.2%	0.40	66.5%	61.8%	57.2%	52.7%	48.2%
0.50	69.3%	63.7%	58.3%	52.9%	47.6%	0.50	67.1%	62.6%	58.2%	53.9%	49.6%
0.60	69.2%	63.5%	57.9%	52.4%	46.9%	0.60	66.9%	62.4%	57.8%	53.3%	49.0%
0.70	68.6%	62.4%	56.3%	50.1%	44.0%	0.70	66.0%	61.1%	56.1%	51.1%	46.2%
0.80	67.5%	60.4%	53.3%	46.2%	39.8%	0.80	64.4%	58.7%	53.0%	47.1%	41.5%
0.90	60.7%	49.2%	48.3%	40.5%	34.5%	0.90	40.3%	35.6%	34.5%	34.6%	35.1%
Trench depth H = 650 μm						Trench depth H = 80 μm					
0.10	65.9%	52.6%	51.5%	42.5%	35.6%	0.10	41.5%	36.4%	35.3%	35.5%	36.1%
0.20	74.3%	65.9%	57.5%	49.3%	42.1%	0.20	70.5%	63.8%	57.1%	50.3%	43.9%
0.30	75.9%	68.5%	61.4%	54.4%	47.4%	0.30	72.9%	67.0%	61.3%	55.5%	49.9%
0.40	76.7%	70.1%	63.8%	57.5%	51.3%	0.40	74.3%	69.1%	63.9%	58.8%	53.8%
0.50	77.1%	70.9%	64.8%	58.8%	52.9%	0.50	75.0%	70.0%	65.0%	60.2%	55.3%
0.60	77.0%	70.7%	64.4%	58.2%	52.0%	0.60	74.8%	69.7%	64.6%	59.6%	54.6%
0.70	76.4%	69.4%	62.6%	55.7%	48.8%	0.70	73.8%	68.3%	62.7%	57.0%	51.5%
0.80	75.3%	67.3%	59.2%	51.3%	44.1%	0.80	72.0%	65.6%	59.1%	52.5%	46.1%
0.90	67.7%	54.7%	53.7%	45.0%	38.2%	0.90	44.8%	39.6%	38.3%	38.4%	39.0%

Table B-5. Theoretical intrinsic thermal-neutron detection efficiency MCNP simulation results for opaque, circular hole DS-MSNDs with conversion material density set at half of the enriched crystalline density of the material to simulate a 50% packing fraction for the powder backfill.

Opaque Dual-Sided MSND, Front-Side Circular Hole, ⁶ LiF						Opaque Dual-Sided MSND, Front-Side Circular Hole, ¹⁰ B					
D/W_{Cell}	Unit Cell Width, W_{Cell} (μm)					D/W_{Cell}	Unit Cell Width, W_{Cell} (μm)				
	20	40	60	80	100		4	6	8	10	12
Trench depth $H = 175 \mu\text{m}$						Trench depth $H = 20 \mu\text{m}$					
0.10	6.1%	6.2%	6.7%	6.6%	6.3%	0.10	5.2%	5.3%	5.4%	5.6%	5.9%
0.20	12.1%	12.5%	10.9%	9.7%	8.9%	0.20	8.3%	9.6%	9.9%	9.5%	9.0%
0.30	22.0%	17.9%	15.0%	13.2%	11.9%	0.30	15.9%	15.5%	14.1%	13.0%	12.1%
0.40	29.1%	22.8%	19.2%	17.0%	15.4%	0.40	23.4%	20.4%	18.4%	16.7%	15.5%
0.50	32.8%	27.2%	23.4%	20.9%	18.9%	0.50	28.5%	24.9%	22.6%	20.6%	19.1%
0.60	35.0%	31.0%	27.3%	24.7%	22.5%	0.60	32.1%	28.8%	26.5%	24.5%	22.7%
0.70	36.5%	33.7%	30.6%	28.1%	25.5%	0.70	34.5%	32.1%	29.8%	27.9%	25.9%
0.80	37.2%	35.4%	33.0%	30.7%	27.5%	0.80	35.9%	34.2%	32.3%	30.5%	28.1%
0.90	37.5%	35.7%	34.2%	31.6%	28.1%	0.90	35.7%	33.5%	31.9%	30.9%	28.6%
Trench depth $H = 350 \mu\text{m}$						Trench depth $H = 40 \mu\text{m}$					
0.10	7.2%	7.6%	8.3%	8.1%	7.6%	0.10	5.4%	5.6%	6.0%	6.3%	6.8%
0.20	17.7%	18.4%	15.5%	13.6%	12.1%	0.20	10.8%	13.1%	13.6%	12.9%	12.1%
0.30	34.6%	27.4%	22.6%	19.6%	17.4%	0.30	24.0%	23.3%	21.0%	19.0%	17.5%
0.40	46.7%	35.8%	29.9%	26.0%	23.2%	0.40	36.8%	31.8%	28.3%	25.5%	23.5%
0.50	52.9%	43.4%	37.0%	32.7%	29.4%	0.50	45.7%	39.5%	35.5%	32.2%	29.7%
0.60	56.6%	49.9%	43.8%	39.3%	35.5%	0.60	51.9%	46.3%	42.3%	38.9%	35.8%
0.70	59.0%	54.6%	49.4%	45.2%	40.6%	0.70	56.0%	51.9%	48.1%	44.8%	41.3%
0.80	60.3%	57.4%	53.5%	49.5%	43.9%	0.80	58.3%	55.6%	52.4%	49.3%	45.1%
0.90	60.8%	57.9%	55.6%	51.0%	45.0%	0.90	58.1%	54.5%	51.7%	50.0%	45.7%
Trench depth $H = 500 \mu\text{m}$						Trench depth $H = 60 \mu\text{m}$					
0.10	7.8%	8.3%	9.2%	9.0%	8.4%	0.10	5.6%	5.8%	6.3%	6.6%	7.3%
0.20	20.8%	21.5%	18.1%	15.6%	13.9%	0.20	12.4%	15.3%	16.0%	15.0%	14.0%
0.30	41.5%	32.7%	26.7%	23.0%	20.3%	0.30	29.0%	28.1%	25.2%	22.8%	20.8%
0.40	56.2%	42.9%	35.6%	30.9%	27.5%	0.40	45.1%	38.8%	34.4%	30.9%	28.3%
0.50	63.9%	52.2%	44.4%	39.2%	35.1%	0.50	56.3%	48.5%	43.5%	39.4%	36.2%
0.60	68.3%	60.2%	52.7%	47.2%	42.5%	0.60	64.1%	57.1%	52.0%	47.8%	43.9%
0.70	71.3%	65.9%	59.6%	54.4%	48.8%	0.70	69.3%	64.1%	59.4%	55.2%	50.8%
0.80	72.8%	69.4%	64.7%	59.6%	52.8%	0.80	72.1%	68.7%	64.7%	60.8%	55.5%
0.90	73.4%	70.0%	67.1%	61.4%	54.1%	0.90	71.8%	67.4%	63.9%	61.6%	56.4%
Trench depth $H = 650 \mu\text{m}$						Trench depth $H = 80 \mu\text{m}$					
0.10	8.3%	8.8%	9.8%	9.5%	8.8%	0.10	5.7%	6.0%	6.5%	6.9%	7.6%
0.20	22.8%	23.6%	19.7%	17.0%	15.1%	0.20	13.4%	16.7%	17.4%	16.3%	15.2%
0.30	46.1%	36.2%	29.4%	25.3%	22.2%	0.30	32.1%	31.1%	27.9%	25.1%	22.9%
0.40	62.6%	47.6%	39.5%	34.1%	30.4%	0.40	50.3%	43.1%	38.2%	34.3%	31.3%
0.50	71.1%	58.0%	49.3%	43.4%	38.9%	0.50	62.9%	54.1%	48.4%	43.8%	40.2%
0.60	76.1%	66.9%	58.6%	52.4%	47.2%	0.60	71.6%	63.7%	58.0%	53.3%	48.9%
0.70	79.4%	73.4%	66.4%	60.5%	54.2%	0.70	77.5%	71.7%	66.3%	61.6%	56.7%
0.80	81.1%	77.2%	71.9%	66.4%	58.7%	0.80	80.6%	76.8%	72.3%	67.9%	62.0%
0.90	81.8%	78.0%	74.7%	68.3%	60.1%	0.90	80.4%	75.4%	71.5%	68.9%	63.0%

Table B-6. Theoretical intrinsic thermal-neutron detection efficiency MCNP simulation results for opaque, circular pillar DS-MSNDs with conversion material density set at half of the enriched crystalline density of the material to simulate a 50% packing fraction for the powder backfill.

Opaque Dual-Sided MSND, Front-Side Circular Pillar, ^6LiF						Opaque Dual-Sided MSND, Front-Side Circular Pillar, ^{10}B					
D/W_{Cell}	Unit Cell Width, W_{Cell} (μm)					D/W_{Cell}	Unit Cell Width, W_{Cell} (μm)				
	20	40	60	80	100		4	6	8	10	12
<i>Trench depth $H = 175 \mu\text{m}$</i>						<i>Trench depth $H = 20 \mu\text{m}$</i>					
0.10	4.7%	4.9%	5.3%	5.2%	4.9%	0.10	3.6%	3.8%	4.0%	4.1%	4.4%
0.20	10.9%	11.4%	9.7%	8.5%	7.7%	0.20	6.8%	8.2%	8.5%	8.1%	7.6%
0.30	21.1%	16.8%	14.0%	12.1%	10.8%	0.30	14.6%	14.3%	12.9%	11.8%	10.9%
0.40	28.5%	21.9%	18.4%	16.0%	14.4%	0.40	22.4%	19.4%	17.3%	15.7%	14.5%
0.50	32.4%	26.5%	22.8%	20.1%	18.2%	0.50	27.8%	24.1%	21.7%	19.8%	18.3%
0.60	34.7%	30.6%	26.9%	24.2%	21.9%	0.60	31.6%	28.3%	25.9%	23.9%	22.1%
0.70	36.3%	33.5%	30.5%	27.9%	25.2%	0.70	34.2%	31.7%	29.5%	27.7%	25.6%
0.80	37.2%	35.3%	33.0%	30.7%	27.5%	0.80	35.7%	34.1%	32.3%	30.5%	28.1%
0.90	37.5%	35.8%	34.5%	31.8%	28.4%	0.90	35.9%	33.9%	32.2%	31.2%	28.9%
<i>Trench depth $H = 350 \mu\text{m}$</i>						<i>Trench depth $H = 40 \mu\text{m}$</i>					
0.10	4.8%	5.1%	5.9%	5.6%	5.2%	0.10	2.7%	2.9%	3.3%	3.6%	4.1%
0.20	15.6%	16.2%	13.3%	11.2%	9.8%	0.20	8.2%	10.7%	11.2%	10.4%	9.6%
0.30	33.0%	25.6%	20.6%	17.4%	15.2%	0.30	21.8%	21.1%	18.8%	16.8%	15.2%
0.40	45.5%	34.3%	28.1%	24.1%	21.4%	0.40	35.0%	29.9%	26.3%	23.5%	21.5%
0.50	52.2%	42.2%	35.7%	31.1%	27.9%	0.50	44.3%	38.0%	33.9%	30.6%	28.1%
0.60	56.1%	49.1%	42.8%	38.2%	34.3%	0.60	50.9%	45.2%	41.1%	37.8%	34.7%
0.70	58.7%	54.1%	48.9%	44.6%	40.0%	0.70	55.4%	51.3%	47.5%	44.2%	40.7%
0.80	60.2%	57.3%	53.4%	49.4%	44.0%	0.80	58.1%	55.4%	52.2%	49.2%	45.1%
0.90	60.9%	58.2%	55.8%	51.4%	45.6%	0.90	58.5%	55.0%	52.2%	50.4%	46.4%
<i>Trench depth $H = 500 \mu\text{m}$</i>						<i>Trench depth $H = 60 \mu\text{m}$</i>					
0.10	4.8%	5.2%	6.1%	5.8%	5.3%	0.10	2.0%	2.3%	2.8%	3.2%	3.9%
0.20	18.1%	18.9%	15.2%	12.7%	11.0%	0.20	9.0%	12.1%	12.8%	11.8%	10.8%
0.30	39.4%	30.3%	24.1%	20.3%	17.6%	0.30	26.1%	25.3%	22.4%	19.8%	17.9%
0.40	54.7%	41.0%	33.4%	28.5%	25.1%	0.40	42.9%	36.4%	31.9%	28.4%	25.7%
0.50	62.8%	50.7%	42.7%	37.2%	33.1%	0.50	54.6%	46.6%	41.5%	37.3%	34.1%
0.60	67.6%	59.1%	51.4%	45.8%	41.0%	0.60	62.9%	55.7%	50.6%	46.3%	42.3%
0.70	70.9%	65.3%	58.9%	53.6%	48.0%	0.70	68.5%	63.4%	58.6%	54.5%	50.1%
0.80	72.7%	69.1%	64.4%	59.6%	52.9%	0.80	71.9%	68.5%	64.6%	60.7%	55.5%
0.90	73.6%	70.3%	67.5%	62.0%	54.9%	0.90	72.4%	68.1%	64.6%	62.4%	57.2%
<i>Trench depth $H = 650 \mu\text{m}$</i>						<i>Trench depth $H = 80 \mu\text{m}$</i>					
0.10	4.8%	5.3%	6.3%	6.0%	5.3%	0.10	1.7%	2.0%	2.6%	3.0%	3.7%
0.20	19.7%	20.6%	16.5%	13.6%	11.7%	0.20	9.6%	13.1%	13.8%	12.7%	11.5%
0.30	43.6%	33.4%	26.5%	22.2%	19.2%	0.30	28.9%	27.9%	24.6%	21.7%	19.5%
0.40	60.8%	45.4%	36.9%	31.4%	27.6%	0.40	47.7%	40.4%	35.4%	31.4%	28.4%
0.50	69.9%	56.2%	47.3%	41.1%	36.6%	0.50	60.9%	51.9%	46.1%	41.5%	37.8%
0.60	75.3%	65.7%	57.0%	50.9%	45.5%	0.60	70.3%	62.2%	56.4%	51.6%	47.1%
0.70	78.9%	72.7%	65.5%	59.6%	53.3%	0.70	76.6%	70.8%	65.4%	60.8%	55.8%
0.80	80.9%	77.0%	71.7%	66.2%	58.7%	0.80	80.4%	76.7%	72.2%	67.9%	62.0%
0.90	82.0%	78.3%	75.2%	69.0%	61.0%	0.90	81.0%	76.2%	72.3%	69.7%	63.9%

Appendix C - Sample MCNP Code for Instrumentation

The following is an MCNP input card used to simulate response of the MND Mk III with 30% intrinsic thermal-neutron detection efficiency MSNDs to moderated ^{252}Cf in Ward Hall, Room 2. The major components of the MND were modeled in the simulations including the battery, FR4 electronics boards, CDBs, and case.

MND 3.2 with 30% MSNDs in Ward 2

```

C =====
C -----CELL CARD-----
C =====
C MSND
100 2 -2.329 -104          u=1 $ Active Fins
101 2 -2.329 -103          u=1 $ Bulk Si
102 1 -0.7638 103 104      u=1 $ LiF
103 0   -100              lat=1 fill=1 u=2 $ Unit Cell
104 0   -105              fill=2 u=3 $ MSND
C CDB & Shield
110 3 -3.97 -111 110       u=3 $ CDB
111 4 -0.001205 -110 #104  u=3 $ Air in CDB
112 5 -8.070 -112 111     u=3 $ Brass Shield
113 4 -0.001205 112       u=3 $ Air outside Shield
114 0   -113              lat=1 fill=3 u=4 $ Shielded CDB Unit Cell
C MND
120 0   -120              fill=4 u=5 $ MSND/CDB Array
121 6 -2.635 -121          u=5 $ FR4 MND Board
122 5 -8.070 -122 123     u=5 $ Brass Sheild MND
123 4 -0.001205 -123      u=5 $ Air in MND Shield
C Communications Boards and Battery
130 6 -2.635 -130          u=5 $ FR4 Comm1
131 6 -2.635 -131          u=5 $ FR4 Comm2
132 7 -2.247 -132          u=5 $ Battery (LiCoO2)
C Case
140 8 -0.90 -141 140       u=5 $ Case (ABS)
C Air in Case
150 4 -0.001205 -140 #132 #131 #130 #123 #122 #121 #120 u=5 $ Air
151 4 -0.001205 141        u=5 $ Air in universe 5
C MND Unit Cell
152 0   -141 TRCL=1       fill=5 $ MND Unit Cell
C Moderator Cask Ours - (smaller one)
300 4 -0.001205 -300       $ Source placement in detector
301 10 -11.35 -301 300     $ 0.5-cm lead
302 9 -7.92 -302 301      $ 1-cm Steel, Carbon
303 11 -0.93 -303 302     $ 2.5-cm HDPE
C Room 2 Walls
900 98 -2.30 900 -901     $ Concrete Walls
C World
998 4 -0.001205 #152 #900 303 -999 $ Air in World
999 0 999                 $ Outside World

```


C =====
C -----SURFACE CARDS-----
C =====

C MSND
100 RPP 0.00 0.0525 -0.5 0.5 -0.0015 0.0015 \$ Unit Cell
103 RPP 0.04 0.0525 -0.5 0.5 -0.0015 0.0015 \$ Bulk Si
104 RPP 0.0 0.04 -0.5 0.5 -0.0005 0.0005 \$ Front Si
105 RPP 0.00 0.0525 -0.5 0.5 -0.5 0.5 \$ MSND
C Ceramic Detector Board (Alumina) CDB & Tin-Brass Shield
110 RPP 0.00 0.20 -0.55 0.55 -0.55 0.55 \$ Inner CDB Wall
111 RPP -0.050 0.22 -0.6 0.6 -0.6 0.6 \$ Outer CDB Wall
112 RPP -0.050 0.24 -0.62 0.62 -0.62 0.62 \$ Outer Wall EM Sheild
113 RPP -0.050 0.24 -0.634 0.634 -0.634 0.634 \$ Shielded CDB UnitCell

C MND
120 RPP -0.050 0.24 -0.634 6.974 -0.634 4.438 \$ MSND Array
121 RPP -0.150 -0.050 -0.823 8.237 -0.823 4.627 \$ FR4 MND Board
122 RPP -0.3586 -0.15 -0.634 7.9512 -0.634 4.438 \$ MND Elec EM Sh out
123 RPP -0.3386 -0.15 -0.614 7.8312 -0.614 4.418 \$ MND Elec EM Sh in

C Communications Boards and Battery
130 RPP -0.8586 -0.7586 -0.823 8.897 3.467 4.627 \$ FR4 Com1
131 RPP -0.8586 -0.7586 7.627 8.897 -0.823 3.467 \$ FR4 Com2
132 RPP -0.9286 -0.3586 -0.703 7.627 -0.773 3.467 \$ Battery

C Case
140 RPP -1.11 0.24 -0.823 9.047 -0.823 4.677 \$ Case Inner Wall
141 RPP -1.25 0.38 -1.123 9.977 -1.123 4.977 \$ Case Outer Wall

C Moderator Cask
300 RCC 27.5 4.0 94.0 0 0 9 1.0 \$ 1.0cm diameter Void where source goes
301 RCC 27.5 4.0 94.0 0 0 9 1.5 \$ 0.5-cm lead
302 RCC 27.5 4.0 93.0 0 0 10 2.5 \$ 1.0-cm steel
303 RCC 27.5 4.0 90.0 0 0 13 5.0 \$ 2.5-cm HDPE

C Room 2 Walls/Floor/Ceiling
900 RPP -288.5 288.5 -350.5 350.5 0 304 \$ Interior of Walls
901 RPP -293.5 293.5 -355.5 355.5 -20 309 \$ Exterior of Walls

C World
999 so 5000 \$ universe

C =====
C -----DATA CARDS-----
C =====

C
C =====

C TRLC Transformations
TR1 -1.905 -0.4 91.0 1 0 0 1 0 0 0 1 1

C =====
C =====

C PHYSICS/CUT OFF
C =====

MODE N T A
IMP:N 1 26R 0
IMP:T 1 26R 0
IMP:A 1 26R 0
PHYS:N 6J 5 \$ NCIA, 5 use NCIA not Table

CUT:N 2J 0
 CUT:T J 0.01 0 \$ 10keV Energy Cut-off
 CUT:A J 0.01 0 \$ 10keV Energy Cut-off
 C =====
 C MATERIALS
 C =====
 M1 \$ 6-Lithium Fluoride RHO = 2.55 (Crystalline 95% Enriched)
 3006.70c -0.227995 \$ 6-Li
 3007.70c -0.013996 \$ 7-Li
 9019.70c -0.758009 \$ 19-F
 C
 M2 \$ NATURAL SILICON, RHO = 2.3290
 14028.70c -9.2223E-01 \$ 28-Si
 14029.70c -4.6850E-02 \$ 29-Si
 14030.70c -3.0920E-02 \$ 30-Si
 C
 M3 \$ Alumina, RHO = 3.97 PNNL
 8016 -0.470749 \$ 16-O
 13027 -0.529251 \$ 27-Al Aluminum
 C
 M4 \$ Air Dry, RHO = 0.001205 PNNL
 6000 -0.000124 \$ C
 7014 -0.755268 \$ 14-N
 8016 -0.231781 \$ 16-O
 18000 -0.012827 \$ Ar
 C
 M5 \$ Brass, RHO = 8.07 PNNL
 26000 -0.000868 \$ Fe
 29000 -0.665381 \$ Cu
 30000 -0.325697 \$ Zn
 50000 -0.002672 \$ Sn
 82000 -0.005377 \$ Pb
 C
 M6 \$ FR4, RHO = 2.3290 Simon Bolding Thesis
 1001 -0.010 \$ 1-H
 5010 -0.0053 \$ 10-B
 5011 -0.0147 \$ 11-B
 6000 -0.040 \$ C
 8016 -0.390 \$ 16-O
 13027 -0.010 \$ 27-Al
 14028 -0.230 \$ 28-Si
 29063 -0.140 \$ 63-Cu
 29065 -0.060 \$ 65-Cu
 35079 -0.050 \$ 79-Br
 35081 -0.050 \$ 81-Br
 M7 \$ Li-ion Battery LiCoO2, RHO = 2.247, RMD Report
 1000 1.81E-02 \$ H
 3006 2.23E-03 \$ 6-Li
 3007 2.76E-02 \$ 7-Li
 6000 2.99E-01 \$ C
 8016 5.95E-02 \$ O
 13027 2.31E-01 \$ Al
 27059 2.98E-02 \$ Co

29000 3.25E-01 \$ Cu
M8 \$ ABS Plastic, RHO = 0.9-1.53 wiki
1001 0.5152 \$ H
6000 0.4545 \$ C
7014 0.0303 \$ N

C

M9 \$ Steel Carbon, RHO = 7.82 PNNL
6000 -0.005 \$ C
26000 -0.995 \$ Fe

C

M10 \$ Lead, RHO = 11.35 PNNL
82000 -1.000000 \$ Pb

C

M11 \$ HDPE, RHO = 0.93 PNNL
1001 -0.143716 \$ H-1
6000 -0.856284 \$ C

C

M98 \$ Concrete, Ordinary (NIST), RHO = 2.3 g/cc PNNL
1001 -0.022100 \$ H
6000 -0.002484 \$ C
8016 -0.574930 \$ O
11023 -0.015208 \$ Na
12000 -0.001266 \$ Mg
13027 -0.019953 \$ Al
14000 -0.304627 \$ Si
19000 -0.010045 \$ K
20000 -0.042951 \$ Ca
26000 -0.006435 \$ Fe

C

C=====

C SOURCE - point isotropic source, Cf-252.

C=====

SDEF POS= 27.5 4.0 95.0 PAR= N ERG= D1

SP1 -3 1.180 1.03419 \$ Watt fission spectrum pg 11-4 MCNP6 manual

C=====

C TALLY

C=====

C --- EFFICIENCY -----

F18:A,T (100)

E18 0 0.3 5

C=====

C Problem Stuff

C=====

TF18 J J J J J J 3 J \$ Select bin I want most precision on

STOP F18 0.01 \$ Runs until 0.01 relative error achieved

The following Monte Python script was used to estimate the energy dependent neutron response for an MRD centrally mounted on a phantom. The input card is written by the Python script and then used in a Monte Carlo MCNP simulation. After the simulation is completed the detection efficiency is read out from the output file and stored in an Efficiency.o file. Then, the neutron energy is updated, a new input card is written, and a new simulation is performed. The process is repeated until all neutron energies defined in the Python script are simulated. The MRDs in this model were populated with 24, 1-cm² DS-MSNDs with intrinsic thermal-neutron detection efficiency of 69%.

```
#####
# Look @ Energy Response of on MND on Phantom
# 1. Define MND Geometry
# 2. Define Source Geometry
# 3. Generate MCNP input file MND.i
# 4. Run MCNP simulation
# 5. Read MCNP output, extract efficiency, write to Efficiency.o
# 6. Repeat
#
# Updated Taylor Ochs, 2018
#####
import os      # Allows for terminal commands
import shutil # Allows for file/directory manipulation
import numpy as np
import pathlib

os.system('cls') # not sure what this does
print("Running.")
#####
# Functions
#####
def inputfile(sxpos, sypos, i_file_name,E): # Write the Input File

    # Writes the input file based on what is sent to it"
    file = ["One MND 3.2 With 69% DS-MSNDs on ANSI 42.53 Phantom (Centrally Located)"]
    file.append("C ===== ")
    file.append("C -----CELL CARD----- ")
    file.append("C ===== ")
    file.append("C DSMSND ")
    file.append(" 100 2 -2.329 -101:-102:-104    u=1 $ Active Fins ")
    file.append(" 101 2 -2.329 -103                u=1 $ Bulk Si ")
    file.append(" 102 1 -1.0184 101 102 103 104    u=1 $ LiF ")
    file.append(" 103 0    -100                lat=1 fill=1 u=2 $ Unit Cell ")
    file.append(" 104 0    -105                fill=2 u=3 $ DS-MSND ")
    file.append("C CDB & Shield ")
    file.append(" 110 3 -3.97  -111 110                u=3 $ CDB ")
    file.append(" 111 4 -0.001205 -110 #104          u=3 $ Air in CDB ")

```

```

file.append(" 112 5 -8.070 -112 111          u=3 $ Brass Shield  ")
file.append(" 113 4 -0.001205 112          u=3 $ Air outside Shield")
file.append(" 114 0   -113   lat=1 fill=3 u=4 $ Shielded CDB Unit Cell ")
file.append("C MND
")
file.append(" 120 0   -120          fill=4 u=5 $ MSND/CDB Array  ")
file.append(" 121 6 -2.635 -121          u=5 $ FR4 MND Board  ")
file.append(" 122 5 -8.070 -122 123          u=5 $ Brass Shield MND  ")
file.append(" 123 4 -0.001205 -123          u=5 $ Air in MND Shield  ")
file.append("C Communications Boards and Battery
")
file.append(" 130 6 -2.635 -130          u=5 $ FR4 Comm1  ")
file.append(" 131 6 -2.635 -131          u=5 $ FR4 Comm2  ")
file.append(" 132 7 -2.247 -132          u=5 $ Battery (LiCoO2)  ")
file.append("C Case
")
file.append(" 140 8 -0.90 -141 140          u=5 $ Case (ABS)  ")
file.append("C Air in Case
")
file.append(" 150 4 -0.001205 -140 #132 #131 #130 #123 #122 #121 #120 u=5 $ Air ")
file.append(" 151 4 -0.001205 141          u=5 $ Air in universe 5 ")
file.append("C MND Unit Cell
")
file.append(" 152 0   -141 *TRCL=1          fill=5 $ MND Unit Cell  ")
file.append("C Phantom ANSI 42.53
")
file.append(" 400 11 -1.19 -400:-401:-402:-403 $ ASNI Phantom PMMA  ")
file.append("C World
")
file.append(" 998 0 #152 #400 -999 $ VOID IN WORLD  ")
file.append(" 999 0 999          $ OUTSIDE WORLD  ")
file.append("
")
file.append("C =====
")
file.append("C -----SURFACE CARDS-----
")
file.append("C =====
")
file.append("C DSMSND
")
file.append(" 100 RPP 0.00 0.15 -0.5 0.5 -0.0015 0.0015 $ Unit Cell  ")
file.append(" 101 RPP 0.00 0.06 -0.5 0.5 -0.0015 -0.001025 $ Back Fin 1  ")
file.append(" 102 RPP 0.00 0.06 -0.5 0.5 0.001025 0.0015 $ Back Fin 2  ")
file.append(" 103 RPP 0.06 0.09 -0.5 0.5 -0.0015 0.0015 $ Bulk Si  ")
file.append(" 104 RPP 0.09 0.15 -0.5 0.5 -0.000475 0.000475 $ Front Si  ")
file.append(" 105 RPP 0.00 0.15 -0.5 0.5 -0.5 0.5 $ DS-MSND  ")
file.append("C Ceramic Detector Board (Alumina) CDB & Tin-Brass Shield
")
file.append(" 110 RPP 0.00 0.20 -0.55 0.55 -0.55 0.55 $ Inner CDB Wall  ")
file.append(" 111 RPP -0.050 0.22 -0.6 0.6 -0.6 0.6 $ Outer CDB Wall  ")
file.append(" 112 RPP -0.050 0.24 -0.62 0.62 -0.62 0.62 $ Outer Wall EM Shield ")
file.append(" 113 RPP -0.050 0.24 -0.634 0.634 -0.634 0.634 $ Shielded CDB UnitCell")
file.append("C MND
")
file.append(" 120 RPP -0.050 0.24 -0.634 6.974 -0.634 4.438 $ MSND Array  ")
file.append(" 121 RPP -0.130 -0.050 -0.823 8.237 -0.823 4.627 $ FR4 MND Board  ")
file.append(" 122 RPP -0.3586 -0.13 -0.634 7.9512 -0.634 4.438 $ MND Elec EM Sh out ")
file.append(" 123 RPP -0.3386 -0.13 -0.614 7.8312 -0.614 4.418 $ MND Elec EM Sh in ")
file.append("C Communications Boards and Battery
")
file.append(" 130 RPP -0.8386 -0.7586 -0.823 8.897 3.467 4.627 $ FR4 Com1  ")
file.append(" 131 RPP -0.8386 -0.7586 7.627 8.897 -0.823 3.467 $ FR4 Com2  ")
file.append(" 132 RPP -0.9286 -0.3586 -0.703 7.627 -0.773 3.467 $ Battery  ")
file.append("C Case
")
file.append(" 140 RPP -1.11 0.24 -0.823 9.047 -0.823 4.677 $ Case Inner Wall ")
file.append(" 141 RPP -1.25 0.38 -1.123 9.977 -1.123 4.977 $ Case Outer Wall ")
file.append("C Phantom ANSI 42.53
")

```

```

file.append(" 400 RPP -7.5 7.5 -20.0 20.0 -37.5 22.5      $ Torso      ")
file.append(" 401 RPP -7.5 7.5 -7.5 7.5  22.5 37.5      $ Head       ")
file.append(" 402 RPP -7.5 7.5 -35.0 -20.0 7.5 22.5      $ Left Arm   ")
file.append(" 403 RPP -7.5 7.5 20.0 35.0  7.5 22.5      $ Right Arm  ")
file.append("C World                                           ")
file.append(" 999 so 200 $ universe                             ")
file.append("                                                    ")
file.append("C =====")
file.append("C -----DATA CARDS-----")
file.append("C =====")
file.append("C TRLC Transformations")
file.append("TR1  7.95 -4.427 1.927  -1 0 0 1 0  0 0 -1  1")
file.append("C =====")
file.append("C =====")
file.append("C PHYSICS/CUT OFF")
file.append("C =====")
file.append("MODE N T A")
file.append("IMP:N 1 22R 0")
file.append("IMP:T 1 1 1 1 1 0 17R 0")
file.append("IMP:A 1 1 1 1 1 0 17R 0")
file.append("PHYS:N 6J 5  $ NCIA, 5 use NCIA not Table")
file.append("CUT:N 2J 0")
file.append("CUT:T J 0.01 0 $ 10keV Energy Cut-off")
file.append("CUT:A J 0.01 0 $ 10keV Energy Cut-off")
file.append("C =====")
file.append("C MATERIALS")
file.append("C =====")
file.append("M1 $ 6-Lithium Fluoride RHO = 2.55 (Crystalline 95% Enriched)")
file.append(" 3006.70c -0.227995  $ 6-Li")
file.append(" 3007.70c -0.013996  $ 7-Li")
file.append(" 9019.70c -0.758009  $ 19-F")
file.append("C")
file.append("M2 $ NATURAL SILICON, RHO = 2.3290")
file.append(" 14028.70c -9.2223E-01 $ 28-Si")
file.append(" 14029.70c -4.6850E-02 $ 29-Si")
file.append(" 14030.70c -3.0920E-02 $ 30-Si")
file.append("C")
file.append("M3 $ Alumina, RHO = 3.97 PNNL")
file.append(" 8016  -0.470749  $ 16-O")
file.append(" 13027  -0.529251  $ 27-Al Aluminum")
file.append("C")
file.append("M4 $ Air Dry, RHO = 0.001205 PNNL")
file.append(" 6000  -0.000124  $ C")
file.append(" 7014  -0.755268  $ 14-N")
file.append(" 8016  -0.231781  $ 16-O")
file.append(" 18000 -0.012827  $ Ar")
file.append("C")
file.append("M5 $ Brass, RHO = 8.07 PNNL")
file.append(" 26000 -0.000868  $ Fe")
file.append(" 29000 -0.665381  $ Cu")
file.append(" 30000 -0.325697  $ Zn")
file.append(" 50000 -0.002672  $ Sn")
file.append(" 82000 -0.005377  $ Pb")

```

```

file.append("C ")
file.append("M6 $ FR4, RHO = 2.3290 Simon Bolding Thesis ")
file.append(" 1001 -0.010 $ 1-H ")
file.append(" 5010 -0.0053 $ 10-B ")
file.append(" 5011 -0.0147 $ 11-B ")
file.append(" 6000 -0.040 $ C ")
file.append(" 8016 -0.390 $ 16-O ")
file.append(" 13027 -0.010 $ 27-Al ")
file.append(" 14028 -0.230 $ 28-Si ")
file.append(" 29063 -0.140 $ 63-Cu ")
file.append(" 29065 -0.060 $ 65-Cu ")
file.append(" 35079 -0.050 $ 79-Br ")
file.append(" 35081 -0.050 $ 81-Br ")
file.append("M7 $ Li-ion Battery LiCoO2, RHO = 2.247 RMD Report")
file.append(" 3006 3.00E-05 $ 6-Li ")
file.append(" 3007 3.67E-04 $ 7-Li ")
file.append(" 6000 1.32E-01 $ C ")
file.append(" 8016 6.80E-02 $ O ")
file.append(" 9019 4.11E-02 $ F ")
file.append(" 12000 4.61E-03 $ Mg ")
file.append(" 13027 6.70E-01 $ Al ")
file.append(" 15031 3.13E-04 $ P ")
file.append(" 25055 3.30E-03 $ Mn ")
file.append(" 26000 1.13E-02 $ Fe ")
file.append(" 27059 5.21E-02 $ Co ")
file.append(" 28000 1.08E-02 $ Ni ")
file.append(" 29000 6.08E-03 $ Cu ")
file.append("M8 $ ABS Plastic, RHO = 0.9-1.53 wiki ")
file.append(" 1001 0.5152 $ H ")
file.append(" 6000 0.4545 $ C ")
file.append(" 7014 0.0303 $ N ")
file.append("C ")
file.append("M9 $ Steel 316 Stainless, RHO = 8.00 PNNL ")
file.append(" 6000 -0.000410 $ C ")
file.append(" 14000 -0.005070 $ Si ")
file.append(" 15031 -0.000230 $ 31-P ")
file.append(" 16000 -0.000150 $ S ")
file.append(" 24000 -0.170000 $ Cr ")
file.append(" 25055 -0.010140 $ Mn ")
file.append(" 26000 -0.669000 $ Fe ")
file.append(" 28000 -0.120000 $ Ni ")
file.append(" 42000 -0.025000 $ Mo ")
file.append("C ")
file.append("M10 $ Lead, RHO = 11.35 PNNL ")
file.append(" 82000 -1.000000 $ Pb ")
file.append("C ")
file.append("M11 $ PMMA, RHO = 1.19 PNNL ")
file.append(" 1001 -0.080538 $ 1-H ")
file.append(" 6000 -0.599848 $ C ")
file.append(" 8016 -0.319614 $ 16-O ")
file.append("C ")
file.append("C ===== ")
file.append("C SOURCE - COLL. 1.5m DISK Variable E ")

```

```

file.append("C =====")
file.append("SDEF POS= {0} [177] 0 PAR= N ERG= [177]" \
    .format(str(sxpos), str(sypos),str(E)))
file.append("   VEC= {0} [177] 0 DIR= 1" \
    .format(str(-1*sxpos), str(-1*sypos)))
file.append("   RAD= D1 AXS= {0} [177] 0 EXT= 0" \
    .format(str(-1*sxpos), str(-1*sypos)))
file.append("SI1  0 50          $ 50 cm radius (150cm diameter)  ")
file.append("SP1  -21 1          $ Radial Sampling in beam      ")
file.append("C =====")
file.append("C TALLY          ")
file.append("C =====")
file.append("C --- Counts -----")
file.append("F18:A,T (100)          ")
file.append("E18  0 0.3 5          ")
file.append("C --- Fluence in Cell -----")
file.append("F4:N (152)          ")
file.append("C =====")
file.append("C Problem Stuff      ")
file.append("C =====")
file.append("nps 1e7          ")

# Write Input File
MCNP_input_file = open(i_file_name,'w') # Creates DSMSND.i input file irl
for line in file: # Writes to input file.
    MCNP_input_file.write("%s\n" % line)
MCNP_input_file.close() # All done!

return;
#####
def mcnp(i_file_name, o_file_name): # Writes .bat file and Runs MCNP;

bat_file =["@ REM - Sets the MCNP Environment Variables for use in standard"]
bat_file.append("@ REM - command prompt. This will help with MatLab functionality.")
bat_file.append("@ set MCNPPATH=C:\\MCNP\\MCNP_CODE\\bin")
bat_file.append("@ PATH %MCNPPATH%;%PATH%")
bat_file.append("@ set DISPLAY=:0.0")
bat_file.append("@ set DATAPATH=C:\\MCNP\\MCNP_DATA")
bat_file.append("")
bat_file.append("mcnp6.exe i={0} o={177}" \
    .format(str(i_file_name),str(o_file_name)))
bat_file.append("erase run*")

BFile = open('MCNP.bat', 'w')
for line in bat_file:
    BFile.write("%s\n" % line)
BFile.close()

# Runs batch file
os.system('MCNP.bat')

return;

```



```

#####
def output(angle, o_file_name,E): # Pulls out information from output file

    output = open(o_file_name) # Opens output file.

    parsing = False      # Flippable variable.
    temp = []
    parsing = False
    for line in output:   # Starts going through the output file.

        if parsing:
            temp.append(line)
        if line.startswith( '1tally   18' ): # Looking for the efficiency tally.
            parsing = True
        elif line.startswith( '   total' ):
            parsing = False

    output.close() # Finished with output file.

    parsing = False
    for line in temp:
        if line.startswith( ' 5.0000E+00' ):
            line = '%s %s' % (E, line)
            with open("Efficiency.o", "a") as myfile:
                myfile.write(line)

    output = open(o_file_name) # Opens output file.

    parsing = False      # Flippable variable.
    temp = []
    parsing = False
    for line in output:   # Starts going through the output file.

        if parsing:
            temp.append(line)
        if line.startswith( ' cell 152' ): # Looking for the flux tally.
            parsing = True
        elif line.startswith( ' =====' ):
            parsing = False

    output.close() # Finished with output file.

    parsing = False
    for line in temp:
        if line.startswith( '      ' ):
            line = '%s %s' % (E, line)
            with open("Flux.o", "a") as myfile:
                myfile.write(line)

#####

```

```

# setting up file names
i_file_name = 'MNDonPhantom1inE.i' # You can change this
o_file_name = 'MNDonPhantom1inE.o' # You can change this too

efficiency = open('Efficiency.o', 'a')
efficiency.write("Energy Efficiency Rel_Error")
flux = open('Flux.o', 'a')
flux.write("Energy Flux Rel_Error")

# Incidence Angles setup
ang_res = 5. # Units degrees
ang_min = 0. # Minimum angle in degrees
ang_max = 0. # Maximum angle in degrees
ang_radius = 150.0 # Radius in cm of source arc path
pi = np.pi

angle = ang_min

with open('Energies.txt') as Efile:
    Energies = Efile.read().splitlines()

# Running through variables
while(angle <= ang_max):

    E_ctr = 0
    while E_ctr < len(Energies):
        E = str(Energies[E_ctr])

        sxpos = ang_radius*np.cos(angle*pi/180) + 0.075 # Update source position
        sypos = ang_radius*np.sin(angle*pi/180) # Update source position

        # Use functions
        inputfile(sxpos, sypos, i_file_name,E) # Make input file
        mcnpl(i_file_name, o_file_name) # Runs MCNP simulation
        output(angle,o_file_name,E) # Pull out the stuff i want and make output files

        # Check to see if output folder exists, if not make one
        pathlib.Path('./output').mkdir(parents=True, exist_ok=True)

        # Move and rename output file
        shutil.move(o_file_name, './output/'+ o_file_name + '_{0}fig_[177].o' \
            .format(str(E),str(angle)))

        print(E)
        E_ctr = E_ctr + 1

    #Updating Counters
    angle = angle + ang_res

efficiency.close() # Close effincinecy file
flux.close() # Close Flux files
print("Fin.")

```

Appendix D - Moving Source Measurements for WDD V.1

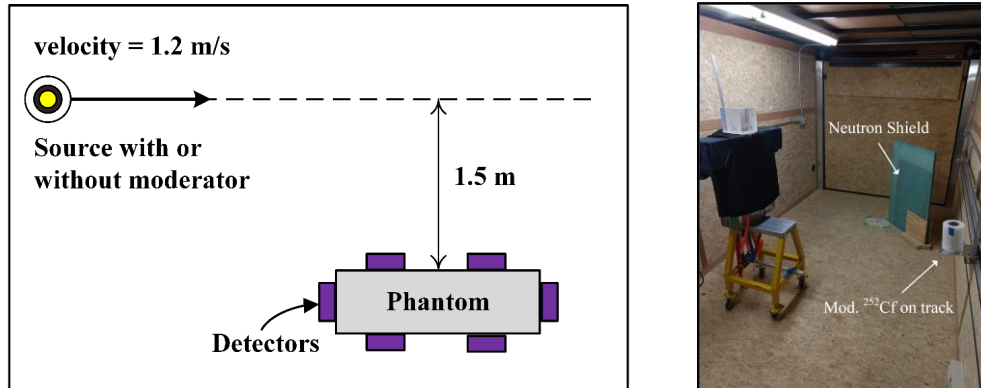


Fig. D-1. (Left) Diagram and (Right) image of experiment configuration for the WDD moving source measurements. Note that the background level with the source behind the neutron shield was 3x-6x the normal background level without a neutron source in the room.

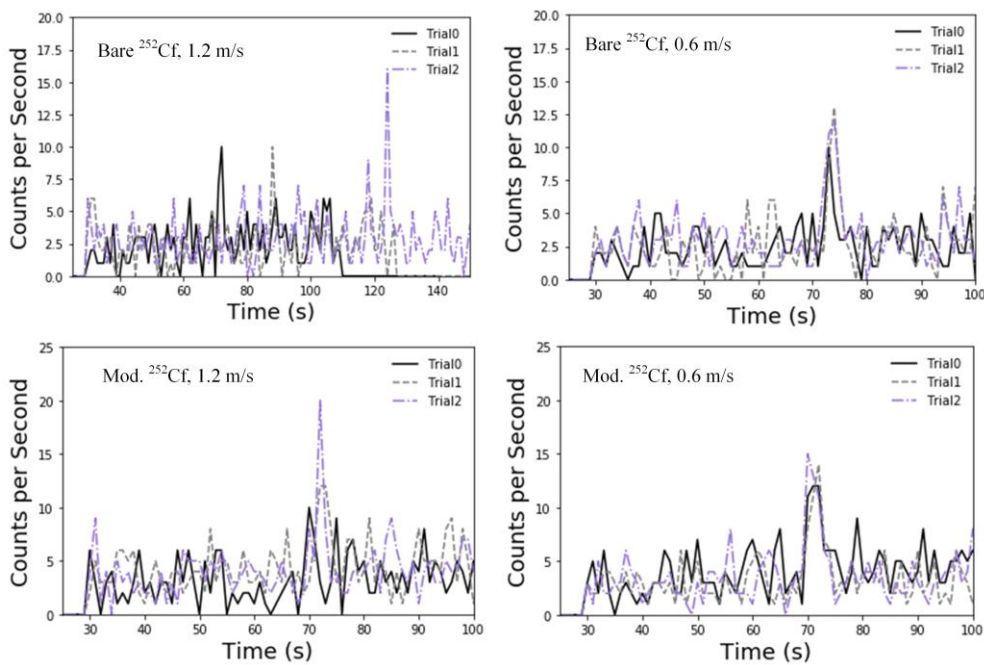


Fig. D-2. WDD V.1 response to a moving neutron source. The distance of closest approach was 1 m and occurred at approximately the 70-second mark except for the 1.2 m/s bare ^{252}Cf measurements. For Bare ^{252}Cf moving at 1.2 m/s the source movements occurred at approximately 70 s, 125 s, and 90 s for Trial0, Trial1, and Trial2, respectively.